

**ELECTROCHEMICAL STUDIES OF CONDUCTING
POLYMER AND ACTIVATED CARBON-BASED
VANADIUM SUBSTITUTED POLYOXOMETALATES
HYBRID ELECTRODE MATERIALS FOR ENERGY
APPLICATIONS**

Thesis

**Submitted in partial fulfillment of the requirements for the degree of
DOCTOR OF PHILOSOPHY**

by

ANJANA A.V.



**DEPARTMENT OF CHEMISTRY
NATIONAL INSTITUTE OF TECHNOLOGY KARNATAKA,
SURATHKAL, MANGALORE-575025**

MAY, 2023

**ELECTROCHEMICAL STUDIES OF CONDUCTING
POLYMER AND ACTIVATED CARBON-BASED
VANADIUM SUBSTITUTED
POLYOXOMETALATES HYBRID ELECTRODE
MATERIALS FOR ENERGY APPLICATIONS**

Thesis

**Submitted in partial fulfillment of the requirements for the degree of
DOCTOR OF PHILOSOPHY**

by

ANJANA A.V.

Reg. No: 187014CY001



NATIONAL INSTITUTE OF TECHNOLOGY KARNATAKA

SURATHKAL, MANGALURU-575025

MAY, 2023

DECLARATION

By the Ph.D. Research Scholar

I hereby *declare* that the Research Thesis entitled “**Electrochemical Studies of Conducting Polymer and Activated Carbon Based Vanadium Substituted Polyoxometalates Hybrid Electrode Materials for Energy Applications,**” which is being submitted to the *National Institute of Technology, Karnataka, Surathkal*, in partial fulfilment of the requirements for the award of the *Degree of Doctor of Philosophy in Chemistry* is a *bonafide report of the research work carried out by me*. The material contained in this thesis has not been submitted to any University or Institution for the award of any degree.



ANJANA A.V.

Register No.: 187014CY001

Department of Chemistry

Place: NITK Surathkal

Date: 22-05-2023

CERTIFICATE

This is to *certify* that the Research Thesis entitled “**Electrochemical Studies of Conducting Polymer and Activated Carbon Based Vanadium Substituted Polyoxometalates Hybrid Electrode Materials for Energy Applications,**” submitted by ANJANA A.V. (Register Number: 187014, Roll No. 187014CY001) as the record of the research work carried out by her, is *accepted* as the *Research Thesis submission* in partial fulfillment of the requirements for the award of the degree of *Doctor of Philosophy*.

Sib Sankar Mal
21/05/23

Dr. Sib Sankar Mal
Supervisor
Assistant Professor
Department of Chemistry
NITK Surathkal-575025

Udayakumar
21/05/23

Chairperson DRPC
(Signature with Date and Seal)
HEAD, DEPARTMENT OF CHEMISTRY
National Institute of Technology Karnataka
Surathkal, Srinivasnagar
MANGALORE- 575 025, D.K.

ACKNOWLEDGEMENT

The completion of this thesis would not have been possible without the support and cooperation of many people along the way. It gives me great pleasure to express my sincere gratitude to Dr. Sib Sankar Mal, Assistant Professor, Department of Chemistry, NITK, for accepting me under his wing as a research student, inspiring me to overcome challenges, mentoring me, standing by my side when I falter, sharing his dazzling insights that have driven me to progress well with research, and, most importantly, for being an elderly friend. It should be noted that my Ph.D. would not have been completed without his skillful mentoring.

I whole-heartedly thank my research progress assessment committee members Dr. Partha Pratim Das, Assistant Professor, Department of Physics, NITK and Dr. Saikat Dutta, Assistant Professor, Department of Chemistry, NITK merit my deepest gratitude for assessing my research time to time, enlightening me with their technical suggestions and motivations right through my entire research period.

I thank the Heads of the Department (present and past), all the faculty members of Department of Chemistry for their support. I also extend my acknowledgement to all the non-teaching staffs of Chemistry Department from whom I have received helps one way or the other, which were important right along the way. I thank Central Research Facility (CRF) of NITK for providing characterization resources.

I have to thank Dr. Debaprasad Shee, Professor, Department of Chemical Engineering, IIT Hyderabad for his technical suggestions during my research period. It would be unfair if I fail to recognize Dr Aranganathan and Dr Brijesh from whom I have received key helps that made me to comprehend my research field better and in turn motivated to flourish further in the research. I wish to thank my fellow research scholars Mrs. Deeksha Shetty, Ms. Navya S. Bhat, Ms. Nivedha Vinod, Mr. Abhijith M. B., Mr. Mohammad Aslam, Dr. Cindrella, Ms. Madhusree J E, Mr. Muhammed Anees P K and Mr. Nagaraj K for their support in completion of this work.

I would like to place a special acknowledgment to my lovely husband and my best friend Mr. Sreekanth P.V who bear with me patiently and stood with me like a pillar in my bad times.

It's my joy to extend my gratitude to my other co-workers and friends from physics and SOM department NITK, for their timely help and motivations. The stipend provided by NITK is sincerely acknowledged.

I express my heartfelt thanks to my lovely parents, brother, in laws and extended family members for their limitless love, cheers, motivation and support.

This thesis is dedicated to my parents

For their endless love, support and encouragement

Abstract

In the modern world, both the energy crisis and environmental degradation are serious issues. This is not just because the supply of fossil fuels, the major energy source, will run out in the near future but also because the combustion of fossil fuels pollutes the environment, particularly through the release of carbon dioxide and harmful pollutants. However, due to the unpredictability and intermittent nature of some renewable energies, such as wind and solar power, energy storage plays a noteworthy part in developing sustainable energy production systems. Batteries of all different types, including Ni/MH, Pb/PbO₂, and lithium-ion batteries, are examples of devices that are utilized to store electric energy and can deliver a high energy density. However, most batteries suffer from sluggish power delivery or absorption, so they cannot fulfill the demand for faster and higher-power energy. In this particular instance, a supercapacitor was developed to store and release energy with a high-rate capability. Because of its high-rate capability has been perfectly adapted to supply the electricity required by electric vehicles, tramways, diesel engine starting, wind turbines, computers, lasers, cranes, etc. In this study, we studied the influence of nanocomposites based on polyoxometalates (POMs) to enhance the performance of various supercapacitor devices. POMs are a kind of polyanionic molecular assemblies based on high-valent transition metal (Mo, V, W) oxide with large libraries of polynuclear metal oxygen clusters known for their strong negative charge, customizable sizes (usually on the nanometer to micrometer scale) and vast structural variation. Rapid, reversible multielectron redox conversions have been investigated in several fields, including pseudocapacitors. Researchers discovered that the synergistic effect between the elements successfully delivers higher device performance for energy storage applications.

Keywords: Supercapacitor, conducting polymer, Activated carbon, Polyoxometalate, Symmetric/Asymmetric devices, Specific capacitance, Energy density, Power density, Cycle stability.

CONTENTS

List of Figures.....	i
List of Schemes.....	ix
List of Tables.....	xi
Nomenclature.....	xiii
List of abbreviation.....	xv
CHAPTER 1	
1.1 Introduction.....	1
1.2 Construction of a supercapacitor.....	4
1.3 Taxonomy of supercapacitor.....	5
1.3.1 Electric Double Layer Capacitor (EDLC).....	6
1.3.2 Pseudocapacitor (PC).....	7
1.3.3 Hybrid supercapacitor (HSC).....	9
1.3.3.1 Composite Materials.....	10
1.3.3.2 Asymmetric materials.....	11
1.3.3.3 Battery-types Materials.....	11
1.4 Electrolytes for Supercapacitor.....	11
1.4.1 Liquid electrolytes.....	12
1.4.1.1 Aqueous electrolytes.....	12
Acid electrolytes.....	13
Basic electrolytes.....	13
Neutral electrolytes.....	13
1.4.1.2 Non-aqueous electrolytes.....	13

1.4.2 Solid electrolytes	14
1.5 Separator	14
1.6 Current Collector	15
1.7 Fundamental Supercapacitor Definitions and Measurements	15
1.7.1 Capacitance (C)	15
1.7.2 The energy density (ED) and efficiency.....	16
1.7.3 Power Density (PD)	17
1.7.4 Cycle life	17
1.8 Electrode Materials.....	17
1.8.1 Carbon materials.....	17
1.8.1.1 Zero-dimensional (0-D) carbon nanoparticles:.....	18
1.8.1.2 One-dimensional (1-D) carbon nanostructures:	18
1.8.1.3 Two-dimensional (2-D) nanosheets:.....	19
1.8.1.4 Three-dimensional (3-D) porous architectures:.....	19
1.8.2 Faradic materials.....	19
1.8.2.1 Polyoxometalates (POMs).....	19
1.8.2.2 Conducting polymer (CP)	21
Polypyrrole (PPy)	23
Polyaniline (PANI).....	23
Polyindole (PIn)	24
1.9 Applications	25
1.9.1 Public sector applications	25
1.9.2 Automobiles and transportation application.....	26
1.9.3 Defense and military applications.....	27

1.9.4 Computers and memory backup chips.....	27
1.9.5 Medical and industrial applications	27
CHAPTER 2	
2.1 Literature Review	29
2.2 Scope of the Work.....	32
2.3 Objectives of the Work.....	33
2.4 Organization of the Thesis	34
2.5 Materials and Methods.....	35
2.5.1 Materials	35
2.5.2 Synthesis.....	36
2.5.2.1 Synthesis of polypyrrole (PPy), $H_4[PVMo_{11}O_{40}]$, and $H_5[PV_2Mo_{10}O_{40}]$.	36
2.5.2.2 Integration of the hybrid PPy/ $H_4[PVMo_{11}O_{40}]$	36
2.5.2.3 Integration of the hybrid PPy/ $H_5[PV_2Mo_{10}O_{40}]$	38
2.5.2.4 Synthesis of polyindole (PIn).	38
2.5.2.5 Synthesis of the PIn/ $PVMo_{11}$ Composite.	38
2.5.2.6 Synthesis of the PIn/ PV_2Mo_{10} Composite.....	39
2.5.2.7 Synthesis of polyaniline (PANI).....	40
2.5.2.8 Synthesis of $PVMo_{11}@PAni$ electrode material.....	40
2.5.2.9 Synthesis of $PV_2Mo_{10}@PAni$ electrode material	41
2.5.2.10 Synthesis of $K_5H_2[PV_4W_8O_{40}]$	42
2.5.2.11 Synthesis of $K_5H_2[PV_4W_8O_{40}]$ onto polypyrrole backbone	42
2.5.2.12 Synthesis of $K_5H_2[PV_4W_8O_{40}]$ onto polyaniline backbone.....	43
2.5.2.13 Synthesis of $K_5H_2[PV_4W_8O_{40}]$ onto activated carbon backbone.....	43

2.5.2.14 Synthesis of potassium 11-vanadomanganate ($K_5Mn^{IV}V_{11}O_{32}.10H_2O$) and potassium 13-vanadomanganate ($K_7Mn^{IV}V_{13}O_{38}.18H_2O$).....	44
2.5.2.15 Synthesis of activated carbon - $K_5Mn^{IV}V_{11}O_{32}.10H_2O$ (AC-MnV ₁₁) or activated carbon - $K_7Mn^{IV}V_{13}O_{38}.18H_2O$ (AC-MnV ₁₃) electrode	44
2.6 Electrode Preparation and Fabrications	44
2.7 Characterizations and Measurements	45
2.7.1 Structural and surface characterizations.....	45
2.7.1.1 Fourier transforms Infrared spectroscopy (FTIR)	45
2.7.1.2 Thermal gravimetric analysis (TGA)	46
2.7.1.4 FESEM and EDS analysis.....	47
2.7.1.5 Brunauer-Emmett-Teller (BET)	48
2.7.1.6 X-ray photoelectron spectroscopy (XPS)	48
2.7.2. Electrochemical characterizations.....	49
2.7.2.1 Cyclic voltammetry (CV)	50
2.7.2.2 Galvanostatic charge-discharge (GCD).....	50
2.7.2.3 Electrochemical impedance spectroscopy (EIS)	51
2.7.2.4 Trasatti method.....	52
CHAPTER 3	
3.1 Structural, chemical, and morphological characterizations	53
3.1.1 Fourier transform infrared spectroscopy	53
3.1.2 Thermogravimetry analysis	54
3.1.3 X-ray diffraction spectroscopy.....	56
3.1.4 Field emission scanning electron microscopy	57
3.1.5 Energy-Dispersive X-ray spectroscopy	58

3.1.6 Brunauer–Emmett–Teller	59
3.2 Electrochemical measurements	59
3.2.1 CV studies	60
3.1.2 GCD studies	61
3.1.3 EIS studies.....	64
3.1.4 Cycle stability studies.....	66
CHAPTER 4	
4 Result and Discussion	67
4.1 Structural, chemical, and morphological characterizations	67
4.1.1 Fourier transform infrared spectroscopy	67
4.1.2 Thermogravimetry analysis	68
4.1.3 X-ray diffraction spectroscopy.....	69
4.1.4 Field emission scanning electron microscopy and Energy-Dispersive X-ray spectroscopy	70
4.1.5 Brunauer–Emmett–Teller	71
4.2 Electrochemical measurements	72
4.2.1 CV studies and GCD studies	72
4.2.2 EIS studies.....	75
4.2.3 Cycle stability studies.....	76
CHAPTER 5	
5 Result and Discussion	79
5.1 Structural, chemical, and morphological characterizations	79
5.1.1 Fourier transform infrared spectroscopy	79
5.1.2 Thermogravimetry analysis	80

5.1.3 X-ray diffraction spectroscopy.....	81
5.1.4 Field emission scanning electron microscopy	82
5.1.5 Energy-Dispersive X-ray spectroscopy	83
5.1.6 Brunauer–Emmett–Teller	84
5.2 Electrochemical measurements	85
5.2.1 CV studies	86
5.2.2 GCD studies	88
5.2.3 EIS studies.....	92
5.2.4 Cycle stability studies.....	95
CHAPTER 6	
6 Result and Discussion	97
6.1 Structural, chemical, and morphological characterizations	97
6.1.1 Fourier transform infrared spectroscopy	97
6.1.2 Thermogravimetry analysis	98
6.1.3 X-ray diffraction spectroscopy.....	99
6.1.4 Field emission scanning electron microscopy and Energy-Dispersive X-ray spectroscopy	100
6.1.5 High Resolution Transmission Electron Microscopy	101
6.1.6 Brunauer–Emmett–Teller	102
6.1.7 X-ray photoelectron spectroscopy	103
6.2 Electrochemical measurements	105
6.2.1 CV studies	105
6.2.2 GCD studies	106
6.2.3 EIS studies.....	109

6.2.4 Cycle stability studies.....	111
CHAPTER 7	
7 Result and Discussion	113
7.1 Structural, chemical, and morphological characterizations.....	113
7.1.1 Fourier transform infrared spectroscopy	113
7.1.2 Thermogravimetry analysis	114
7.1.3 X-ray diffraction spectroscopy.....	115
7.1.4 Field emission scanning electron microscopy and Energy-Dispersive X-ray spectroscopy	116
7.1.5 Brunauer–Emmett–Teller	117
7.1.6a X-ray photoelectron spectroscopy	119
7.1.6b X-ray photoelectron spectroscopy	120
7.2 Electrochemical measurements	121
7.2.1 CV studies	122
7.2.2 GCD studies	125
7.2.3 EIS studies.....	127
7.2.4 Cycle stability studies.....	129
CHAPTER 8	
8 Result and Discussion	131
8.1 Structural, chemical, and morphological characterizations.....	131
8.1.1 Fourier transform infrared spectroscopy	131
8.1.2 Thermogravimetry analysis	132
8.1.3 X-ray diffraction spectroscopy.....	134

8.1.4 Field emission scanning electron microscopy and Energy-Dispersive X-ray spectroscopy	135
8.1.5 Brunauer–Emmett–Teller	137
8.1.5 X-ray photoelectron spectroscopy	138
8.2 Electrochemical measurements	139
8.2.1 CV studies	139
8.2.2 GCD studies	140
8.2.3 EIS studies.....	142
8.2.4 Cycle stability studies.....	144
CHAPTER 9	
9.1 Summary.....	147
9.2 Conclusions.....	150
9.3 Scope for future work.....	151
List of Publication.....	153
Journal publications from other projects	153
Patents.....	155
Workshops and Conferences Attended.....	155
References	157

List of Figures

Fig. 1.1 Ragone plot for various energy storage devices (Saikia et al. 2020)	3
Fig. 1.2 Representation of SC (Murali et al. 2021).	4
Fig. 1.3 Representation of SC flowchart.	5
Fig. 1.4 A mechanism of the electrochemical double-layer capacitor (Vangari et al. 2013).	6
Fig. 1.5 Mechanism of the PC materials (Vangari et al. 2013).	8
Fig. 1.6 Mechanism of the electrochemical hybrid capacitor (Vangari et al. 2013)	10
Fig. 1.7 Charge storage mechanism of supercapacitors, (a) EDLCs, (b) pseudocapacitors, and (c) hybrid supercapacitors (Swain et al. 2021).....	11
Fig. 1.8 Flowchart for Classification of electrolytes (Zhong et al. 2015).	12
Fig. 1.9 A) Polyhedron representation of Keggin structure, B) Polyhedron representation of Well-Dawson structure	20
Fig. 1.10 Polymerization Mechanism of pyrrole to polypyrrole	23
Fig. 1.11 Polymerization Mechanism of aniline to polyaniline.....	24
Fig. 1.12 Polymerization Mechanism of indole to polyindole	25
Fig. 1.13 The fundamental design of a SC device and its diverse uses in energy storage. (Forouzandeh et al. 2022)	28
Fig. 2.1 Schematic representation of $[\text{PVMo}_{11}\text{O}_{40}]^{4-}$ / $[\text{PV}_2\text{Mo}_{10}\text{O}_{40}]^{5-}$ impregnated into the PPy surface.....	38
Fig. 2.2 Synthesis of the PIn/PV ₂ Mo ₁₀ and PIn/PVMo ₁₁	40
Fig. 2.3 Synthesis of the PVMo ₁₁ @PAni and PV ₂ Mo ₁₀ @PAni.....	42
Fig. 2.4 Synthesis of the PV ₄ W ₈ /PPy.	43
Fig. 2.5 A) Symmetric and B) Asymmetric representation of the supercapacitor cell setup.	45
Fig. 2.6 FTIR setup (Image courtesy: Chemistry department, NITK, Surathkal)	47
Fig. 2.7 TGA setup (Image courtesy: Chemistry department, NITK, Surathkal)	46

Fig. 2.8 Powder XRD setup (Image courtesy: Central research facility (CRF), NITK, Surathkal).....	46
Fig. 2.9 FESEM and EDS setup (Image courtesy: Central research facility (CRF), NITK, Surathkal).....	47
Fig. 2.10 BET setup (Image courtesy: Central research facility (CRF), NITK, Surathkal).....	48
Fig. 2.11 XPS setup (Image courtesy: Advanced material research center. IIT Mandi) ..	49
Fig. 2.12 Electrochemical workstation setup (Image courtesy: (Chemistry department, NITK, Surathkal) ..	49
Fig. 3.1 FTIR of a) PPy, b) pure H ₄ [PVMo ₁₁ O ₄₀], c) pure H ₅ [PV ₂ Mo ₁₀ O ₄₀], d) PPy-H ₄ [PVMo ₁₁ O ₄₀] composite and e) PPy-H ₅ [PV ₂ Mo ₁₀ O ₄₀].....	54
Fig. 3.2 TGA curves of a) PPy, b) pure H ₄ [PVMo ₁₁ O ₄₀], c) pure H ₅ [PV ₂ Mo ₁₀ O ₄₀], d) PPy-H ₄ [PVMo ₁₁ O ₄₀] composite, and e) PPy-H ₅ [PV ₂ Mo ₁₀ O ₄₀].....	55
Fig. 3.3 P-XRD patterns of a) PPy, b) pure H ₄ [PVMo ₁₁ O ₄₀], c) pure H ₅ [PV ₂ Mo ₁₀ O ₄₀], d) PPy- H ₄ [PVMo ₁₁ O ₄₀] composite, and e) PPy-H ₅ [PV ₂ Mo ₁₀ O ₄₀].....	56
Fig. 3.4 FESEM image of a) PPy, b) pure H ₄ [PVMo ₁₁ O ₄₀], c) pure H ₅ [PV ₂ Mo ₁₀ O ₄₀], d) PPy- H ₄ [PVMo ₁₁ O ₄₀] composite, and e) PPy-H ₅ [PV ₂ Mo ₁₀ O ₄₀] composite.	57
Fig. 3.5 EDS spectra of two composite electrodes, namely a) PPy- H ₄ [PVMo ₁₁ O ₄₀] composite, b) PPy-H ₅ [PV ₂ Mo ₁₀ O ₄₀] composite c) H ₄ [PVMo ₁₁ O ₄₀], d) H ₅ [PV ₂ Mo ₁₀ O ₄₀] and e) Pure PPy.....	58
Fig. 3.6 Nitrogen adsorption/desorption isotherm of PPy- H ₄ [PVMo ₁₁ O ₄₀] composite and PPy-H ₅ [PV ₂ Mo ₁₀ O ₄₀] composite.	59
Fig. 3.7 Cyclic voltammograms and Oxidation-reduction peaks of PPy and two composite potentials at 10 mV s ⁻¹ scan rates at 0.1 M H ₂ SO ₄	60
Fig. 3.8 GCD curves of a) PPy-H ₄ [PVMo ₁₁ O ₄₀] and b) PPy-H ₅ [PV ₂ Mo ₁₀ O ₄₀]. c) The capacitance at current densities of 0.2–10 A g ⁻¹ . d) the Ragone plots at various current densities of 0.2–10 A g ⁻¹	62

Fig. 3.9 a) Nyquist plots, and b) Bode plots for the PPy, PPy-H ₄ [PVMo ₁₁ O ₄₀], and PPy-H ₅ [PV ₂ Mo ₁₀ O ₄₀] electrodes.	64
Fig. 3.10 The equivalent circuit is used for fitting the Nyquist plots.	65
Fig. 3.11 a) Cycle stability of PPy, PPy-H ₄ [PVMo ₁₁ O ₄₀], and PPy-H ₅ [PV ₂ Mo ₁₀ O ₄₀] electrodes, and b) 1st and last cycles for PPy-H ₅ [PV ₂ Mo ₁₀ O ₄₀] after 4500 cycles at 500 mV s ⁻¹	66
Fig. 4.1 FTIR of A) PIn, B) PIn/PVMo ₁₁ , and C) PIn/PV ₂ Mo ₁₀	67
Fig. 4.2 TGA of pure PIn, PVMo ₁₁ , PV ₂ Mo ₁₀ , PIn/PVMo ₁₁ , and PIn/PV ₂ Mo ₁₀	68
Fig. 4.3 PXRD pattern of PIn, PVMo ₁₁ , PV ₂ Mo ₁₀ , PIn/PVMo ₁₁ , and PIn/PV ₂ Mo ₁₀	70
Fig. 4.4 FESEM images of A) pure PIn, B) PIn/PVMo ₁₁ , and C) PIn/PV ₂ Mo ₁₀ . EDS spectra of D) pure PIn, E) PIn/PVMo ₁₁ , and F) PIn/PV ₂ Mo ₁₀ , respectively.	71
Fig. 4.5 shows the N ₂ adsorption/desorption isotherm of PIn, PIn/PVMo ₁₁ , and PIn/PV ₂ Mo ₁₀ materials.	71
Fig. 4.6 CVs of (A)PIn, (C) PIn/PVMo ₁₁ , and (E) PIn/PV ₂ Mo ₁₀ at various scan rates. GCD curves of (B)PIn, (D) PIn/PVMo ₁₁ , and (F) PIn/PV ₂ Mo ₁₀	74
Fig. 4.7 A) specific capacitance vs current density, B) Power density vs energy density of PIn/PVMo ₁₁ , and PIn/PV ₂ Mo ₁₀ electrodes.	75
Fig. 4.8 Nyquist plots for the PIn, PIn/PVMo ₁₁ , and PIn/ PV ₂ Mo ₁₀ electrodes.	76
Fig. 4.9 a) Cycle stability of PIn, PIn/PVMo ₁₁ , and PIn/PV ₂ Mo ₁₀ . (b) 1 st three cycles of PIn/PV ₂ Mo ₁₀ based on GCD at 4 A g ⁻¹	76
Fig. 5.1 FTIR spectrum of A) PVMo ₁₁ , B) PV ₂ Mo ₁₀ , C) pure PANi, D) PVMo ₁₁ @PANi, and E) PV ₂ Mo ₁₀ @PANi	79
Fig. 5.2 TGA spectrum of PANi, PVMo ₁₁ , B) PV ₂ Mo ₁₀ , PVMo ₁₁ @PANi, and PV ₂ Mo ₁₀ @PANi	80
Fig. 5.3 PXRD patterns of A) PANi, B) H ₅ [PV ₂ Mo ₁₀ O ₄₀], C) H ₄ [PVMo ₁₁ O ₄₀], D) PV ₂ Mo ₁₀ @PANi, and E) PVMo ₁₁ @PANi electrode.	82

Fig. 5.4 FESEM micrograms of A) pure PANi, B) PVMo ₁₁ @PANi, and C) PV ₂ Mo ₁₀ @PANi electrode.....	83
Fig. 5.5 EDS spectra of A) pure PANi, B) PVMo ₁₁ @PANi, and C) PV ₂ Mo ₁₀ @PANi.....	84
Fig. 5.6 A) Nitrogen adsorption/desorption isotherms and B) Pore volume graph of pure PANi, PVMo ₁₁ @PANi, and PV ₂ Mo ₁₀ @PANi electrode.....	85
Fig. 5.7 Cyclic Voltammetry at various scan rates a) pure PANi, b) PVMo ₁₁ @PANi, and c) PV ₂ Mo ₁₀ @ PANi at 0.25 M H ₂ SO ₄ electrolyte medium.....	87
Fig. 5.8 A) Comparative GCD plot of pure PANi, PVMo ₁₁ @PANi, and PV ₂ Mo ₁₀ @PANi electrode at a constant charge/discharge current density at 3 A g ⁻¹ . GCD plot of B) PVMo ₁₁ @PANi and C) PV ₂ Mo ₁₀ @PANi electrode materials.....	89
Fig. 5.9 A) plot of capacitance vs. current densities and B) Ragone plot of pure PANi, PVMo ₁₁ @PANi, and PV ₂ Mo ₁₀ @PANi electrodes.....	92
Fig. 5.10 Comparative Nyquist plots of pure PANi, PVMo ₁₁ @PANi, and PV ₂ Mo ₁₀ @PANi.....	93
Fig. 5.11 (A) The equivalent circuit is used for fitting the Nyquist plots. (B) The fabricated supercapacitors are energizing red light-emitting diodes.....	95
Fig. 5.12 (a) Cycle stability plot of the variation of average capacitance vs. cycle number of pure PANi, PVMo ₁₁ @PANi, and PV ₂ Mo ₁₀ @PANi electrodes at 500 mV s ⁻¹ . (b) 1 st and last cycle stability plot of PVMo ₁₁ @PANi.....	95
Fig. 6.1 FTIR spectra of PPy, PV ₄ W ₈ , and PV ₄ W ₈ /PPy.....	98
Fig. 6.2 Thermogravimetry plot of PPy, PV ₄ W ₈ , and PV ₄ W ₈ /PPy.....	98
Fig. 6.3 PXRD spectra of A) PPy, and PV ₄ W ₈ /PPy and B) PV ₄ W ₈	100
Fig. 6.4 FESEM images of A) PV ₄ W ₈ , B) PV ₄ W ₈ /PPy, C) EDS of PV ₄ W ₈ , and D) PV ₄ W ₈ /PPy.....	101
Fig. 6.5 TEM image of PV ₄ W ₈ /PPy at a different scale.....	102
Fig. 6.6 Nitrogen adsorption/desorption isotherms of pure PPy pure PV ₄ W ₈ and PV ₄ W ₈ /PPy nanohybrid composite.....	103
Fig. 6.7 a) XPS survey b) N 1s c) W 4f d) C 1s e) V 2p f) O 1s and g) P 2p.....	104

Fig. 6.8 A) CV plot of all electrodes at 100 mV/s scan rate. B) the bar chart of the specific capacitance at the 100 mV s ⁻¹ scan rate at 0.25M H ₂ SO ₄	106
Fig. 6.9 GCD curves of A) asymmetric PV ₄ W ₈ -PPy/PPy, B) current density vs capacitance of PPy, PV ₄ W ₈ , and PV ₄ W ₈ /PPy at 0.4 A g ⁻¹ C) Capacitance vs Current density graph for all system. D) Energy Density vs Power density graph for all systems.	108
Fig. 6.10 EIS graph for PV ₄ W ₈ , PV ₄ W ₈ /PPy (symmetric), and PV ₄ W ₈ -PPy/PPy (asymmetric).	109
Fig. 6.11 (A) and (B) are the fabricated supercapacitors are energizing red and yellow light-emitting diodes by PV ₄ W ₈ -PPy/PPy (asymmetric) composite (C) The equivalent circuit is used for fitting the Nyquist plots.	110
Fig. 6.12 A) Cycle stability of symmetric PPy, PV ₄ W ₈ , and PV ₄ W ₈ -PPy/PPy (asymmetric) and B) 1 st and final cycle of PV ₄ W ₈ -PPy/PPy electrodes at a current density of 500 mV s ⁻¹ after 4500 cycles.	111
Fig. 7.1 a) FTIR spectra of PANI, PV ₄ W ₈ , PANI-PV ₄ W ₈ , and AC-PV ₄ W ₈	113
Fig. 7.2 TGA Curve of PANI, PV ₄ W ₈ , PANI-PV ₄ W ₈ , and AC-PV ₄ W ₈	114
Fig. 7.3 Powder XRD spectrum of A) PANI, PANI-PV ₄ W ₈ , and AC-PV ₄ W ₈ B) PV ₄ W ₈	115
Fig. 7.4 FESEM image of a) PANI-PV ₄ W ₈ , and b) AC-PV ₄ W ₈ , EDS spectrum of c) PANI-PV ₄ W ₈ , and d) AC-PV ₄ W ₈	117
Fig. 7.5 Nitrogen adsorption/desorption isotherms of A) pure PANI, PV ₄ W ₈ , PANI-PV ₄ W ₈ , B) pure AC and AC-PV ₄ W ₈ composite. Pore volume curve for C) pure PANI, PV ₄ W ₈ , and PANI-PV ₄ W ₈ D) pure AC and AC-PV ₄ W ₈ composite.	118
Fig. 7.6 XPS spectrum of PANI-PV ₄ W ₈	120
Fig. 7.7 XPS spectrum of AC-PV ₄ W ₈	121
Fig. 7.8 A) CV graph for PANI-PV ₄ W ₈ and AC-PV ₄ W ₈ at 30mV s ⁻¹ scan rate B) CV graph for PANI-PV ₄ W ₈ at different scan rate, C) CV graph for PANI-PV ₄ W ₈ , PV ₄ W ₈ , and PANI at a 10mV s ⁻¹ scan rate and D) CV graph for AC-PV ₄ W ₈ at various scan rates.	123

Fig. 7.9 (a) Plots of C^{-1} vs $v^{0.5}$ (b) Plots of C vs $v^{-0.5}$ (c) pseudocapacitance capacitance (%) and EDL (%) for AC-PV ₄ W ₈ by Trasatti method (d) Plots of C^{-1} vs $v^{0.5}$ (e) Plots of C vs $v^{-0.5}$. (f) pseudocapacitance capacitance (%) and (%) for PANI-PV ₄ W ₈ by the Trasatti method.....	124
Fig. 7.10 A) GCD graph for PANI-PV ₄ W ₈ at different current densities, B) GCD graph for AC-PV ₄ W ₈ at different current densities, and C) GCD graph for PANI-PV ₄ W ₈ , PV ₄ W ₈ , and PANI at 1 A g ⁻¹ , D) Ragone plot for PANI-PV ₄ W ₈ and AC-PV ₄ W ₈	127
Fig. 7.11 A) EIS graphs for PANI-PV ₄ W ₈ and AC-PV ₄ W ₈ and B) Original and fitted EIS data of PANI-PV ₄ W ₈ with knee frequency and equivalent Circuit.	128
Fig. 7.12 (a) and (b) are the fabricated supercapacitors that energize red and yellow light-emitting diodes.....	129
Fig. 7.13 A) Cycle stability of PANI-PV ₄ W ₈ and B) First and final cycle of PANI-PV ₄ W ₈	130
Fig. 8.1 FTIR of MnV ₁₁ , AC-MnV ₁₁ , MnV ₁₃ , and AC-MnV ₁₃	131
Fig. 8.2 a) All TGA curves, TGA curves, and DTA graphs of b) MnV ₁₁ , c) MnV ₁₃ , d) AC-MnV ₁₁ , and e) AC-MnV ₁₃	133
Fig. 8.3 Powder XRD patterns for AC, AC-MnV ₁₁ , AC-MnV ₁₃	134
Fig. 8.4 FESEM image for A) MnV ₁₁ , B) MnV ₁₃ , C) AC-MnV ₁₁ , D) AC-MnV ₁₃ and E) Pure AC.....	135
Fig. 8.5 EDS image for A) MnV ₁₁ , B) MnV ₁₃ , C) AC-MnV ₁₁ , and D) AC-MnV ₁₃	136
Fig. 8.6 A) N ₂ adsorption/desorption isotherm. B) pore distribution of AC, AC-MnV ₁₁ , and AC-MnV ₁₃	137
Fig. 8.7 XPS image of AC-MnV ₁₁ a) V 2p b) Mn 2p c) C 1s and d) O.....	138
Fig. 8.8 CV graph of a) AC-MnV ₁₁ and b) AC-MnV ₁₃ at various scan rates at 0.1M H ₂ SO ₄ electrolyte solution.....	140
Fig. 8.9 Galvanic charge-discharge curves of (a) AC-MnV ₁₁ and (b) AC-MnV ₁₃ -based supercapacitors at different current densities, c) capacitance retention vs current density,	

and d) Ragone plot (Specific Energy vs Power) for AC-MnV ₁₁ and AC-MnV ₁₃ electrodes.	142
Fig. 8.10 Nyquist Plot for AC-MnV ₁₁ and AC-MnV ₁₃	143
Fig. 8.11 (A) and (B) are the fabricated supercapacitors that are energizing red and yellow light-emitting diodes by AC-MnV ₁₁ composite, (C) The equivalent circuit is used for fitting the Nyquist plots.	144
Fig. 8.12 a) cycle stability of AC-MnV ₁₁ , AC-MnV ₁₃ , MnV ₁₁ and MnV ₁₃ stability response of (b) first cycle of AC-MnV ₁₁ , and (b) last cycle of AC-Mn ₁₁ over 10000 cycles at a fixed current density of 10 A g ⁻¹	145

List of Schemes

Scheme 2.1 Schematic representation of $[\text{PVMo}_{11}\text{O}_{40}]^{4-}$ / $[\text{PV}_2\text{Mo}_{10}\text{O}_{40}]^{5-}$ impregnated into the PPy surface. Orange octahedra = V, Red = O, and gray octahedra=Mo.	37
Scheme 2.2 Schematic representation of the synthesis of the PIn/PVMo ₁₁ and PIn/PV ₂ Mo ₁₀	39
Scheme 2.3 Possible reaction mechanism of polyaniline- $[\text{PV}_2\text{Mo}_{10}\text{O}_{40}]^{5-}$	41

List of Tables

Table 1.1 Comparison of Capacitor, Batteries, Fuel Cell, SC	3
Table 1.2 Comparison of Capacitor, Batteries, Fuel Cell, SC.	8
Table 1.3 Theoretical and experimental capacitance values of common CPs (Snook et al. 2011).	22
Table 3.1 Fitting Data of Equivalent Circuit Elements Obtained by Nyquist plots.....	65
Table 3.2 Fitting Data Obtained from Bode plots.....	66
Table 5.1 Elemental composition of PANi, PVMo ₁₁ @PANi, and PV ₂ Mo ₁₀ @PANi from EDS.....	84
Table 5.2 Specific capacitance of pure PANi, PVMo ₁₁ @PANi, and PV ₂ Mo ₁₀ @PANi electrodes at various scan rate.....	88
Table 5.3 Specific capacitance of pure PANi, PVMo ₁₁ @PANi, and PV ₂ Mo ₁₀ @PANi.....	90
Table 5.4 R _{ct} , R _s , and R _p values of PANi, PVMo ₁₁ @PANi, and PV ₂ Mo ₁₀ @PANi electrode from Nyquist plot.....	94

Nomenclature

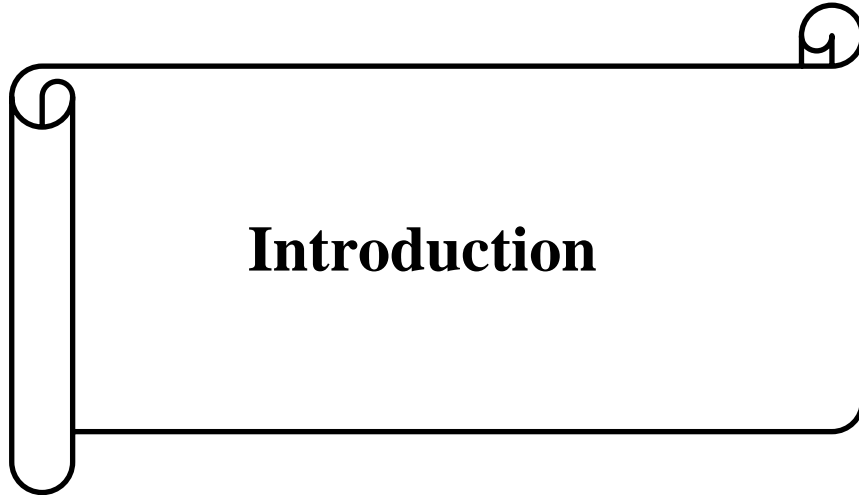
Symbol	Description
ϵ_r	Relative permittivity of the electrolyte
ϵ_0	Permittivity of free space,
A	Surface area of the electrode
d	Thickness of HDL
Q	Electrical charge
V_R	Voltage
I	Discharge current
<i>m</i>	Mass of active material
<i>v</i>	Scan rate
ΔV	Potential window
C_s	Specific capacitance
X	Hetero atom
M	Addenda atom
Δt	Discharge time
Re(C)	Real part of the capacitance
Im(C)	Complex part of the capacitance
ω	Angular frequency
f_0	Cut-off frequency
C_{Tf}	Cell capacitance
R_s	Circuit resistance
R_{ct}	Series resistance
f	Minimum frequency applied
C^{-1}	Reciprocal of gravimetric capacitance
$v^{1/2}$	Square root of scan rate

List of abbreviations

Abbreviation	Full Form
PD	Power density
ESCs	Electrochemical supercapacitors
SCs	Supercapacitors
ED	Energy density
EDLC	Electric double layer capacitor
PC	Pseudocapacitor
HC	Hybrid capacitor
HSC	Hybrid supercapacitor
HDL	Helmholtz double layer
CP	Conducting polymer
ESR	Equivalent series resistance
SSA	Specific surface area
C	Capacitance
CNTs	Carbon nanotubes
AC	Activated carbon
G	Graphene
CNFs	Carbon nanofibers
GO	Graphene oxide
rGO	Reduced graphene oxide
POMs	Polyoxometalates
PPy	Polypyrrole
PANI/PAni	Polyaniline
PTh	Polythiophene
PIn	Polyindole
PEDOT	Poly (3,4- ethylenedioxythiophene)
UPS	Uninterruptible power supply

SSDs	Solid-state drives
AMR	Automated meter reading
HPA	Heteropolyacid
FTIR	Fourier transforms Infrared spectroscopy
TGA	Thermal gravimetric analysis
XRD	X-ray diffraction
FESEM	Field emission scanning electron microscopy
EDS	Energy dispersive X-ray Analysis
BET	Brunauer-Emmett-Teller
XPS	X-ray photoelectron spectroscopy
HR-TEM	High Resolution Transmission Electron Microscopy
CV	Cyclic voltammetry
GCD	Galvanostatic charge-discharge
EIS	Electrochemical impedance spectroscopy
CRF	Central research facility

CHAPTER 1



Introduction

1.1 Introduction

Energy has become an irreplaceable factor in our lives. The current condition states that fossil fuels in various forms, like coal, oil, and natural gas, constitute 81% of total energy consumption. The situation will get complex due to the increase in population, an elevated standard of living, and the growth of numerous industries (Rajaiitha et al. 2022). Current fossil fuel reserves are estimated to sustain the demands of the global economy for 40, 60, and 156 years for oil, natural gas, and 156 coal, respectively. (Iordache et al. 2013; Luo et al. 2015).

The rapid depletion of these non-renewable energy sources severely threatens the worldwide economy. Fossil fuels are a serious environmental threat because they release greenhouse gases and other pollutants, making them unfriendly to the environment. These atmospheric gases emit cause air pollution and global warming. Consequently, it is vital to identify an alternative source of renewable energy. Due to economic and environmental concerns, numerous studies have been investigated to determine an alternate energy source (Midilli et al. 2005).

In order to produce energy sustainably, renewable energy sources like wind and solar power are essential replacements for fossil fuels. Sustainable energy is easily accessible and environment-friendly but cannot fulfill storage for the distant future because of its irregularities (Panwar et al. 2011). Consequently, the energy must be stored in a ready-to-use manner. Batteries are one of the energy storage technologies capable of storing significant quantities of energy and supplying power to consumer electronics and automobiles. However, batteries have a low power density (PD), which makes them unsuitable in the vehicle.

Future energy demand growth requires low-cost, lightweight, flexible, non-toxic, environmentally friendly, high-performance energy storage devices. Scientists worldwide

are researching ways to store and convert energy using sustainable energy materials. Electrochemical supercapacitors (ESCs) can store energy and deliver it even at higher rates than conventional batteries because of their high PD, fast charge-discharge process, and long life.

Supercapacitors (SCs), also referred to as electric double-layer capacitors or ultracapacitors, are energy storage devices with extremely high capacity and low internal resistance that can store and deliver energy at relatively higher rates than batteries due to the energy storage mechanism, which involves a simple charge separation at the electrode-electrolyte interface (Wu et al. 2010a). SC is made of two electrodes, an electrolyte, and a separator that electrically separates the two electrodes; electrode material is the essential part of an SC. The most effective applications for SCs demand applications with a short load cycle and high dependability. Some examples of such applications are energy recapture sources like forklifts, load cranes, and electric cars, as well as power quality enhancement. SCs have unique qualities that make them suitable short-term energy storage devices when combined with batteries or fuel cells. They can provide high power and store energy gained from braking (Iro et al. 2016). Due to their high power, SCs can bridge the short period between a power outage and the activation of backup generators. SCs have more energy than regular capacitors but less than batteries or fuel cells. Surface area, electrical conductivity, electrode wetting, and electrolyte permeability affect an electrode's electrochemical performance (Rajagopalan and Chung 2014).

Ragone Plot is a chart (as shown in **Fig. 1.1**) for all energy sources that give highly important information on power and energy density (ED). It is a chart initially created to compare the performance of batteries but has been used to explain and compare all energy storage systems. This graph's horizontal axis depicts ED, and the vertical axis depicts PD. The ED is the energy stored per unit mass (or per unit volume) or "how much" energy is accessible. The PD is the quantity of energy delivered per unit of time, or "how rapidly" energy may be produced.

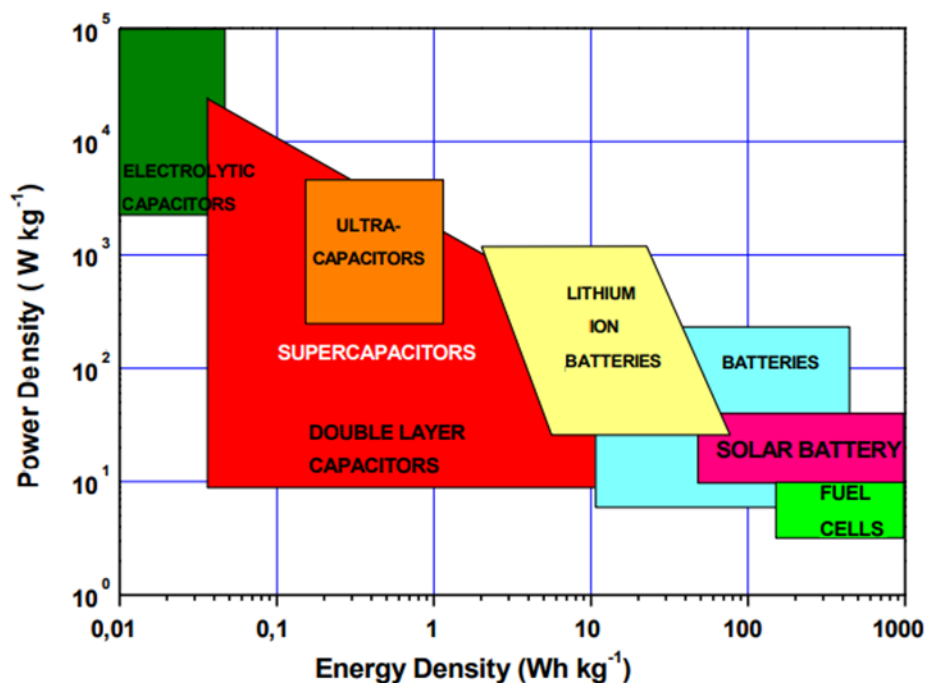


Fig. 1.1 Ragone plot for various energy storage devices (Saikia et al. 2020)

Contrary to batteries and fuel cells, conventional capacitors have a high PD but a poor ED. In SCs, charge or discharge occurs very fast, but they cannot store much energy. Whereas battery and fuel cells can save more energy, charge, and discharge take longer (Table 1.1) (Bose et al.,2010).

Table 1.1 Comparison of Capacitor, Batteries, Fuel Cell, SC

Parameters	Supercapacitors	Capacitors	Batteries	Fuel Cells
Charge/discharge time	1 ms ⁻¹ s	1ps ⁻¹ ms	1-10 hours	Not applicable
Cycle life (Cycles)	Up to 1 million	More than 1million	150-2,000	Not applicable
Energy Density (Wh kg ⁻¹)	0.5-20	0.001-.03	30-265	500-2,000
Power Density (W kg ⁻¹)	5,000-10,000	>5,000	100-3,000	--1,000

Cost per Wh	10-20	0.10-1.00	01-02	0.035-0.005
Operating Voltage (V)	1.0-5.5	6-800	1.2-4.2	0.6-0.7
Operating Temperature (°C)	-40 to +85	-20 to +100	-20 to +65	+65 to +1000

1.2 Construction of a supercapacitor

An SC is a device with two electrodes connected ionically by an electrolyte and separated by an ion-permeable membrane, or separator, as shown in **Fig. 1.2**. An electrolyte is a medium comprised of both positive and negative ions. A collector layer is formed on the two electrode's outer surfaces to link the electrodes to the electrical circuit. Based on their technique of charge storage, SCs may be divided into three categories: electric double-layer capacitor (EDLC), pseudocapacitor (PC), and hybrid capacitor (HC) (**Fig. 1.7**) (Wang et al. 2012).

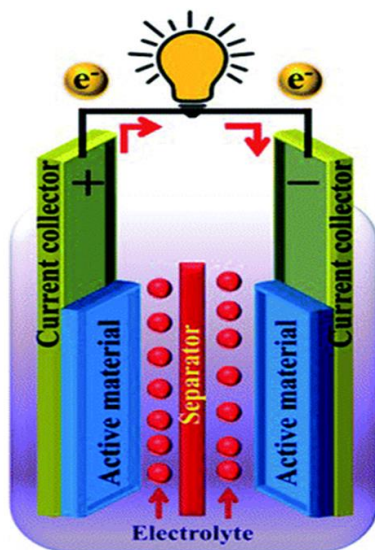


Fig. 1.2 Representation of SC (Murali et al. 2021).

1.3 Taxonomy of supercapacitor

The operation of a SC is predicated on the storage and distribution of ions from the electrolyte to the electrode's surface area. Based on the energy storage method, there are three kinds of SCs:

- ❖ Electrochemical double-layer supercapacitor (EDLC)
- ❖ Pseudocapacitor (PC)
- ❖ Hybrid supercapacitor (HSC)

The following flowchart provides a classification of SCs and a list of the materials used to make SCs.

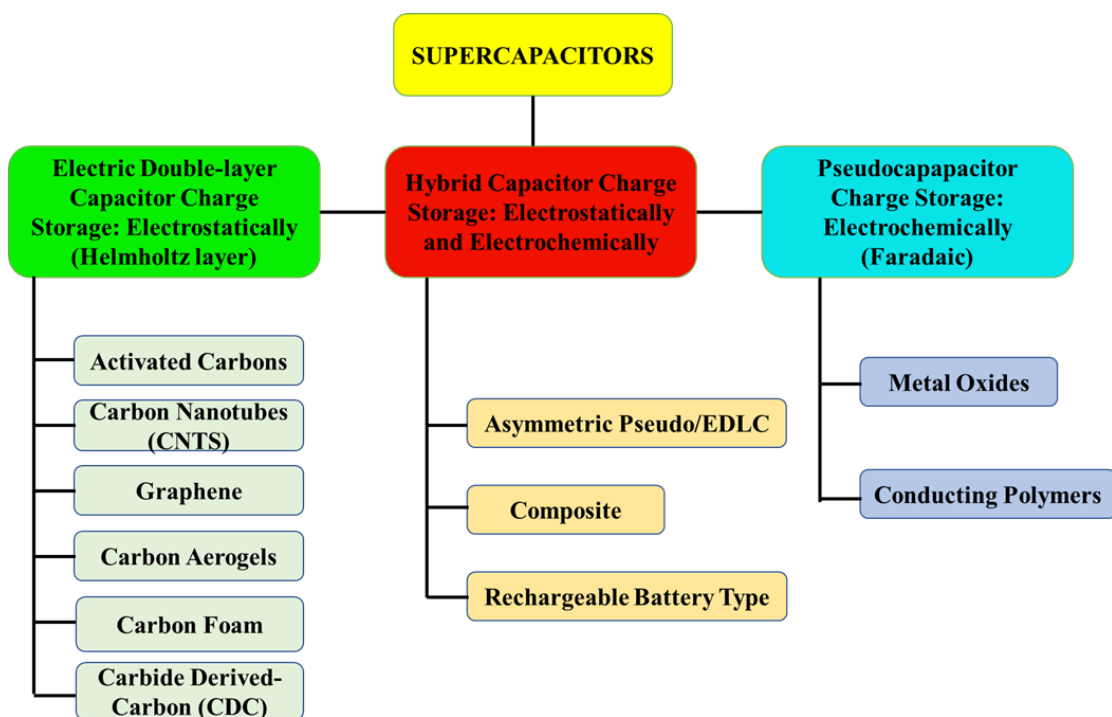


Fig. 1.3 Representation of SC flowchart.

1.3.1 Electric Double Layer Capacitor (EDLC)

EDLC stores energy electrostatically by separating ions to create a Helmholtz double layer (HDL) at the electrolyte-electrode interface (**Fig. 1.4**). When a voltage is placed between the electrodes of a SC, charges build up on the electrodes, creating a potential difference across the electrolytic medium. Due to the potential difference, positively and negatively charged ions diffuse toward electrodes with opposing charges. In the meantime, solvent molecules become polarized and adhere to the electrode's surface, preventing the combination of oppositely charged ions with the electrodes. Consequently, an electrostatic double layer (or HDL) forms at the electrode's surface. Each HDL may be seen as a conventional capacitor with polarized solvent molecules serving as the dielectric media (González et al. 2016).

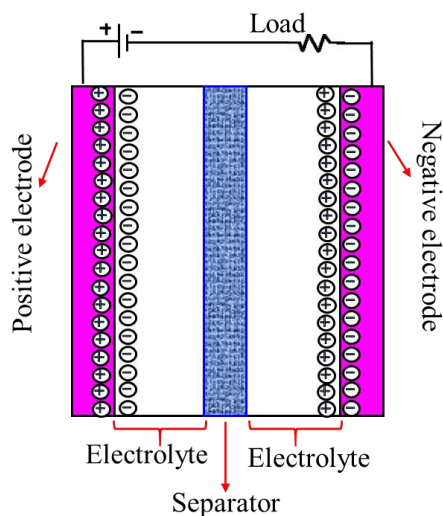


Fig. 1.4 A mechanism of the electrochemical double-layer capacitors (Vangari et al. 2013).

The capacitance across the HDL is expressed as,

$$C = \frac{\epsilon_0 \epsilon_r A}{d} \quad 1.1$$

ϵ_r is the relative permittivity of the electrolyte, where ϵ_0 is the permittivity of free space, A surface area of the electrode, and d thickness of HDL (in order of nm).

According to **Equation 1.1**, the electrode material's porosity influences the electrode's a SC's charge-storage capacity increases as the electrode material's porosity influences the electrode's effective surface area. The connection between a SC's porosity and capacitance has been investigated by Largeot and colleagues (Largeot et al. 2008). They discovered that pores that are close to that of ions yield the maximum capacitance values. According to their findings, EDLC is capacitance depends on the total porous volume and pore size distribution. In EDLC, there is no chemical reaction; therefore, it can withstand many charging-discharging cycles and has a very long lifespan. Due to its rapid charge-discharge capabilities can also provide a suitably significant PD (Choudhary et al. 2020).

1.3.2 Pseudocapacitor (PC)

PC store charge by a faradic process involving charge transfer between electrode and electrolyte. When a voltage is supplied to a PC, reduction, and oxidation occur on the electrode material, resulting in the transfer of charge across the double layer and the flow of faradic current in the SC cell. Electrolyte ions typically move to the negatively and positively charged electrodes when a voltage is placed between the two electrodes of a SC, forming a double layer at the electrolyte electrode interface. Certain adsorbed ions of the electrolyte penetrate the double layer and transmit their charge to the electrodes in a PC.

This charge transfer is caused by the highly reversible redox reaction processes, intercalation, and electro-sorption. The faradic technique PCs utilize enables them to attain larger specific capacitance and energy densities than EDLCs. Conductive polymers and metal oxides are examples. Due to its faradic nature, there is a reduction-oxidation process, much like in batteries. As a result, these materials suffer from a lack of stability during cycling and a low PD. **Fig. 1.5** represents the Mechanism of the PC (Chen and Dai 2013).

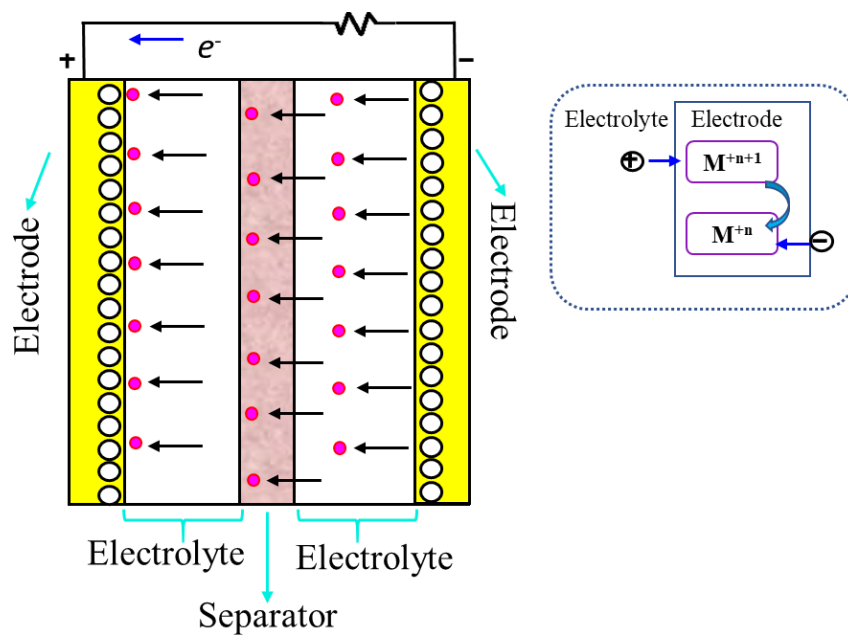


Fig. 1.5 Mechanism of the PC materials (Vangari et al. 2013).

Table 1.2 Comparison of Capacitor, Batteries, Fuel Cell, SC.

Parameters	EDLC	PC
Charge storage mechanism	Helmholtz double layer formation at electrode/electrolyte interface	Faradic charge transfer throughout the bulk of the interface
Specific capacitance	0.1-0.2 F m ⁻²	1-5 F m ⁻²
Electrode materials	Carbon materials.	Conducting polymers (CPs) or transition metal oxides/sulfides.

Specific energy	1.5–4 Wh kg ⁻¹	10–15 Wh kg ⁻¹
Charging/Discharging time	0.3–30 s	More than 30 s
Cycle life (in thousand cycles)	100–1000	20–100

1.3.3 Hybrid supercapacitor (HSC)

The EDLC and PC are the two components that go into making up a hybrid SC. It consists of two asymmetric electrodes, one with high pseudocapacitance and the other with high electrostatics double-layer capacitance. The pseudocapacitive electrode increases the supercapacitor's specific capacitance, operating voltage, and specific energy. On the other hand, the double-layer capacitive electrode offers superior cyclic stability and larger specific power. The electrochemical performance of a hybrid SC can be said to be significantly improved in this way. As a result, the majority of scientists and researchers focused nowadays on the many different forms of hybrid SCs. It is also possible to manufacture hybrid SCs by combining composites of pseudocapacitive materials with double-layer capacitive materials (Choudhary et al. 2020). The Mechanism of the hybrid SC is given in **Fig. 1.6**.

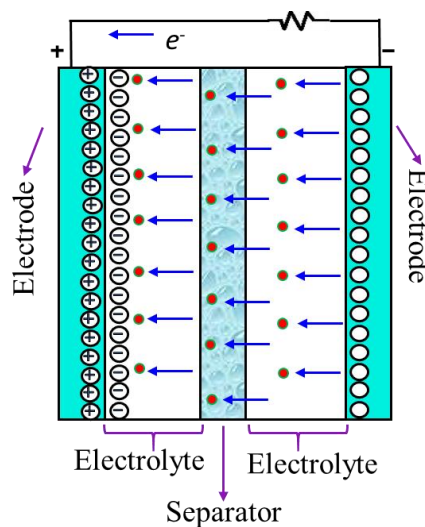


Fig. 1.6 Mechanism of the electrochemical hybrid capacitor (Vangari et al. 2013)

Researchers are now concentrating their efforts on three distinct categories of hybrid SCs, which may be separated from one another based on the arrangements of their electrodes: composite, asymmetric, and battery-type SCs.

1.3.3.1 Composite Materials

In composite electrodes, metal oxides or a CP are combined with carbon-based materials to create a single electrode with a physical and chemical charge storage mechanism. Carbon-based materials provide a capacitive double layer of charge and a high specific surface area, enhancing the interaction between pseudocapacitive materials and electrolytes. A pseudocapacitive substance increases the capacitance of a composite electrode via a Faradaic reaction, and it forms two distinct binary and ternary composite forms of composites. Binary composites employ two different electrode materials, whereas ternary composites use three different electrode materials to produce a single electrode (Halper and Ellenbogen 2006).

1.3.3.2 Asymmetric materials

Asymmetric hybrids combine non-Faradic processes with Faradic processes through linking and EDLC with a PC electrode. The carbon substance acts as the negative electrode. At the same time, metal oxide or CP is the positive electrode (Iro et al. 2016).

1.3.3.3 Battery-types Materials

Battery-type hybrids link two electrodes similarly to asymmetric hybrids, but they are distinct in that they couple a SC electrode with a battery electrode. This particular design, which combines the energy properties of batteries with the power, cycle life, and recharges durations of SCs, responds to the demand for more energy SCs and higher-power batteries. Nickel hydroxide, lead dioxide, and LTO ($\text{Li}_4\text{Ti}_5\text{O}_{12}$) have been the primary materials studied, with activated carbon as the other electrode (Halper and Ellenbogen 2006).

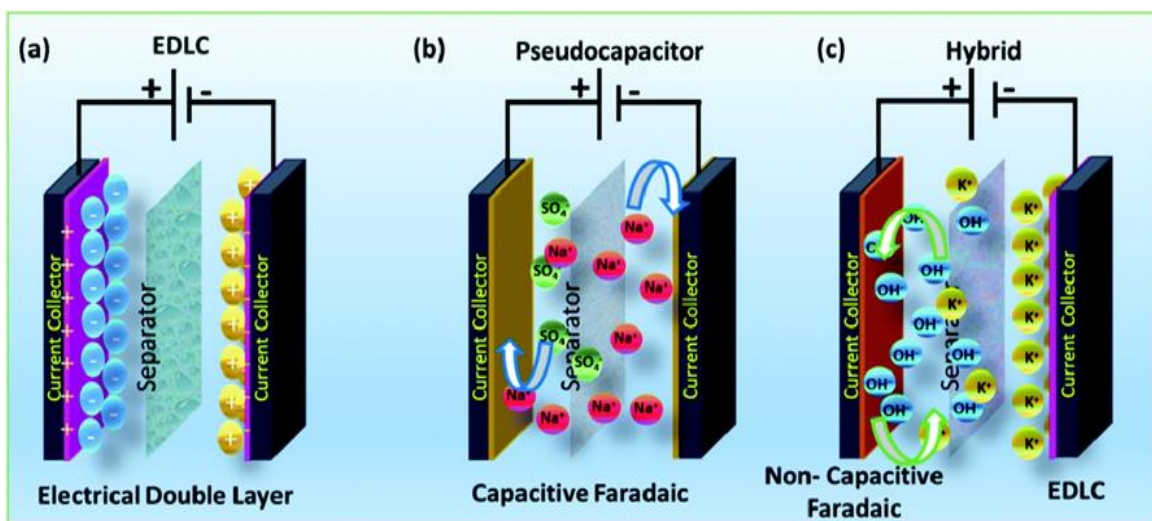


Fig. 1.7 Charge storage mechanism of SCs, (a) EDLCs, (b) pseudocapacitors, and (c) HSC (Swain et al. 2021).

1.4 Electrolytes for Supercapacitor

An electrolyte is significant in SC applications. It supplies a conductive medium between the two electrodes. It determines several of the supercapacitor's distinctive

features, including ED, PD, cyclic stability, equivalent series resistance (ESR), potential window, etc. To improve the quality of a SC, its electrolyte ought to have high conductivity, a broad electrochemically stable high thermal stability, a potential window, and low toxicity. The classification of the electrolytes is given below in flowchart **Fig. 1.8**.

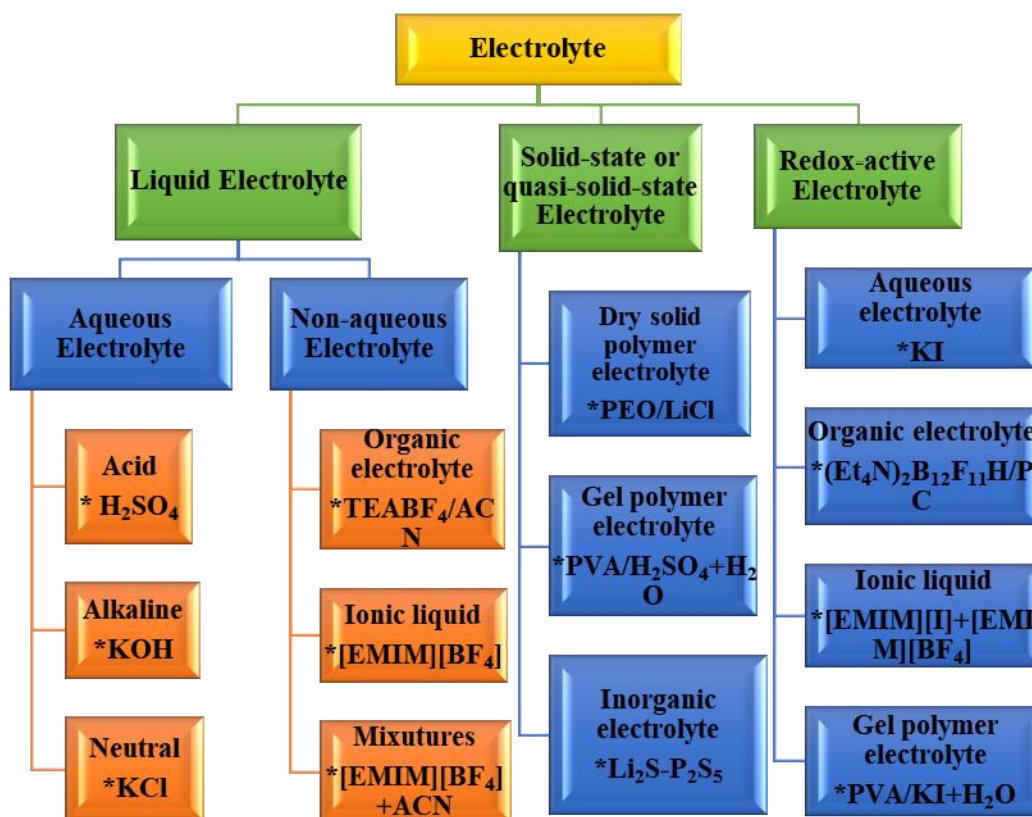


Fig. 1.8 Flowchart for Classification of electrolytes (Zhong et al. 2015).

1.4.1 Liquid electrolytes

It contains an electrolyte that has a liquid phase. It is further classified into two types, aqueous and nonaqueous electrolytes.

1.4.1.1 Aqueous electrolytes

The most often employed electrolytes for SC applications are aqueous. It offers a SC with enormous specific capacitance and high conductivity (on the order of 1 S cm^{-1}). In addition, it can be handled quickly and requires no special conditions. However, its small

potential window ~ 1.2 V) reduces ED and limits its use. The aqueous electrolyte can be further categorized into acidic, basic, and neutral categories (Zhong et al. 2015).

Acid electrolytes

Acid is an excellent electrical conductor; several researchers utilize acidic electrolytes to fabricate SCs. The most common acidic electrolyte is 1 M H_2SO_4 . Because of the corrosive nature of the acidic electrolyte, which can lead to the breakdown of the current collector, one must be extremely careful while selecting both the electrolyte and the current collector for an acidic electrolyte (Shao et al. 2018).

Basic electrolytes

Basic electrolytes are naturally non-corrosive, which enables the use of low-cost metals (such as Ni, Co, etc.) as the current collector. Since it has high ionic conductivity (0.6 S/cm), 6 M KOH is the most common aqueous electrolyte with a basic charge. However, several articles on SCs include other basic electrolytes such as LiOH, NaOH, $\text{Co}(\text{OH})_2$, etc. (Krishnan et al. 2015).

Neutral electrolytes

Neutral electrolytes are non-corrosive and have a relatively broad potential window. Several researchers working on SCs have therefore utilized a wide range of neutral electrolytes, including K_2SO_4 , KCl, LiCl, KNO_3 , NaCl, Li_2SO_4 , Na_2SO_4 , LiClO_4 , NaNO_3 , $\text{Ca}(\text{NO}_3)_2$, etc. The most often employed neutral aqueous electrolyte is Na_2SO_4 (Yan et al. 2014).

1.4.1.2 Non-aqueous electrolytes

Non-aqueous electrolytes are favored over aqueous electrolytes from a business perspective because non-aqueous electrolytes have a wider voltage window (2.5–2.8 V) and are less corrosive than aqueous electrolytes. The ED and PD of the SC are greatly increased due to their wide voltage window.

Often used organic electrolytes include triethylmethylammonium tetrafluoroborate (TEMABF₄), tetraethylammonium tetrafluoroborate (TEABF₄), and spiro- (1,10)-bipyrrolidinium tetrafluoroborate (SBPBF₄). These electrolytes are typically dissolved in organic solvents such as acetonitrile. This type of electrolyte is rarely extensively employed despite having a high ED and PD. This is due to the several drawbacks of this type of electrolyte, including its low conductivity, low capacitance, toxicity, flammability, and expensiveness of components (Zhong et al. 2015).

1.4.2 Solid electrolytes

The development of electrochemical energy devices based on solid-state electrolytes has attracted significant interest in recent years. The solid-state electrolytes can serve not only as the ionic conducting media but also as the electrode separators in the system. The primary benefits of solid-state electrolytes are the ease of packaging and fabrication methods for ESCs and the absence of liquid leakage. Little research has been done on inorganic solid materials, and the bulk of solid-state electrolytes developed for ESCs to date. Generally, it is divided into two.

1.5 Separator

The term "separator" refers to the barrier that plays a functional role between the two electrodes. It is responsible for critical activities that keep the cell alive. Poor quality separators can have a negative impact on the overall performance of the cell by causing an increase in the amount of resistance present. While in the worst situation, the possibility exists that the entire cell may have a short circuit. As a result, choosing the separator is an essential step that must be completed before the cell can be formed. The separators are made up of various materials, including glass, paper, ceramics, etc. In addition, polymer-based separators, which are characterized by their low cost, porous nature, and flexibility, have seen widespread application in SCs. When choosing the separator, the following factors are considered (Muzaffar et al. 2019).

- Separators must not carry electricity.

- It should be able to determine the minimum ionic resistance from the permeability of ions through the electrolyte.
- Separators should be easy for the electrolyte to hold to.
- It should supply mechanical resistance to counteract the pressure and volume changes happening within the cell. These alterations may result in cell expansion.
- Adding a chemical offers intrinsic resistance to the electrolytes and electrode materials.

1.6 Current Collector

The performance of active materials with insufficient conductivity might benefit from adding current collectors to the system. The current collector acts as a conduit for the current flow between the electrode and the current source and between the electrode and the external load. Additionally, the current collector is responsible for the secondary function of dispersing heat that is created within the cell. Additionally, current collectors are associated with the process of recharging the electrodes after they have been used. It has good electrical conductivity and can survive the harsh conditions of the cell while also preventing chemical deterioration caused by the electrolytes. Aluminum, steel, iron, and alloys are some materials that can be used as current collectors (Lei et al. 2011; Wu et al. 2009).

1.7 Fundamental Supercapacitor Definitions and Measurements

1.7.1 Capacitance (C)

The SCs capacitance is a constant property measured in Farad (F). It is related to the amount of electrical charge Q (in Coulombs) that can be stored in the SC when it is at its rated voltage V_R , according to the following equation:

$$C = Q/V_R \quad 1.2$$

The suggested standard method for measuring capacitance is the "constant current discharge method" and is based on the discharge curve. The capacitance is calculated using the following equation:

$$C = \frac{I(t_2 - t_1)}{(V_1 - V_2)} \quad 1.3$$

where I (in A) is the discharge current, $t_2 - t_1$ is the discharge time difference, and $V_1 - V_2$ is the potential window employed. This approach is primarily predicated on the premise that the discharge behavior of the SC stays linear.

An alternate solution can be implemented to reduce the potential voltage differences caused by the discharge curve's nonlinearity. The 'energy conversion capacitance approach' is then recommended for calculating the SC capacitance; it is derived from the energy equation:

$$C = 2 \frac{E}{V_2^2 - V_1^2} \quad 1.4$$

where E, in Joule (J), is the amount of energy efficiently discharged when the SC voltage changes from V_1 to V_2 , where V_1 and V_2 are the starting and ending voltages (Conte 2010).

1.7.2 The energy density (ED) and efficiency

Electrical energy can be evaluated as follows:

$$E_{MAX} = \frac{1}{2} CV_R^2 \quad 1.5$$

where C represents capacitance, and V_R represents rated voltage. In real applications, a complete discharge to zero volts is not possible; instead, useful energy content is established, which considers the energy delivered when the SC is discharged in a specific manner (e.g., at the constant current or constant power) from the rated voltage V_R to $1/2 V_R$.

According to the definition of delivered energy, energy efficiency is defined as the ratio in the percentage of energy produced by a SC given to it during a specified cycle. This ratio is based on the definition of delivered energy (Conte 2010; Sarno 2020).

1.7.3 Power Density (PD)

PD is the load's rate at which energy may be transferred to or absorbed. The PD is determined gravimetrically in kWkg^{-1} or volumetrically in kWL^{-1} . The below equation is used to calculate PD:

$$P = \frac{E}{t_d} \quad 1.6$$

where the E and t_d are ED (kWkg^{-1}) and discharge time in an hour.

1.7.4 Cycle life

Cycle life testing methodologies are typically based on a constant current profile. The SCs are charged and discharged at a constant current between the rated voltage and a specified end-of-discharge voltage arbitrarily chosen as a percentage of the rated voltage (often half or one-third of the rated voltage). After a specified number of complete charge and discharge cycles, the SC's fundamental parameters are monitored, and their variations are estimated. The measurement is completed when the capacitance (or energy) lowers by at least 20 or 30 percent compared to the beginning value.

1.8 Electrode Materials

The electrode material used significantly impacts how well a SC performs electrochemically. As a result, several electrode materials, including transition metal oxides/sulphides, carbon-based materials, CPs, etc., have been studied by various researchers to develop SCs.

1.8.1 Carbon materials

Carbon-based compounds are regarded to be the most promising industrial electrode materials. Carbons are the most attractive materials to date due to their low cost, simple processing, substantial specific surface area, excellent electrical conductivity, nontoxicity, natural abundance, eco-friendliness, and remarkable stability (Singh et al. 2015). Carbons

are also the most abundant element in the natural world. In the case of carbon materials, having a large specific surface area leads to a high capacity for charge build-up at the electrode and electrolyte contact. In addition to pore size and high specific surface area, surface functionalization must be considered when enhancing specific capacitance for carbon materials. Typically, carbon materials store charges primarily in an electrochemical double layer produced at the interface of the electrode and the electrolyte, as opposed to in the bulk of the active material. Consequently, capacitance is mainly determined by the surface area accessible to electrolyte ions (Zhang et al. 2009b).

Electrodes for EDLC SCs are made from carbon-based materials, such as carbon nanotubes (CNTs), activated carbon (AC), graphene (G), carbon nanofibers (CNFs), and carbon aerogel. Graphitic and natural materials, such as coconut shells, sugar cane, green leaf, and wood dust, are typically used to produce these items. Those are very porous substances with an enormous specific surface area (1000–3000 m²/g) for charge accumulation. Materials made of porous carbon usually have pores of many different sizes, which can be included into three main groups based on their diameters: 1) micropores (<2 nm), 2) mesopores (2-50 nm), and 3) macropores (>50 nm) (Simon and Burke 2008).

1.8.1.1 Zero-dimensional (0-D) carbon nanoparticles:

0-D carbon particles are spherical with a ratio near 1. 0-D carbon particles include AC, nanospheres, and mesoporous carbon (specific area (AC-3000 m² g⁻¹)). The pore concentration and size distribution may be adjusted, making them ideal for supporting SC electrode metal oxides (Zhi et al. 2013).

1.8.1.2 One-dimensional (1-D) carbon nanostructures:

High-aspect-ratio fibers are 1-D nanostructures. 1-D carbon nanostructures include carbon nanofibers (CNF), carbon nanotubes (CNT), and carbon nano coils. Since they have a high aspect ratio and outstanding electronic transport qualities, these characteristics are anticipated to make it easier for the kinetics of the electrochemical processes to occur.

1.8.1.3 Two-dimensional (2-D) nanosheets:

Materials having a high aspect ratio are considered to be sheet-shaped 2-D nanostructures. 2-D carbon nanosheets are represented by graphene, graphene oxide (GO), and reduced graphene oxide (rGO). Graphene and graphene oxide are interesting possibilities for SC electrodes due to their high mechanical strength, outstanding electrical conductivity, and large specific surface area. For instance, the theoretical surface area of a single sheet of graphene is $2756 \text{ m}^2\text{g}^{-1}$, and its charge mobility is $200000 \text{ cm}^2 \text{ V}^{-1} \text{ s}^{-1}$ (Zhi et al. 2013).

1.8.1.4 Three-dimensional (3-D) porous architectures:

Low-dimensional building components compose three-dimensional structures. The SC electrodes consist primarily of carbon nanofoams or carbon nano sponges. This foam offers a high specific surface area, a significant electrolyte–electrode contact area, and a continuous electron transport channel when utilized in SC electrodes (Zhi et al. 2013).

1.8.2 Faradic materials

1.8.2.1 Polyoxometalates (POMs)

Polyoxometalates (POMs) are a type of inorganic compound formed by transition metals in their most oxidized forms of groups V (V, Nb, Ta) and VI (Mo, W). POMs have the generic formula $[\text{X}_x\text{M}_m\text{O}_y]^n$ and are composed of one or more transition metals connected by oxo-ligands (Long et al. 2010). In the general formula, X denotes the hetero atom, often a main group of elements (e.g., P, Si, Ge, As). Occasionally, transition metals also function as heteroatoms, with M representing the addenda atom (V, Mo, or W) (**Fig.1.9**). Unique self-assembly mechanisms in an aqueous acidic medium result in the formation of POMs. POMs are used in many fields, including catalysis, medicine, materials research, photochemistry, analytical chemistry, and magnetochemistry, because of their wide range of stoichiometries, architecture, acid-base, and redox characteristics properties (Genovese and Lian 2017).

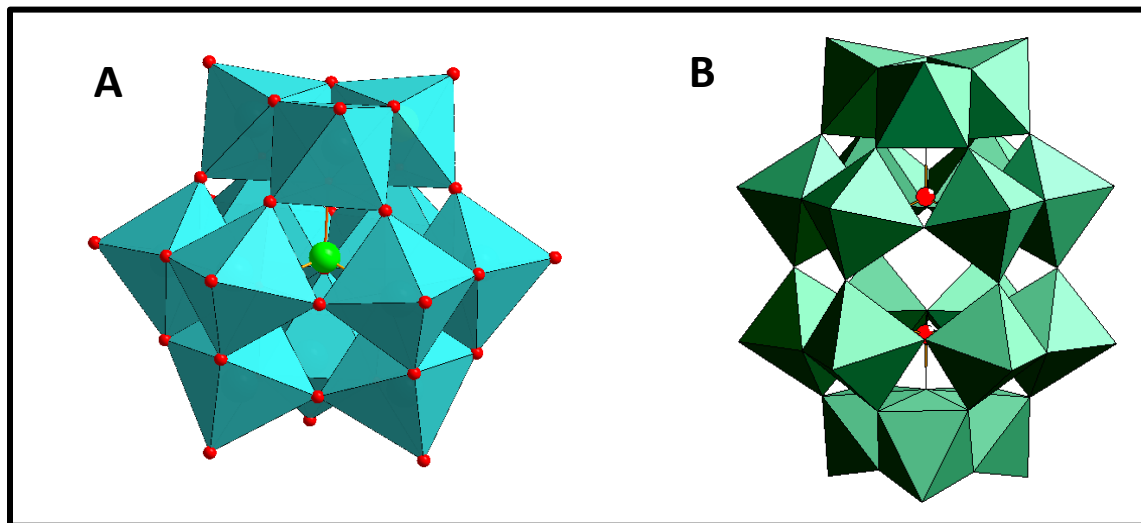


Fig. 1.9 A) Polyhedron representation of Keggin structure, B) Polyhedron representation of Well-Dawson structure.

POMs have exceptional catalytic activity in addition to ionic conductivity, photo- and electrochromic, magnetism, and antiviral activity. Nevertheless, the essential role of POMs is their distinctive electrochemical activity. The redox states of POMs are highly stable, and they can take part in rapid, reversible multielectron transfer processes. These characteristics have led to the designation of POMs as electron reservoirs or sponges, which is an attractive trait for energy storage applications (Genovese and Lian 2017).

According to the published research, Some Keggin-type POMs were doped onto CPs to prevent POM leaching, improve conductivity, and boost the energy storage capabilities of the polymer structure. The structure of POMs stays intact, which increases their insolubility in an aqueous solution. During charge/discharge operations, electroactive POMs perform various dual functions, such as accommodating cations at the surface or in the interlayer gaps. The second function is to transfer electrons from redox sites to conducting substances (Salanne et al. 2016; Vannathan et al. 2022).

1.8.2.2 Conducting polymer (CP)

In the four decades after the invention of polyacetylene in the 1970s, CPs have earned popularity in a wide range of applications (Chiang et al. 1978). This is due to the uniqueness of their physical and chemical properties. Several CPs, such as polypyrrole (PPy), polyaniline (PANI), polythiophene (PTh), Polyindole (PIn), and poly(3,4-ethylenedioxythiophene) (PEDOT) are the most extensively studied for the fabrication of SC electrodes. This is mainly because of their high conductivity, large porosity, wide potential window, synthesis feasibility, and less environmental effect (Basnayaka and Ram 2017). A common characteristic of CPs is the delocalized-conjugated backbone of polymer chains, which can be ultra-conductive after particular redox or doping processes.

CPs can be p-doped or n-doped depending on the polarity of dopant chemicals or the redox type. The former represents oxidized CPs with anion dopants, whereas the latter represents reduced CPs with cation dopants. According to reports, p-doped CPs are more stable than n-doped CPs. Compared to n-doped CPs, p-doped CPs have been investigated extensively in ES applications. Due to the quick and reversible reaction of doping-dedoping in bulk instead of an interface area, CPs offer greater specific capacitance and significantly lower specific surface area (SSA) requirements than other carbon materials. CPs are more ecologically friendly, less expensive, and electrically conductive than metal oxides. Numerous variables, including the choice of monomer, electrolyte, substrate, nano-morphology, and dopant use, significantly impact on the electrochemical uses of CPs. Dopant molecules profoundly impact the shape and capacitance of CPs (Chiang et al. 1978; Conway 2013; Snook et al. 2011).

CPs have extensive applications as antistatic materials in everyday life. These CPs were utilized in batteries, displays, and electronic gadget's. Their applications were restricted due to their instability, low solubility in solvents, toxicity, inability to undergo direct melting, and rising production costs. The applications of conductive polymers are gaining great interest in cheaper, processable materials with exceptional electrical and physical

properties. The large surface area and better dispersibility are the important characteristics of nanostructured CPs (Naarmann 2000)

Table 1.3 Theoretical and experimental capacitance values of common CPs (Snook et al. 2011).

Conducting polymers	Molecular weight (g L ⁻¹)	Potential range (V)	Theoretical SC (F g ⁻¹)	Measured SC (F g ⁻¹)
PANI	93	0.7	750	240
PPy	67	0.8	620	530
PTh	84	0.8	485	-
PEDOT	142	1.2	210	92

According to a literature review, CPs have been used in a variety of fields with remarkable properties, such as biosensors, organic solar cells, electronic organic light-emitting diodes, printing circuits, electrochromism, chemical sensors, SCs, microwave- and radar-absorbent coatings, stealth aircraft, and organic light-emitting diodes (Lange et al. 2008).

CPs-based SCs are available in three distinct configurations it is given below:

Type I Configuration:

This setup is symmetric, with identical p-dopable polymer samples at both electrodes. This gives a potential voltage range of 0.8–1 V.

Type II Configuration:

This is an asymmetric arrangement in which the two electrodes are composed of two distinct p-dopable polymers. This results in a slightly larger potential window (~1.5 V).

Type III Configuration:

The same polymer is utilized at both electrodes in this symmetrical design. In contrast, one of the electrodes is p-doped, and the other is n-doped. This setup offers a potential window exceeding 3 V.

Polypyrrole (PPy)

PPy is one of the most studied polymeric materials for making electrodes because it has unique properties like high conductivity, fast charge/discharge, high ED, easy synthesis, flexibility, high mass density, and low cost (Wang et al. 2020b). Due to its high mass density, PPy has a high value of volumetric specific capacitance ($400\text{--}500\text{ F cm}^{-2}$) and flexibility, allowing it to be molded into any desired shape without substantially reducing electrochemical performance (Wang et al. 2020b). The reaction mechanism of the pyrrole to polypyrrole is given in **Fig. 1.10**.

PPy can render flexible, highly capacitive, lightweight SCs and flexible electronic devices like flexible wristwatches, roll-up displays, smartphones, wearable sensors, and smart textiles. So, researchers are very interested in PPy because of what it could mean for the future of energy storage devices and electronic applications (Shown et al. 2015).

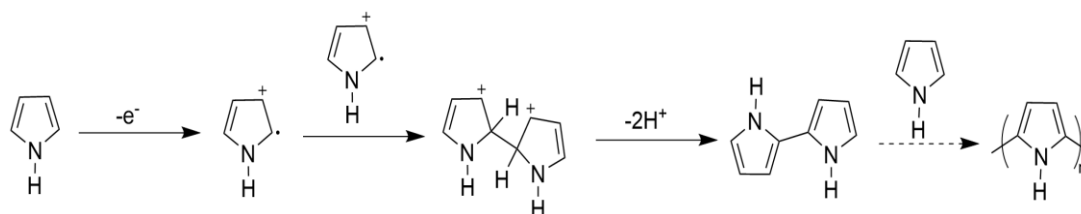


Fig. 1.10 Polymerization Mechanism of pyrrole to polypyrrole

Polyaniline (PANI)

Polyaniline (PANI) is seen to be the most promising SC electrode material due to its high conductivity in doped states ($100\text{--}10,000\text{ S/m}$). The simplicity of fabrication for large-scale devices provides high pseudocapacitance, lightweight, tunable electrical conductivity, high ED, environmental friendliness, simplicity in synthesis, superior capacity for energy storage, and inexpensive cost (Cheng et al. 2013). PANI is vulnerable to a quick decline in performance because of the swelling and shrinking caused by repeated cycles (charge/discharge process). This restriction can be overcome by mixing PANI with carbon materials, which has been shown to increase PANI's stability and capacitance.

PANI has exhibited a wide range of applications due to its high stability and reproducible dispersion.

Additionally, depending on preparation circumstances, it provided outstanding specific capacitance (500 and 3400 F g^{-1}), which is much higher than that of traditional carbon-based electrodes ($100\text{-}200 \text{ F g}^{-1}$) and similar to pseudocapacitive metal oxides (Zhang et al. 2013). The primary use of PANI is in the printed circuit board manufacturing process (Li et al. 2011a; Pan et al. 2016). The Mechanism of polyaniline formation from aniline is shown in **Fig.1.11**.

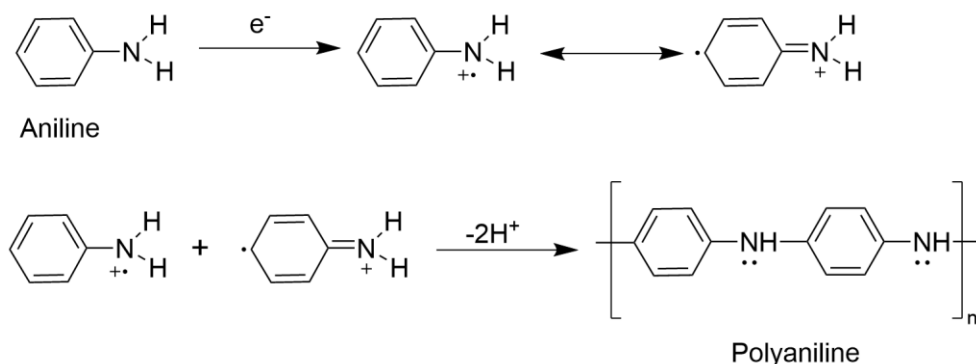


Fig. 1.11 Polymerization Mechanism of aniline to polyaniline

Polyindole (PIn)

Polyindole (PIn) is a polymer of indole (**Fig.1.12**), a heterocyclic aromatic molecule with a hexagonal benzene ring fused within a pentagonal pyrrole ring. As a result, PIn and its derivatives display poly(paraphenylene) and polypyrrole characteristics. High redox activity, excellent thermal stability, cheap cost, high pseudocapacitance, ease of synthesis, and environmental friendliness are some favourable qualities (Choudhary et al. 2020). In addition, PIn is more resistant to hydrolytic degradation than PANI. PPy has demonstrated its ability to store energy for a more significant duration of time characteristics and is more thermally stable. All of these characteristics make PIn a very desirable electrode material for the creation of high-performance and long-lasting SCs. Nevertheless, because of its two

fundamental drawbacks, poor cycle stability, which is caused by a weak backbone, and low electrical conductivity, its application on a broad scale is not even close to being a possibility at this point (Gómez Costa et al. 2012; Wang and Wu 2017).

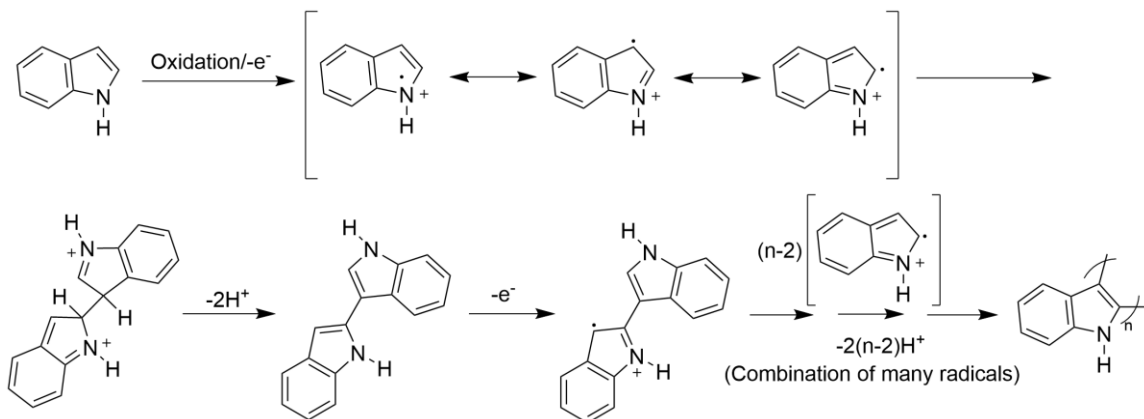


Fig. 1.12 Polymerization Mechanism of indole to polyindole

1.9 Applications

SCs are being utilized in many applications as their performance improves. Rechargeable batteries have been the most popular energy storage method for the past 10 years. The number of applications needing better energy storage, from portable electronics to hybrid electric vehicles, is growing. In the realm of energy storage, what is required, is to increase performance while simultaneously reducing prices. The applications of the SCs are given below.

1.9.1 Public sector applications

SCs are utilized in digital cameras to create flashes. The most recent addition is the set of portable speakers that Sam Beck (Blueshift) produced with an integrated SC assembly. SCs were primarily employed in actuator and memory backup applications. They are employed in renewable and sustainable energy sources because they act as stabilizers in

solar and wind energy-based power line systems. Hybrid SCs give short bursts of energy to wind turbines because the SCs respond immediately to changes in the weather.

HSCs are used when the power supply needs to be quick. In security systems, the HSC function is equivalent to a computer's uninterruptible power supply (UPS) function. The Emirates Airline cable cars also use HSC energy systems that power the lighting and air conditioning. In 2010 three Japanese companies worked together to use solar energy and SCs as energy storage units to create eco-friendly street lighting in Japan (Nippon-Chemi-Con).

1.9.2 Automobiles and transportation application

In the automotive industry, energy storage systems run multiple functions simultaneously, such as the ignition, starting, security, transmission, lighting, etc. For example, in the case of an internal combustion engine, the HSC can be used to start the engine by giving it a quick burst of energy. Using a HSC, creating a power pulse for electric or hybrid electric cars is simple, requiring a high current for a brief period while charging. Toyota and Mazda are examples of such vehicles. Aowei Technology Co., Ltd.'s e-buses are an excellent example of a big electric vehicle that uses HSCs. This is another important use that is becoming popular (Shanghai, China). The hybrid configuration of Ni(OH)₂-AC is used in trolley buses, which take 90 seconds to charge and can travel 7.9 km at a top speed of 44.8 km/h and an average speed of 22 kmh⁻¹ while going from 0 to 40 kmh⁻¹ in 16.5 seconds. CSR Co. Ltd. (China) has also made a tramcar that works on an EDLC configuration and can be charged in 30 seconds. It can go 3–5 km before it needs to be charged again. Railways and metro trains will utilize HSCs as part of the expanded transportation system (Wang et al. 2016). In August 2012, CSR Zhuzhou Electric Locomotive Corporation of China developed a two-car light metro system prototype (Muzaffar et al. 2019). A HSC unit is located on the light metro's roof. Some other examples of railways that use HSCs are the South Island metro lines in Hong Kong and the metros built by SYTRAL in Lyon, France (Walkowiak et al. 2015).

1.9.3 Defense and military applications

Using batteries, such as navigators, sensors, and communication tools, is an excellent place to use HSCs. A HSC assembly can also run the radar system, electromagnetic pulse weapons, torpedoes, etc.; the military uses radar antennas, avionics display gadgets, airbag exploitation power, GPS, and missiles.

1.9.4 Computers and memory backup chips

As a stabilizer for the power supply, HSCs are used in things like laptops, portable media players, etc. They give backup power to low-power components like RAM, SRAM, PC cards, and UPS so they can be turned off. The ability lies in that it can make a short burst of high power. Using a HSCs protects memory from a drop in the main power source that could be significant. The HSC assembly works better than the technology that is currently used in UPS devices. The solid-state drives (SSDs) that are used to store memory also use HSCs as a backup power source. The HSC greatly helps the SSD when it needs to clear its cache and gracefully shuts down when the power goes out without losing any data (Chen and Xue 2016; Muzaffar et al. 2019).

1.9.5 Medical and industrial applications

HSCs have the potential to be used in high-voltage pulse delivery applications in the field of medicine. As a result, they are placed in defibrillators, sending a 500-Joule electrical surge to the heart to recover its normal function. Patients who are suffering from emotional trauma typically undergo the same kinds of procedures in treatment. HSCs may find a new use in the backup of ventilators in addition to their current use in dental science and other areas. JSR Micro designed a HSC specifically for application in medical imaging equipment as part of their work on developing emergency power supply (Kumar and Renuga 2012).

To the emergency backup power supply, industrial electronics, such as automated meter reading (AMR), help prevent any catastrophic breakdowns before the power is restored (Muzaffar et al. 2019).

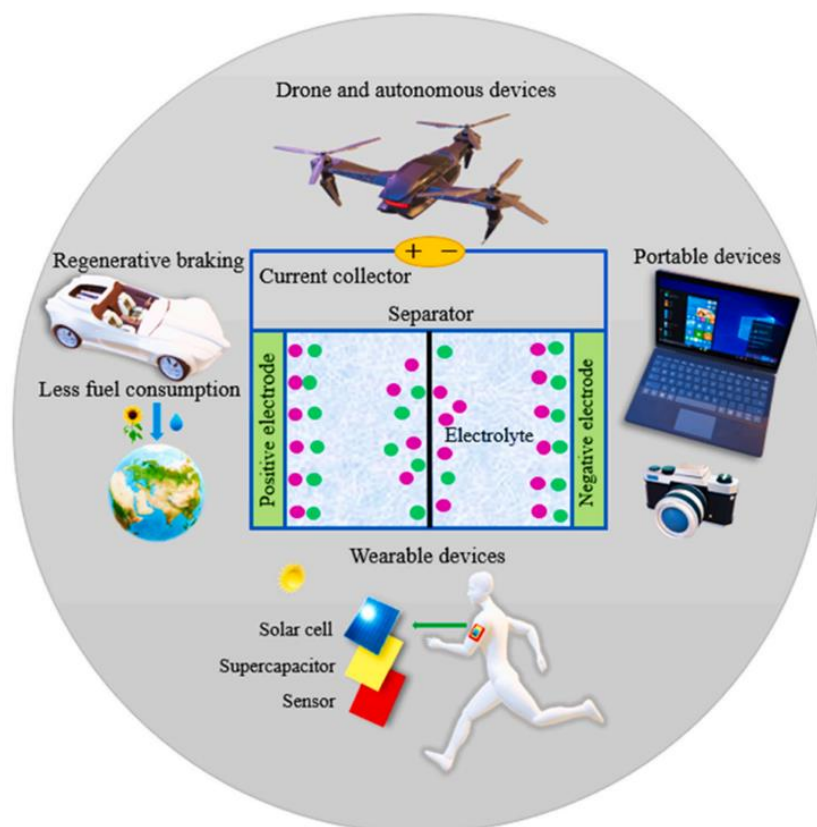


Fig. 1.13 The fundamental design of a SC device and its diverse uses in energy storage. (Forouzandeh et al. 2022)

CHAPTER 2



Literature Review

2.1 Literature Review

CPs are a pseudocapacitance material; however, it tussles to reach the theoretical capacitance values. There has been mounting interest in the field of CPs (organic), and combination with redox-active POMs (inorganic) due to the well-defined structure of POMs and reversible redox behavior makes them useful for application in energy storage materials.

The electrochemical and electrocatalytic capabilities of manufactured conductive polyaniline were found to include hetropolyacid (HPA) anions, according to the research done by Marek Barth and colleagues in 1998. They supported $\text{H}_4\text{PMo}_{11}\text{VO}_{40}$, $\text{H}_5\text{PMo}_{10}\text{V}_2\text{O}_{40}$, and $\text{H}_6\text{PMo}_9\text{V}_3\text{O}_{40}$ over polyaniline and investigated the electrochemical characteristics of these materials using a three-electrode setup while immersed in 1M H_2SO_4 electrolyte (Barth et al. 1999).

Pedro Gomez-Romero and colleagues synthesized the $\text{H}_3\text{PMo}_{12}\text{O}_{40}/\text{PAni}$ (PAni-polyaniline) material in 2003. They then conducted electrochemical studies by the two-electrode system (symmetric device) using membrane Poly(2,5-benzimidazole and discovered a specific capacitance of 195 mF cm^{-2} at a scan rate of 0.125 mA cm^{-2} . The material was stable until the 2000 cycle (85%) (Gómez-Romero et al. 2003).

A.M. White and colleague created a hybrid electrode material consisting of $\text{H}_3\text{PMo}_{12}\text{O}_{40}/\text{PPy}$ and $\text{H}_5\text{PV}_2\text{Mo}_{10}\text{O}_{40}/\text{PPy}$ in the same year. These materials exhibited capacitance values of 22.9 F g^{-1} and 27.6 F g^{-1} , respectively, and were scanned at a rate of 1 mV s^{-1} using a three-electrode setup using Nafion 115 as a solid electrolyte for the analysis of both hybrid materials (White and Slade 2003a).

In 2003, A. M. White and colleague synthesized $\text{H}_5\text{PMo}_{10}\text{V}_2\text{O}_{40}/\text{PPy}$, $\text{H}_3\text{PMo}_{12}\text{O}_{40}/\text{PPy}$ and $\text{H}_4\text{SiMo}_{12}\text{O}_{40}/\text{PPy}$. Using a three-electrode setup, they found that the specific capacitance of 422 F g^{-1} , 130 F g^{-1} , and 266 F g^{-1} in a 1 mV s^{-1} scan rate was observed respectively in 0.1M H_2SO_4 electrolyte (White and Slade 2003b).

Cuentas-Gallegos et al. produced $\text{H}_3\text{PMO}_{12}\text{O}_{40}/\text{PAni}$ hybrid material in 2005 and discovered 120 F g^{-1} SC by the symmetric device at 0.4 A g^{-1} current density up to 4000 cycles (almost 68%) stability of the composite electrode. In addition, Nafion117 and sulfuric acid were employed as the electrolyte (Cuentas-Gallegos et al. 2005).

In 2006, Vaillant et al. measured 168 F/g specific capacitance at 0.4 A g^{-1} current density and 200 cycle stability (almost 60%) for $\text{H}_3\text{PMO}_{12}\text{O}_{40}/\text{PAni}$ material in solid electrolyte membrane Nafion 117. These results were found for the material in solid electrolyte membrane Nafion 117 (Vaillant et al. 2006).

Ruiz et al. (2012) developed SCs with activated carbon and phosphomolybdic acid (PMO_{12}). The electrolyte was 1M sulphuric acid, and PMO_{12} was bonded to activated carbon to provide 160 F g^{-1} and 183 F g^{-1} (at 2 A g^{-1}) for the positive and negative hybrid electrodes, respectively. It had lost 9% of its capacitance after 8000 cycles at 1.6 A g^{-1} (Ruiz et al. 2012).

In 2013, J. Suárez-Guevara et al. synthesized phosphotungstic acid ($\text{H}_3\text{PW}_{12}\text{O}_{40}$, PW_{12}) and activated carbon (AC), which enables the manufacture of highly durable, high-voltage aqueous SCs (1.6 V). The electrolyte was 1 M sulphuric acid, and specific capacitance ranged from 185 F g^{-1} for AC to 254 F g^{-1} for AC- PW_{12} . In addition, the hybrid AC- PW_{12} electrode material exhibited remarkable stability even after 30000 cycles (0 to 1.6 V), retaining 98% of its original capacity (Suárez-Guevara et al. 2014).

Hereafter Wang et al. improved the hybrid electrode by combining AC with $(\text{NH}_4)_6[\text{P}_2\text{Mo}_{18}\text{O}_{62}]\cdot 14.2\text{H}_2\text{O}$ (P_2Mo_{18}), a POM of the Dawson type. The first use of P_2Mo_{18} as an SC electrode. AC/ P_2Mo_{18} demonstrated a capacitance of 275 F g^{-1} at a current density of 6 A g^{-1} , which is 51% greater than the capacitance of the AC electrode (182 F g^{-1}) at the same current density. The AC/ P_2Mo_{18} displayed the maximum capacitance of 308 F g^{-1} at a current density of 2 A g^{-1} due to its high proton conductivity and characteristic redox behavior. And 70% cycle stability was achieved after 2000 cycles at 6 A g^{-1} current density (Mu et al. 2015).

Chenchen Hu et al. (2016) produced SCs using activated carbon and phosphotungstic acid (PMo_{12}). Ionic liquid served as the electrolyte, and a three-electrode and two-electrode setup was used for the experiment. A capacitance reading of 223 F g^{-1} was recorded when the voltage applied was 1 mVs^{-1} . After 10,000 cycles, a POM-based positive electrode in an asymmetric capacitor containing a P-IL aqueous electrolyte showed decreased capacitance (Hu et al. 2016).

Palomino et al. (2017) created SCs by combining activated carbon and phosphotungstic acid (PMo_{12}). The experiment was carried out using a setup consisting of two electrodes. With the addition of PMo_{12} to the original carbon electrodes, capacitances of up to 293 F g^{-1} of the electrode were achieved. This is a significant increase compared to the $206\text{--}240 \text{ F g}^{-1}$ achieved by the unmodified activated carbon (Palomino et al. 2017).

Deepak P Dubal et al. synthesized new organic-inorganic hybrid materials for symmetric SCs based on open-end porous 1D polynanopipes (ppy-Npipes) and POMs (phosphotungstate or phosphomolybdate) that display excellent areal capacitances and specific capacitance. Three-electrode system electrochemical measurements showed capacitance of 341 F g^{-1} and 294.1 F g^{-1} for $\text{PW}_{12}/\text{PPy}$ and $\text{PMo}_{12}/\text{PPy}$, respectively nanopipe showed only 204.5 F g^{-1} at 2 mA cm^{-2} in $1 \text{ M H}_2\text{SO}_4$ electrolyte (Dubal et al. 2017a).

Same year Sven Herrmann et al. synthesized polypyrrole-Lindqvist-type molecular metal oxide anions $[\text{V}_n\text{M}_{6-n}\text{O}_{19}]^{(2+n)-}$ ($M = \text{W(VI)}$ or Mo(VI) ; $n = 0, 1, 2$) material and studied the electrochemical performance using 0.1 M Tetra-*n*-butyl ammonium tetrafluoroborate ($n\text{Bu}_4\text{NBF}_4$) as electrolyte for three-electrode systems. The capacitance was observed $\approx 25\text{--}38 \text{ F g}^{-1}$ specific capacitance in in a 0.2 to 1.0 V potential window at 50 mV s^{-1} (Herrmann et al. 2017).

Very recently, Jingjing Lin et al. synthesized Fe-Anderson-type polyoxometalate/polyaniline/graphene (PPG) hybrid materials; They used Anderson-type polyoxometalates $[\text{FeMo}_6\text{O}_{24}\text{H}_6]^{3-}$ (FeMo_6) onto graphene modified with polyaniline by hydrothermal treatment. The composite showed a high specific capacitance of 1366 F g^{-1}

at 1 A g^{-1} current density and ED of $24.65 \text{ W h kg}^{-1}$ at a low PD of 326.25 W kg^{-1} and excellent cycling stability (94.82% capacitance retention after 5000 cycles). The three-electrode system in $1 \text{ M H}_2\text{SO}_4$ electrolyte measured this electrochemical performance (Lin et al. 2019).

Incorporating PANI-PW₁₂, PANI-PMO₁₂, and PANI-PMO₁₂ & PW₁₂ composites, Dongming Cheng et al. created three new symmetric devices in 2021. Polyvinyl alcohol was utilized as the electrolyte, and the composites exhibited good specific capacitance at 0.5 mA cm^{-2} : 3.88 F cm^{-2} for PANI-PMO₁₂&PW₁₂, 3.12 F cm^{-2} for PANI-PMO₁₂, and 2.51 F cm^{-2} for PANI-PW₁₂. Simultaneously, composites demonstrated a maximum ED of $0.533 \text{ mWh cm}^{-2}$ and an outstanding cycle stability of 90.0% after 400 cycles (Cheng et al. 2021).

Maity et al. reported new SC electrode material by doping porous activated carbon with $\text{K}_2\text{H}_5[\text{NiV}_{14}\text{O}_{40}]$ (NiV₁₄) (AC). The resultant compound, AC-NiV₁₄, was shown to have much improved electrochemical properties (for both symmetric and asymmetric SC cells), operating at a substantially higher potential of 1.2 V (in $0.5 \text{ M H}_2\text{SO}_4$). A capacitance of 316 F g^{-1} was found for 15 wt.% (AC-NiV₁₄) at a current density of 1 A g^{-1} , while a specific energy value of 63.2 Wh kg^{-1} and a maximum power of $3,140 \text{ W kg}^{-1}$ were attained at a high current density of 2 A g^{-1} (Maity et al. 2021a).

Maity et al. synthesized AC with vanadomolybdates (VMo₁₁, V₂Mo₁₀) hybrid materials in 2021; the composite AC- VMo₁₁ and AC- V₂Mo₁₀ exhibited a high specific capacitance of 430 F g^{-1} and 214 F g^{-1} , respectively, at 0.2 A g^{-1} current density. This electrochemical performance was measured by a two-electrode system in the Ionic liquid electrolyte (Maity et al. 2021b).

2.2 Scope of the Work

The combination of organic-inorganic hybrid materials has recently attracted much attention, especially in material science. CPs have extended π -conjugation throughout the polymer chain to form a network, which is insufficient to behave in metal-like conductivity. Generally, CPs have low conductivity in neutral form, and to increase the conductivity, a charge carrier (dopant) needs to be introduced into their extended polymer (Bhadra, S. et

al., 2009). The conductivity range of CPs could be tuned by controlling the amount of dopant present in the polymer chain.

A literature survey indicates very little work has been done in the SC field using vanadium-substituted polyoxometalates (VPOMs) composites as electrode materials for energy and power devices. Mainly, commercially available POMs such as $\text{H}_3[\text{PMo}_{12}\text{O}_{40}]$ and $\text{H}_3[\text{PW}_{12}\text{O}_{40}]$ have been used to synthesize the composite electrode using FeCl_3 as an oxidant and showed moderate capacitance values in the H_2SO_4 electrolyte. A few POMs have also been applied to integrate the CP-VPOM composite electrodes for SCs application. For this purpose, even the POV- $\text{H}_3[\text{PMo}_{12}\text{O}_{40}]$ -CP hybrid materials were synthesized in the H_2SO_4 electrolyte. Thus, there are plenty of venues for integrating CPs using VPOM (active oxidizing agent) without any external oxidizing agent. It can be employed as an electrode material to increase the material's capacitance. At the same time, electrolytes also played a crucial role in SC applications. Thus, choosing suitable electrolytes varies the electrochemical performance of those electrodes.

POMs can compensate for some of the limitations of carbon-based materials in nanocomposites based on carbon. In addition, the carbon matrix gives POMs better conductivity and mechanical strength while preserving the chemical stability of the overall complex.

This thesis studies the use of POM-CPs and POM-carbon based material complexes as electrodes in SCs and attempts to improve several performance factors connected to their use.

2.3 Objectives of the Work

- To synthesize the various pseudocapacitive materials CPs (polypyrrole (PPy), polyaniline (PAni) and polyindole (PIn)), vanadium substituted polyoxometalates (VPOMs) and activated carbon (EDLC material).

- The different composite electrode materials will be prepared by depositing pseudocapacitive materials (POMs) on CP and AC materials using a single-pot synthesis method.
- To characterize the structural, chemical, and morphological properties of the prepared electrode materials.
- To investigate the electrochemical behaviour of the electrode material using cyclic voltammetry (CV), galvanostatic charge-discharge (GCD), electrochemical impedance spectroscopy (EIS), etc., through symmetrical and asymmetrical cells.

2.4 Organization of the Thesis

The work presented in this thesis spans nine chapters.

Chapter 1 incorporates available energy storage methods in general and SC specifically. Various facets of the Mechanism of charge storage in SC have been addressed. Additionally, the different electrode and electrolyte media are explored in detail for SC, followed by their practical application.

Chapter 2 provides a comprehensive literature review of several POM-based electrode materials for SC applications. The scope and objectives of this thesis are then discussed, and describe the materials and methods used in this research and the experimental methodologies used to build and characterize the SC electrode.

Chapter 3 demonstrates two different vanadomolybdates POMs molecules doped on polypyrrole backbone and thoroughly studies their electrochemical properties using 0.1M H₂SO₄ electrolyte for SC electrodes.

Chapter 4 describes two classes of nanohybrid by incorporating vanadomolybdates POM on polyindole in acid electrolyte media and studies structural and electrochemical performances.

Chapter 5 introduces a concise, one-pot synthesis for vanadomolybdate-induced in situ polymerization of polyaniline: this nanocomposite shows excellent ED and electrochemical properties in acidic electrolytes.

Chapter 6 delivers a case study of two cell types (symmetric and asymmetric); the cell was fabricated using vanadotungstate polyoxometalate and polypyrrole as supporting material. The substrate material governs nanohybrid's structural, topological, and electrochemical behavior.

Chapter 7 shows a comparative study of vanadium-substituted POM doped on the surface of polyaniline and vanadium-substituted POM doped on the surface of activated carbon.

Chapter 8 describes two nanohybrids produced by integrating vanadium-substituted POM onto activated carbon in an acid electrolyte medium. The varying vanadium content determines the structural and electrochemical performance of the hybrid.

Chapter 9 outlines the summary of the study conducted for this thesis. It also seeks to facilitate future study in this field and beyond.

2.5 Materials and Methods

2.5.1 Materials

Pyrrole was purchased from Spectrochem Pvt. Ltd., and Aniline (99%) was acquired from Loba Chem. Pvt. Ltd. was distilled under a vacuum before use. Indole (99%) as a monomer was purchased from SRL Chem. Pvt. Ltd. NMP (N-methyl pyrrolidone) and Carbon black were purchased from Sigma-Aldrich. Polyvinylidene (PDVF) was obtained from the Alfa Aesar, sodium metavanadate (NaVO_3), sodium molybdate (Na_2MoO_4), sodium hydrogenphosphate (Na_2HPO_4), hydrochloric acid (HCl), sulphuric acid (H_2SO_4), phosphoric acid (H_3PO_4), sodium tungstate (Na_2WO_4), potassium chloride (KCl), nitric acid (HNO_3), methanol (CH_3OH), potassium metavanadate (KVO_3), manganese sulfate ($\text{MnSO}_4 \cdot \text{H}_2\text{O}$), and potassium persulfate ($\text{K}_2\text{S}_2\text{O}_8$) diethyl ether, $\text{FeCl}_3 \cdot 6\text{H}_2\text{O}$ and HPLC

grade water were purchased from Loba Chem. Pvt. Ltd. Carbon cloth was purchased from Sainergy Fuel Cell India Pvt. Ltd.

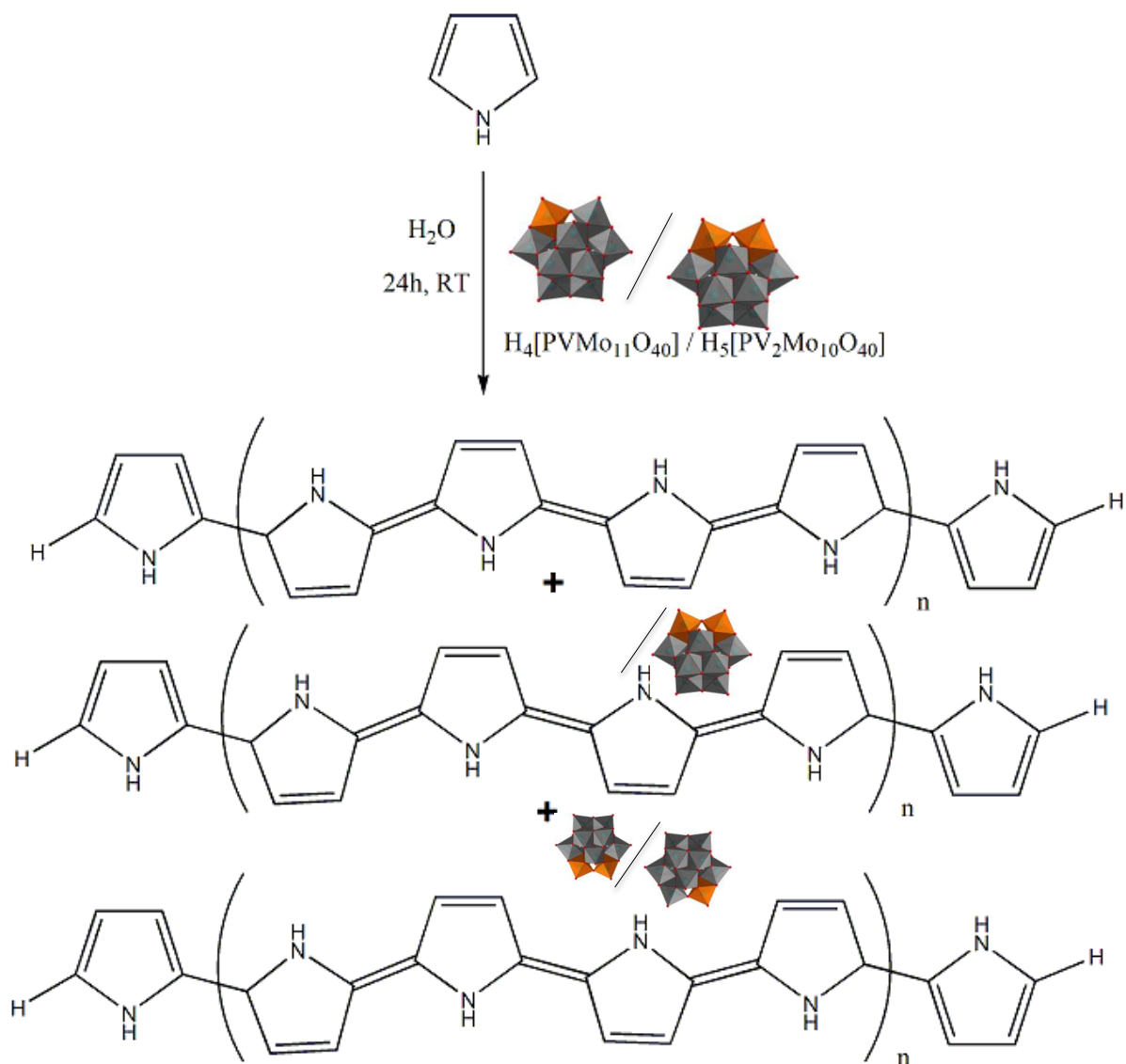
2.5.2 Synthesis

2.5.2.1 Synthesis of polypyrrole (PPy), $H_4[PVMo_{11}O_{40}]$, and $H_5[PV_2Mo_{10}O_{40}]$.

PPy was synthesized according to the published procedure (Kato et al. 1991). The redox-active polyoxometalates clusters $H_4[PVMo_{11}O_{40}]$ and $H_5[PV_2Mo_{10}O_{40}]$ were synthesized using the original synthesis procedure as reported by Akba et al. (Akba et al. 1997).

2.5.2.2 Integration of the hybrid PPy/ $H_4[PVMo_{11}O_{40}]$

About 0.135ml (0.01mmol) of pyrrole was added to the 50 ml water containing beaker. The pyrrole-water mixture was stirred for a few minutes. Then 2g (4.75 mmol) of $H_4[PVMo_{11}O_{40}]$ was added slowly to the pyrrole/water mixture. The orange color solution was slowly turned to dark blue color, and black precipitate began to form. The resulting reaction was kept stirring for 24h at room temperature. The black wad was filtered off under vacuum using membrane filter paper and washed many times with water until the filtrate appeared colorless.



Scheme 2.1 Schematic representation of $[\text{PVMo}_{11}\text{O}_{40}]^{4+}$ / $[\text{PV}_2\text{Mo}_{10}\text{O}_{40}]^{5-}$ impregnated into the PPy surface. Orange octahedra = V, Red = O, and gray octahedra=Mo.

2.5.2.3 Integration of the hybrid PPy/H₅[PV₂Mo₁₀O₄₀].

The procedure is the same as above, except H₅[PV₂Mo₁₀O₄₀] was taken instead of H₄[PVMo₁₁O₄₀].

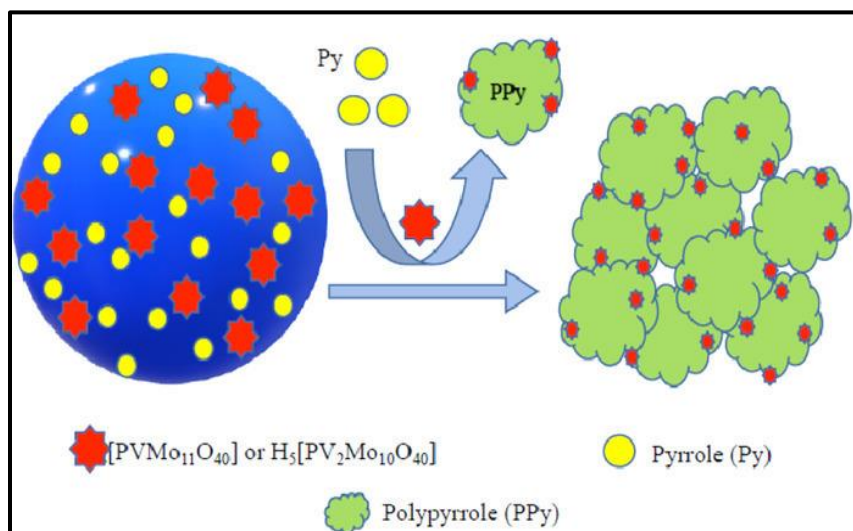


Fig. 2.1 Schematic representation of [PVMo₁₁O₄₀]⁴⁻/ [PV₂Mo₁₀O₄₀]⁵⁻ impregnated into the PPy surface.

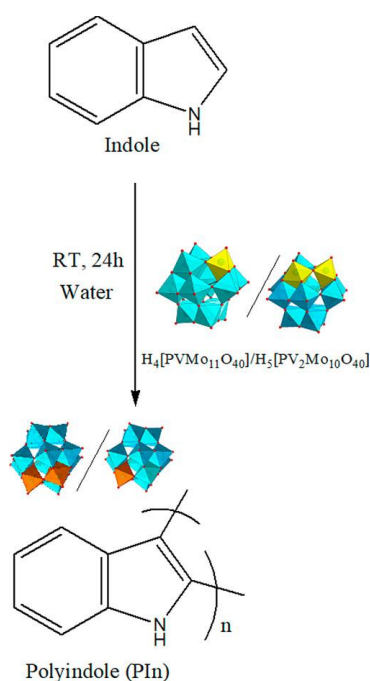
2.5.2.4 Synthesis of polyindole (PIn).

Pure PIn was synthesized using a simple and inexpensive chemical method at room temperature. In this method, 1.0 g (0.04 mmol) of indole and 1.00 g (0.27 mmol) of FeCl₃·6H₂O were mixed in 50 mL of distilled water. The dark brown solid PIn started to form. The resulting solution was continuously stirred for 24 h at room temperature to complete the reaction. The dark brown solid was filtered off under vacuum using a membrane filter paper and washed several times with HPLC grade water until the colorless filtrate's appeared.

2.5.2.5 Synthesis of the PIn/PVMo₁₁ Composite.

The PIn/PVMo₁₁ was synthesized via an oxidative polymerization in situ method where PVMo₁₁ acts as an oxidant and Bronsted acid. One gram (0.12 mmol) of indole(monomer) was mixed with 50 mL of distilled water in a beaker. The indole/water mixture was stirred

for a few minutes. Then, 2 g (4.75 mmol) of acidic $H_4[PVMo_{11}O_{40}]$ was added slowly to the indole/water mixture. The orange solution slowly turned brown, and brown salt began forming. The resulting reaction was continuously stirred for 24 h at room temperature. The deep brown solid was filtered off under vacuum using a membrane filter paper and washed many times with HPLC-grade water until the filtrate appeared colorless to wash out excess POM present in the reaction medium. Finally, the substantial solid was air-dried, and we used it for our study.



Scheme 2.2 Schematic representation of the synthesis of the PIn/PVMo₁₁ and PIn/PV₂Mo₁₀.

2.5.2.6 Synthesis of the PIn/PV₂Mo₁₀ Composite.

The PIn/PV₂Mo₁₀ electrode was prepared similarly to PIn/PVMo₁₁, except that $H_5[PV_2Mo_{10}O_{40}]$ was used instead of $H_4[PVMo_{11}O_{40}]$.

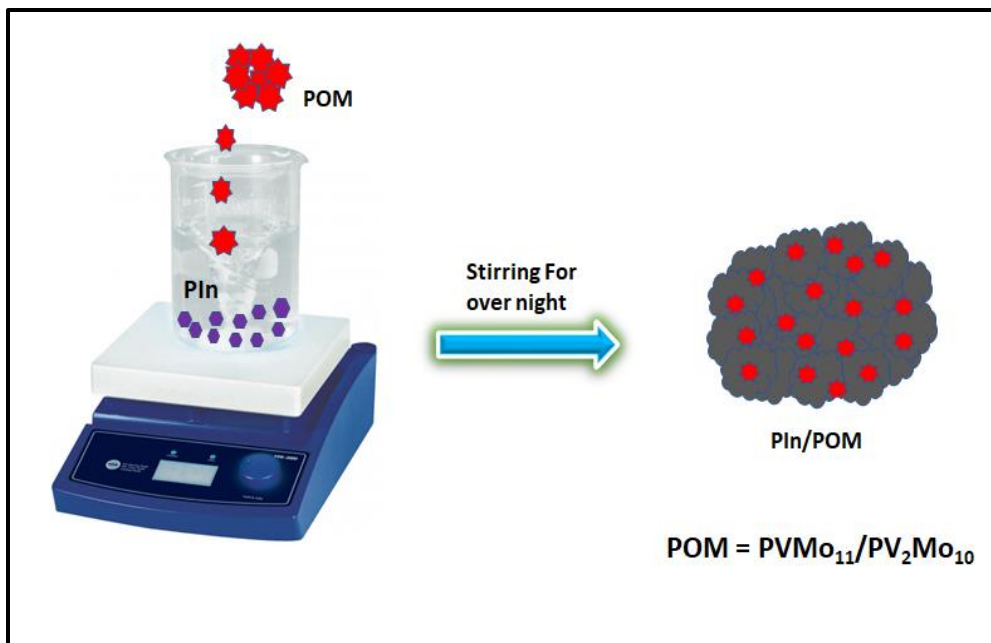


Fig. 2.2 Synthesis of the PIn/ $PVMo_{11}$ and PIn/ PV_2Mo_{10} .

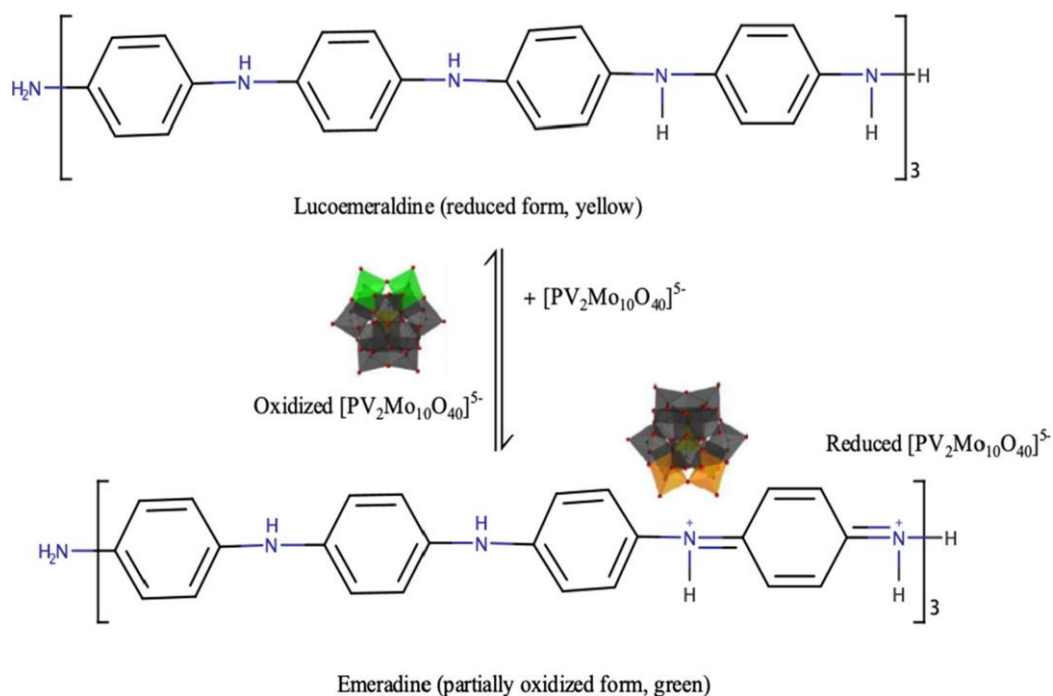
2.5.2.7 Synthesis of polyaniline (PANI)

Pure PANI was synthesized at room temperature by a simple chemical bath deposition technique. This technique contained 0.38 ml (0.04 mmol) of aniline and 800 mg (0.22 mmol) of $FeCl_3 \cdot 6H_2O$ in 50 ml of distilled water. The dark yellow color of the mixture was gradually turned to green color, and salt began to form. The reaction mixture was stirred for 24 h at room temperature to ensure completion of the reaction. The green wed was filtered under vacuum using membrane filter paper and washed several times with distilled water till the colorless filtrate was obtained.

2.5.2.8 Synthesis of $PVMo_{11}@PAni$ electrode material

The $PVMo_{11}@PAni$ was synthesized through oxidative polymerizations in situ method where $PVMo_{11}$ acts as an oxidant and proton source in an acidic medium. Aniline (0.76 ml, 0.08 mmol) was added to 50 ml of distilled water. Subsequently, 2 g (4.75 mmol) of $H_4[PVMo_{11}O_{40}]$ crystal was added directly to the resulting solution. The orange solution gradually turned into a green color, and a green solid started to form. After 24 h, the green

solid was filtered off using membrane filter paper under a vacuum. Then the solid was washed. The excess POMs were removed by washing the green solid several times with deionized (DI) water until the colorless filtrate appeared.



Scheme 2.3 Possible reaction mechanism of polyaniline- $[PV_2Mo_{10}O_{40}]^{5-}$

2.5.2.9 Synthesis of $PV_2Mo_{10}@PAni$ electrode material

The $PV_2Mo_{10}@PAni$ electrode was prepared similarly to that $PVMO_{11}@PAni$, except $H_5[PV_2Mo_{10}O_{40}]$ was taken instead of $H_4[PVMO_{11}O_{40}]$.

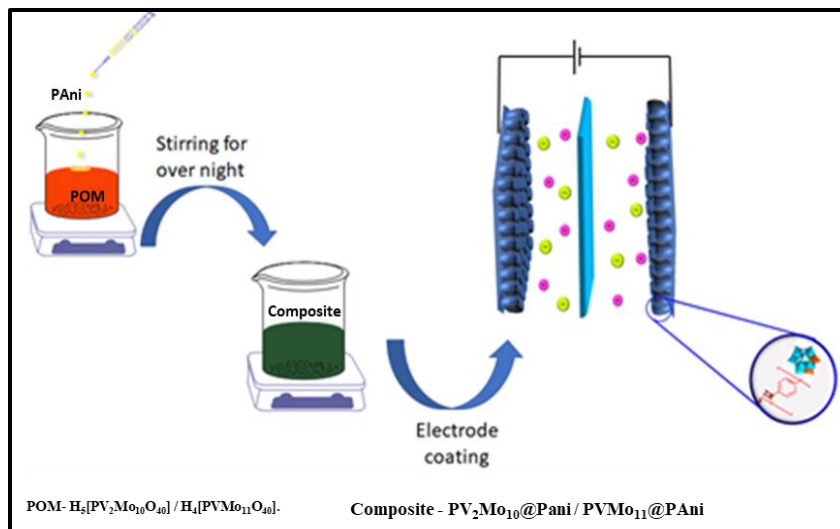


Fig. 2.3 Synthesis of the $\text{PVMo}_{11}@Pani$ and $\text{PV}_2\text{Mo}_{10}@Pani$

2.5.2.10 Synthesis of $\text{K}_5\text{H}_2[\text{PV}_4\text{W}_8\text{O}_{40}]$

The redox-active polyoxometalate cluster $\text{K}_5\text{H}_2[\text{PV}_4\text{W}_8\text{O}_{40}]\cdot 11\text{H}_2\text{O}$ was synthesized following the procedure reported by Smith et al. (Smith and Pope 1973).

2.5.2.11 Synthesis of $\text{K}_5\text{H}_2[\text{PV}_4\text{W}_8\text{O}_{40}]$ onto polypyrrole backbone

The pyrrole water mixture was prepared by adding 0.135 ml (0.01 mmol) of pyrrole (**PPy**) in 40 ml of the water taken in a beaker, and the resultant mixture was stirred for a few minutes. Next, an accurate weight of 1 g (2.74 mmol) of $\text{K}_5\text{H}_2[\text{PV}_4\text{W}_8\text{O}_{40}]\cdot 11\text{H}_2\text{O}$ (**PV₄W₈**) (deep orange color) was slowly mixed with the pyrrole/water mixture, and the solution became orange in color. After that, 0.6 g of $\text{FeCl}_3\cdot 6\text{H}_2\text{O}$ was added into the orange color solution, which was slowly changed dark color, and the black precipitate was formed immediately. The resulting reaction mixture was stirred continuously for 24 h at room temperature. The solid black residue obtained was then filtered off under vacuum using membrane filter paper. Finally, the black residue was washed thoroughly with HPCL grade water until the filtrate appeared colorless (unreacted $\text{K}_5\text{H}_2[\text{PV}_4\text{W}_8\text{O}_{40}]\cdot 11\text{H}_2\text{O}$ was removed with water). The residue was finally air-dried before use as an electrode material.

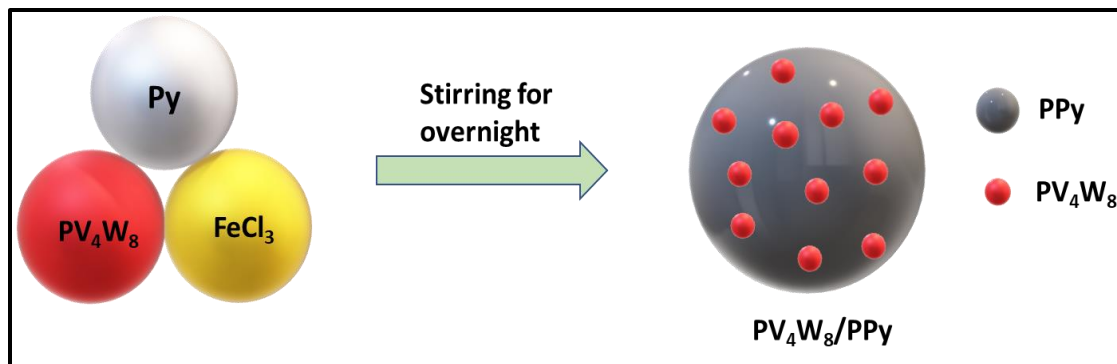


Fig. 2.4 Synthesis of the PV_4W_8/PPy .

2.5.2.12 Synthesis of $K_5H_2[PV_4W_8O_{40}]$ onto polyaniline backbone

0.175 ml (0.01mmol) of aniline was added to the 40 ml water-containing beaker. The pyrrole-water mixture was stirred for a few minutes. Next, an accurate weight of 1g (2.74 mmol) of $K_5H_2[PV_4W_8O_{40}].11H_2O$ (deep orange color) was dissolved in a minimum amount of water, and the solution was then added slowly to the aniline/water mixture. About 0.8mg of $FeCl_3.6H_2O$ was added as an oxidizing agent. The orange color solution was slowly turned to dark color, and black precipitate began to form. The resulting reaction mixture was continued stirring for 24h at room temperature. The solid black residue was collected after filtration under vacuum using membrane filter paper. Finally, the residue was washed with HPLC grade water until the filtrate appeared colorless (unreacted $K_5H_2[PV_4W_8O_{40}].11H_2O$ was removed with water). The residue was finally air-dried before use as an electrode material.

2.5.2.13 Synthesis of $K_5H_2[PV_4W_8O_{40}]$ onto activated carbon backbone

900mg of AC powder was accurately weighed and dispersed in 30mL of methanol in a 100mL round bottom flask, and a magnetic stirrer was used to disperse AC in the methanol solution for nearly 5-10 min. Then 100mg of PV_4W_8 powder was dissolved in a minimum amount of HPLC water (less than 5 mL). Then the PV_4W_8 solution was added dropwise into the AC-methanol solution with constant stirring and was kept stirring the resulting solution for 24 hrs. A rotary evaporator was used to evaporate the solution, and the remaining solid reaction mixture was left to air dry.

2.5.2.14 Synthesis of potassium 11-vanadomanganate ($\text{K}_5\text{Mn}^{\text{IV}}\text{V}_{11}\text{O}_{32}\cdot 10\text{H}_2\text{O}$) and potassium 13-vanadomanganate ($\text{K}_7\text{Mn}^{\text{IV}}\text{V}_{13}\text{O}_{38}\cdot 18\text{H}_2\text{O}$)

Potassium 13-vanadomanganate was synthesized using the procedure reported elsewhere. (Flynn and Pope 1970a; b)

2.5.2.15 Synthesis of activated carbon - $\text{K}_5\text{Mn}^{\text{IV}}\text{V}_{11}\text{O}_{32}\cdot 10\text{H}_2\text{O}$ (AC-MnV₁₁) or activated carbon - $\text{K}_7\text{Mn}^{\text{IV}}\text{V}_{13}\text{O}_{38}\cdot 18\text{H}_2\text{O}$ (AC-MnV₁₃) electrode

The AC-MnV₁₁ or AC-MnV₁₃ composite was prepared using the bottom-up approach. 900 mg of AC was dispersed in 40 ml of methanol taken in a 100 ml round bottom flask, and the dispersed solution was stirred for an ample amount of time to ensure well dispersion of AC in methanol. The MnV₁₁ or MnV₁₃ solution was prepared by dissolving the required amount in 5 ml of HPLC grade water. The prepared MnV₁₁ or MnV₁₃ solution was added slowly dropwise into the already prepared AC-methanol dispersion solution. The resulting solution was kept stirring for about 24 h at room temperature. Finally, the solution was dried in a rotary vacuum evaporator and washed with plenty of distilled water to remove the excess MnV₁₁ or MnV₁₃, then diethyl ether to dry the composite.

2.6 Electrode Preparation and Fabrications

The working electrode was prepared by mixing accurately measured 80% of fine powdered active materials, 10% carbon black, and 10% of PVDF along with 2 ml of NMP (N-Methyl-2- Pyrrolidone) to make a slurry. The slurry was kept for sonication for about one and a half hours to disperse the electrode materials. Finally, this slurry was slowly and uniformly coated on a 1 ×1 cm carbon cloth (mass of the active material 0.8 mg) using a micropipette. It dried at 80 °C for over 24 h, which was used further as a working electrode for the current study. The electrodes were constructed into a symmetric 2-electrode setup using a stainless-steel split cell. The working electrodes were arranged so that both the coated side faced the separator (Whatman No 41 filter paper), and the outer side was attached to the current collector. This whole layout was then treated with an aqueous electrolyte, and subsequently, the electrochemical performance was carried out.

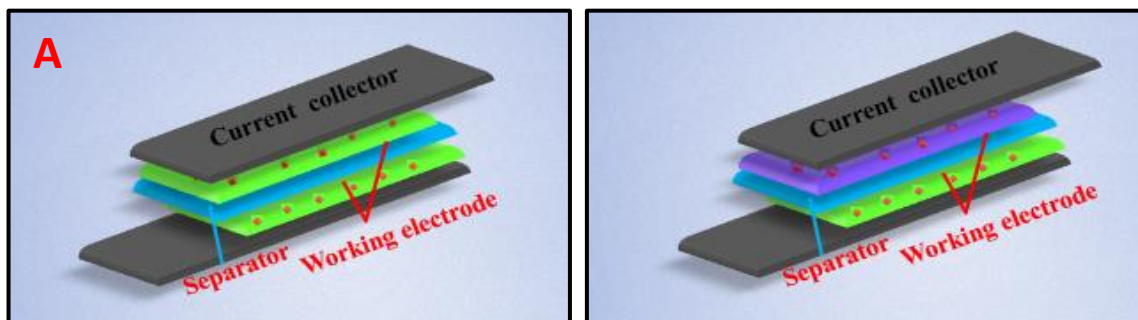


Fig. 2.5 A) Symmetric and B) Asymmetric representation of the supercapacitor cell setup.

2.7 Characterizations and Measurements

2.7.1 Structural and surface characterizations

2.7.1.1 Fourier transforms Infrared spectroscopy (FTIR)

This spectroscopy was used to determine the functional group present in the synthesized composite in the region of 400 cm^{-1} - 4000 cm^{-1} by using Bruker 4000 (USA) spectrometer through the KBr pellet method.



Fig. 2.6 FTIR setup (Image courtesy: Chemistry department, NITK, Surathkal)

2.7.1.2 Thermal gravimetric analysis (TGA)

The thermal stability measurement of all the electrode materials was performed using PerkinElmer TGA4000 (USA) at the heating rate of 5 °C/min inflowing of 20 ml/min N₂.



Fig. 2.7 TGA setup (Image courtesy: Chemistry department, NITK, Surathkal)

2.7.1.3 Powder XRD studies

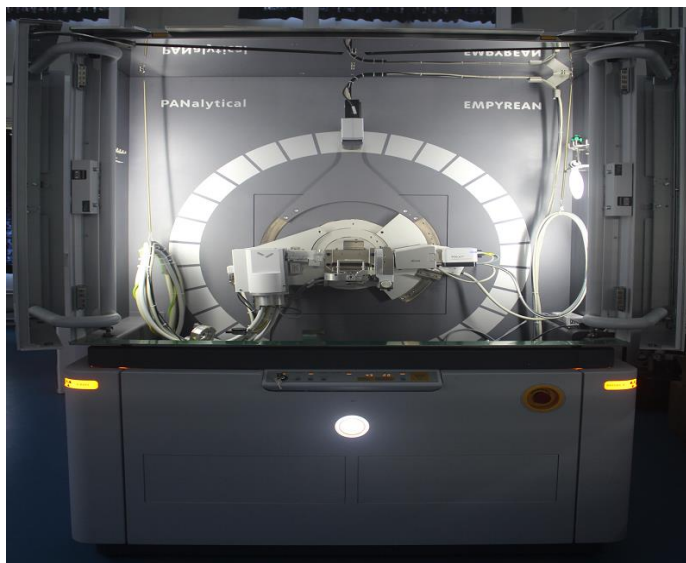


Fig. 2.8 Powder XRD setup (Image courtesy: Central research facility (CRF), NITK, Surathkal)

The X-ray diffraction (XRD) patterns were recorded using Rigaku Mini Flex 600 (Japan) diffractometer to analyze the synthesized composite and confirm the recorded diffraction peaks with JCPDS reference files. And XRD pattern was given clear information about the crystalline and amorphous nature of the composite.

2.7.1.4 FESEM and EDS analysis

This FESEM analysis was given in detailed structural morphology of the synthesized composites in different magnification. It provides particle size, shapes, imperfections, metallographic details, and topology of the composites. Energy dispersive X-ray Analysis (EDS) studies give a clear idea that elements present in the composites were investigated using Field emission scanning electron microscopy (FESEM) (Carl Zeiss Sigma, Germany).



Fig. 2.9 FESEM and EDS setup (Image courtesy: Central research facility (CRF), NITK, Surathkal)

2.7.1.5 Brunauer-Emmett-Teller (BET)



Fig. 2.10 BET setup (Image courtesy: Central research facility (CRF), NITK, Surathkal)

The BET surface area was measured using a Micromeritics physisorption analyzer (Model ASAP 2020, USA). It is used to calculate the specific surface area of the powder sample based on nitrogen adsorption isotherm measurement at 77K.

2.7.1.6 X-ray photoelectron spectroscopy (XPS)

This technique is mainly used to find out the elements in the composite or material; it is also a surface-sensitive quantitative spectroscopic technique based on the photoelectric effect. It can find out the elements from the surface of the material, the overall electronic structure and as well as their chemical state, etc. This spectroscopy is a powerful complete measurement technique because it can find out the elements present in the material and the other elements bound to it. Here we used to record XPS data through Thermofisher Scientific equipment (Model Nexsa base).



Fig. 2.11 XPS setup (Image courtesy: Advanced material research center. IIT Mandi)

2.7.2. Electrochemical characterizations

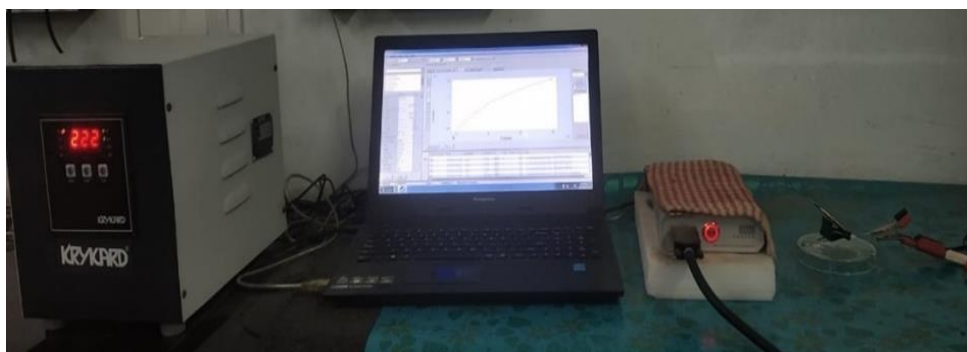


Fig. 2.12 Electrochemical workstation setup (Image courtesy: (Chemistry department, NITK, Surathkal)

Complete electrochemical characterizations such as cyclic voltammetry (CV), chronopotentiometry (galvanostatic charge-discharge (GCD)), and Electrochemical impedance spectroscopy (EIS) are used to analyze the newly fabricated supercapacitor; the entire work was done by using the two-electrode method in the different potential window (1.0V, 0.8V, etc.) and various concentration of sulphuric acid (0.1M, 0.25M and 0.5M). The

measurements were carried out using an electrochemical workstation (IVIUM Technologies BV Co., The Netherlands, Model: Vertex).

2.7.2.1 Cyclic voltammetry (CV)

This method was used to find reduction, oxidation peaks (redox property), specific capacitance, reversibility, etc., for the synthesized composite in the different potential windows for different materials, and scan rate was used in the range of $100 \text{ mV s}^{-1} - 5 \text{ mV s}^{-1}$. The formula was used for the calculation is given below (Hou et al. 2020).

$$\text{Specific capacitance } (C_s): \quad C_s = \frac{1}{2 \times m \times v \times \Delta V} \int I(V) dV \quad 2.1$$

where m , v , and ΔV is the mass of active material, scan rate, and potential window, respectively.

2.7.2.2 Galvanostatic charge-discharge (GCD)

Chronopotentiometry was used to measure the charge-discharge behavior of the synthesized supercapacitor composite at different current densities as same as the CV potential window. From GCD, the specific capacitance (C_s), the energy density (ED), power density (PD), etc., were calculated using the below equations (Chandran et al. 2020)

For the linear GCD plot,

$$\text{Specific Capacitance } (C_s) = \frac{I \times \Delta t}{\Delta V} \text{ F/g} \quad 2.2$$

For non-linear GCD plot,

$$\text{Specific Capacitance } (C_s) = \frac{\int_{V_i}^{V_f} i v dt}{\int_{V_i}^{V_f} v dV} = \frac{2i_m \int v dt}{V^2 \left\{ \begin{matrix} V_f \\ V_i \end{matrix} \right\}} = \frac{i(\Delta t * \Delta V)}{m(\Delta V)^2} \text{ F/g} \quad 2.3$$

Where I , Δt , and ΔV represent the current density (A g^{-1}), discharge time (Sec), and operating cell potential (V).

$$\text{Power density (P)} = \frac{E}{\Delta t (s)} \times 3600 \text{ Wh/kg} \quad 2.4$$

$$\text{Energy (E)} = \frac{1}{2} \times C \times \Delta V^2 \times \frac{1000}{3600} \text{ Wh/kg} \quad 2.5$$

$$\text{Energy density (E)} = i \int V dt \text{ Wh/kg} \quad 2.6$$

Where E is the energy density, Δt is the discharge time in seconds, C is the capacitance, and ΔV is the potential window.

2.7.2.3 Electrochemical impedance spectroscopy (EIS)

$$Z = [C_1 || R_{ct1}] + R_s + [C_2 || R_{ct2}] \quad 2.7$$

$$Z = R_s + 2 [C || R_{ct}] = R_s + 2 [C * R_{ct} / (C + R_{ct})] \quad 2.8$$

The cell capacitance and impedance were calculated from the EIS data for the device (laboratory scale) applications using the following equations

$$\text{Re}(C) = -\text{Im}(Z) / \omega |Z|^2 \quad 2.9$$

$$\text{Im}(C) = \text{Re}(C) / \omega |Z|^2 \quad 2.10$$

$$Z = \text{SQRT}[\text{Re}^2(Z) + \text{Im}^2(Z)] \quad 2.11$$

$\text{Re}(C)$ is the real part, and $\text{Im}(C)$ is the complex part, respectively. These two values are calculated using the real and imaginary parts of the impedance (Z) values. ω is the angular frequency, where f_0 is the cut-off frequency or the minimum frequency applied (Taberna et al. 2003).

$$C_{TF} = 1 / (2\pi f * \text{Im}[z]) \quad 2.12$$

C_{Tf} is the cell capacitance, f is the minimum frequency applied, $\text{Im}(z)$ is the complex impedance at the minimum frequency.

2.7.2.4 Trasatti method

$$C^{-1} = \text{Constant} * \nu^{0.5} + C_T^{-1} \quad 2.13$$

C^{-1} is the reciprocal of gravimetric capacitance, and $\nu^{1/2}$ is the square root of scan rate.

$$C = \text{Constant} * \nu^{-0.5} + C_{EDL} \quad 2.14$$

C is the gravimetric capacitance, and $\nu^{-1/2}$ is the reciprocal of the square root of scan rate.

$$C_T = C_{EDL} + C_{PSUEDO} \quad 2.15$$

CHAPTER 3



**In situ Vanadophosphomolybdate
Impregnated into Conducting Polypyrrole
for Supercapacitor**

This chapter describes the synthesis of two vanadophosphomolybdates ($\text{H}_4[\text{PVMo}_{11}\text{O}_{40}]$ (PVMo_{11}) and $\text{H}_5[\text{PV}_2\text{Mo}_{10}\text{O}_{40}]$ ($\text{PV}_2\text{Mo}_{11}$)) and one-pot oxidation reaction with pyrrole. The combination of redox-active inorganic metal oxides, such as polyoxometalates (multi-metal oxide cluster) with conduction polymers, could enhance the material's stability due to its fast multi-electron redox property. However, its application has been restricted because of swelling and shrinking capability during the charge and discharge cycle. The combination of redox-active inorganic metal oxides, such as polyoxometalates (multi-metal oxide cluster) with conduction polymers, could enhance the material's stability due to its fast multi-electron redox property. Here, we report the two polypyrroles combined vanadophosphomolybdates, namely PPy- $\text{H}_4[\text{PVMo}_{11}\text{O}_{40}]$ and PPy- $\text{H}_5[\text{PV}_2\text{Mo}_{10}\text{O}_{40}]$ nanohybrid electrode materials and their studies in detail.

3. Result and Discussion

3.1 Structural, chemical, and morphological characterizations

3.1.1 Fourier transform infrared spectroscopy

Fig. 3.1 displays the FTIR spectra of PPy, pure POMs, and composite materials PPy- $\text{H}_4[\text{PVMo}_{11}\text{O}_{40}]$ and PPy- $\text{H}_5[\text{PV}_2\text{Mo}_{10}\text{O}_{40}]$, respectively. The broad IR band at 3400 cm^{-1} in PPy is assigned to the adsorbed water adsorbed. The small peak at 3250 cm^{-1} was attributed mainly to the pyrrole ring's N-H stretching vibration (Ameen et al. 2014). The bands at 1550 and 1470 cm^{-1} are assigned to the C=C and C-N stretching vibration of PPy, respectively (Ruckenstein and Chen 1991). All the stretching vibration bands observed in PPy match well with the available literature (Konwer et al. 2011), thereby confirming polypyrrole polymer formation. PPy synthesized with $\text{H}_4[\text{PVMo}_{11}\text{O}_{40}]$ and $\text{H}_5[\text{PV}_2\text{Mo}_{10}\text{O}_{40}]$ show similar band characteristics of PPy. However, few new bands have been noticed at 1061 , 960 , 866 , 596 , and 775 cm^{-1} , respectively, in the PPy- $\text{H}_4[\text{PVMo}_{11}\text{O}_{40}]$ composite electrode material, indicating the presence of $\text{H}_4[\text{PVMo}_{11}\text{O}_{40}]$.

The IR bands at 1061, 960, 866, 596, and 792 cm^{-1} could be assigned to the P–O, terminal Mo=O, bridged Mo–O–Mo, and V–O bonds vibration, respectively, for $\text{H}_4[\text{PVMo}_{11}\text{O}_{40}]$ compound. In contrast, the bands at 1061, 960, 866, 596, and 792 cm^{-1} could be assigned to the P–O, terminal Mo = O, bridged Mo–O–Mo, and V–O vibration, respectively, for $\text{H}_5[\text{PV}_2\text{Mo}_{10}\text{O}_{40}]$ compound (Akba et al. 1997). All the above vibrational frequencies are matched with the pure $\text{H}_4[\text{PVMo}_{11}\text{O}_{40}]$ and $\text{H}_5[\text{PV}_2\text{Mo}_{10}\text{O}_{40}]$, respectively, which affirms the presence of vanadophosphomolybdates on the PPy surface.

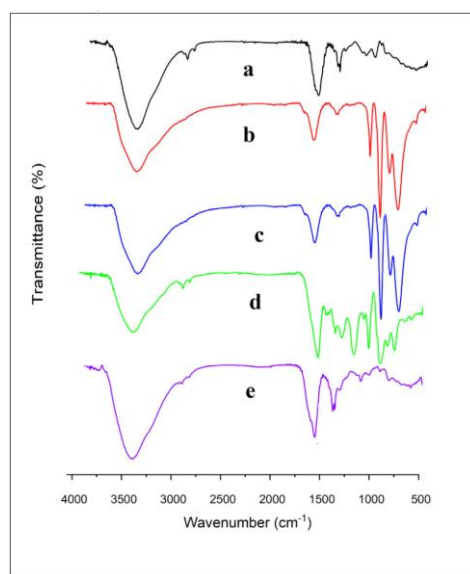


Fig. 3.1 FTIR of a) PPy, b) pure $\text{H}_4[\text{PVMo}_{11}\text{O}_{40}]$, c) pure $\text{H}_5[\text{PV}_2\text{Mo}_{10}\text{O}_{40}]$, d) PPy- $\text{H}_4[\text{PVMo}_{11}\text{O}_{40}]$ composite and e) PPy- $\text{H}_5[\text{PV}_2\text{Mo}_{10}\text{O}_{40}]$.

3.1.2 Thermogravimetry analysis

One of the most critical electrode materials properties for energy storage applications is thermal stability. Generally, COPs are not considered appropriate materials for fabricating energy storage devices due to their swelling and shrinking behavior during charging and discharging cycles. The thermal stability of the composite electrode materials, mainly PPy- $\text{H}_4[\text{PVMo}_{11}\text{O}_{40}]$ and PPy- $\text{H}_5[\text{PV}_2\text{Mo}_{10}\text{O}_{40}]$, was analyzed by TGA (PerkinElmer TGA 4000) (**Fig.3.2**) to know the working temperature. The TGA thermogram of PPy revealed 9.1% of weight loss up to the glass transition temperature of 68.4 $^{\circ}\text{C}$, and the complete

decomposition of the PPy was noticed at 832.32 °C, as shown in DTGA. **Fig. 3.2b and 3.2c** represent the TGA curve of pure PPy- $H_4[PVMo_{11}O_{40}]$ and $H_5[PV_2Mo_{10}O_{40}]$. The weight loss (22.1% and 18.62%, observed till 125 °C for both the POMs attributed to removing the moisture and crystal water molecules and further heating both the POMs showed extreme phase transition stability at 343.8 °C, and 291.5 °C, respectively. However, both the POMs were decomposed by following **scheme 2.1** above 800 °C (Uma and Nogami 2007).

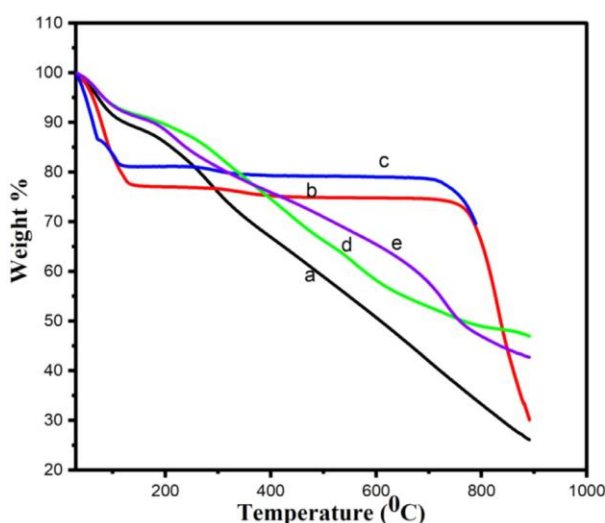


Fig. 3.2 TGA curves of a) PPy, b) pure $H_4[PVMo_{11}O_{40}]$, c) pure $H_5[PV_2Mo_{10}O_{40}]$, d) PPy- $H_4[PVMo_{11}O_{40}]$ composite, and e) PPy- $H_5[PV_2Mo_{10}O_{40}]$.

The thermogram of POMs doped PPy hybrid materials, namely PPy- $H_4[PVMo_{11}O_{40}]$ and PPy- $H_5[PV_2Mo_{10}O_{40}]$, presented in **Fig. 3.2d and 3.2e**, suggests combined weight loss of PPy and $H_4[PVMo_{11}O_{40}]$ and $H_5[PV_2Mo_{10}O_{40}]$, respectively. **Fig. 3.2d and 3.2e** revealed that the first weight loss (7.6% and 7.5%) at 59.7 °C and 69.9 °C are because of the moisture removal from the hybrid materials. Beyond 100 °C, the steady weight loss (33.6%) till 545 °C and 787.5 °C is attributed to the phase transition and decomposition of inorganic moieties of the vanadophosphomolybdate in the PPy- $H_4[PVMo_{11}O_{40}]$ composite respectively (**Fig. 3.2d**). Similarly, it shows the weight loss (6.86%) till 501.7 °C and 731.8 °C for phase transition temperature and decomposition of inorganic moieties of another vanadophosphomolybdate in the PPy- $H_5[PV_2Mo_{10}O_{40}]$,

respectively, and suggests that the PPy-H₅[PV₂Mo₁₀O₄₀] is more stable than the PPy-H₄[PVMo₁₁O₄₀] composite hybrid material. Further, the thermal stability of the hybrid materials is increased by more than 100 °C than the PPy (500 °C), which can be explained by the presence of electrostatic interaction between highly negatively charged POMs and cationic PPy.

3.1.3 X-ray diffraction spectroscopy

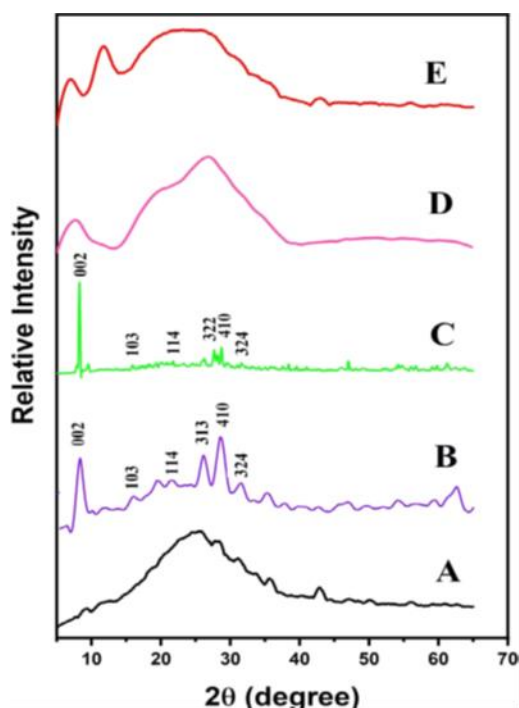


Fig. 3.3 P-XRD patterns of a) PPy, b) pure H₄[PVMo₁₁O₄₀], c) pure H₅[PV₂Mo₁₀O₄₀], d) PPy- H₄[PVMo₁₁O₄₀] composite, and e) PPy-H₅[PV₂Mo₁₀O₄₀].

Powder X-ray diffraction (P-XRD) patterns of PPy, pure H₄[PVMo₁₁O₄₀], pure H₅[PV₂Mo₁₀O₄₀], PPy-H₄[PVMo₁₁O₄₀], and PPy-H₅[PV₂Mo₁₀O₄₀] composite were recorded and are presented in **Fig. 3.3**. The P-XRD patterns of pure H₄[PVMo₁₁O₄₀] and H₅[PV₂Mo₁₀O₄₀] endorse well the published literature reports (Li et al. 2014). However, the acidic H₄[PVMo₁₁O₄₀] and H₅[PV₂Mo₁₀O₄₀] polyanions are highly crystalline materials and showed characteristics of diffraction peaks, as shown in **Fig. 3.3B and C**. The PPy is amorphous in nature and exhibits a broad diffraction peak in the P-XRD pattern (**Fig.**

3.3A). The characteristics diffraction peaks of $H_4[PVMo_{11}O_{40}]$ and $H_5[PV_2Mo_{10}O_{40}]$ disappeared in the P-XRD patterns of respective PPy-based hybrid composites (**Fig. 3.3D and E**), suggesting the loss of the crystallinity and showing the amorphous nature.

3.1.4 Field emission scanning electron microscopy

The surface morphology of PPy, pure $H_4[PVMo_{11}O_{40}]$, pure $H_5[PV_2Mo_{10}O_{40}]$, and composite hybrid materials are shown in **Fig. 3.4**. The field emission scanning electron microscopy (FESEM) image of pure $H_4[PVMo_{11}O_{40}]$ and pure $H_5[PV_2Mo_{10}O_{40}]$ show plate-like shapes, as shown in **Fig. 3.4 B and C**. It is discernible from **Fig. 3.4 A** that all the PPy particles formed densely packed spherical-like shapes agglomerates of around $0.6 \mu m$ (Chitte et al. 2011). In contrast, composite hybrid materials containing vanadium substituted Keggin ions show densely packed, somewhat larger spongy, and spherical-like microstructure shapes (**Fig. 3.4D and E**) with 202.7 and $103.1 \mu m$ size, respectively. This can be ascribed to the vanadium substituted Keggin ions, which are surrounded by COPs due to the electrostatic interactions and show several shapes.

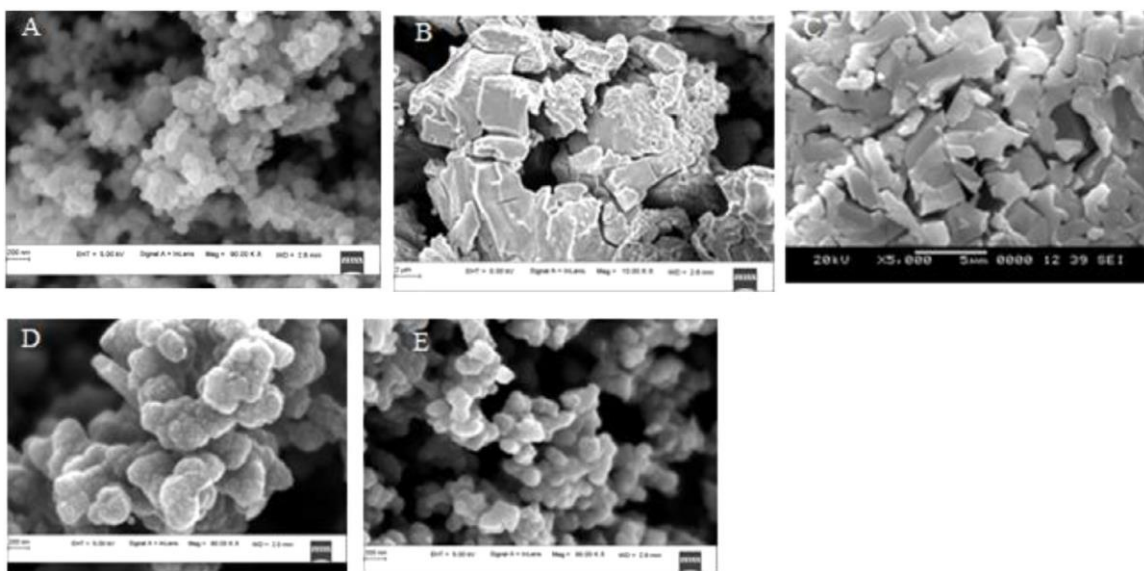


Fig. 3.4 FESEM image of a) PPy, b) pure $H_4[PVMo_{11}O_{40}]$, c) pure $H_5[PV_2Mo_{10}O_{40}]$, d) PPy- $H_4[PVMo_{11}O_{40}]$ composite, and e) PPy- $H_5[PV_2Mo_{10}O_{40}]$ composite.

3.1.5 Energy-Dispersive X-ray spectroscopy

Fig. 3.5 exhibits the energy-dispersive X-ray spectra (EDS) of two composite electrodes, mainly PPy-H₄[PVMo₁₁O₄₀] and PPy-H₅[PV₂Mo₁₀O₄₀]. The presence of elements O, N, C, P, V, and Mo was confirmed from the composite materials EDS spectra. The EDS spectra of the reference samples were also examined, as shown in **Fig. 3.5**. The FESEM and EDS combined results confirm that the two POMs (H₄ [PVMo₁₁O₄₀] and H₅[PV₂Mo₁₀O₄₀]) clusters are doped on the PPy network surface and held together by the electrostatic interaction between them. Tang et al. have stated that the deposition of POM on PPy is the cation-radical electro polymerization process, during spin coating for humidity sensing application (Miao et al. 2018).

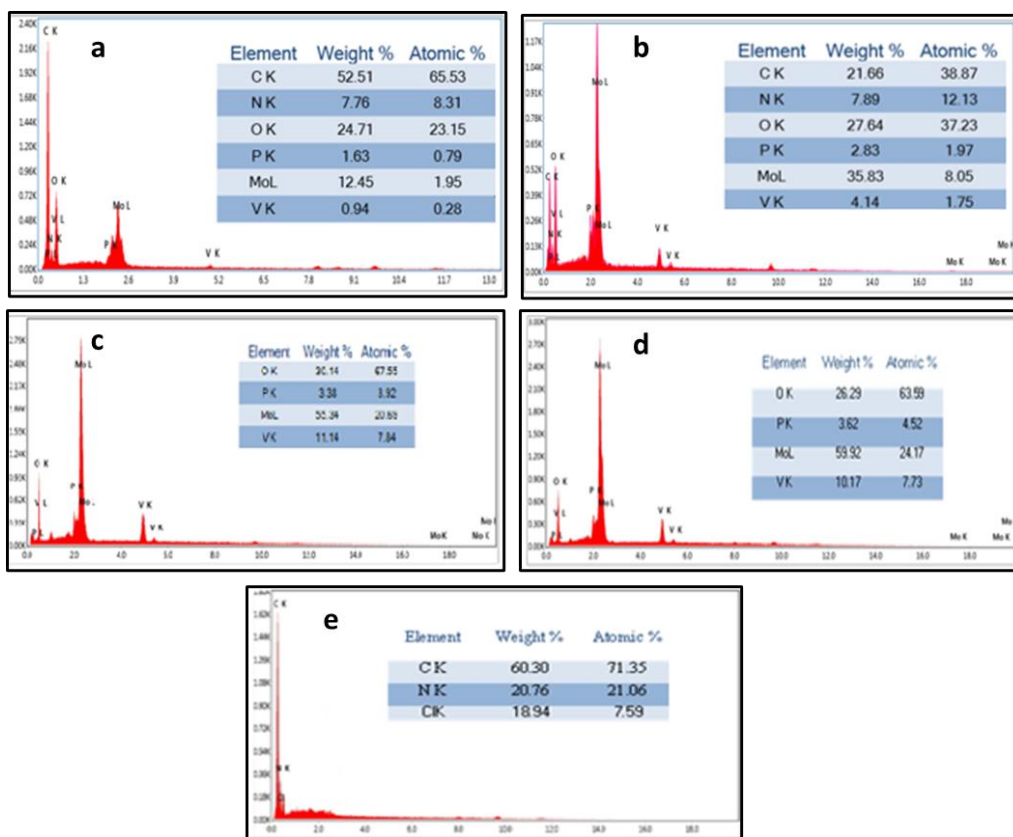


Fig. 3.5 EDS spectra of two composite electrodes, namely a) PPy- H₄[PVMo₁₁O₄₀] composite, b) PPy-H₅[PV₂Mo₁₀O₄₀] composite c) H₄[PVMo₁₁O₄₀], d) H₅[PV₂Mo₁₀O₄₀] and e) Pure PPy.

3.1.6 Brunauer–Emmett–Teller

PPy-H₄[PVMo₁₁O₄₀], and PPy-H₅[PV₂Mo₁₀O₄₀] composites middle BET surface area is 22 and 9 m²/g, respectively. The composite material showed type IV nitrogen adsorption isotherm with no well-defined hysteresis loop, as shown in **Fig. 3.6**. However, the PPy-H₄[PVMo₁₁O₄₀] composite exhibits hysteresis in the low relative pressure region. The low relative pressure hysteresis may arise due to the lack of equilibrium during the composite material's adsorption and/or swelling.

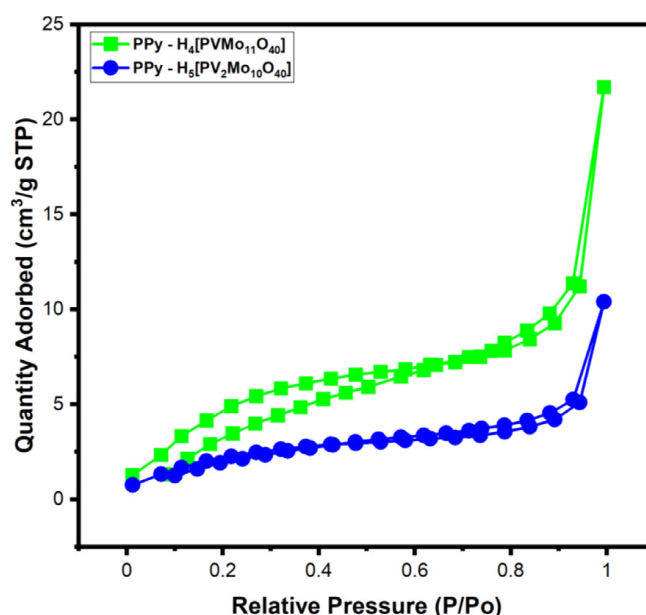


Fig. 3.6 Nitrogen adsorption/desorption isotherm of PPy- H₄[PVMo₁₁O₄₀] composite and PPy-H₅[PV₂Mo₁₀O₄₀] composite.

3.2 Electrochemical measurements

Two electrodes system cyclic voltammetry (CV) method was employed in order to know the electrochemical properties (applied potential and current response) and pseudocapacitance behavior changes in the redox activity of the two Keggin type polyanions upon doping in situ formation conducting PPy matrix (e.g., PPy-H₄[PVMo₁₁O₄₀], PPy-H₅[PV₂Mo₁₂O₄₀]), respectively in 0.1 M aqueous H₂SO₄ electrolyte medium. Moreover, the decomposition potential of an electrolyte determines the electrochemical

windows of a capacitor. Zhu et al. have extensively studied the influence of different electrolyte cations (H^+ , Li^+ , Na^+ , and K^+) on graphene/polypyrrole-based SCs and observed that there was a significant difference in specific capacitance with a decrease in cations size and hydrate cation radius leading to the higher ion's mobility, and diffusion (Miao et al. 2018). However, the aqueous acidic electrolyte was used in this report because of its high cationic mobility. It helps in fast charge transfer, which allows more ion adsorption into electrolyte-electrode interphase. The high ion adsorption facilitates the extent of faraday reaction, even though it has limitations in practical applications (e.g., corrosion). Another disadvantage of treating aqueous electrolytes is that it restricts the operating voltage within 1 V due to the low thermodynamic voltage of water decomposition (1.23V). However, selecting organic electrolytes and ionic liquids (ILs) raises the potential working window up to 5 V. Still, a few deficiencies, such as insufficient conductivity, purity, and economic and safety barriers, restrict it from practical applications (e.g., electric car).

3.2.1 CV studies

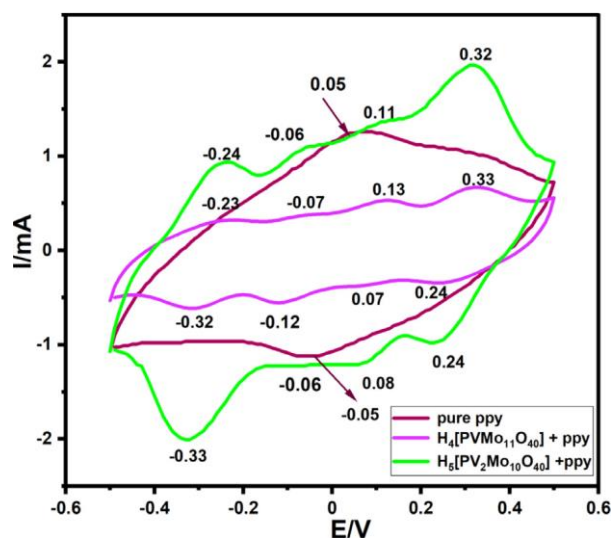


Fig. 3.7 Cyclic voltammograms and Oxidation-reduction peaks of PPy and two composite potentials at 10 mV s^{-1} scan rates at $0.1 \text{ M H}_2\text{SO}_4$.

Thus, in the present investigation, we have examined supercapacitive properties of the PPy, and hybrid composite electrode materials using CV in different concentrations of an aqueous solution of H₂SO₄ medium, keeping in mind the operational voltage range. The CV provides beneficial information on the charge-discharge characteristics of the electrode cell. The gravimetric specific capacitance of electrodes were calculated (CV graphs) from the **equations (2.1)**.

3.1.2 GCD studies

Galvanostatic charge-discharge in different current densities was studied to look into the electrochemical performance of the electrode materials under a particular potential window to know the electrochemical behavior of the electrode materials. **Fig. 3.8a and 3.8b** show the GCD curves of PPy-H₄[PVMo₀₁₁O₄₀] and PPy-H₅[PV₂Mo₀₁₀O₄₀] at various current densities in 0.1 M H₂SO₄ aqueous electrolyte, which gave rise to perfect pseudocapacitance behavior. The GCD of PPy exhibits the linear charge-discharge curves, indicating material's capacitive nature. The capacitance was calculated using equation 3 and found to be a maximum of 25.15 F g⁻¹ in 1 A g⁻¹. However, unlike SCs, Faradaic reactions are also responsible for rechargeable batteries but do not produce rectangular CV or linear GCD curves. High energy density is also recommended for device application purposes, which are often generated using GCD curves. Therefore, redox-active transition metal oxide impregnated on PPy electrode composite material might benefit from achieving high energy density, as redox-active metal oxide stores electrical charge via either electron transfer (Faradaic reaction) or oxidation-reduction reaction (chemical redox reactions).

Since the GCD shows a non-linear curve, the conventional equation cannot be used to calculate the capacitance (C). Thus, the C of all electrode materials was assessed from the GCD profile for a 2-electrode system (charge/discharge) using **equation (2.3)** (Mai et al. 2013).

The power density (P) and energy density (E) were assessed from the GCD profile using the equations (2.4) and (2.6), respectively:

Fig. 3.8a shows the GCD plot of the PPy-H₄[PVMo₁₁O₄₀] composite electrode, which was recorded at different current densities (0.2 to 10 A g⁻¹) in 0.1 M H₂SO₄. The non-linear charge-discharge curves show the supercapacitor behavior of the electrode (Mai et al. 2013). It can be seen that the lower the current densities, the discharging times take longer than charging (due to intercalation). The shapes changed to non-symmetrical triangular because of the charge transfer behavior of the electrode.

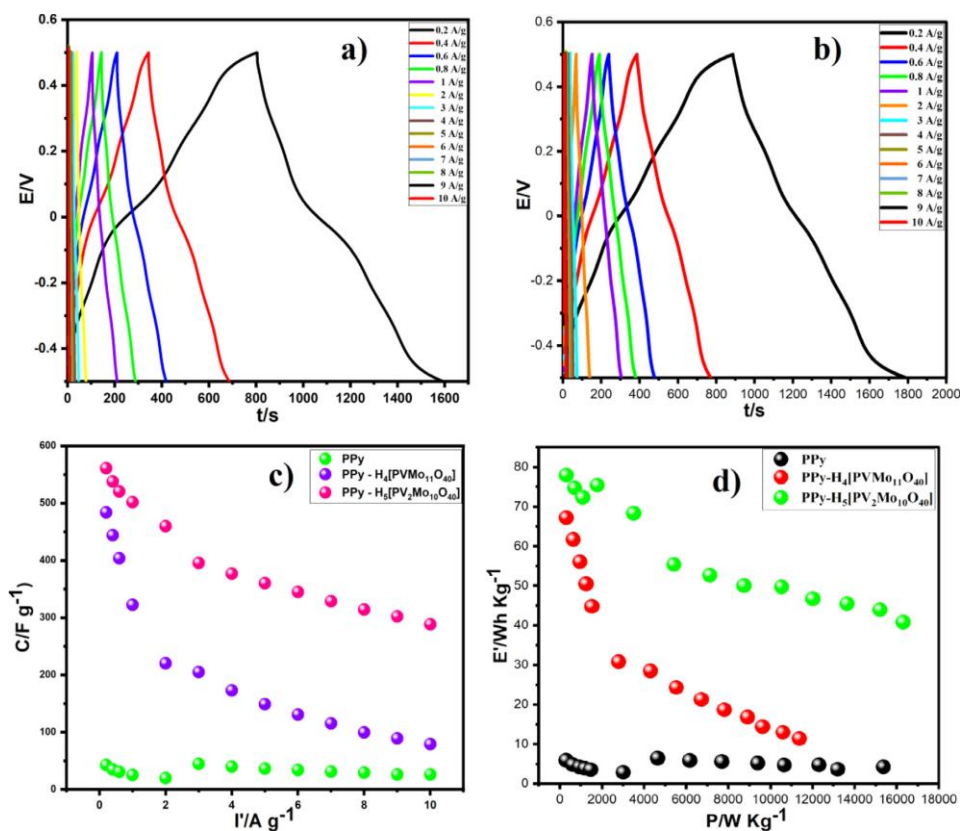


Fig. 3.8 GCD curves of a) PPy-H₄[PVMo₁₁O₄₀] and b) PPy-H₅[PV₂Mo₁₀O₄₀]. c) The capacitance at current densities of 0.2–10 A g⁻¹. d) the Ragone plots at various current densities of 0.2–10 A g⁻¹.

The capacitance, energy, and power densities of the active electrode materials (PPy-H₄[PVMo₁₁O₄₀] and PPy-H₅[PV₂Mo₁₀O₄₀]) at various currents densities from 10 to 0.2 A

g^{-1} are presented in **Fig. 3.8c and 3.8d**, respectively. The PPy-H₄[PVMo₁₁O₄₀] electrode material provides the highest capacitance of 483.9 F g^{-1} at current densities of 0.2 A g^{-1} . The energy and power densities were determined based on **equations (2.6) and (2.4)** at the same current densities. Since the PPy-H₄[PVMo₁₁O₄₀] electrode was providing higher capacitance, high energy, and power densities compared to PPy, we integrated another vanadium-containing Keggin ion (H₅[PV₂Mo₁₀O₄₀]) into PPy (PPy-H₅[PV₂Mo₁₀O₄₀]) and investigated its electrochemical performance (**Fig.3.8b**). As expected, PPy-H₅[PV₂Mo₁₀O₄₀] provides significantly higher capacitance and higher energy density at various current densities in the same electrolyte concentration than PPy-H₄[PVMo₁₁O₄₀] and PPy. This may be because the number of conducting PPy was needed to balance the charge neutrality of PPy-H₅[PV₂Mo₁₀O₄₀], or the presence of two active vanadium centers in the Keggin ions to enhance the redox reaction (observed in the CV graph, **Fig. 3.7**), which was also suggested by Chen et al. **Fig. 3.8b** also shows the non-linear GCD curves of PPy-H₅[PV₂Mo₁₀O₄₀] at the various current densities ranging from 0.2 to 6 A g^{-1} . A remarkable 561 F g^{-1} capacitance value was obtained at 0.2 A g^{-1} , applying equation 3. The energy and power densities were determined using **equations (2.6) and (2.4)** for PPy-H₅[PV₂Mo₁₀O₄₀] at 0.1 M H₂SO₄ and provided high power density values of 19.48 Wh kg^{-1} and 78.07 W kg^{-1} , respectively, at the same current density. However, at a high current density of 10 A g^{-1} , the PPy-H₄[PVMo₁₁O₄₀] and PPy-H₅[PV₂Mo₁₀O₄₀] provide a capacitance of 79.1 and 288.4 F g^{-1} , respectively. The capacitance is larger for PPy-H₅[PV₂Mo₁₀O₄₀] at lowering current densities due to the mass transfer limitation of electrolyte ions inside the electrode's pores (Chen et al. 2015). It has also been observed from **Figs. 3.8a and 3.8b** that all the composites take much longer to discharge, lowering the current densities and eventually providing higher capacitance and power density, respectively. The surface diffusion of ions is ceased to exist. In addition, more charges are being stored in the electrode due to the bulk diffusion, which eventually increases the capacitance and the power density of the PPy-H₅[PV₂Mo₁₀O₄₀] electrode. **Fig. 3.8c** shows the capacitance at current densities of 0.2-10 A g^{-1} , and PPy-H₅[PV₂Mo₁₀O₄₀] shows the highest capacitance at 0.2 A g^{-1} current density. It can be seen from Figure 8d that PPy-

H₅[PV₂Mo₁₀O₄₀] provides the highest (19.48 Wh kg⁻¹) energy density. In contrast, the PPy and PPy-H₅[PVMo₁₁O₄₀] provide 1.48 Wh kg⁻¹ and 16.8 Wh kg⁻¹ of energy density in 0.2 A g⁻¹ current density.

3.1.3 EIS studies

In order to know the electrical characteristics of the electrode-electrolyte interface, electrochemical impedance spectroscopy (EIS) was carried out for PPy, PPy-H₄[PVMo₁₁O₄₀], and PPy-H₅[PV₂Mo₁₀O₄₀], two new composites, and data are expressed as Nyquist plot over 1 to 10⁵ Hz frequency range (Figure 3.9) with 10 mV dc applied potential. The insert pictured in **Fig. 3.9**, a small arc in the high-frequency region, shows dominating the supercapacitor's resistive nature within electrode/electrolyte/current-collector better for PPy-H₅[PV₂Mo₁₀O₄₀] than PPy-H₄[PVMo₁₁O₄₀] and PPy.

An appropriate equivalent circuit for two composite electrode materials is presented in **Fig. 3.10**, and their fitting data are summarized in **Table 3.1** from the Nyquist plot. Since its symmetric arrangement so $C_1 = C_2 = C$; and similarly, $R_{ct1} = R_{ct2} = R_{ct}$. Thus, the total impedance is represented in the cell **equation (2.7) and (2.8)**.

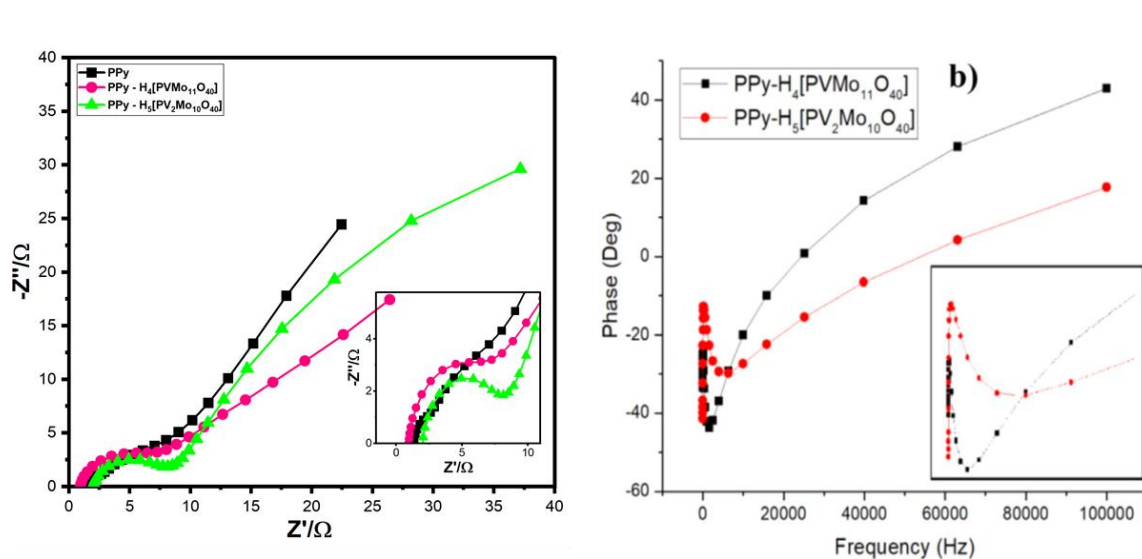


Fig. 3.9 a) Nyquist plots, and b) Bode plots for the PPy, PPy-H₄[PVMo₁₁O₄₀], and PPy-H₅[PV₂Mo₁₀O₄₀] electrodes.

The cell capacitance values were observed as 9.15 mF and 5.38 mF for PPy-H₄[PVMO₁₁O₄₀] and PPy-H₅[PV₂MO₁₀O₄₀], respectively (**Table 3.1**). EIS testing is used for dielectric spectroscopy analysis, which measures the power cell impedance as a frequency function. This frequency range is adjusted by employing a low amplitude alternative voltage superimposed on a steady-state potential. The responses are usually explicit as a Nyquist plot (**Fig. 3.9a**) and Bode plot (**Fig. 3.9b**). The cell capacitance and impedance were calculated from the EIS data for the device (laboratory scale) applications using **equations (2.9), (2.10), and (2.11)**, and the following information is summarized in **Table 3.2**.

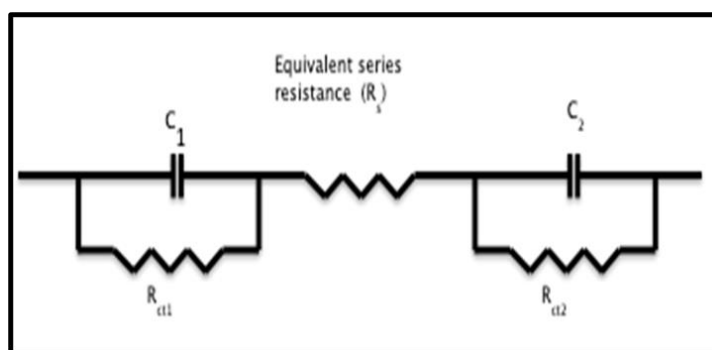


Fig. 3.10 The equivalent circuit is used for fitting the Nyquist plots.

Table 3.1 Fitting Data of Equivalent Circuit Elements Obtained by Nyquist plots

Materials	R_s (Ω)	R_{ct} (Ω)	$R_p = R_s + R_{ct}$ (Ω)	Cell capacitance $C_{Tf}^* = 1/(2\pi f * I$ $m[z])$	f_k (Hz)	Max Peak currents ($I_{max} = 0.5 * C_T$ $V_0 / (1 + C_T R_{ct})$)
PPy-H ₄ [PVMO ₁₁ O ₄₀]	0.95	5.55	6.5	9.15 mF	1 x 10 ⁴	4.35 mA
PPy-H ₅ [PV ₂ MO ₁₀ O ₄₀]	1.98	6.16	8.14	5.38 mF	100	2.603 mA
PPy	1.32	1.03	2.35	6.51 mF	251	2.58 mA

**If we divided C_{Tf} with the mass of the one electrode, then it'll be the capacitance (which is frequency-dependent and calculated at the lowest frequency) from EIS.*

Table 3.2 Fitting Data Obtained from Bode plots.

Materials	Phase changing frequency (f_0)	Phase changing angle (ϕ)	Angular velocity ($\omega=2\pi f_0$)	Time constant ($\tau=C_T R_{ct}$)	Relaxation time constant ($\tau_0 = 1/ f_0$)
PPy-H ₄ [PVMo ₁₁ O ₄₀]	1585 Hz	-44°	9958.85	50.78 ms	0.63 ms
PPy-H ₅ [PV ₂ Mo ₁₀ O ₄₀]	6310 Hz	-30°	39,646.8 rad/s	33.14 ms	0.16 ms

3.1.4 Cycle stability studies

The capacitance retention plots of the PPy-H₅[PV₂Mo₁₀O₄₀], PPy-H₄[PVMo₁₁O₄₀], and PPy are shown in Fig. 3.11a, respectively show using a cyclic voltammetry test at 500 mV s⁻¹ scan rate. After 4500 cycles, the PPy-H₅[PV₂Mo₁₀O₄₀] electrode shows superior cycling stability, with capacitance retention of ~95% and 99% retention stability for PPy. The PPy-H₄[PVMo₁₁O₄₀] electrode offers lesser cyclic stability, with particular retention of the capacitance of ~91%. As presented in **Fig. 3.11b**, the 1st and 4500th cycle stability of PPy-H₅[PV₂Mo₁₀O₄₀] proves the electrode's excellent stability.

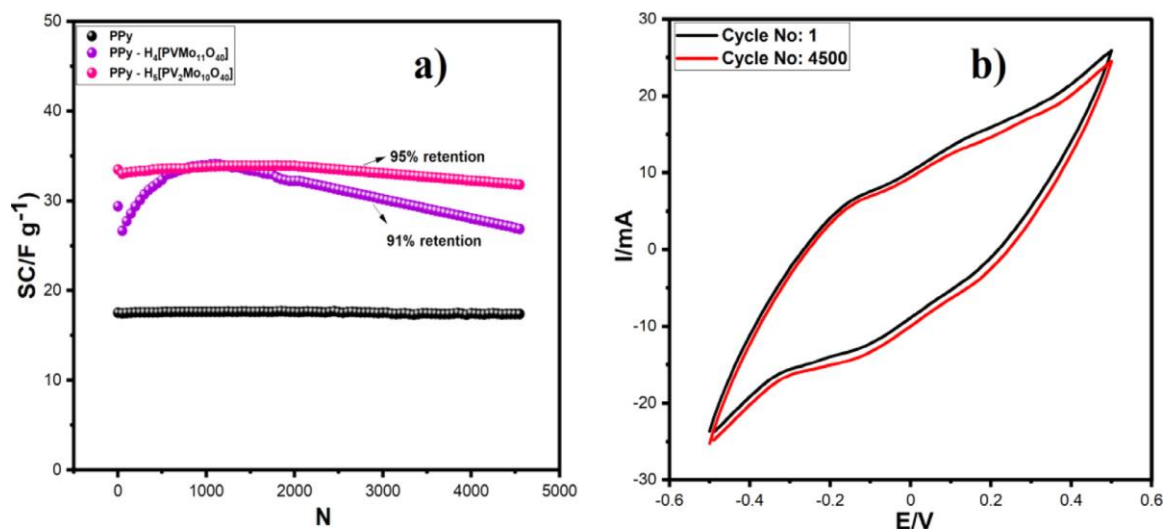


Fig. 3.11 a) Cycle stability of PPy, PPy-H₄[PVMo₁₁O₄₀], and PPy-H₅[PV₂Mo₁₀O₄₀] electrodes, and b) 1st and last cycles for PPy-H₅[PV₂Mo₁₀O₄₀] after 4500 cycles at 500 mV s⁻¹

CHAPTER 4



**One-Pot Synthesis of Polyoxometalate
Decorated polyindole for
Energy Storage Supercapacitor**

This chapter dealt with the one-pot synthesis of PIn/PV₂Mo₁₀ and PIn/PVMO₁₁ and their symmetric cell arrangement. Here, we report a simple method of two polyoxomolybdate (H₄[PVMo₁₁O₄₀] and H₅[PV₂Mo₁₀O₄₀]) doped polyindole (PIn) composites for ECSs. The overall electrochemical performance was improved due to the faradic contribution of POMs and polyindole. Moreover, the stability of polyindole was increased after the formation of composites.

4 Result and Discussion

4.1 Structural, chemical, and morphological characterizations

4.1.1 Fourier transform infrared spectroscopy

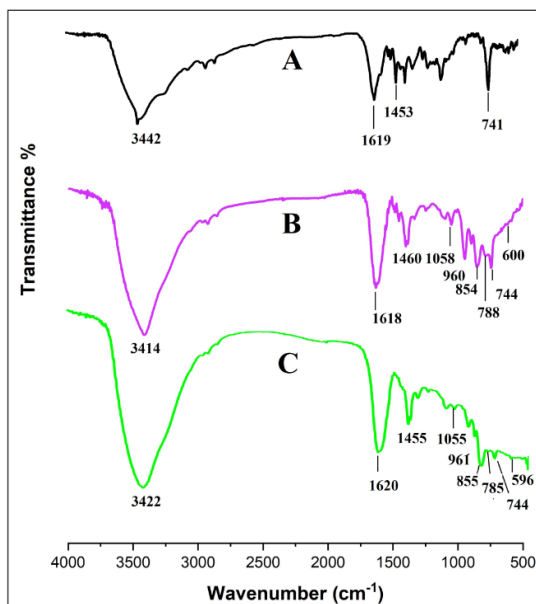


Fig. 4.1 FTIR of A) PIn, B) PIn/PVMO₁₁, and C) PIn/PV₂Mo₁₀.

Fig. 4.1 depicts the comparative FTIR of Polyindole (PIn), PIn/PVMO₁₁, and PIn/PV₂Mo₁₀. PIn revealed the characteristic absorption bands at 3400 (νN–H), 3000 (sp² C–H), 1619 and 1490 (ν C–C, Ar), 1460 (ν C–N) 1365 (ν C=N), and 741 cm⁻¹ out of plane

deformations (ν C–H, Ar), respectively (Mudila et al. 2015). The FTIR of the two POMs (PVMo₁₁ and PV₂Mo₁₀) is reported elsewhere (Vannathan et al. 2020). **Fig. 4.1B and C** represent the FTIR of PIn/PVMo₁₁ and PIn/PV₂Mo₁₀ hybrid electrode, which showed the retained chemical structure of both POMs (PVMo₁₁ and PV₂Mo₁₀) and characteristic bands at 1058 (1055, ν P–O), 960 (961, ν Mo=O), 744 (ν V=O) cm⁻¹, respectively. Further, the POMs characteristic bands were also observed in the hybrid materials and confirmed the impregnation of POMs on the PIn surface.

4.1.2 Thermogravimetry analysis

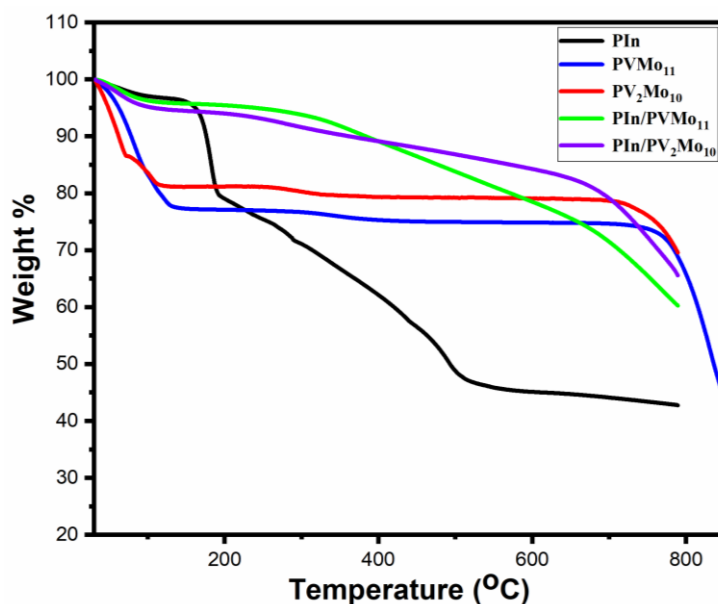


Fig. 4.2 TGA of pure PIn, PVMo₁₁, PV₂Mo₁₀, PIn/PVMo₁₁, and PIn/PV₂Mo₁₀.

Fig. 4.2 depicts the TGA of PIn, PVMo₁₁, PV₂Mo₁₀, PIn/PVMo₁₁, and PIn/PV₂Mo₁₀ electrode materials. As seen from the thermal decomposition, the doping of redox-active polyoxometalates increases thermal stability. The DTG and the TGA curve of PIn show the first weight loss of 2.95% at 61.71 °C because of the moisture removal (Anjitha et al. 2019). Several-weight losses were observed after the glass transition temperature, indicating the polymer backbone's stage-wise decomposition. The 50% weight loss of PIn was observed until 500 °C, which was prepared from the aqueous solution, using FeCl₃ as

an oxidant. The higher thermal stability of the PIn was varied depending on the synthesis medium. For example, 50% weight loss was observed at 681.85 °C when synthesized from CH₃CN/Bu₄NBF₄ medium (Choi et al. 1992). The PIn generally has higher thermal stability, possibly due to the absence of counterions and a change in the molecular structure (Zhou and Xu 2017). The weight loss of pure PVMo₁₁ and PV₂Mo₁₀ was observed till 123 °C and 101 °C, for both the POMs ascribed to the expelling of the moisture and crystal water molecules, and further heating of both the POMs exhibited utmost phase transition stability at 343.8 °C, and 291.5 °C, respectively. The thermal decomposition of both the POMs is well documented in the published article (Vannathan et al. 2020). The weight losses of doped PVMo₁₁ and PV₂Mo₁₀ on PIn are depicted in **Fig. 4.2**. The first weight loss of 3.55% at 63.56 °C corresponds to the moisture removal from the hybrid material. The final weight loss (14.3%) to 765.81 °C is ascribed to the degradation of inorganic moieties of the PIn/PVMo₁₁. Likewise, the inorganic moieties in PIn/PV₂Mo₁₀ decompose above 750 °C. **Fig. 4.2** shows that both the PIn/PVMo₁₁ and PIn/PV₂Mo₁₀ electrode materials are more stable than the pure PIn. In other words, doping POMs increased the electrode materials stability by many folds. This phenomenon can be explained due to the synergistic interaction between the anionic PVMo₁₁ and PV₂Mo₁₀ with Polyindole.

4.1.3 X-ray diffraction spectroscopy

In agreement with the Powder X-ray diffraction (PXRD) patterns (**Fig. 4.3**), the deposition of pure H₄[PVMo₁₁O₄₀] and H₅[PV₂Mo₁₀O₄₀] on PIn shows the amorphous nature of PIn/PVMo₁₁ and PIn/PV₂Mo₁₀O₄₀. The PIn shows characteristic broad peaks at $2\theta = 7.89^\circ$, 18.75° , and 23.834° with 11.2, 4.73, and 3.73 Å lattice spacing and broad peaks indicating the microsphere structure of the material (Vannathan et al. 2020). The P-XRD pattern of PVMo₁₁ showed peaks at 2θ of 9.7° , 16.8° , 21.8° , 26.8° , 27.6° , 28.98° , and 31.8° with a high percentage of crystalline material. Similarly, the PXRD pattern of PV₂Mo₁₀ showed similar diffraction angles (2θ) (9.76° , 16.96° , 21.41° , 26.45° , 27.75° , 28.99° , and 31.72°) and exhibited high crystalline material. After doping both the POMs on the backbone of PIn in situ, the number of diffraction angles reduced, indicating the

material's amorphous nature. The loss of crystallinity of POMs is distinctly visible in **Fig. 4.3**.

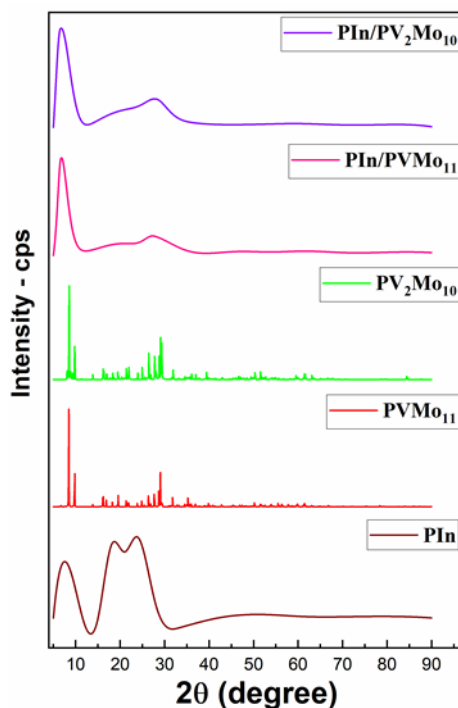


Fig. 4.3 PXRD pattern of PIn, PVMo₁₁, PV₂Mo₁₀, PIn/PVMo₁₁, and PIn/PV₂Mo₁₀

4.1.4 Field emission scanning electron microscopy and Energy-Dispersive X-ray spectroscopy

In order to have further insight, the surface morphology (FESEM) of all the hybrid materials (PIn, PIn/PVMo₁₁, and PIn/PV₂Mo₁₀) was performed under identical conditions presented in **Fig. 4.4A-C**. FESEM reveals porous, rough surfaces with the non-uniform distribution of the PIn with 0.964 μm size (**Fig. 4.4A**). **Fig. 4.4B-C** shows the FESEM images of the two new PIn/PVMo₁₁ and PIn/PV₂Mo₁₀ hybrid electrodes synthesized in situ by doping redox-active POMs on Indole.

The energy dispersive X-ray (EDS) spectroscopy analysis was supported by the presence of all elements in PIn, PIn/PVMo₁₁, and PIn/PV₂Mo₁₀, as shown in **Fig. 4.4D-F**.

The EDS spectra confirmed C and N in pure PIn and C, N, O, P, V, and Mo, in PIn/PV₂Mo₁₀ and PIn/PV₂Mo₁₁ hybrid electrodes, respectively.

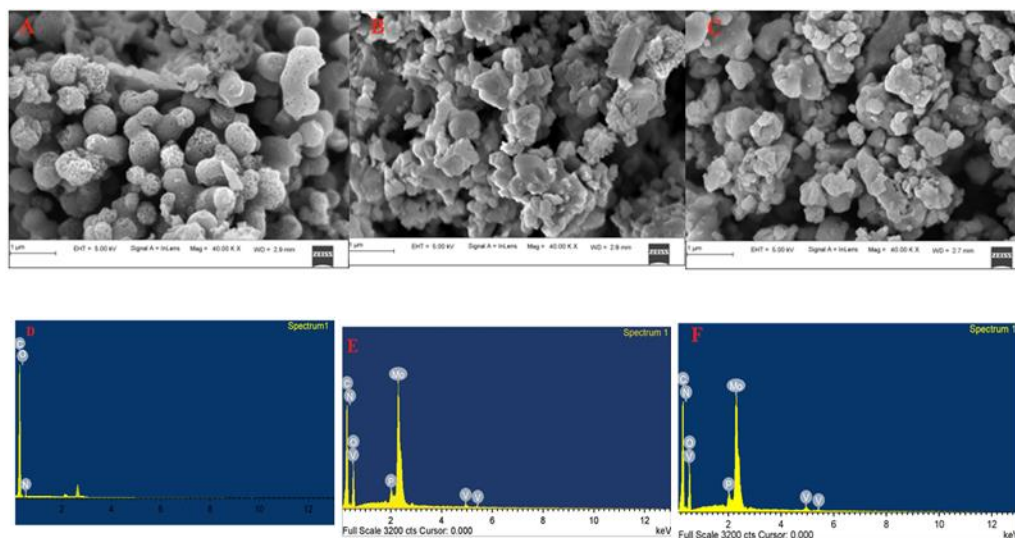


Fig. 4.4 FESEM images of A) pure PIn, B) PIn/PV₂Mo₁₁, and C) PIn/PV₂Mo₁₀. EDS spectra of D) pure PIn, E) PIn/PV₂Mo₁₁, and F) PIn/PV₂Mo₁₀, respectively.

4.1.5 Brunauer–Emmett–Teller

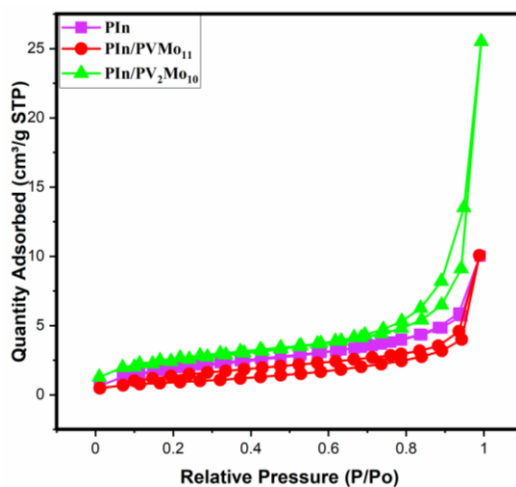


Fig. 4.5 shows the N₂ adsorption/desorption isotherm of PIn, PIn/PV₂Mo₁₁, and PIn/PV₂Mo₁₀ materials.

The specific BET surface area of PIn, PIn/PV₂Mo₁₁, and PIn/PV₂Mo₁₀ composites is 3.3,

7.52, and 9.3 m²/g. The composite materials exhibited type IV nitrogen adsorption isotherm without a defined hysteresis loop suggesting nonporous in nature, as shown in **Fig. 4.5**. Lower the newly synthesized electrode material's surface area, offering a high amount of doping of PVMo₁₁ and PV₂Mo₁₀ into the PIn surface. The lower surface area indicates that the PIn/PVMo₁₁ and PIn/PV₂Mo₁₀ composites were fully integrated into the polymer matrix surfaces and may deliver substantial capacitance.

4.2 Electrochemical measurements

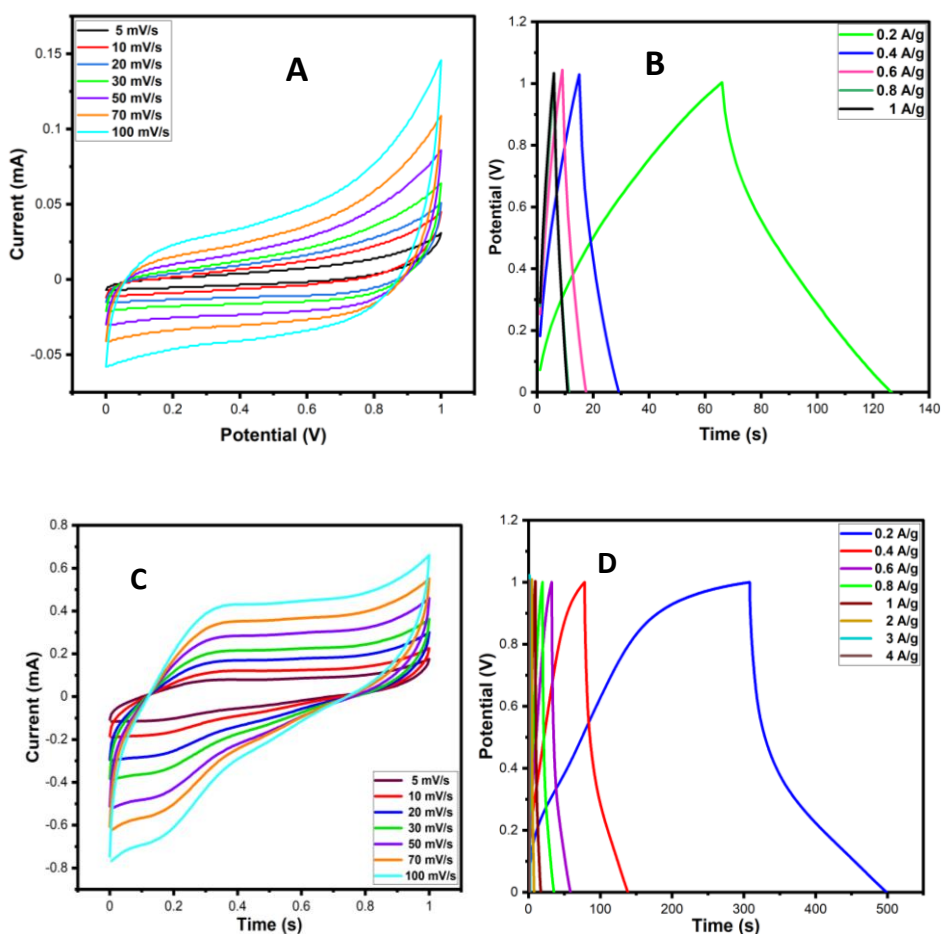
4.2.1 CV studies and GCD studies

The pseudocapacitive materials (e.g., transition metal oxide, conduction organic polymers) exhibit high specific capacitance and large energy density, making them ideal electrode materials for SCs. The electrochemical measurements of PIn, PIn/PVMo₁₁, and PIn/PV₂Mo₁₀ electrodes were studied by cyclic voltammetry (CV) and galvanostatic charge-discharge (GCD) at 0.25 M H₂SO₄ electrolyte solution using 2-electrode systems.

As depicted in **Fig. 4.6A**, the pure PIn electrode's CV curves were determined at various scan rates from 5-100 mV s⁻¹. It reveals a quasi-rectangular shape without noticeable redox peaks, indicating an excellent electrical double layer charge storage performance. Although PIn has been considered superior electrode material for SCs due to its high thermal stability, slow degradation, and fast redox reaction (Adhikari et al. 2018). Moreover, the specific capacitance of pure PIn has been reported, and capacitance varies from 93-114 F g⁻¹ in the various electrolyte solution in three-electrode systems (Majumder et al. 2017; Purty et al. 2019). It exhibits low specific capacitance because of the low electrical conductivity compared to other CPs. However, the obtained linear plot in the potential range of 0-1V of charge-discharge curves revealed the good capacitive property (**Fig. 4.6B**) of the PIn at 0.25M electrolyte solution. The specific capacitance was observed significantly less (33.50 F g⁻¹) even at a lowering current density (0.2 A g⁻¹).

Moreover, the PIn/PVMo₁₁ and PIn/PV₂Mo₁₀ electrodes show distorted rectangular shapes with a few redox peaks in the CV curves (**Fig. 4.6C and 4.6E**) with similar scan

rates of 50-100 mV s^{-1} . This could be due to the pseudocapacitive behavior of both PIn and redox-active polyoxometalates (PVMo_{11} and $\text{PV}_2\text{Mo}_{10}$). The specific capacitance was calculated to be 26.4 F g^{-1} for PIn/ PVMo_{11} and 60.81 F g^{-1} for PIn/ $\text{PV}_2\text{Mo}_{10}$ electrodes at the same scan rates of 5 mV s^{-1} . The capacitance decreases with increasing the scan rates for all the above cases due to the faster kinetics at higher scan rates. Eventually, the electrolyte ion takes less time to penetrate the electrode (Zhou et al. 2016). The electrolyte ion's kinetic energy is reduced and has enough time to diffuse to the electrode surface, causing higher specific capacitance upon lowering the scan rates.



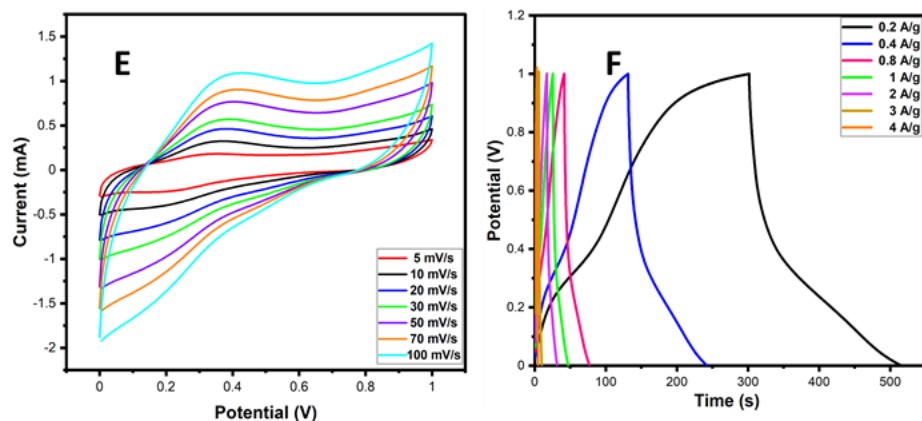


Fig. 4.6 CVs of (A)PIn, (C) PIn/PVMO₁₁, and (E) PIn/PV₂Mo₁₀ at various scan rates. GCD curves of (B)PIn, (D) PIn/PVMO₁₁, and (F) PIn/PV₂Mo₁₀

The capacitance of PIn/PVMO₁₁ and PIn/PV₂Mo₁₀ electrodes was estimated by GCD (Fig. 4.6D and 4.6F) measurements at various current densities. The pseudocapacitive nature of the electrodes could be visible in the charge-discharge curves, suggesting reversibility characters. The specific capacitance was estimated to be 177.36 and 198.54 F g⁻¹ for PIn/PVMO₁₁ and PIn/PV₂Mo₁₀ electrodes, respectively, at 0.2 A g⁻¹ current density, which is significantly higher values than the pure PIn under the same conditions. Equation (2.1), (2.2), (2.5), and (2.4) are used for the calculations of specific capacitance, energy, and power density. The much higher capacitance is probably due to the increment in the conductivity derived from PIn and the combination with redox-active polyoxometalates ions (PVMO₁₁ and PV₂Mo₁₀) ions movements become faster. Simultaneously, the PIn/PVMO₁₁ and PIn/PV₂Mo₁₀ electrodes displayed an energy density of 9.77 and 10.19 Wh kg⁻¹, respectively, at the same 0.2 current density (Fig. 4.7B). As seen in Fig. 4.6D and 4.6F, the specific capacitance values decrease with an increase in current density (Fig. 4.7A), illustrating that the electrochemical diffusion mechanism leads to energy storage. We envisaged that the electrolyte ions have higher kinetic energy, less diffusion time and increasing current density (Padmanathan and Selladurai 2014).

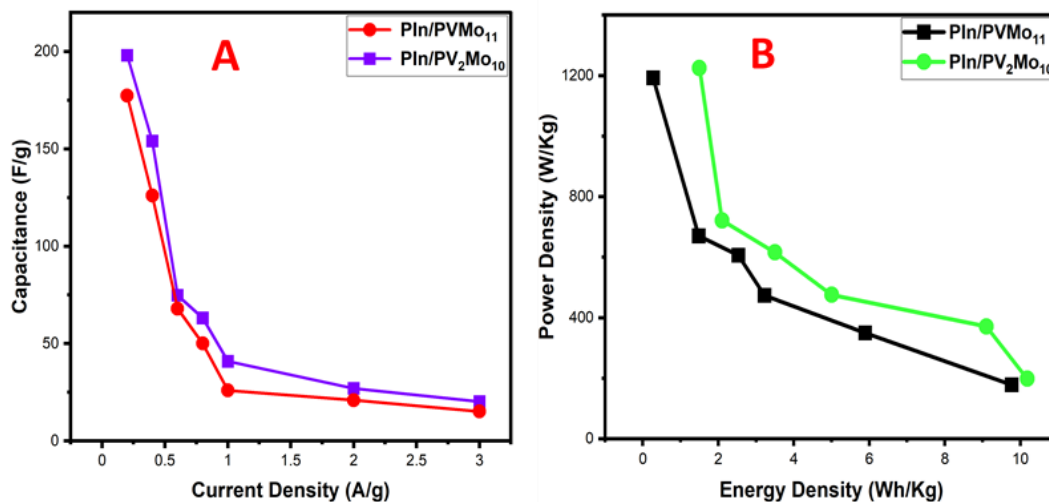


Fig. 4.7 A) specific capacitance vs current density, B) Power density vs energy density of PIn/PVMO₁₁, and PIn/PV₂Mo₁₀ electrodes.

4.2.2 EIS studies

The electrochemical impedance spectroscopy (EIS) analysis has been performed to examine the resistance at all composite's electrode-electrode interfaces. All the data are presented as the Nyquist plot over 1 to 10⁵ Hz frequency range (**Fig. 4.8**) with 0.01 mV dc applied potential.

In **Fig. 4.8**, the insert pictured a small arc in the high-frequency region for PIn/PV₂Mo₁₀ electrodes, indicating the dominating supercapacitor's resistive nature within the electrode-electrode interface. Pure PIn and PIn/PVMO₁₁ have a minimal arc in the high frequency, suggesting the flawed resistive character.

The cell capacitance calculated based on **equation (2.11)** (*vide infra*) observed that PIn/PV₂Mo₁₀ electrode material could apply to a small cell. So, the pseudocapacitance arises either from the electrolyte or redox reaction of PIn and POMs. (P. Chithralekha et al., 2009).

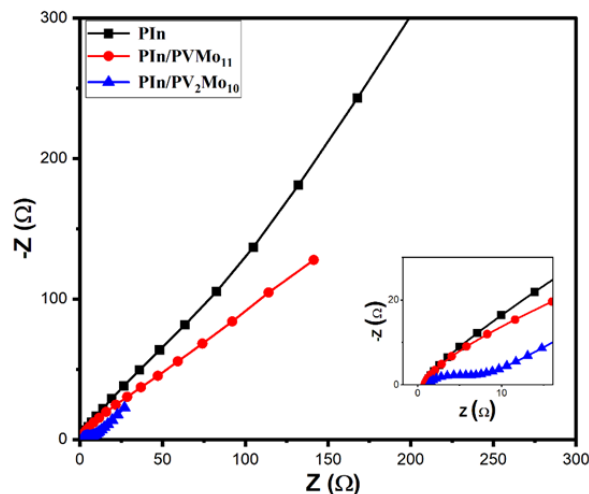


Fig. 4.8 Nyquist plots for the PIn, PIn/PVMO₁₁, and PIn/ PV₂MO₁₀ electrodes.

The cell capacitance and impedance were estimated using the EIS data for the device (laboratory scale) applications. The cell capacitance values of PIn, PIn/PVMO₁₁, and PIn/PV₂MO₁₀ were calculated and observed as 0.56, 1.13, and 5.9 mF, respectively.

4.2.3 Cycle stability studies

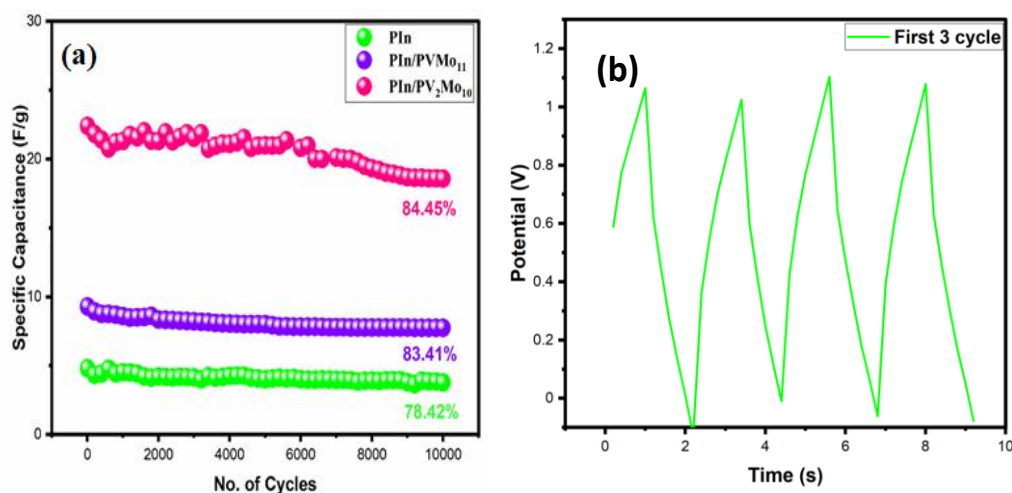


Fig. 4.9 a) Cycle stability of PIn, PIn/PVMO₁₁, and PIn/PV₂MO₁₀. (b) 1st three cycles of PIn/PV₂MO₁₀ based on GCD at 4 A g⁻¹.

The capacitance retention plots of the PIn, PIn/PVMO₁₁, and PIn/PV₂MO₁₀, respectively, shown in **Fig. 4.9a**, exhibit a cyclic voltammetry test at 4 A g⁻¹ current density based on

the GCD curve. After 10,000 cycles, the PIn, PIn/PVMO₁₁, and PIn/PV₂Mo₁₀ electrodes retain their cycling stability of 78.4, 83.4, and 84.5%, respectively.

CHAPTER 5



**Investigations of Redox-Active Polyoxomolybdate
Embedded Polyaniline-Based Electrode
Material for Energy Application**

This chapter describes the oxidation-based formation of new nanohybrids from two isostructural POMs ($H_4[PVMo_{11}O_{40}]$ and $H_5[PV_2Mo_{10}O_{40}]$) and polyaniline (PAni). The POMs oxidize the aniline monomer to polyaniline, and POMs dwell on the backbone of polyaniline to produce two nanohybrids, $PVMo_{11}@PAni$ and $PV_2Mo_{10}@PAni$, for SC applications. POMs will help to provide protons to the polyaniline throughout the electrochemical process.

5 Result and Discussion

5.1 Structural, chemical, and morphological characterizations

5.1.1 Fourier transform infrared spectroscopy

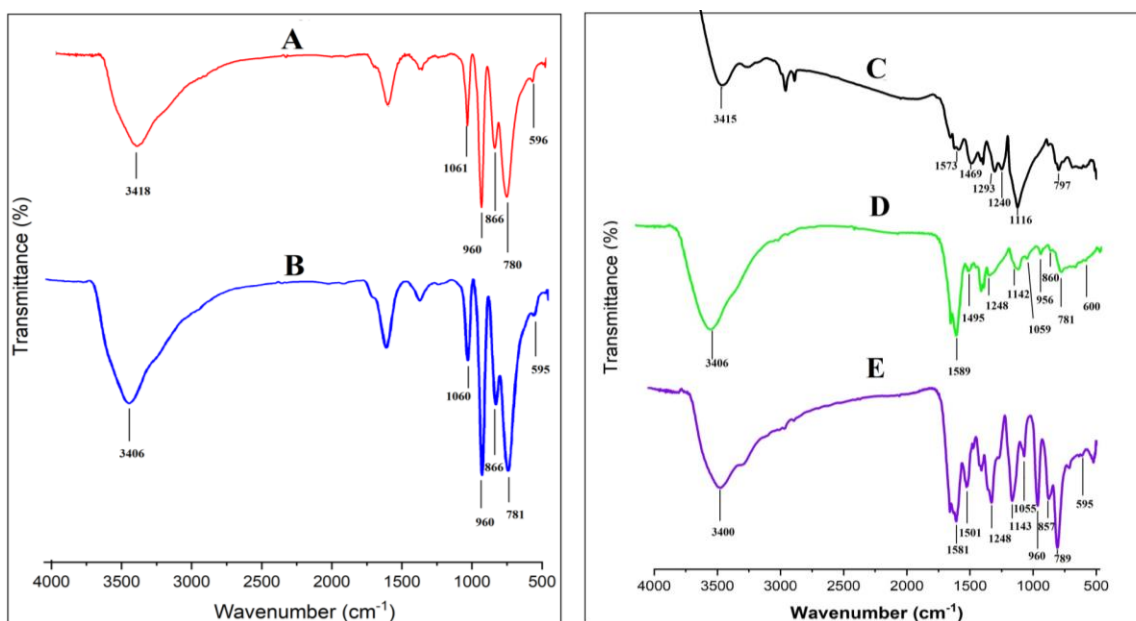


Fig. 5.1 FTIR spectrum of A) $PVMo_{11}$, B) PV_2Mo_{10} , C) pure PAni, D) $PVMo_{11}@PAni$, and E) $PV_2Mo_{10}@PAni$

The Fourier-transform infrared spectroscopy of $PVMo_{11}@PAni$ and $PV_2Mo_{10}@PAni$ were recorded (**Fig. 5.1B-C**) to ascertain the presence of POMs and get insights into the anchoring of POMs at the PAni surface. The FTIR spectrum of pure PAni is also provided

in **Fig. 5.1A** for comparison. Both the Keggin ions PVMo_{11} (**Fig. 5.1D**) and $\text{PV}_2\text{Mo}_{10}$ (**Fig. 5.1E**), were retained their chemical structure, confirmed by the evolution of the characteristic bands of the P-O bond at 1059 cm^{-1} (1055 cm^{-1} for **E**) followed by the $\text{Mo}=\text{O}_t$ at 956 cm^{-1} (960 cm^{-1} for **E**), M-Oe-M at 860 cm^{-1} (857 cm^{-1} for **E**) and 600 cm^{-1} (595 cm^{-1} for **E**), M-Oc-M at 781 cm^{-1} (789 cm^{-1} for **E**). These bands match with the earlier reported compounds in the literature (Lin et al. 2019). However, for pure PANi, the corresponding FTIR bands are corroborated well with those reported by Gómez-Romero and coworkers (Ran et al. 2018) (**Fig. 5.1C**). The peak at 1581 cm^{-1} (1586 cm^{-1} for **E**) corresponds to the presence of a deformation mode of benzene rings in aniline, the peak at 1495 cm^{-1} (1501 cm^{-1} for **E**) is attributed to the deformation of quinoid rings, 1248 cm^{-1} and 1142 cm^{-1} (1248 , and 1143 cm^{-1} for **E**) to C=N (**Fig. 5.1D**) stretching of a secondary amine for the characteristic band of pure PANi.

5.1.2 Thermogravimetry analysis

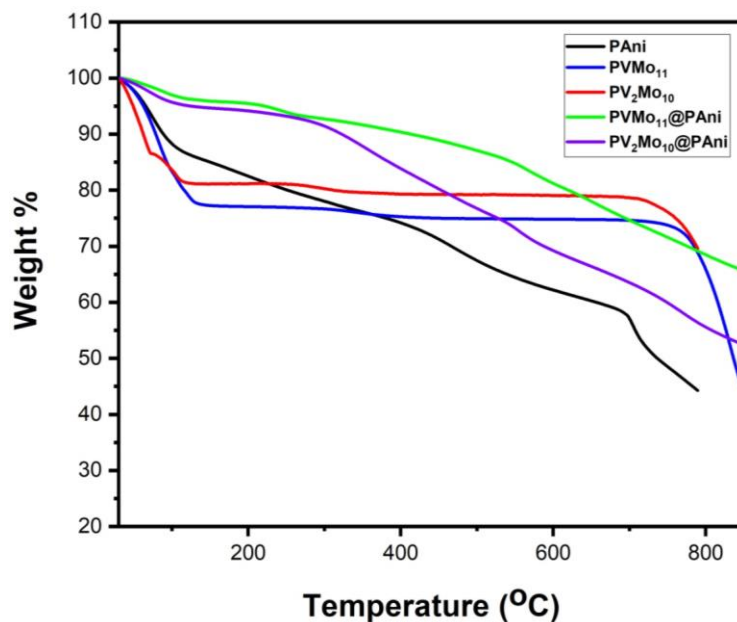


Fig. 5.2 TGA spectrum of PANi, PVMo₁₁, B) PV₂Mo₁₀, PVMo₁₁@PAni, and PV₂Mo₁₀@PAni

Because of the swelling (charging, oxidation) and shrinking (discharging, reduction) properties of conducting polymers, applications in energy storage devices are scarce. Impregnated or doping of redox-active transition metal oxide, mainly acid Keggin-type POMs, into the conducting polymer backbone might increase the thermal stability and be useful in electronic devices. Therefore, all electrode's thermal stability in this study was examined by TGA analysis. **Fig. 5.2** depicts the combined TGA graphs of pure PANi, PVMo_{11} , $\text{PV}_2\text{Mo}_{10}$, $\text{PVMo}_{11}@\text{PANi}$, and $\text{PV}_2\text{Mo}_{10}@\text{PANi}$. The DTG graph of pure PANi revealed a first weight loss of about 12.39% at the glass transition temperature of 74.63 °C, and the complete decomposition was observed at a quite high temperature at 707.78 °C, as shown in the DTG graph. The thermal decomposition of both the POMs is well described in the reported article (Tan et al. 2012). The thermogram of POMs, impregnated PANi hybrid materials, $\text{PVMo}_{11}@\text{PANi}$, and $\text{PV}_2\text{Mo}_{10}@\text{PANi}$, is presented in **Fig. 5.2**. The first weight loss (3.65%) at 62.48 °C is attributed to the hybrid material's moisture removal. Beyond 500 °C, the steady weight loss (23.25%) till 800 °C is assigned to the decomposition of POMs moieties of the vanadophosphomolybdate $\text{PVMo}_{11}@\text{PANi}$ electrode (**Fig. 5.2**). Likewise, the weight loss (4.74%) until 68 °C is attributed to moisture removal. Beyond that temperature, further weight loss is assigned to the decomposition POMs moieties of other vanadophosphomolybdate in the $\text{PV}_2\text{Mo}_{10}\text{O}_{40}@\text{PANi}$.

5.1.3 X-ray diffraction spectroscopy

The XRD patterns of pure polyaniline are depicted in **Fig. 5.3A**. The broad diffraction peak appears at $2\theta = 25.42$ with 3.501 Å lattice spacing of PANi. The broad diffraction peak could be because of the parallel and perpendicular periodicity of the PANi chain (Akba et al. 1997). The XRD pattern exhibits low crystallinity of the conducting polymers because of repeating benzenoid and quinoid rings in the PANi Emaradine backbone (Barth et al. 1999). The XRD pattern of PVMo_{11} (**Fig. 5.3C**) showed diffraction peaks at 2θ of 9.7°, 16.8°, 21.8°, 26.8°, 27.6°, 28.98°, and 31.8°. Similarly, the $\text{PV}_2\text{Mo}_{10}$ (**Fig. 5.3B**) showed diffraction peaks at 2θ of 9.8°, 16.9°, 21.4°, 26.4°, and 27.9°, respectively (Chandrasekhar and Gumbs 1991; Cuentas-Gallegos et al. 2005). Such a pattern can be indexed with

triclinic symmetry, indicating a high percentage of crystalline material. On doping two protonated Keggin-type POMs on PANi, the characteristic XRD peaks of 9.8 and 26.4 of 2θ for PV_2Mo_{10} (**Fig. 5.3D**) were disappeared entirely, suggesting the loss of crystallinity of the $PV_2Mo_{10}@PAni$ material,

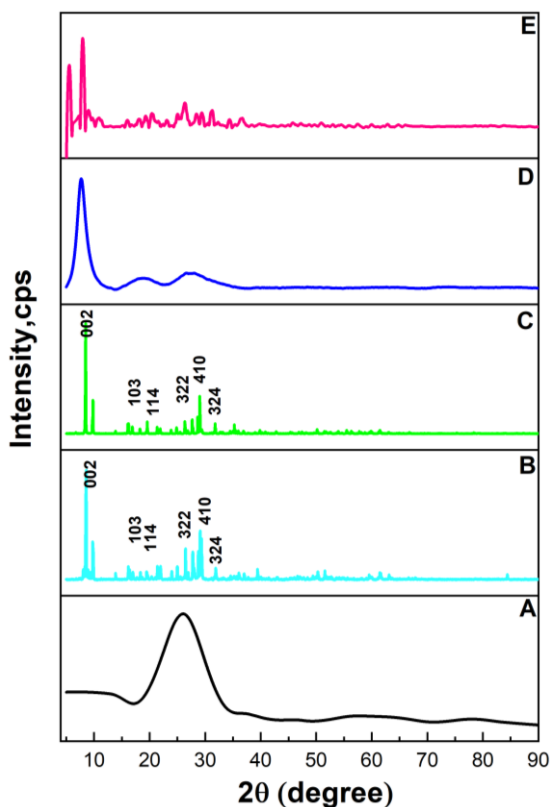


Fig. 5.3 PXRD patterns of A) PANi, B) $H_5[PV_2Mo_{10}O_{40}]$, C) $H_4[PVMo_{11}O_{40}]$, D) $PV_2Mo_{10}@PAni$, and E) $PVMo_{11}@PAni$ electrode.

5.1.4 Field emission scanning electron microscopy

Fig. 5.4 presents the typical field emission scanning electron microscopy of pure PANi, $PVMo_{11}@PAni$, and $PV_2Mo_{10}@PAni$, respectively, composite electrode materials. FESEM analyzed the surface morphology of the above electrode materials. The uneven square structure is noticed for PANi, as shown in **Fig. 5.4A**. The different morphology for

PV₂Mo₁₀@PAni than pure PAni is illustrated in **Fig. 5.4B** due to the mainly doping effect of PV₂Mo₁₀ on the PAni surface. **Fig. 5.4C** depicts the surface morphology of the PV₂Mo₁₀@PAni composite. This clearly shows the spherical shape with an agglomerated structure. The average diameter of the pure PAni, PV₂Mo₁₀@PAni, and PV₂Mo₁₀@PAni are observed at 4.7, 0.59, and 0.6 μm , respectively.

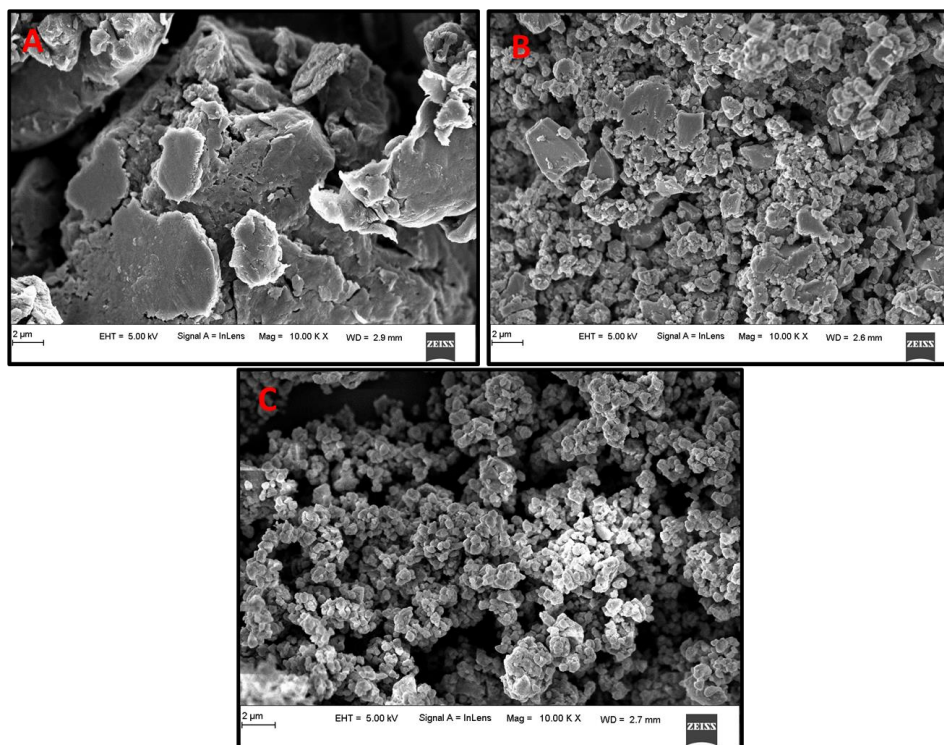


Fig. 5.4 FESEM micrograms of A) pure PAni, B) PV₂Mo₁₀@PAni, and C) PV₂Mo₁₀@PAni electrode.

5.1.5 Energy-Dispersive X-ray spectroscopy

The EDS (energy-dispersive-X-ray) spectroscopy analysis was exhibited to check PV₂Mo₁₀ and PV₂Mo₁₀ in the PV₂Mo₁₀@PAni PV₂Mo₁₀@PAni, respectively. The EDS of pure PAni was also analyzed to compare with PV₂Mo₁₀@PAni and PV₂Mo₁₀@PAni. **Fig. 5.5** illustrates the typical EDS spectra of pure PAni, PV₂Mo₁₀@PAni, and PV₂Mo₁₀@PAni composite, respectively. It is confirmed from the EDS spectra that the presence of P, V, Mo, C, and N in PV₂Mo₁₀@PAni and PV₂Mo₁₀@PAni composite (**Table 5.1**).

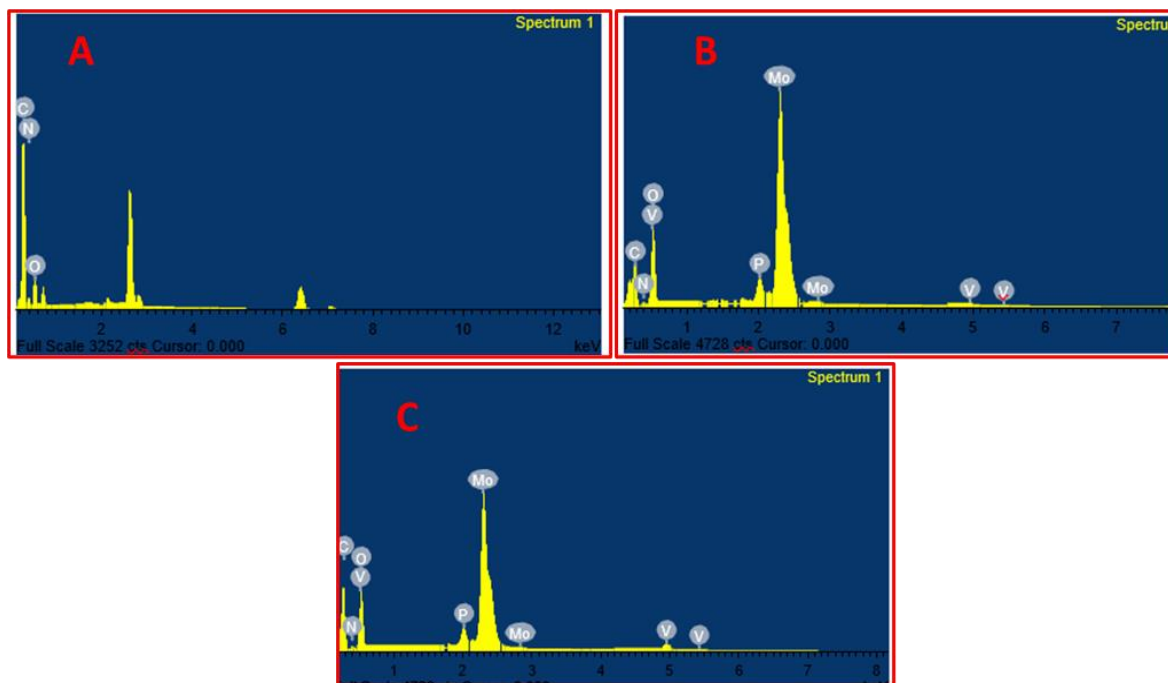


Fig. 5.5 EDS spectra of A) pure PANi, B) PVMo₁₁@PANI, and C) PV₂Mo₁₀@PANI

Table 5.1 Elemental composition of PANi, PVMo₁₁@PANI, and PV₂Mo₁₀@PANI from EDS.

Materials	Atomic (%)					
	N	O	C	P	V	Mo
PANI	22.4	51.73	25.87	-	-	-
PVMo ₁₁ @PANI	0.49	55.64	27.82	1.16	0.44	14.46
PV ₂ Mo ₁₀ @PANI	1.57	54.9	27.45	1.15	1.52	13.41

5.1.6 Brunauer–Emmett–Teller

The N₂ adsorption/desorption studies were performed to determine the specific BET surface area of PANi, PVMo₁₁@PANI, and PV₂Mo₁₀@PANI, respectively, as shown in **Fig.**

5.6. The specific BET surface area of PANi, PVMo₁₁@PANi, and PV₂Mo₁₀@PANi, composites are 2.48, 7.3, and 5.6 m²g⁻¹, respectively. The electrode materials exhibited the type IV nitrogen adsorption isotherm with no well-defined hysteresis loop. However, all the composites exhibited hysteresis in the low relative pressure region.

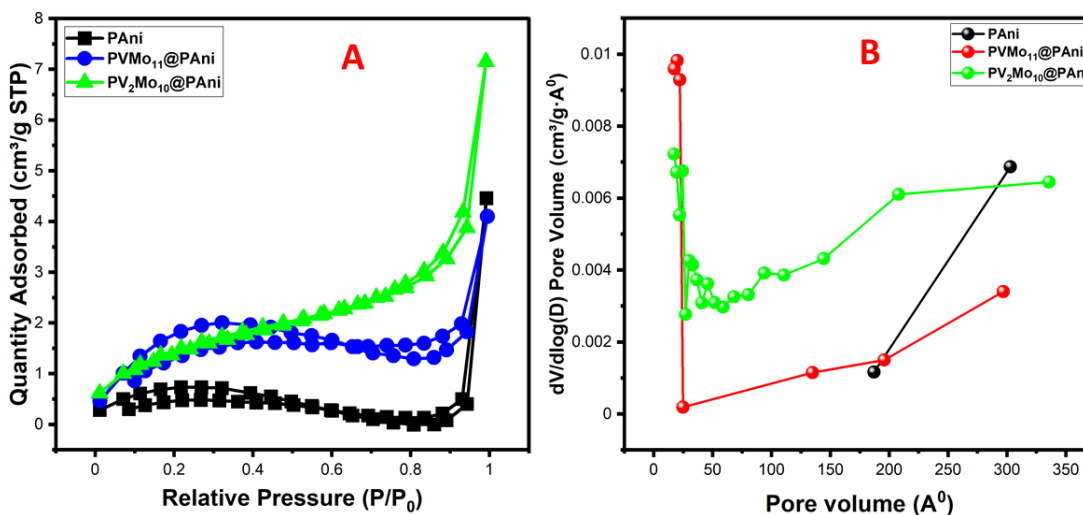


Fig. 5.6 A) Nitrogen adsorption/desorption isotherms and B) Pore volume graph of pure PANi, PVMo₁₁@PANi, and PV₂Mo₁₀@PANi electrode.

5.2 Electrochemical measurements

All the electrochemical characterization, such as cyclic voltammetry (CV), Electrochemical impedance spectroscopy (EIS) analyses, Galvanostatic charge-discharge (GCD), and cycle stability, were performed in a two-electrode electrochemical system in 0.25 M aqueous H₂SO₄ electrolyte solution at various scan rates ranging from 5 to 100 mV s⁻¹ for CV and 3 to 15 A g⁻¹ current density for GCD. **Equation (2.1)** calculates the specific capacitances (C_s) of all the electrode materials from the CV data.

One of the basic requirements for a high-demand supercapacitor is the high-power characteristic (Vannathan et al. 2020). Thus, the energy density of PANi, PVMo₁₁@PANi, and PV₂Mo₁₀@PANi electrodes was examined by the CV at different scan rates and the GCD for various current densities. CV details the electrode materials' oxidative/reductive nature in a suitable electrolyte. It also includes essential information on the specific

capacitance in different scan rates for an energy storage device.

For the first time, Diaz and his coworkers reported the electrochemical behavior of PANi in 0.25 M, H₂SO₄ by electropolymerization method in 1980 (Pawar et al. 2010). Lokhande and coworkers investigated the electrochemical performance of three forms of PANi, mainly leucoemeraldine, emeraldine, and pernigraniline, in a 1 M H₂SO₄ aqueous electrolyte medium at different scan rates. They observed that emeraldine (E) provides the highest (258 F g⁻¹) specific capacitance (Mostafaei and Zolriasatein 2012), which is much lower than earlier reported by the same group.

5.2.1 CV studies

We have investigated first the electrochemical measurements of pure PANi at various scan rates (**Fig. 5.7a**) in 0.25 M H₂SO₄ and observed that the emeraldine form's lower specific capacitance is about 33.45 F g⁻¹ at 5 mV s⁻¹. Notably, lowering the C_s values typically depends on the surface morphology, size, and thickness of the PANi film.

The CV of PVMo₁₁@PANi and PV₂Mo₁₀@PANi are illustrated in **Fig. 5.7b and 5.7c** within the potential window of 1 V at 0.25 M H₂SO₄ electrolyte medium at several scan rates of 5 to 100 mV s⁻¹. The CV graph of pure PANi (**Fig. 5.7a**) shows only one redox peak, and it also has been noticed that the large capacitive current slowly swallows the redox peaks at a high scan rate.

The CV of pure PANi represents the pseudocapacitive nature of the electrode. Similarly, the CV of PVMo₁₁@PANi and PV₂Mo₁₀@ PANi electrodes show oxidation and reduction peaks and describe the electrode's pseudocapacitive nature. One redox peak is visible for the PVMo₁₁@PANi electrode. The specific capacitance of all electrode materials was calculated using **equation (2.1)**, and the capacitance values at various scan rates are given in **Table 5.2**.

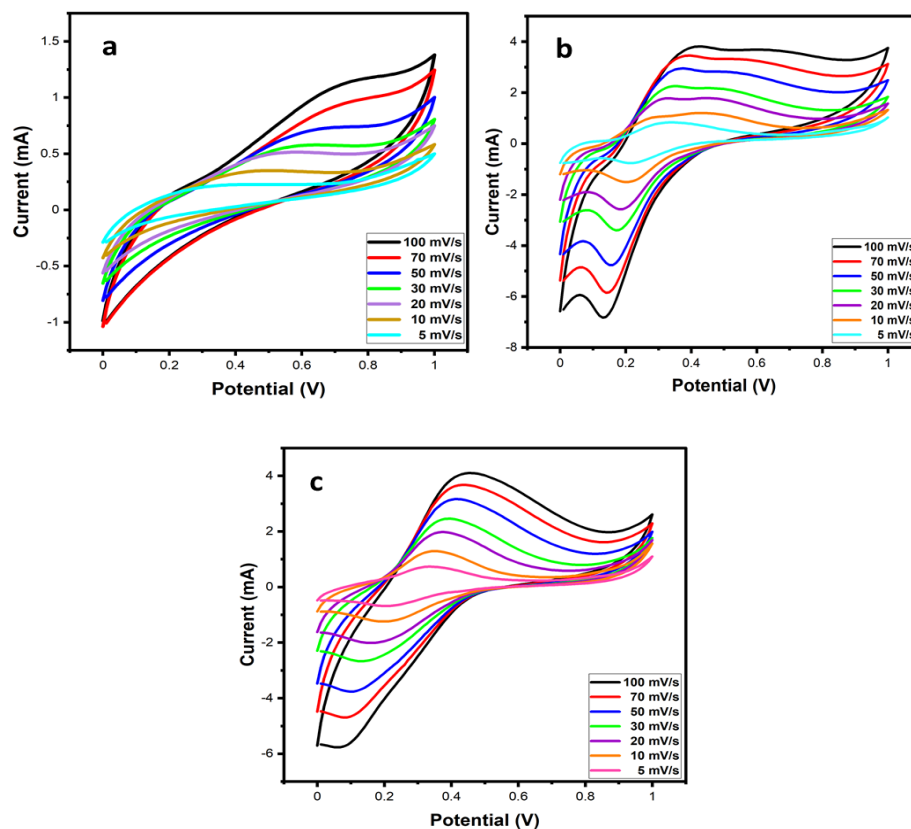


Fig. 5.7 Cyclic Voltammetry at various scan rates a) pure PANi, b) PVMo₁₁@PANi, and c) PV₂Mo₁₀@ PANi at 0.25 M H₂SO₄ electrolyte medium.

The PVMo₁₁@PANi electrode exhibits the highest specific capacitance of 150.01 F g⁻¹ at a 5 mV s⁻¹ scan rate compared with pure PANi and PV₂Mo₁₀@PANi specific capacitance of 33.45 and 119.61 F g⁻¹ at a 5 mV s⁻¹ scan rate, respectively. The specific capacitance of PVMo₁₁@PANi and PV₂Mo₁₀@PANi is higher than pure PANi due to the strong electrostatic interactions of two POMs (e.g., PVMo₁₁ and PV₂Mo₁₀) with the π -conjugated structure of PANi, helps to acquire more POMs on the PANi polymer backbone (PXRD analysis also supports). Due to the strong interaction of PANi with POMs (M=O bonds), there is a high possibility of charge transfer between the POM and PANi. Therefore increases the active sites for faradaic reaction to happen, hence elevating the specific capacitance (Boudjema et al. 2015). The diffusion of protons hinders the reaction at higher scan rates. The specific capacitance increases with a decreasing scan rate because the proton diffusion

occurs within the electrode's inner active sites allowing the redox reaction to complete (Sapurina et al. 2002).

Table 5.2 Specific capacitance of pure PANi, PVMo₁₁@PANi, and PV₂Mo₁₀@PANi electrodes at various scan rate

Scan Rate (mVs ⁻¹)	Specific Capacitance (F g ⁻¹)		
	Pani	PVMo ₁₁ @PANi	PV ₂ Mo ₁₀ @PANi
100	7.12	41.75	37.48
70	8.2	53.56	47.55
50	11.21	63.06	55.71
30	13.09	79.17	69.63
20	17.62	91.72	81.71
10	24.46	125.00	103.93
5	33.45	150.01	119.61

5.2.2 GCD studies

A galvanostatic charge-discharge (GCD) at a constant current density and various current densities was studied to estimate all electrode material's electrochemical performance. The GCD for all electrode materials was demonstrated at the constant potential window of 0 to 1 V at various current densities. **Fig. 5.8A** represents the combined GCD plot of pure PANi, PVMo₁₁@PANi, and PV₂Mo₁₀@PANi composite at a constant current density of 3 A g⁻¹. The GCD curves of all the electrodes are not perfectly triangular because of the oxidation/reduction properties of the PANi. The redox-active POMs impregnated on the COPs could be allowed to be studied in a wide potential window (Diaz and Logan 1980). **Fig. 5.8A** illustrates that in pure PANi, the discharge plot at a constant voltage shows huge IR drops and decreases the capacitance. In the case of PVMo₁₁@PANi and PV₂Mo₁₀@PANi composite, the discharge occurs in two steps two redox reactions as also visible by the two peaks of the CVs.

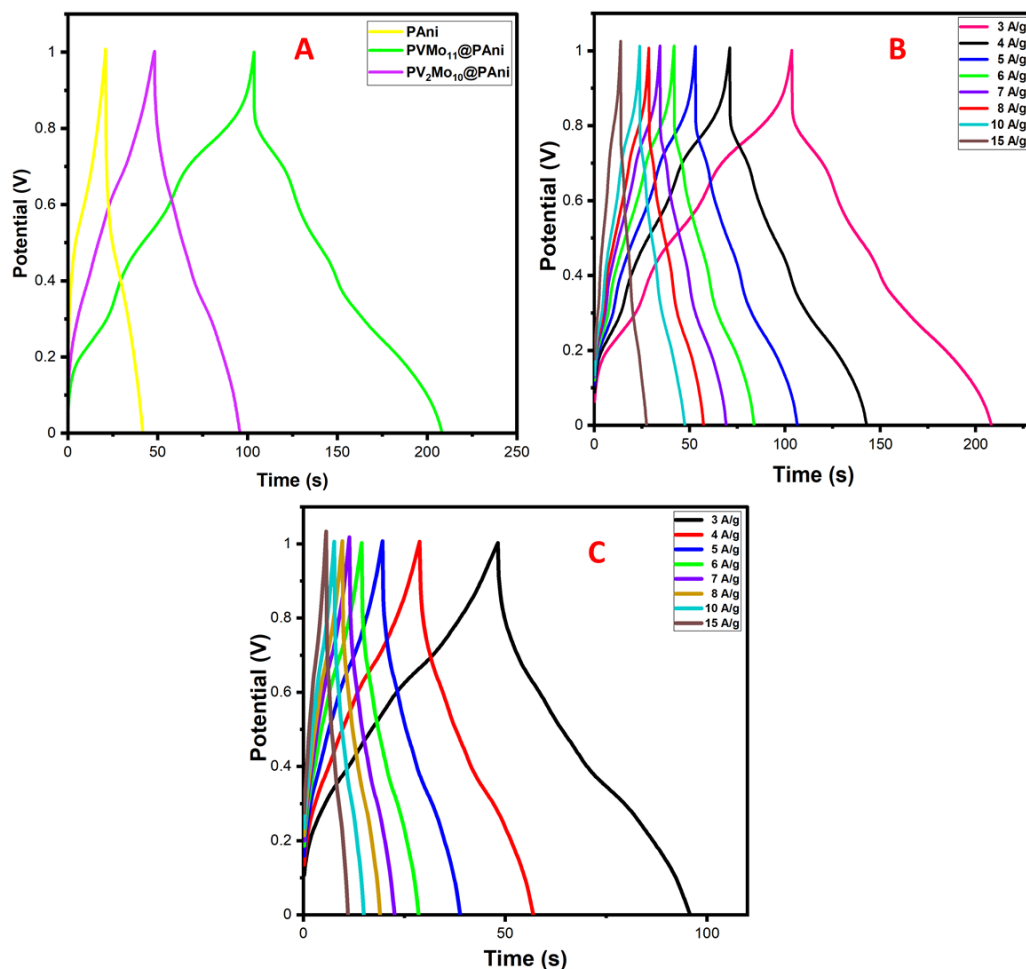


Fig. 5.8 A) Comparative GCD plot of pure PANi, PVMo₁₁@PANi, and PV₂Mo₁₀@PANi electrode at a constant charge/discharge current density at 3 A g⁻¹. GCD plot of B) PVMo₁₁@PANi and C) PV₂Mo₁₀@PANi electrode materials.

Moreover, the longer discharge durations are attributed to the combination of both EDLC and pseudocapacitance. The non-linear GCD plots of PVMo₁₁@PANi and PV₂Mo₁₀@PANi electrode materials at various current density densities of 3 to 15 A g⁻¹ are presented in **Fig. 5.8C and D** (excluding IR drop). The decreasing discharge time with an increasing current density is due to the faster movement of the electrolyte ions. It takes less time to penetrate through the electrode's pores at a higher current density and decreases capacitance with lowering current densities (Jamadade et al. 2010). The shape of the curve instead depends on mass transport phenomena and electrokinetics.

The perfect triangle linear curve does not observe in this case because of the presence of the redox-active materials, which lead to the Faradaic reaction (pseudocapacitance) and hence non-linear curved attributes. The capacitance (C) of all electrode materials was calculated based on the non-linear GCD plots using **equation (2.3)**. All specific capacitance values at various current densities are tabulated in **Table 5.3**. The specific capacitance was calculated, excluding the IR drop shown in **Fig. 5.8B** due to the non-linear curve of the GCD.

Table 5.3 Specific capacitance of pure PANi, PVMo₁₁@PANi, and PV₂Mo₁₀@PANi electrodes at various current densities from GCD plot at 1 V potential windows.

Current density (A g ⁻¹)	Specific Capacitance (F g ⁻¹)		
	PAni	PVMo ₁₁ @PANi	PV ₂ Mo ₁₀ @PANi
3	316	1371	602
4	262	1289	486
5	245	1223	437
6	233	1164	373
7	223	1134	349
8	213	1072	347
9	205	1104	316
10	199	1065	304
15	162	934	238

The PVMo₁₁@PANi shows an outstanding capacitance of 1371 F g⁻¹ at 3 A g⁻¹ current density, which is much higher than that of PANi (316 F g⁻¹) and PV₂Mo₁₀@PANi (602 F g⁻¹) under the same measurement conditions. The excellent result might be due to the enhancement of electrical conductivity derived from PANi and the association with PVMo₁₁ and PV₂Mo₁₀, making ions transportation faster. Also, these capacitance values are significantly higher than the reported work (Manivel et al. 2014).

The capacitance of all electrode materials decreases (tabulated in **Table 5.3**) with an increase in current density (**Fig. 5.9A**). Both the redox reaction and the charge diffusion rate cannot match the rise in the current density (Dhawale et al. 2010; Zhang et al. 2009a). Nonetheless, we still have observed the PVMo₁₁@PAni hybrid material shows a steady decrease of its capacitance by 68.13% (from 1371 to 934 F g⁻¹) with an increase in current densities from 3 to 15 A g⁻¹. In contrast, the PAni hybrid decreases the capacitance very fast, 51.27% (from 316 to 162 F g⁻¹) from 3 to 15 A g⁻¹. Similarly, the other electrode, PV₂Mo₁₀@PAni (39.53%), shows the same trend as pure PAni, showing a fast decrease of the capacitance from 602 to 238 F g⁻¹ at the same current density (**Table 5.3**). The PVMo₁₁@PAni electrode showed better penetration of the electrolyte than the other electrodes. The capacitance vs. different current density plots (**Fig. 5.9A**) stipulates that the PVMo₁₁@PAni electrode exhibits higher capacitance than the pure PAni and PV₂Mo₁₀@PAni electrodes.

The energy density and power were studied for pure PAni, PVMo₁₁@PAni, and PV₂Mo₁₀@PAni electrode materials (**Fig. 5.9B**). One of the most significant drawbacks of any supercapacitor electrode materials is having sparse energy density, albeit with a high power density. In this study, two composites, PVMo₁₁@PAni, and PV₂Mo₁₀@PAni showed high energy density and power at 3 A g⁻¹ current density compared to pure PAni. All electrode's energy density and power were calculated using **equations (2.4) and (2.6)** from the charge/discharge profile.

The PVMo₁₁@PAni composite electrode showed an outstanding energy density of 137.5 Wh Kg⁻¹ at a power density of 4715.6 W kg⁻¹ at 3 A g⁻¹ current density. Furthermore, even at a higher current density (15 A g⁻¹), the electrode shows an energy density of 73.2 Wh Kg⁻¹ at a higher power density of 19367.7 W kg⁻¹, indicating excellent electrochemical features PVMo₁₁@PAni SCs. For example, Chen et al. reported an energy density of 6.4 Wh Kg⁻¹ at a power density of 22.5 W kg⁻¹ for the SWCNT-TBA-PV₂Mo₁₀ symmetric cell (Dhawale et al. 2010). These values are substantially higher than reported symmetric cells of POMs-based SCs (Dubal et al. 2017b; Li et al. 2010). Moreover, the

PV₂Mo₁₀@PAni composite gives a comparatively much better energy density of 62.3 Wh Kg⁻¹ than pure PAni (22.8 Wh Kg⁻¹) at the same current density. The maximum power density of 10046.5 W Kg⁻¹ was achieved for PV₂Mo₁₀@PAni with a significantly less energy density of 14.54 Wh Kg⁻¹ at 15 A g⁻¹. A Ragone (energy density vs. Power) plot is depicted in **Fig.5.9B**, indicating that the PVMo₁₁@PAni exhibits higher energy density than the other electrodes.

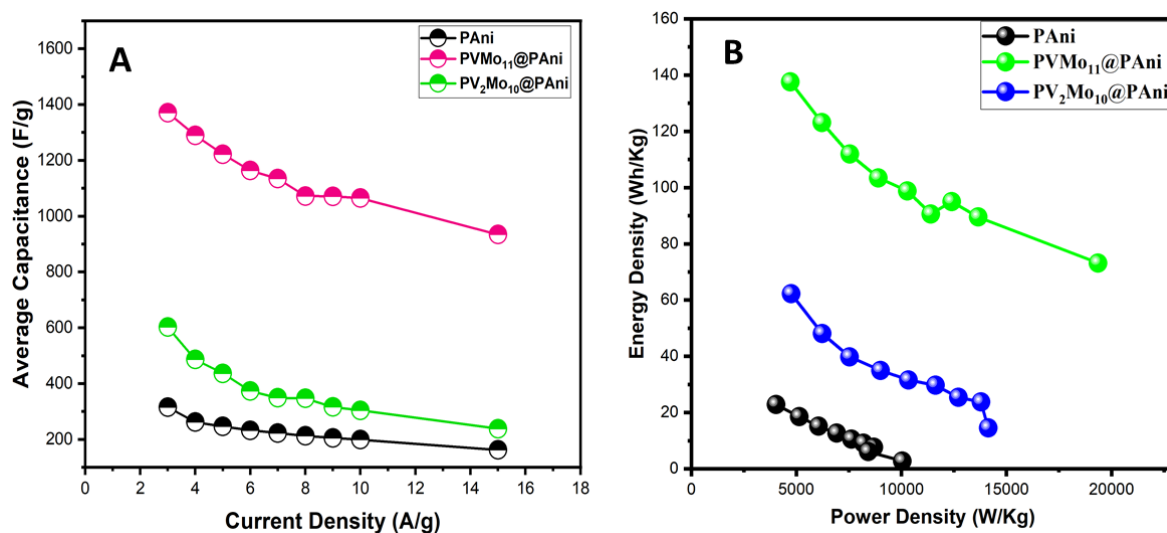


Fig. 5.9 A) plot of capacitance vs. current densities and B) Ragone plot of pure PAni, PVMo₁₁@PAni, and PV₂Mo₁₀@PAni electrodes.

5.2.3 EIS studies

Electrochemical impedance spectroscopy (EIS) was performed to explore the internal resistance measurement, charge transfer kinetics, and ion diffusion process for all electrode materials for SCs applications. **Fig. 5.10** exhibits the Nyquist plots for pure PAni, PVMo₁₁@PAni, and PV₂Mo₁₀@PAni composite and, in the insert, the semicircle arc of all three electrodes. The EIS data were analyzed from the Nyquist plots, plotted against the impedance's imaginary component ($-Z''$) vs. the real component (Z') of the impedance over a 0.01 to 10⁵ Hz frequency range of 0.01 V amplitude.

The Nyquist plots illustrate the frequency response of the electrode/electrolyte system

in a capacitor. The Nyquist plots of pure PANi show the incomplete semicircle over the high-frequency region. This exhibits the electron transfer kinetics of redox reactions electrode-electrolyte interface interfacial charge-transfer resistance R_{ct} is about 4.25Ω for pure PANi at room temperature. The Nyquist plot of the $PVMo_{11}@PANi$ electrode reveals that the interfacial charge transfer R_{ct} value is about 1.19Ω . Likewise, the R_{ct} value for $PV_2Mo_{10}@PANi$ was measured from the Nyquist plot's semicircle arc and observed a value of about 3.18Ω . The lower value of R_{ct} suggests the reduction of the internal resistance of the hybrid (Chen et al. 2015). The cell capacitance is calculated based on the **equation (2.12)**. All values are summarized in **Table 5.4**, and it is observed that all electrode materials could be applicable to a small cell.

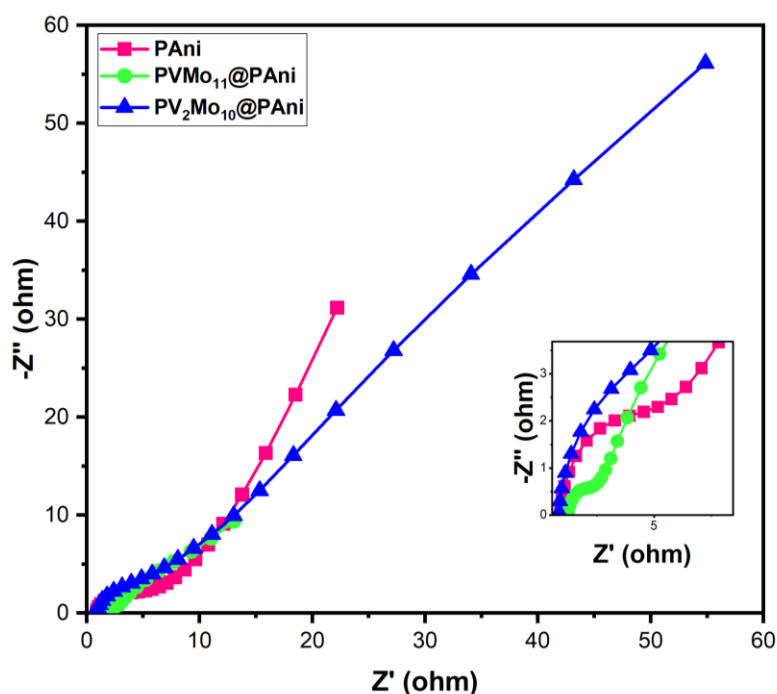


Fig. 5.10 Comparative Nyquist plots of pure PANi, $PVMo_{11}@PANi$, and $PV_2Mo_{10}@PANi$.

Table 5.4 R_{ct} , R_s , and R_p values of PANi, PVMo₁₁@PANi, and PV₂Mo₁₀@PANi electrode from Nyquist plot.

Electrode	R_{ct} (Ω)	R_s (Ω)	$R_p = R_s + R_{ct}$ (Ω)	f_k (Hz)	Cell capacitance (mF)
PAni	4.25	0.91	5.15	251	5.1
PVMo ₁₁ @PANi	1.19	2.551	1.33	1000	78.4
PV ₂ Mo ₁₀ @PANi	3.18	0.84	4.02	631	2.77

The Nyquist plot of pure PANi and PV₂Mo₁₀@PANi SCs goes even more outward towards lower frequencies, indicating the pseudocapacitance effect materials. Since its symmetric arrangement (**Fig. 5.11A**), then $C_1 = C_2 = C$; and likewise, $R_{ct1} = R_{ct2} = R_{ct}$.

The capacitance is dependent on the mass and the size of the device. Zhang et al. have mentioned that for a microcell, the cell capacitance value should be 1mF for a small cell, and for a medium cell, the cell capacitance value should be in the range between 1 mF-10 F (Morishita et al. 2007). In this case, all electrodes, pure PANi, PVMo₁₁@PANi, and PV₂Mo₁₀@PANi, show the cell capacitance of 72.3 mF (within the range of 1 mF-10 F), which could be applicable for the small SC cell application.

PVMo₁₁@PANi was coated on two pairs of carbon clothes of dimension 4 cm \times 4 cm, following the fabrication mentioned above method (250 mg of active electrode material coated) were connected in a series. When charged with an electrochemical workstation, and this setup was adequate to light up red light-emitting diodes of 2 V (**Fig. 5.11 B**). After setting, upon removing the electrochemical workstation, the LED continued to glow for the following 20 s, taking energy from the device, which shows the device's incredible energy density.

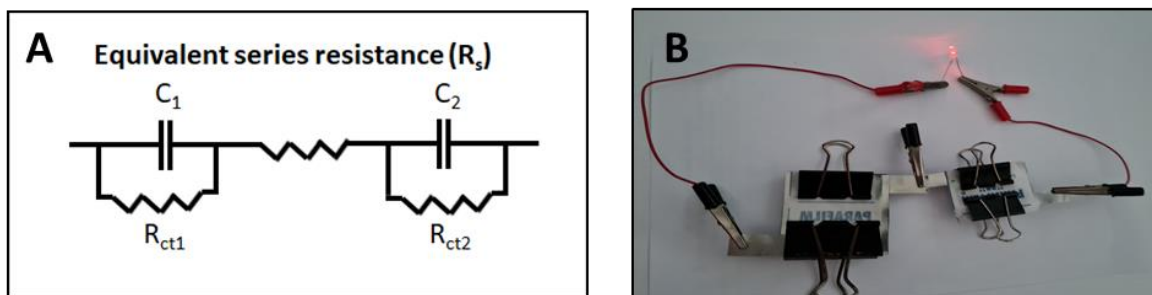


Fig. 5.11 (A) The equivalent circuit is used for fitting the Nyquist plots. (B) The fabricated SCs are energizing red light-emitting diodes.

5.2.4 Cycle stability studies

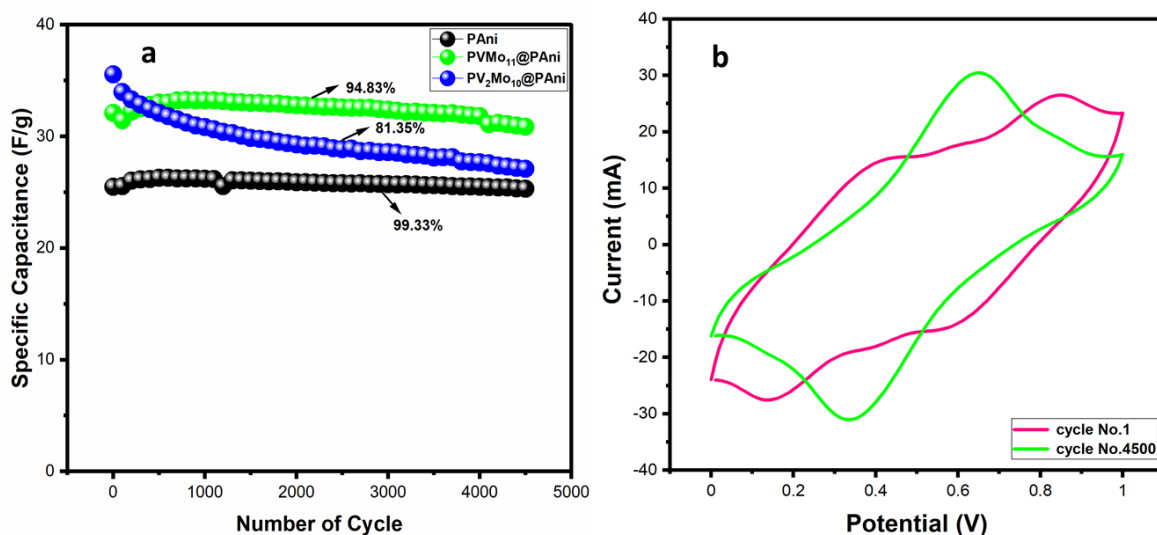
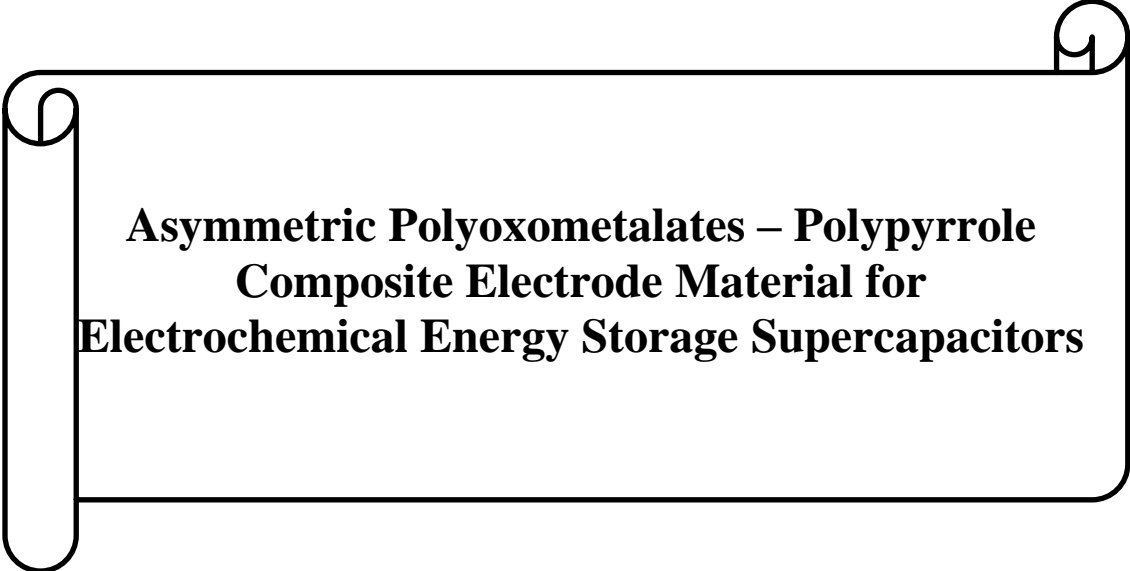


Fig. 5.12 (a) Cycle stability plot of the variation of average capacitance vs. cycle number of pure PANi, PVMo₁₁@PAni, and PV₂Mo₁₀@PAni electrodes at 500 mV s⁻¹. (b) 1st and last cycle stability plot of PVMo₁₁@PAni.

High cycle stability is a desire for any electronic device to maintain its cost. All electrode materials' cycle stability was studied using 0.25 M H₂SO₄ at a 500 mV s⁻¹ scan rate illustrated in **Fig. 5.12a**. Notably, the cycle stability measurements for electrode materials are critical parameters for supercapacitor's practical applications. As shown in **Fig. 5.12a**, the PVMo₁₁ doped on PANi, PVMo₁₁@PAni electrode retains about 94.83% capacitance after 4500 cycles, identifying as long-term electrochemical stability. However,

Pure PANi and PV₂Mo₁₀@PANi displayed 99.33 % and 81.35% retentions after the same number of cycles. The first and last cycles of the retention plot of PVMo₁₁@PANi are depicted in **Fig. 5.11b**. The improved cycle stability of the PVMo₁₁@PANi composite is because of the uniform deposition of PVMo₁₁ on the PANi surface, which might increase the electrode's active sites and enhance the cycle stability.

CHAPTER 6



**Asymmetric Polyoxometalates – Polypyrrole
Composite Electrode Material for
Electrochemical Energy Storage Supercapacitors**

This chapter is dealing the symmetrical and asymmetric studies of the novel pseudo-electrode materials. Nowadays, metal-oxides impregnated conducting polymers as electrode materials are attracting much attention due to their higher stability. Here, the metal-oxide cluster, polyoxometalate ($K_5H_2[PV_4W_8O_{40}] \cdot 11H_2O, PV_4W_8$), was introduced into the polypyrrole (PPy) matrix to overcome the polymer's stability issues. Thus, the resulting novel PV_4W_8/PPy (symmetric) composite electrode has been reported. XPS confirmed the presence of all atoms on the polymer backbone with respective oxidation states. Nevertheless, doping of PV_4W_8 on the conductive PPy matrix's surface can effectively improve the ion's transfer.

6 Result and Discussion

6.1 Structural, chemical, and morphological characterizations

6.1.1 *Fourier transform infrared spectroscopy*

Fig. 6.1 exhibits the FTIR spectra of PPy, PV_4W_8 , and PV_4W_8/PPy composite. All FTIR bands observed in the PPy are corroborated well with the literature (Vannathan et al. 2020) and confirm the doping of PV_4W_8 on the PPy matrix. Two new bands originated at 1537 and 1405 cm^{-1} in the FTIR spectrum of PV_4W_8/PPy composite and are attributed to C=C and C-N stretching vibration. The FTIR bands at 1090, 937, 864, 786, and 600 cm^{-1} are ascribed to the P-O, terminal W=O, bridged W-O_b-W, W-O_c-W, and V-O-V bonds vibration originated from the PV_4W_8 compound. Hence, it confirms the presence of PV_4W_8 on the PPy backbone.

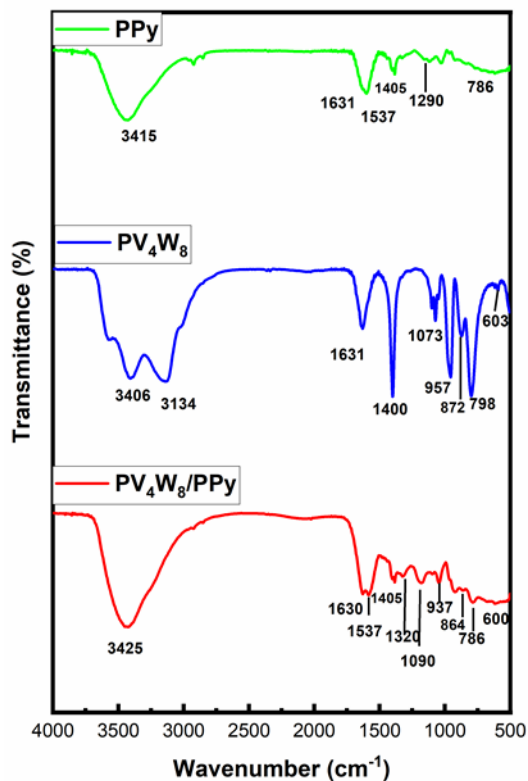


Fig. 6.1 FTIR spectra of PPy, PV_4W_8 , and $\text{PV}_4\text{W}_8/\text{PPy}$.

6.1.2 Thermogravimetry analysis

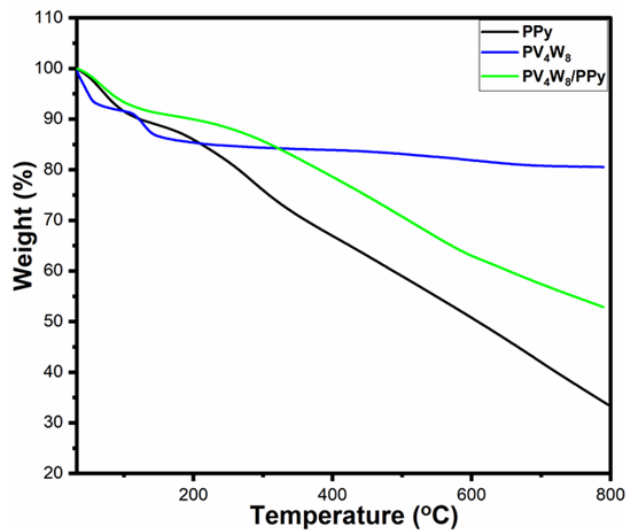
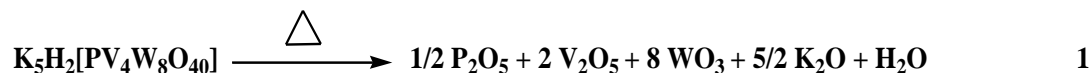


Fig. 6.2 Thermogravimetry plot of PPy, PV_4W_8 , and $\text{PV}_4\text{W}_8/\text{PPy}$.

The thermal stability was measured by the thermogravimetric analysis of the PV₄W₈/PPy, which is illustrated in **Fig. 6.2**. It is well acknowledged in the literature that CPs alone are not appropriate for energy storage applications due to structural deformation during the charging and discharging cycle. Hence, the measurement of the thermal stability of any electrode material is paramount. **Fig. 6.2** attributed that the thermal stability of the composite was increased due to the doping of PV₄W₈. The thermal stability of PPy, PV₄W₈, and PV₄W₈/PPy was measured from room temperature to 800 °C. The TGA curve of PPy is similar to our recently reported work (Vannathan et al. 2020), and the same can be found in the supporting information. The TGA of PV₄W₈ depicts the water loss until 129 °C. Next, weight loss was observed at 606 °C, which was attributed decomposition of PV₄W₈ following the below **reaction 1**.



The thermogram of PV₄W₈/PPy illustrates the combined weight loss of PPy and PV₄W₈. The DTGA plot ascribes the first weight loss (7.28%) at 69.94 °C due to the moisture removal from the composite material. Subsequent weight loss (16.21%) to 653.79 °C is because of the disintegration of organic and inorganic moieties in the PV₄W₈/PPy composite. Nevertheless, the PV₄W₈/PPy composite material's thermal stability is increased by many folds than the pure PPy (284 °C), indicating the presence of electrostatic interaction between highly negatively charged PV₄W₈ and cationic PPy after doping on the backbone of the polymer.

6.1.3 X-ray diffraction spectroscopy

Powder XRD patterns for PPy and PV₄W₈/PPy composite are shown in **Fig. 6.3A**, and PV₄W₈ POM is given in **Fig. 6.3B**. The pure PPy powder XRD pattern is similar to the published research report (Vannathan et al. 2020). The PPy is amorphous in nature and shows a broad diffraction peak, as shown in **Fig. 6.3**. PV₄W₈ POM shows a crystalline

nature which is evident in **Fig. 6.3B**. The characteristics diffraction peaks of PV_4W_8 disappear in the powder-XRD pattern of PPy-based composite, PV_4W_8/PPy suggesting crystallinity loss, meaning the amorphous nature.

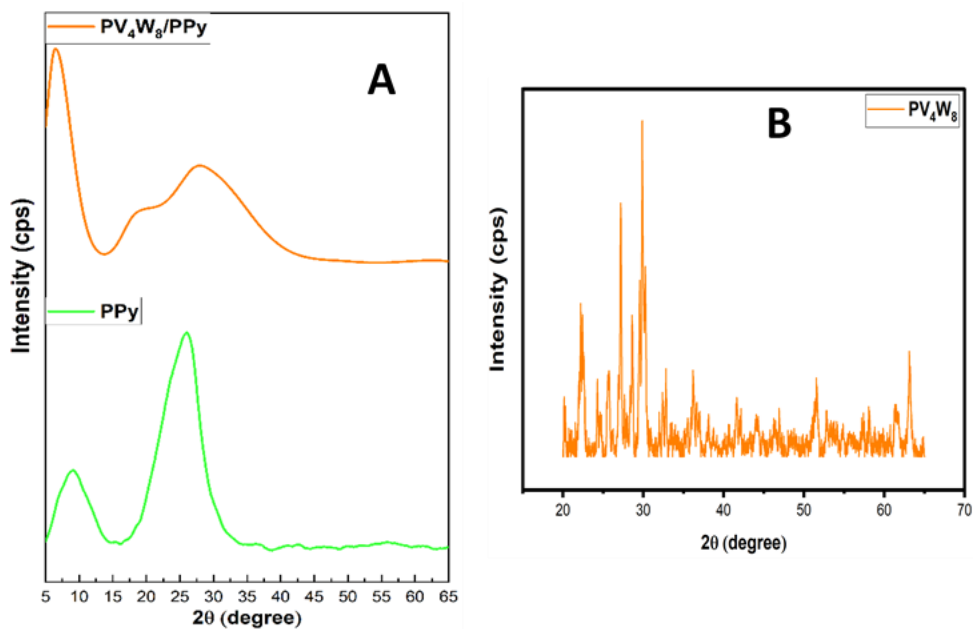


Fig. 6.3 XRD spectra of A) PPy, and PV_4W_8/PPy and B) PV_4W_8

6.1.4 Field emission scanning electron microscopy and Energy-Dispersive X-ray spectroscopy

The FESEM images of pure PPy, PV_4W_8 , and PV_4W_8/PPy composite electrode materials are shown in **Fig. 6.4**. FESEM measured the surface morphology of all electrode materials. It is discernible from **Fig. 6.4A** that the pure PV_4W_8 forms granular uneven shapes. The FESEM images has reported in the literature (Vannathan et al. 2020). The PV_4W_8/PPy composite's surface morphology is shown in **Fig. 6.4B**, indicating the spherical shape with an agglomerated structure of an average diameter of $0.377\mu\text{m}$.

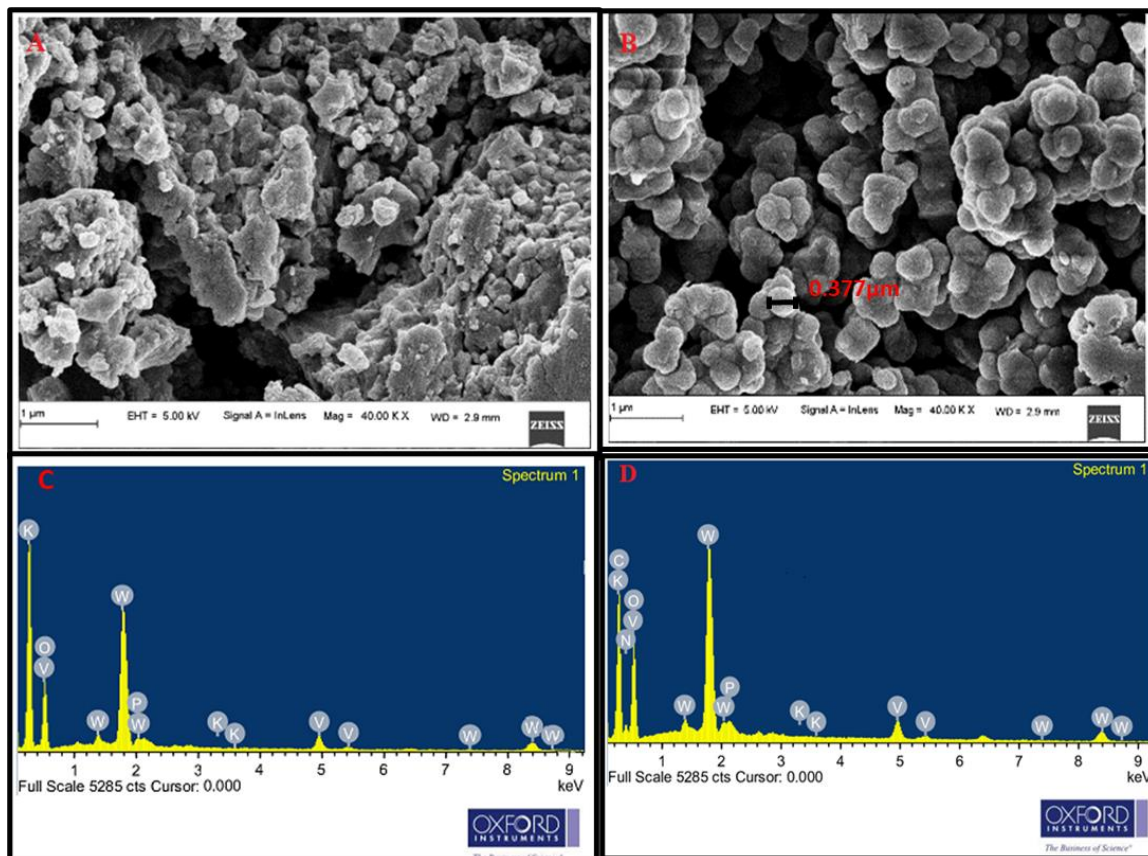


Fig. 6.4 FESEM images of A) PV_4W_8 , B) PV_4W_8/PPy , C) EDS of PV_4W_8 , and D) PV_4W_8/PPy .

The energy-dispersive spectroscopy (EDS) analysis has also been performed to check the amount of doping of PV_4W_8 onto the PPy matrix, as shown in **Fig. 6.4B**. The EDX of pure PV_4W_8 confirms K, P, V, Mo, and O (**Fig. 6.4C**) elements. The composite's EDS also confirms K, P, V, Mo, O, C, and N elements.

6.1.5 High Resolution Transmission Electron Microscopy

Additionally, the material's morphology was elucidated by HR-TEM, as shown in **Fig 6.5**. The HR-TEM image confirms the successful impregnation of the PV_4W_8 into the PPy matrix. The high-resolution lattice fringes with the d-spacing value of 3.57\AA confirm the higher crystallinity of PV_4W_8 .

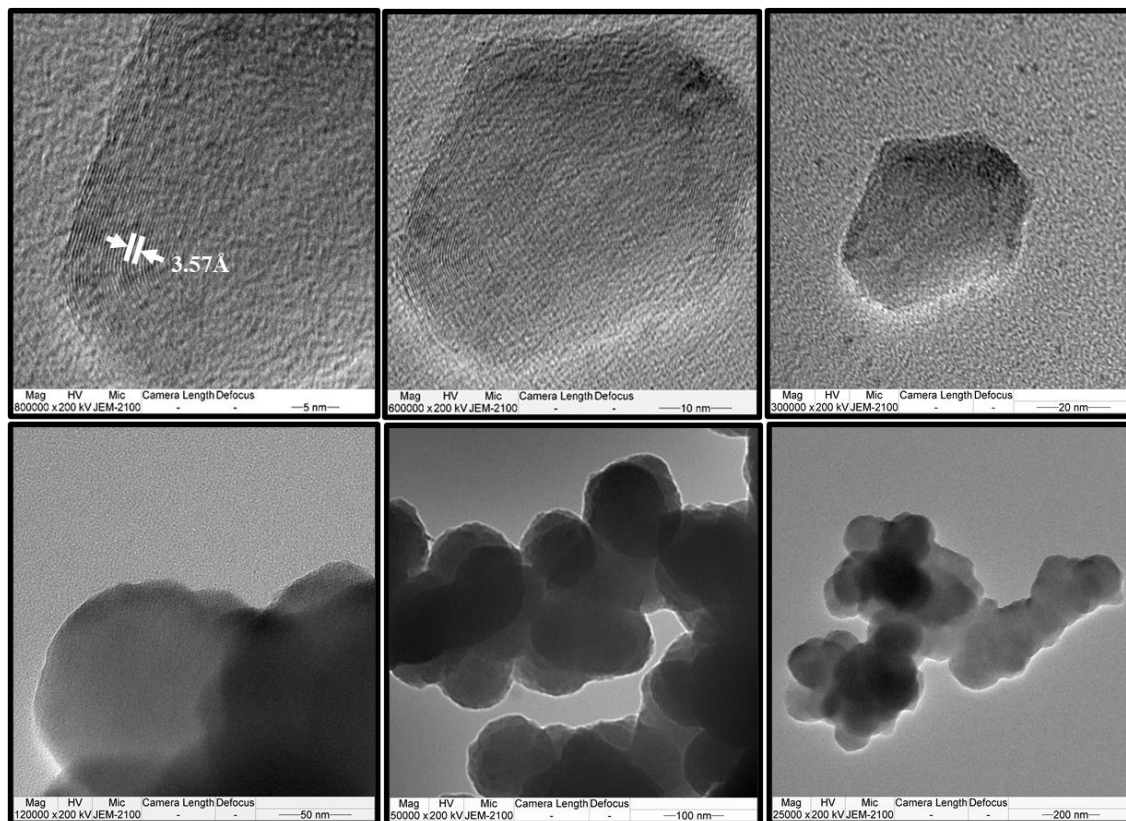


Fig. 6.5 HR-TEM image of PV₄W₈/PPy at a different scale.

6.1.6 Brunauer–Emmett–Teller

The electrode material's porosity and surface area play an important role in the electrochemical charge storage properties. The nitrogen adsorption-desorption studies were performed to determine the porous nature and the specific surface areas of pure PPy, PV₄W₈, and PV₄W₈/PPy nanohybrids material, as shown in **Fig. 6.6**. The type-IV adsorption-desorption isotherms with no hysteresis loop were obtained for PV₄W₈/PPy nanohybrid's suggesting nonporous material. SSA of ~ 28.3896 m²/g, ~ 7.6 m²/g, and ~ 17.58 m²/g were obtained for pure PPy, PV₄W₈, and PV₄W₈/PPy, respectively. The enhancement of the specific surface area of PV₄W₈/PPy compared to PV₄W₈ could be ascribed to the dispersion of PV₄W₈ on the PPy matrix. The pore volume of pure PPy,

PV₄W₈, and PV₄W₈/PPy are observed to be insignificant, which further affirms the nonporous nature of the material. Nevertheless, increasing the surface area enhanced the electrode and electrolyte contact area, improving the electrochemical performance of PV₄W₈/PPy.

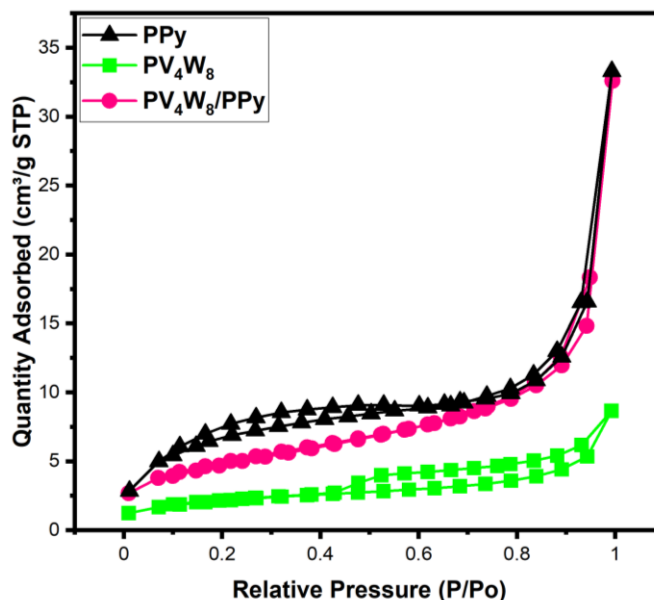


Fig. 6.6 Nitrogen adsorption/desorption isotherms of pure PPy pure PV₄W₈ and PV₄W₈/PPy nanohybrid composite.

6.1.7 X-ray photoelectron spectroscopy

The high-resolution XPS spectra of PV₄W₈/PPy are displayed in **Fig. 6.7**. It shows the survey spectra displaying the peaks corresponding to the elements present of N 1s, W 4f, C 1s, V 2p, O 1s, and P 2p of the PV₄W₈/PPy (**Fig. 6.7a**). The two strong peaks at 402.2 and 400.3eV in **Fig. 6.7b** correspond to the PPy's N⁺ and -NH- binding energy, which comes from the PPy matrix. Likewise, the peaks at 37.8 and 35.78 eV in **Fig. 6.7c** correspond to W 4f_{5/2} and W 4f_{7/2} of the Keggin ion, which confirms the presence of W⁺⁶ (Ponja et al. 2016). The C 1s region in the XPS of PV₄W₈/PPy fits with three peaks at

284.81, 286.42, 287.65, and 289.25 eV. These binding energies correspond to C-C, C-N, C=N, and C-N⁺, respectively (**Fig. 6.7d**) (Wang et al. 2020a).

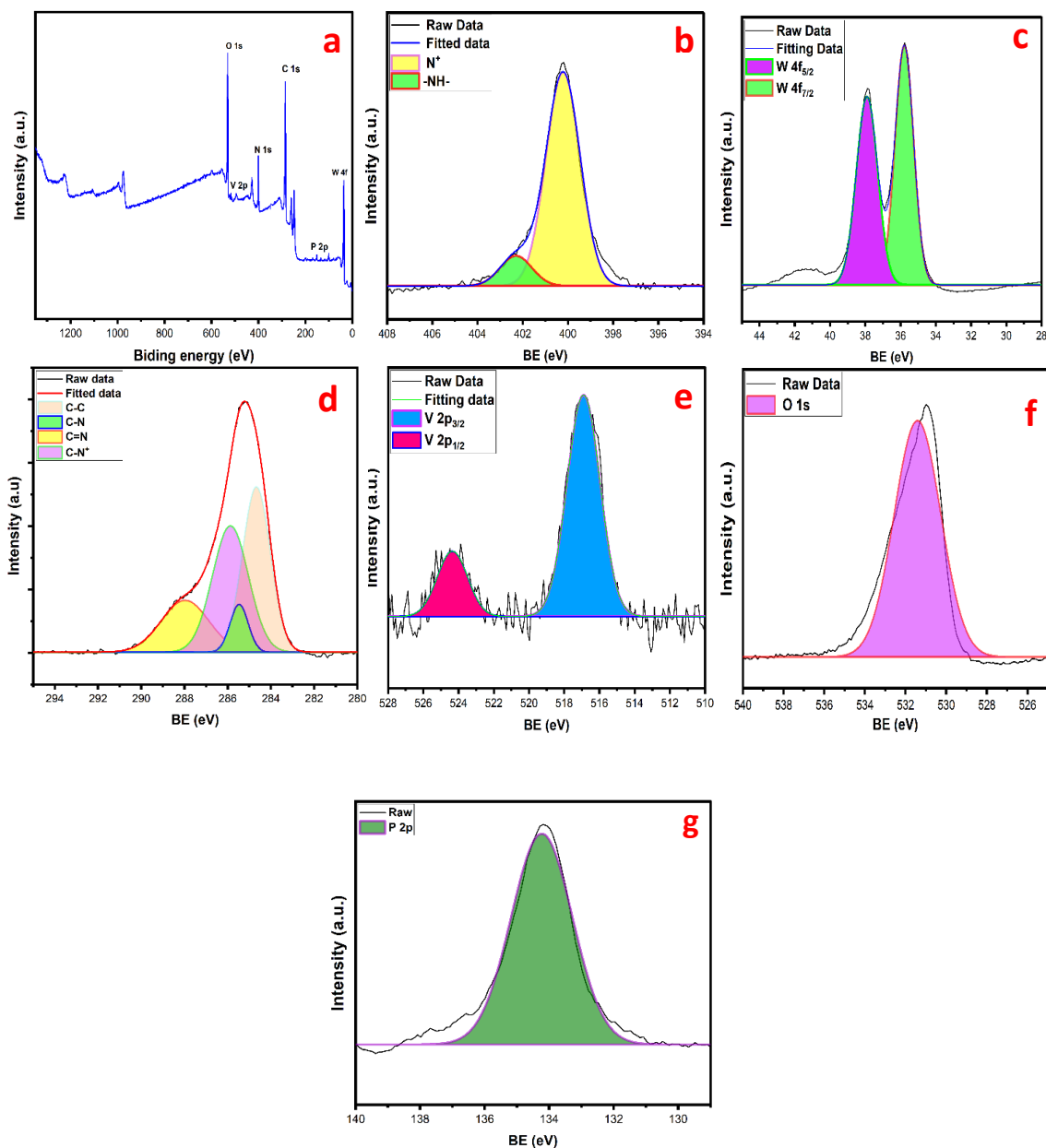


Fig. 6.7 a) XPS survey b) N 1s c) W 4f d) C 1s e) V 2p f) O 1s and g) P 2p.

The binding energy of V peaks at 524.3 and 516.9 eV corresponds to the V 2p_{3/2} and 2p_{1/2}, indicating the presence of V⁺⁵ and V⁴⁺ oxidation states in the Keggin structure (**Fig. 6.7e**) (Wang et al. 2020a). The occurrence of V's partially reduced oxidation states on the PPy matrix might be because of the photoreduction of vanadium species during exposure to the X-ray source (Benadji et al. 2010; Zhang et al. 2020). A strong peak fitted of O2p at the binding energy of 531.4eV designated to the oxygen atoms of the Keggin unit (**Fig. 6.7f**) (Gao et al. 2018). Finally, the deconvoluted P 2p_{3/2} at 134.2 eV is attributed to the P atom (+5) in the Keggin anion in [PV₄W₈O₄₀]⁵⁻ (**Fig. 6.7g**) (Zheng et al. 2018).

6.2 Electrochemical measurements

6.2.1 CV studies

Cyclic voltammetry (CV) measurement in a two-electrode system was employed to investigate PPy, PV₄W₈, PV₄W₈/PPy (symmetric), and PV₄W₈-PPy/PPy (asymmetric) electrode material's electrochemical performance. The potential window range of 0-0.8 V at different scan rates from 10 to 100 mV s⁻¹ was considered. CV is an efficacious characterization technique to evaluate the electrode's capacitive behavior, the shape of CV's anodic and cathodic peaks, and the current density area (**Fig. 6.8A**). The specific capacitance of PPy, PV₄W₈, PV₄W₈/PPy, and PV₄W₈-PPy/PPy (asymmetric) electrodes was evaluated from the CV plots using the following **equation (2.1)**.

The specific capacitance increased when PV₄W₈ was immobilized into the polymer matrix rather than PPy and PV₄W₈ at the same scan rate. **Fig. 6.8A** exhibits the cyclic voltammogram PPy, PV₄W₈, PV₄W₈-PPy/PPy (asymmetric) at various scan rates of 10, 20, 30, 50, 70, 100 mV s⁻¹ in the potential window of 0-0.8V, respectively. It has been noticed from the CV that the profile of asymmetric PV₄W₈-PPy/PPy shows pseudocapacitance behavior which indicates the materials had good capacitive behavior (**Fig. 6.8A**). Notably, at a higher scan rate, no significant oxidation or reduction peaks in the CV profile of PPy, PV₄W₈, PV₄W₈-PPy/PPy (asymmetric) demonstrated that all electrodes are charged and

discharged pseudo-constant rate. However, the CV curve area for asymmetric PV₄W₈-PPy/PPy increases with increasing scan rates, and the shape of the CV profile is more prominent, indicating high electrochemical stability. Similarly, the same trend has been observed for the symmetric PV₄W₈-PPy electrode. At higher scan rates, the electrolyte ion's movements increase, and the accumulation of charges near the electrode and electrolyte surfaces reduces and, thus, reduces the specific capacitance. On the contrary, decreasing the scan rate increases the proliferation of charges near the electrode and the electrolyte surface, enhancing the capacitance. Nevertheless, compared with PPy, PV₄W₈, introducing PV₄W₈ into the PPy matrix improves the electrode material's specific capacitance. The scan rates vs specific capacitance graph are demonstrated in **Fig. 6.8B**.

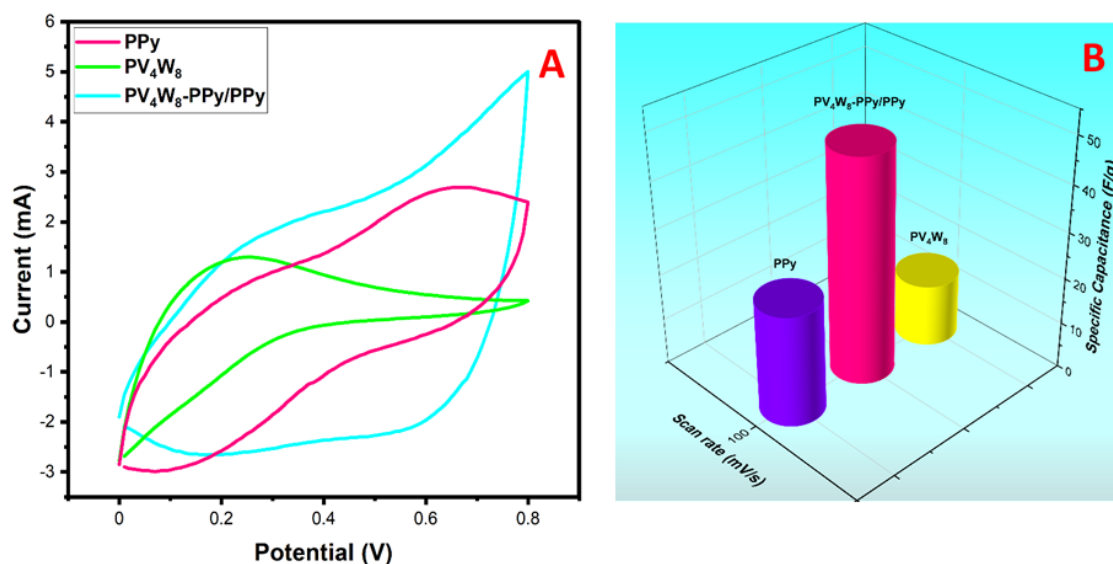


Fig. 6.8 A) CV plot of all electrodes at 100 mV/s scan rate. B) the bar chart of the specific capacitance at the 100 mV s⁻¹ scan rate at 0.25M H₂SO₄.

6.2.2 GCD studies

The specific capacitance of PPy, PV₄W₈, PV₄W₈/PPy, and PV₄W₈-PPy/PPy electrode materials is calculated using the galvanostatic charge-discharge (GCD) curves under various current densities shown in **Fig. 6.9A**. The asymmetric PV₄W₈-PPy/PPy electrode's

GCD curves show the perfect shape of pseudocapacitance behavior (**Fig. 6.9A**), similar to the PPy, revealed the longest discharge time and showed the highest specific capacitance of 291.00 F g⁻¹ (excluding IR drops) at 0.4 A g⁻¹ current density (**Fig. 6.9B**). The PPy and pure PV₄W₈ offer the specific capacitance of 90.01F g⁻¹ and 39.03 F g⁻¹ (excluding IR drops), respectively, at the same current density in 0.5 M H₂SO₄ electrolyte. Interestingly, electrode charging and discharging steps for symmetric PV₄W₈ /PPy and asymmetric PV₄W₈-PPy/PPy (**Fig. 6.9A**) revealed internal resistance (IR) drop along with the symmetric charge and discharge curves which suggest the pseudocapacitance behavior. Notably, the capacitance varies with the morphologies of the composite materials. Here, we have applied the linear equation to evaluate the specific capacitance, energy, and power density (**Equations (2.1), (2.5), and (2.4)**) for the triangular shape of the GCD of PPy.



The GCD plot of PV₄W₈ shows the faradaic behavior because an oxidation-reduction reaction occurs within the PV₄W₈ (Fig. S3B) metal-oxide clusters (**reaction 2**). However, it has been observed that the discharge current exhibits a non-linear graph shape. This can be ascribed to the Faradaic material behavior. The energy and power density of the PV₄W₈, PV₄W₈/PPy, and PV₄W₈-PPy/PPy (asymmetric) were calculated using **equations (2.5) and (2.4)**, respectively. All electrodes comparing graphs of capacitance vs current density and energy density vs power density are presented in **Fig. 6.9C-D**, depicting that the asymmetric PV₄W₈-PPy/PPy electrode delivers the highest energy density of 16.40 Wh kg⁻¹ at 0.4 A g⁻¹ current density. The asymmetric composite PV₄W₈-PPy/PPy electrode provided the highest power density of 756.78 W kg⁻¹ than the pure PPy (526.61 W kg⁻¹) and higher than PV₄W₈ (190.82 W kg⁻¹) at 0.4 A g⁻¹ current density. Notably, the capacitance and energy density decreased with increasing the current density which could be due to the slow rapturing of the hierarchical structure of the electrode at a higher current density. For pure PV₄W₈, GCD could run till 2 A g⁻¹ current density due to the high solubility in an aqueous electrolyte.

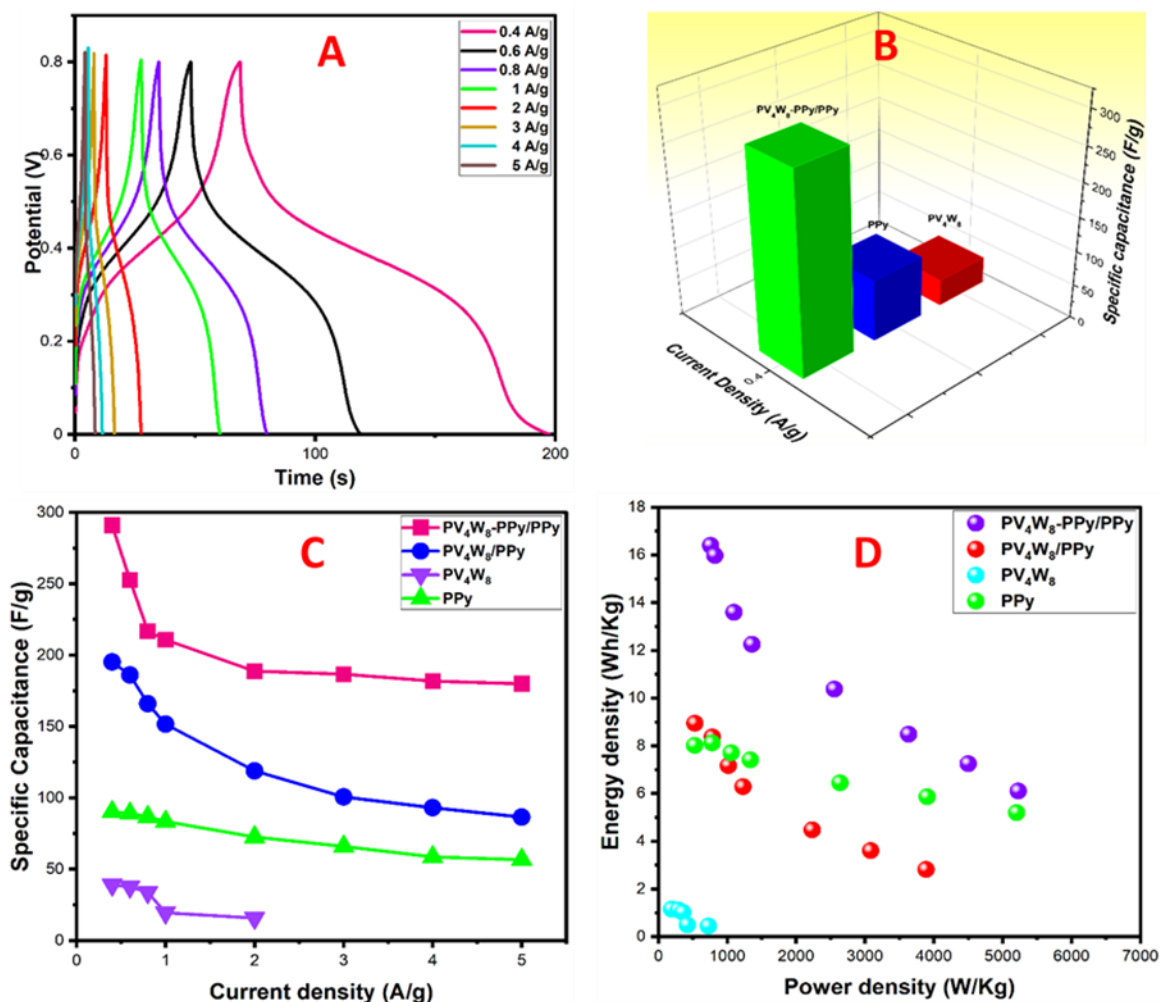


Fig. 6.9 GCD curves of A) asymmetric PV₄W₈-PPy/PPy, B) current density vs capacitance of PPy, PV₄W₈, and PV₄W₈/PPy at 0.4 A g⁻¹ C) Capacitance vs Current density graph for all system. D) Energy Density vs Power density graph for all systems.

The PV₄W₈/PPy symmetric composite electrode exhibits the highest specific capacitance of 195.27 F g⁻¹ (without IR drop) at 0.4 A g⁻¹ current density and the lower energy density of 8.94 Wh kg⁻¹ and power density of 530.84 W kg⁻¹. The capacitance decays with rising current density, attributed to either the electrode's incomplete redox reactions because of the poor connection of the electrochemical device or instability of the electrode materials at a higher current (Wang et al. 2018a, 2017). The comparisons between

energy densities and power densities under various current densities for both symmetric and asymmetric devices are demonstrated in Ragone plots (**Fig. 6.9D**).

6.2.3 EIS studies

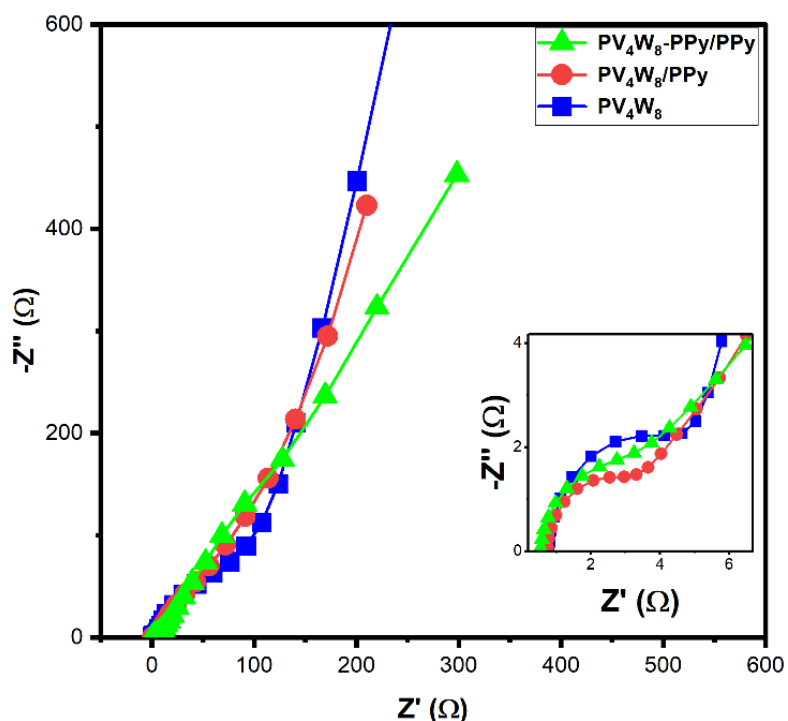


Fig. 6.10 EIS graph for PV_4W_8 , PV_4W_8/PPy (symmetric), and PV_4W_8-PPy/PPy (asymmetric).

Electrochemical impedance spectroscopy (EIS) was performed on all electrodes for symmetric and asymmetric systems to verify the electrochemical performance and explore the electron transfer kinetics of redox reactions electrode-electrolyte interface are shown in Nyquist plots in **Fig. 6.10**. The impedance spectroscopy results display the semicircle arc for all three electrodes (Symmetric system) as shown in **Fig. 6.10** over the high-frequency region. The impedance measurement exhibits the electron transfer kinetics of redox reactions electrode-electrolyte interface at lower frequencies due to the limiting mass transport. A partial semicircle has been observed at higher frequencies, indicating the charge transfer resistance. The R_s values of PV_4W_8 , PV_4W_8/PPy , and PV_4W_8-PPy/PPy

(asymmetric) are at 0.79, 0.74, and 0.54 Ω , respectively. The symmetric PV₄W₈/PPy exhibits less resistance than PV₄W₈ because of the presence of PV₄W₈ on the PPy matrix and transports good conductivity on PPy. Likewise, the asymmetric PV₄W₈-PPy/PPy shows even lesser resistance than PV₄W₈/PPy, indicating an increase in the PPy matrix's conductivity.

Moreover, the higher the conductivity, the higher the charge transfer between the PPy and PV₄W₈, and enhanced the capacitance efficiency observed in both cases (Zheng et al. 2018). Protons present in the PV₄W₈ play a vital role in improving this electrode material's conductivity mechanism. Additionally, the PV₄W₈-PPy/PPy asymmetric electrode offers a lower knee frequency (f_k) than PV₄W₈/PPy suggesting the capacitive responsive, in which the electrolyte ions could quickly disseminate through the electrode apertures (Chen et al. 2003; Wang et al. 2018b).

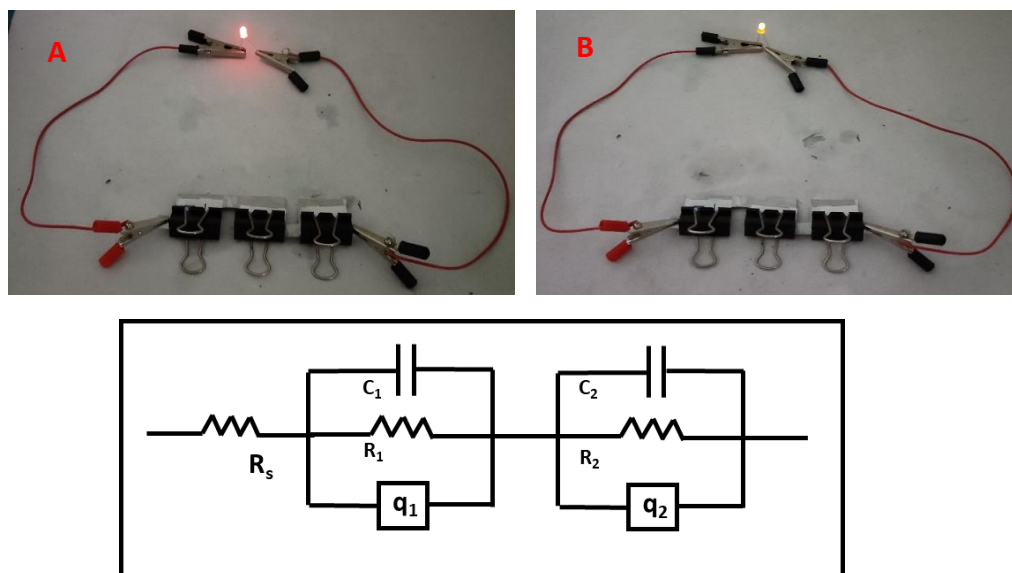


Fig. 6.11 (A) and (B) are the fabricated SCs energizing red and yellow light-emitting diodes by PV₄W₈-PPy/PPy (asymmetric) composite (C) The equivalent circuit is used for fitting the Nyquist plots.

The equivalent circuit for PV₄W₈-PPy/PPy electrode material is presented in **Fig.**

6.11C. q_1 and q_2 are the phase factors. They are generated due to the faradaic reactions. The PV_4W_8 -PPy/PPy electrode material was coated on four pairs of carbon clothes of dimension $2\text{ cm} \times 2\text{ cm}$ following the fabrication mentioned above method (mentioned in the above experimental part) using 72 mg of active electrode material in total to investigate the practical application. The circuit was connected in a series, as shown in **Fig. 6.11a** and **6.11b**. This setup was suitable to light up red (1.8 V) and yellow (2.0-2.3 V) light-emitting diodes when charged with an electrochemical workstation. Upon discharging, the LED continued to glow for the following 80 s (red) and 60s (yellow), taking energy from the device.

6.2.4 Cycle stability studies

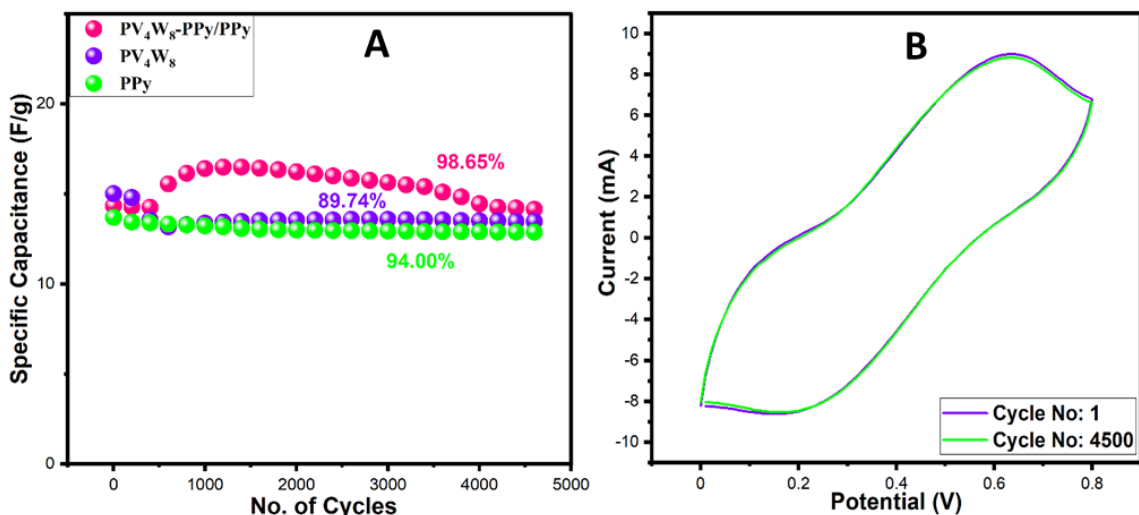


Fig. 6.12 A) Cycle stability of symmetric PPy, PV_4W_8 , and PV_4W_8 -PPy/PPy (asymmetric) and B) 1st and final cycle of PV_4W_8 -PPy/PPy electrodes at a current density of 500 mV s^{-1} after 4500 cycles.

The cycle stability of PPy, PV_4W_8 , and PV_4W_8 -PPy/PPy (asymmetric) was assessed by CV (**Fig. 6.12A**). The PV_4W_8 -PPy/PPy electrode showed a remarkable cycle stability of 98.65 % after 4500 cycles at a 500 mV s^{-1} scan rate for an asymmetric system, indicating the long-term electrochemical capacitor and the last cycles are indistinguishable from the 1st cycle (**Fig. 6.12B**). Thus, the PV_4W_8 -PPy/PPy electrode retains its pseudocapacitance

behavior even after 4500 cycles (**Fig. 6.12B**). The remarkable stability may be due to the uniform doping of PV_4W_8 on the PPy matrix. Pure PV_4W_8 also shows a very high stability of 87.94 % at the same scan rate and stability cycle. The dissolution of PV_4W_8 is less in this case, which is surprising because, generally, polyoxometalates are highly soluble in an aqueous medium. Pure PPy offers a plateau stability graph by retaining 94% stability after 4500 cycles, indicating pseudocapacitance behavior retained after a long process.

CHAPTER 7

**Polyoxometalate ($[\text{PV}_4\text{W}_8\text{O}_{40}]^{7-}$) Integrated
into Polyaniline and Activated Carbon-Based Electrode
for High-Performance Electrochemical Supercapacitors**

This chapter describes the detailed comparison study of conducting polymer (CPs)- $[\text{PV}_4\text{W}_8\text{O}_{40}]^{7-}$ composites and activated charcoal (AC)- $[\text{PV}_4\text{W}_8\text{O}_{40}]^{7-}$ composites materials for supercapacitor applications. The CPs damage the hierarchical structure during the charging and discharging process and will start swelling. Incorporating polyoxometalate into the CP system will increase the stability of the electrode material. This entire article is based on a comparative study of two newly synthesized composites with the same polyoxometalate ($\text{K}_5\text{H}_2[\text{PV}_4\text{W}_8\text{O}_{40}]\cdot 11\text{H}_2\text{O}$, (PV_4W_8)), incorporated into polyaniline (PANI) and activated carbon (AC) matrix.

7 Result and Discussion

7.1 Structural, chemical, and morphological characterizations

7.1.1 Fourier transform infrared spectroscopy

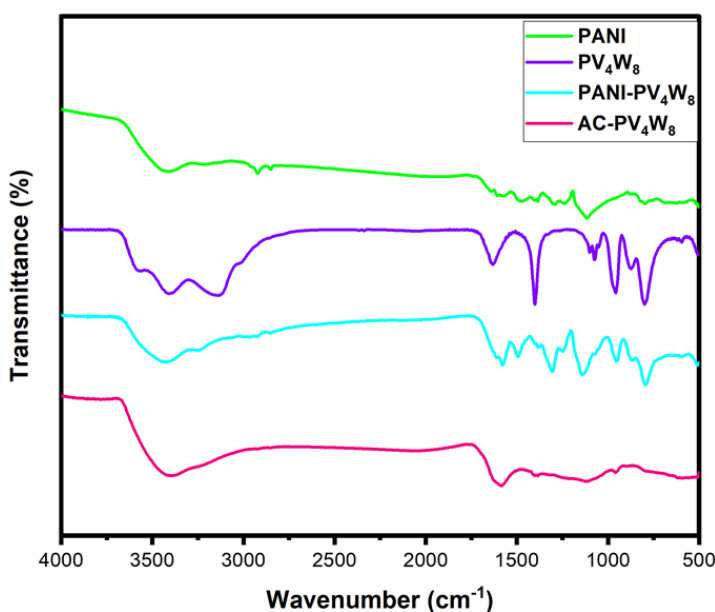


Fig. 7.1 a) FTIR spectra of PANI, PV_4W_8 , PANI- PV_4W_8 , and AC- PV_4W_8 .

The FTIR spectra of PANI, PV_4W_8 , PANI- PV_4W_8 , and AC- PV_4W_8 are given in **Fig. 7.1**. The PV_4W_8 IR bands primarily appeared within $500\text{-}1100\text{ cm}^{-1}$, corroborating well

with reported work. The IR bands at 1060-1070 and 950-957 cm^{-1} are designated to the P-O and terminal $\text{W}=\text{O}_t$ vibrational PANI-PV₄W₈ and AC-PV₄W₈ hybrid composites, respectively. Moreover, V-O-V and W-O-W bonds vibrational stretch noticed at 598-603 and 865-896, 780-796 cm^{-1} , respectively, confirming PV₄W₈ polyanions integration onto the PANI and AC surfaces, which is in corroboration with the published literature (Ruiz et al. 2012; Viswanathan and Shetty 2017). Similarly, all the IR bands observed for the PANI, as shown in **Fig. 7.1**, corroborated well with the literature (Viswanathan and Shetty 2017). A few new bands also originated in the IR spectrum of PANI-PV₄W₈ composite, designated to C=C and C-N stretching vibrations confirming the presence of PANI polymers. The broad peak at 3300-3400 cm^{-1} represents the -OH groups in the composite.

7.1.2 Thermogravimetry analysis

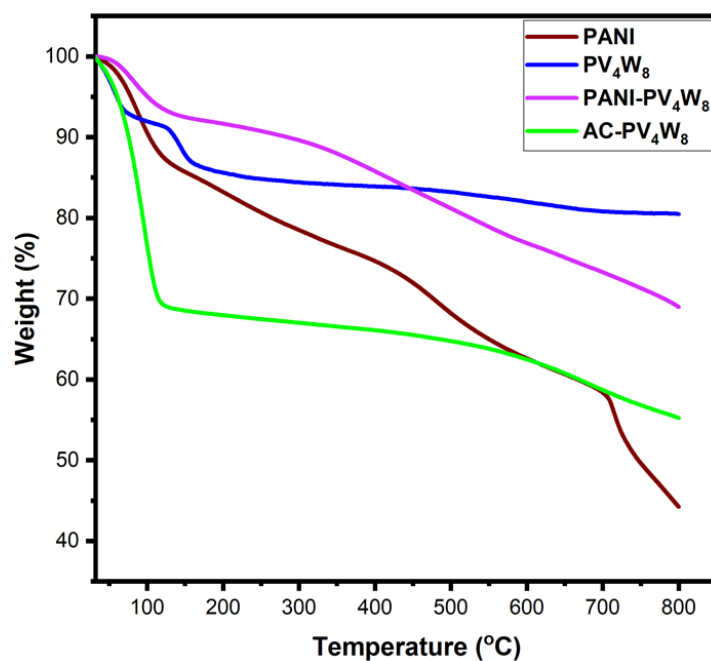


Fig. 7.2 TGA Curve of PANI, PV₄W₈, PANI-PV₄W₈, and AC-PV₄W₈.

Thermal stability is an integral property of energy storage devices for electrode materials. **Fig. 7.2** demonstrates the thermogravimetric analysis curves (TGA) of PANI,

PV₄W₈, PANI-PV₄W₈, and AC-PV₄W₈. The TGA curve shows that the decomposition of the composite is slowed down after the deposition of the redox-active material PV₄W₈ to the polymer matrix and AC materials (Vannathan et al. 2021). The initial weight loss of 11.81% at 88 °C of PANI is due to moisture removal. Above 200°C, the steady weight loss corresponds to removing organic moieties from the polymer backbone (Wang et al. 2006). Similarly, the weight losses of pure PV₄W₈ at 55 and 143 °C correspond to removing absorbed moisture and crystalline water molecules. Moreover, the complete decomposition of PV₄W₈ is observed at 643°C (Vannathan et al. 2021). Furthermore, the initial weight loss of PANI-PV₄W₈ at 83°C is the removal of the absorbed and crystal water molecules. The final weight loss is observed at 731 °C and is assigned to the decomposition of the inorganic moieties of the hybrid material, which is higher than the pure PV₄W₈. On the other hand, the AC-PV₄W₈ hybrid material's first decomposition was observed at 96 °C. The complete degradation of the PV₄W₈ 's inorganic moieties was noticed at 683 °C (Anandan Vannathan et al. 2022).

7.1.3 X-ray diffraction spectroscopy

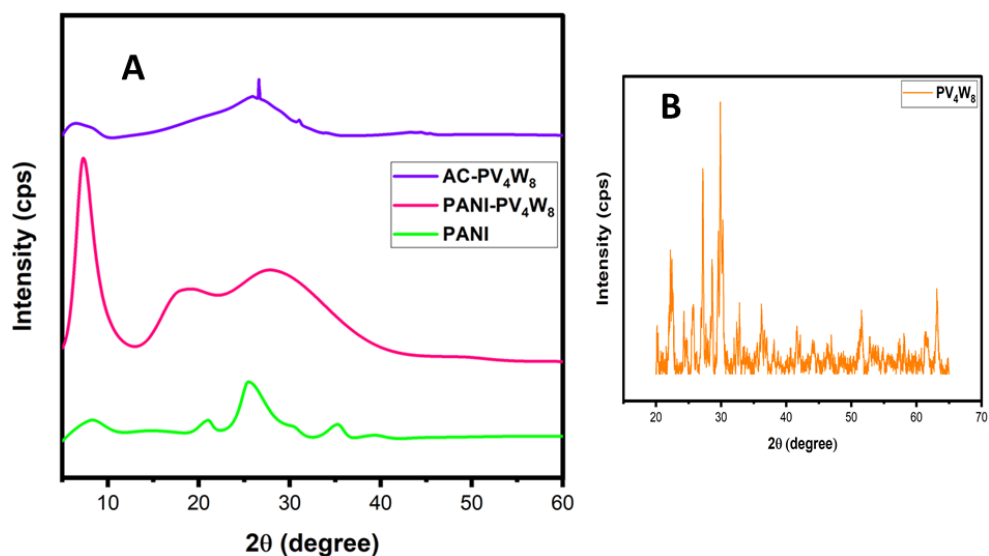


Fig. 7.3 Powder XRD spectrum of A) PANI, PANI-PV₄W₈, and AC-PV₄W₈ B) PV₄W₈

The Powder X-ray diffraction (XRD) patterns of PANI, PANI-PV₄W₈, and AC-PV₄W₈ composites are illustrated in **Fig. 7.3A**, and the XRD pattern of PV₄W₈ is shown in **Fig. 7.3B**. The powder XRD pattern of pure PANI shows typical diffraction peaks at 21.05° and 25.42°, consisting of an account in the literature (Viswanathan and Shetty 2017). The diffraction peaks at 22.37°, 25.62°, 27.23°, 28.62°, 29.89°, 32.81°, and 36.57°, respectively, are shown in **Fig. 7.3A** for PV₄W₈ portrayed crystalline nature. In the PANI-PV₄W₈ composite, the PANI peaks are shifted considerably to a lower angle (20.0° and 28.12°), and a few new peaks are also observed, confirming the integration of PV₄W₈ on the polymer matrix. Pure activated carbon shows broad peaks at 25° and 41.6° (Jain and Tripathi 2015). At the same time, the composite AC-PV₄W₈ shows peaks at 7.20°, 26.5°, 33.84°, and 43.23°, respectively, indicating the presence of PV₄W₈ on the AC surface. A few new peaks are also observed due to the adsorption of PV₄W₈ on the AC surface. From **Fig. 7.3A**, it is clear that both of the composites are amorphous in nature. The characteristic peaks of the PV₄W₈ are discernible in the XRD pattern for PANI-PV₄W₈ and AC-PV₄W₈ composites, exhibiting no loss of crystallinity of the PV₄W₈ after integrating on the respective surfaces.

7.1.4 Field emission scanning electron microscopy and Energy-Dispersive X-ray spectroscopy

Fig. 7.4a and **b** show the field emission scanning electron microscopy (FESEM) of the composite PANI-PV₄W₈ and AC-PV₄W₈ to acquire morphological features of PV₄W₈'s impregnated PANI and AC surfaces. The FESEM images indicate the polyanions are well disseminated on the polymer and AC surfaces. It is evident from **Fig. 7.4** that various nanostructures were formed after the doping of PV₄W₈ to the PANI and AC surface, respectively. The PANI-PV₄W₈ nanostructure is different from the PANI and PV₄W₈ nanostructure. It shows an agglomerated and spherical structure of an average diameter between 100-200 nm. The EDS spectrum also confirms the occurrence of C, P, V, W, O, N, and K elements (**Fig. 7.4a and c**). The AC-PV₄W₈ composites, a different structure from PV₄W₈, show a very smooth granular form with a diameter of less than 70 nm, and

the EDS spectrum confirms that C, P, V, W, O, and K elements are present in the composites (**Fig. 7.4b and d**).

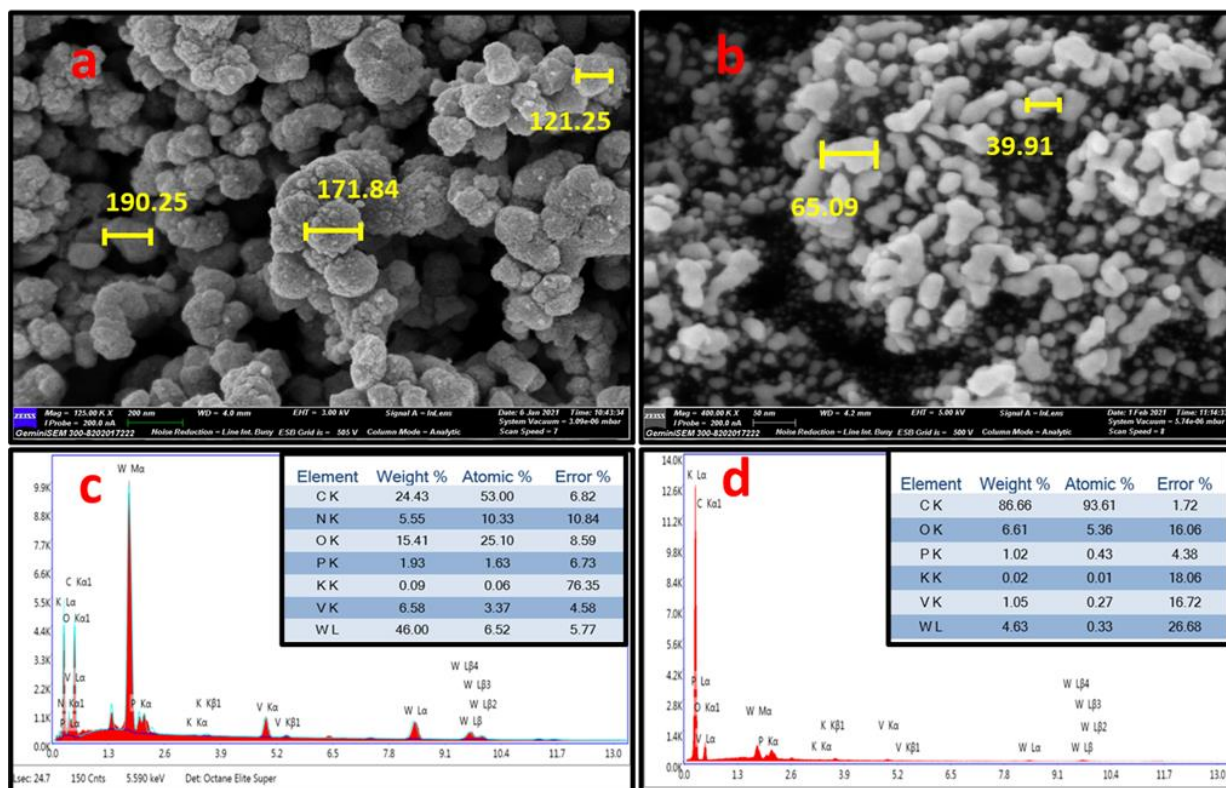


Fig. 7.4 FESEM image of a) PANI-PV₄W₈, and b) AC-PV₄W₈, EDS spectrum of c) PANI-PV₄W₈, and d) AC-PV₄W₈.

7.1.5 Brunauer–Emmett–Teller

Nitrogen adsorption/desorption studies were performed to measure the specific surface area and pore size distribution (PSD) of PANI, PV₄W₈, PANI-PV₄W₈, pure AC, and AC-PV₄W₈. **Fig. 7.5A** shows the nitrogen adsorption/desorption isotherms of PANI, PV₄W₈, and PANI-PV₄W₈. **Fig. 7.5B** shows the nitrogen adsorption/desorption isotherms of pure AC and AC-PV₄W₈. The pure PANI and PV₄W₈ exhibit the BET surface area of 34 m²g⁻¹ and 7.6 m²g⁻¹ with a micropore area of 0.6296 m²g⁻¹ and 0.2458 m²g⁻¹, respectively. The surface area was reduced to 18.9 m²g⁻¹ on the deposition of PV₄W₈ on the polymer surface.

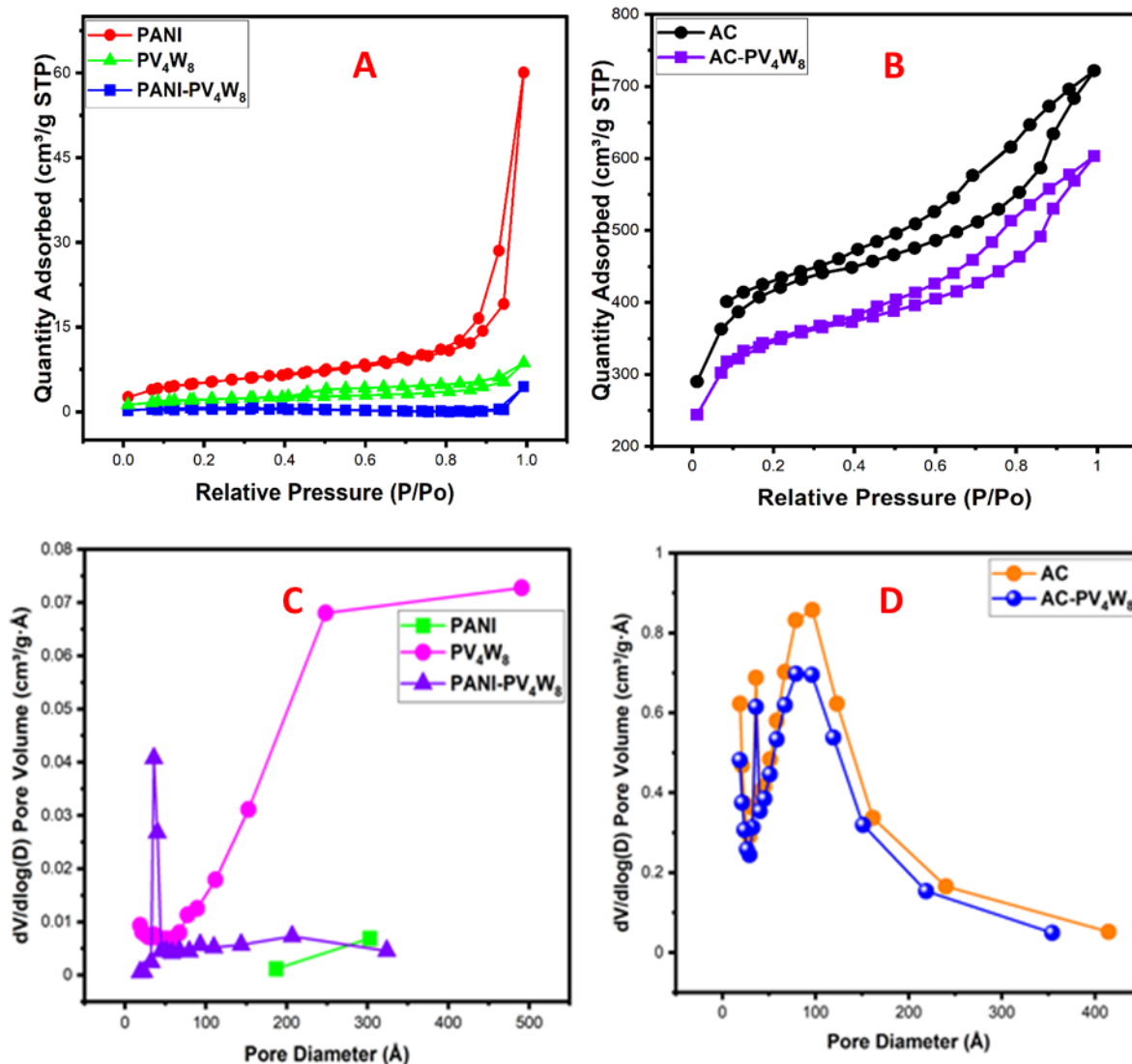


Fig. 7.5 Nitrogen adsorption/desorption isotherms of A) pure PANI, PV₄W₈, PANI-PV₄W₈, B) pure AC and AC-PV₄W₈ composite. Pore volume curve for C) pure PANI, PV₄W₈, and PANI-PV₄W₈ D) pure AC and AC-PV₄W₈ composite.

The decrease in surface area is attributed to the coverage of PANI surfaces and the blockage of narrow pores. The pure PANI exhibit types I isotherm with a sharp capillary condensation step and narrow hysteresis loop, indicating the presence of narrow-width mesopores. The absence of a capillary condensation step and hysteresis loop confirms the blockage of narrow-width pores on the deposition of PV₄W₈. The pure PANI surface area

is similar to the reported literature (Xu et al. 2013). Likewise, the pure AC possesses a specific BET surface area of $1340 \text{ m}^2\text{g}^{-1}$ with a micropore area of $717 \text{ m}^2\text{g}^{-1}$. The pristine AC and AC-PV₄W₈ exhibit type IV isotherm with hysteresis loop and extended capillary condensation step. The symbolic capillary condensation step indicates broad pore size distribution. The pore filling at a lower relative pressure (<0.05) confirms the existence of micropores. The pure AC exhibits a higher surface area than the AC-PV₄W₈ because of the highest availability of the micropore, and the isotherms show hysteresis loops (Maity et al. 2021a). The composite shows a specific surface area of $1117 \text{ m}^2\text{g}^{-1}$ with a micropore area of $604 \text{ m}^2\text{g}^{-1}$. The drastic drop in the micropore area confirms the deposition of PV₄W₈ in micropores. The surface area reduces upon the deposition of PV₄W₈ due to the surface coverage, differences in mass, and blockage of pores. Pore size distribution (PSD) graphs of pure PANI, PV₄W₈, PANI-PV₄W₈, AC, and AC-PV₄W₈ composites are shown in **Fig. 7.5C and D**.

7.1.6a X-ray photoelectron spectroscopy

The XPS spectrum of the PANI-PV₄W₈ composite shows six peaks corresponding to C 1s, N 1s, O 1s, P 2p, V 2p, and W 4f, respectively. The XPS spectrum of the C 1s (**Fig. 7.6a**) indicates that there are three types of carbon: C-C/C=C (284.2 eV), C-N (284.9 eV), and C-O (286.0 eV). The XPS spectra of N 1s (**Fig. 7.6b**) revealed two nitrogen species as -NH- (399.7 eV) and -NH⁺- (400.9 eV) (Liu et al. 2015). The peak corresponding to the binding energy 531.1 eV is due to O 1s from the Keggin-type structure (**Fig. 7.6c**) (Gao et al. 2018). A strong peak located at 134.0 eV (**Fig. 7.6d**) is due to the presence of P 2p_{3/2} in the Keggin structure (Zheng et al. 2018). The XPS spectrum of V 2p (**Fig. 7.6e**) indicates two binding energy peaks at 524.2 (V 2p_{3/2}) and 516.9 eV (2p_{1/2}), confirming the occurrence of V⁺⁵ and V⁺⁴ oxidation states in the POM (Zhang et al. 2020). The binding energy peaks of W 4f_{5/2} and W 4f_{7/2} are visible at 37.8 and 35.7 eV in the POM are illustrated in **Fig. 7.6f** (Ponja et al. 2016).

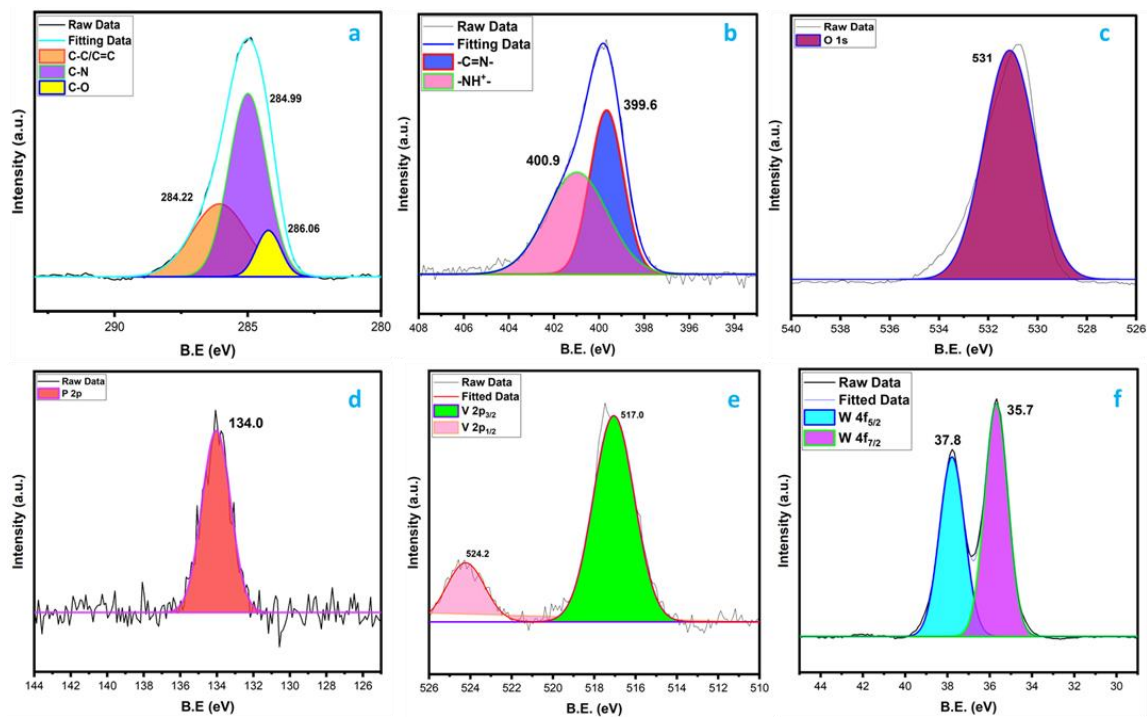


Fig. 7.6 XPS spectra of PANI-PV₄W₈.

7.1.6b X-ray photoelectron spectroscopy

The XPS spectrum of the AC-PV₄W₈ composite has five peaks which represent C 1s, O 1s, P 2p, V 2p, and W 4f, respectively. The XPS spectrum of the C 1s (**Fig. 7.7a**) indicates only one strong peak at 284.9 eV (Anandan Vannathan et al. 2022). The peak corresponding to the binding energy of 532.2 eV is due to O 1s from the Keggin structure (**Fig. 7.7b**) (Gao et al. 2018). A strong peak appeared at 134.1 eV (**Fig. 7.7c**) due to the presence of P 2p_{3/2} in the Keggin-type structure (Zheng et al. 2018). The XPS spectrum (**Fig. 7.7d**) confirms that the vanadium is present in V⁺⁵ and V⁺⁴ oxidation states in the POM structure, resulting in peaks at 525.1 and 517.0 eV corresponding to the V 2p_{3/2} and 2p_{1/2} (Zhang et al. 2020). Similarly, the XPS spectrum of W 4f_{5/2} and W 4f_{7/2} of the POM confirm the occurrence of W⁺⁶ at 37.9 and 35.8 eV in **Fig. 7.7e** (Ponja et al. 2016).

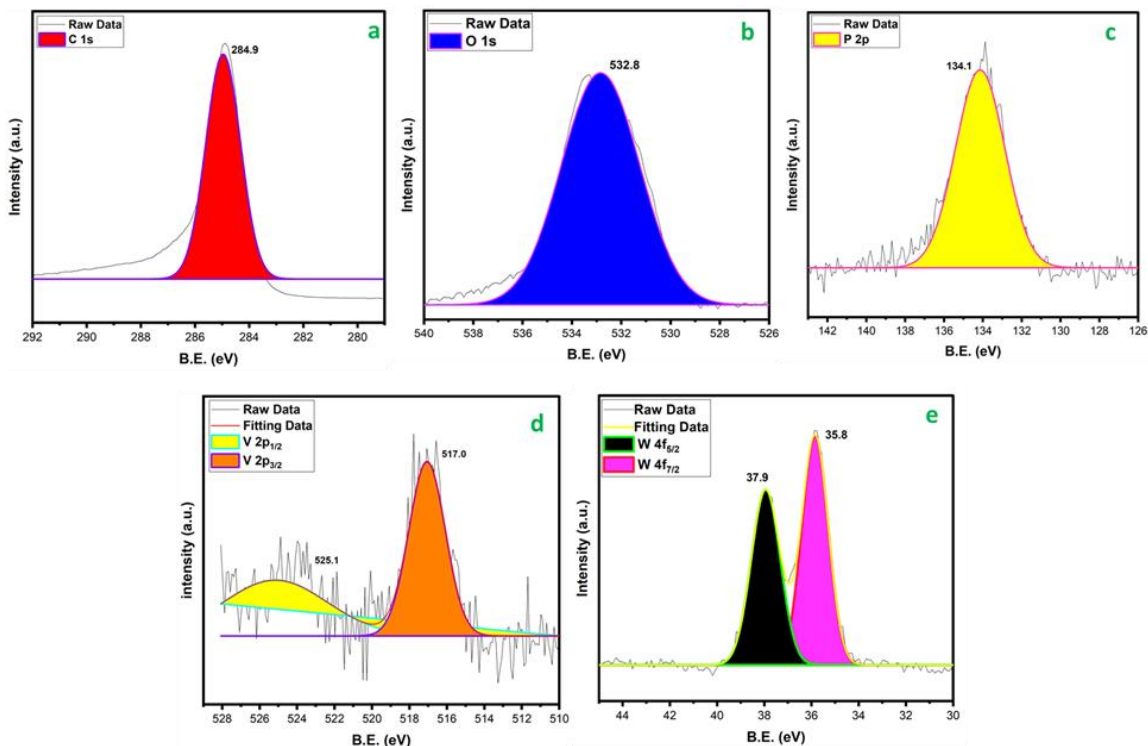


Fig. 7.7 XPS spectra of AC-PV₄W₈.

7.2 Electrochemical measurements

The present electrochemical studies mainly focused on the electrochemical performance of two different composites prepared by different supports. The composites are prepared using the same PV₄W₈ deposited on two different supporting materials (PANI and AC). The electrochemical studies of newly synthesized composites were evaluated by using cyclic voltammetry (CV), galvanostatic charge-discharge (GCD), electrochemical impedance spectroscopy (EIS) analysis, and cycle stability. All studies were performed using the two-electrode (symmetric) system in 0.5M H₂SO₄. The active mass of all composites on two electrodes are ~1.28 mg, which was employed for entire calculations.

7.2.1 CV studies

Cyclic voltammograms of PANI-PV₄W₈ and AC-PV₄W₈ were recorded at a 30 mV s⁻¹ scan rate to investigate the potential range of 0-1V in a two-electrode system, as presented in **Fig. 7.8A**. From the CV curve, the PANI-PV₄W₈ composite exhibits a very good rectangularity, indicating the perfect capacitive nature of PANI-based electrode material (Viswanathan and Shetty 2017). On the other hand, 10wt% AC-PV₄W₈ composites do not offer an exquisite capacitive nature compared to PANI-PV₄W₈, as shown in **Fig. 7.8A**. The area under the PANI-PV₄W₈ composite curve is more than the AC-PV₄W₈ composite because PANI-PV₄W₈ stores more energy than the AC-PV₄W₈ composite. The pure PANI itself acts as pseudocapacitive material and contributes to capacitance enhancement. The contribution of EDLC and pseudocapacitance in AC-PV₄W₈ and PANI-PV₄W₈ are given in **Fig. 7.9**. The CVs of PANI-PV₄W₈ composite at higher and lower scan rates are illustrated in **Fig. 7.8B** to determine the kinetics of the electrode materials.

Only one redox peak at a higher scan rate was observed because of the emergence of pseudocapacitance. The pseudocapacitance arises from the faradaic reaction of PANI through its reduction and oxidation transformation between a semiconducting leucoemeraldine form to emeraldine and emeraldine to pernigraniline (Wu et al. 2010b; Xia et al. 2012). The redox peaks of PV₄W₈ were not noticed because of the rapid kinetics of the electrolyte. In a lower scan rate, more than one pairs of redox peaks are present due to the pseudo-reversible redox reaction of vanadium ions (Vannathan et al. 2020) and the lowering of the movements of the electrolytes. It is evident from **Fig. 7.8C** that the composite PANI-PV₄W₈ shows ample charge storage compared to pure PANI and PV₄W₈, which is attributed to the uniform distribution of PV₄W₈ on the PANI surface.

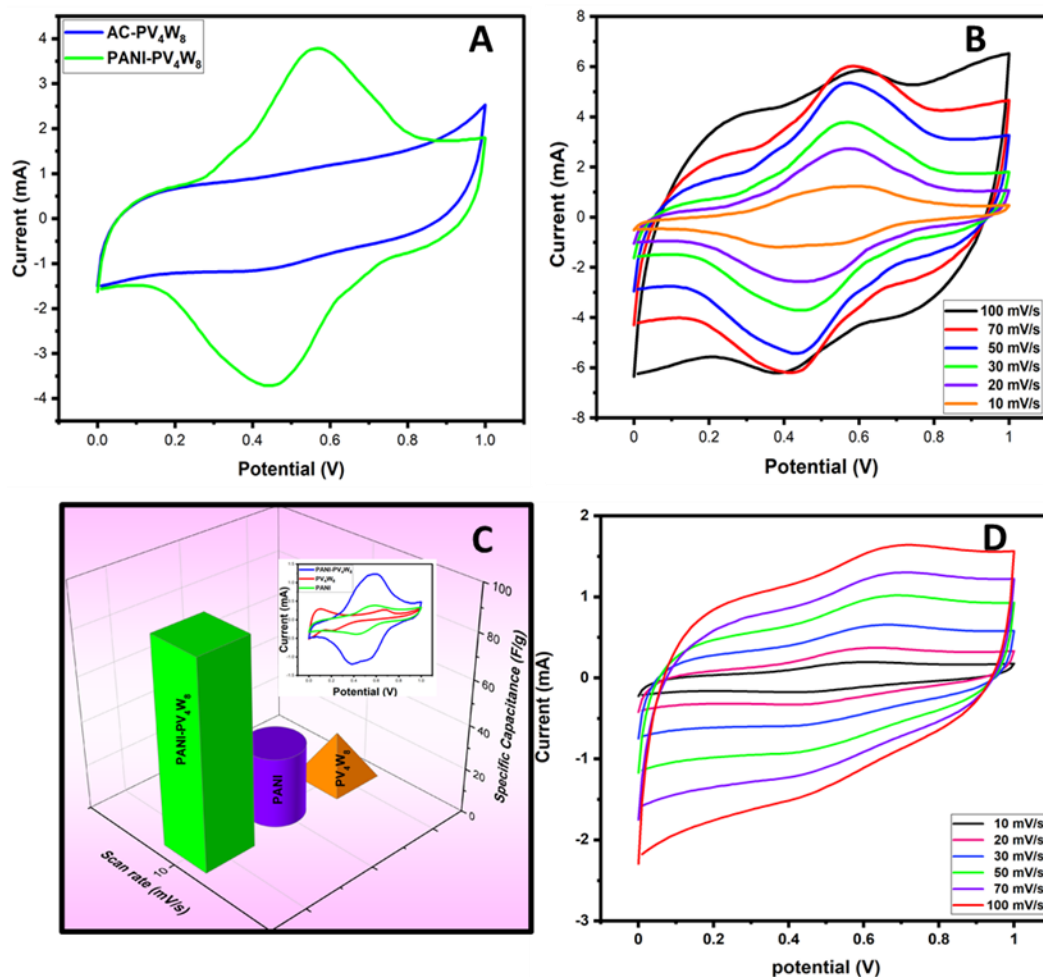


Fig. 7.8 A) CV graph for PANI-PV₄W₈ and AC-PV₄W₈ at 30 mV s⁻¹ scan rate B) CV graph for PANI-PV₄W₈ at different scan rate, C) CV graph for PANI-PV₄W₈, PV₄W₈, and PANI at a 10 mV s⁻¹ scan rate and D) CV graph for AC-PV₄W₈ at various scan rates.

Similarly, the CV curve of AC-PV₄W₈ (**Fig. 7.8D**) offers a rectangular shape at different scan rates, suggesting more EDLC character in the composite, which is confirmed by the Trasatti method (**Fig. 7.9c**).

The EDLC and pseudocapacitance contributions are calculated from the CV using a 1-10 mV s⁻¹ scan rate with the help of the Trasatti method. The total gravimetric capacitance (C_T) and surface contribution to the capacitance of the electrode material (C_{EDL}) are extracted from **Equations (2.13) and (2.14)**.

$C_T = C_{EDL} + C_{PSUEDO}$; C_{PSUEDO} is calculated by **equation (2.15)**. **Fig. 7.9a** (AC-PV₄W₈) and **Fig. 7.9d** (PANI-PV₄W₈) show the graphs of the reciprocal of gravimetric capacitance (C^{-1}) versus the square root of scan rate ($v^{1/2}$) (Chandran et al. 2020).

Fig. 7.9b (AC-PV₄W₈) and **Fig. 7.9e** (PANI-PV₄W₈) show the graphs of gravimetric capacitance (C) versus the reciprocal of the square root of scan rate ($v^{-1/2}$).

The Trasatti method found that AC-PV₄W₈ exhibits 27.65% EDL capacitance and 72.32% pseudocapacitance **Fig. 7.9c** and PANI-PV₄W₈ exhibits 31.15% EDL and 68.53% pseudocapacitance **Fig. 7.9f**.

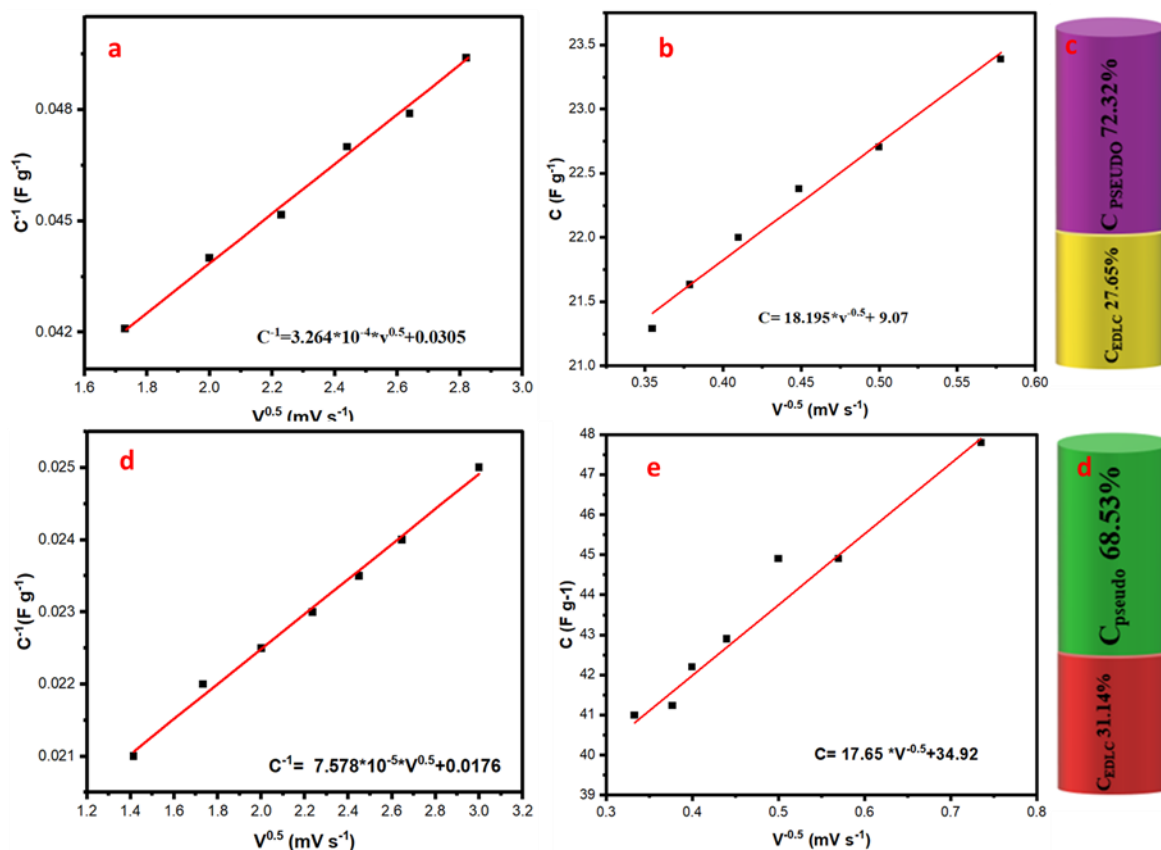


Fig. 7.9 (a) Plots of C^{-1} vs $v^{0.5}$ (b) Plots of C vs $v^{-0.5}$ (c) pseudocapacitance capacitance (%) and EDL (%) for AC-PV₄W₈ by Trasatti method (d) Plots of C^{-1} vs $v^{0.5}$ (e) Plots of C vs $v^{-0.5}$. (f) pseudocapacitance capacitance (%) and (%) for PANI-PV₄W₈ by the Trasatti method.

7.2.2 GCD studies

GCD of the two electrodes cell was effectuated to estimate the composite electrode's efficiency in SC applications. The GCD plot of composite PANI-PV₄W₈ was obtained at various current densities of 0.8, 1, 2, 3, 4, 5, 6, 7, 8, 9, 10 A g⁻¹, as presented in **Fig. 7.10A**. The GCD plot of the PANI-PV₄W₈ exhibited an equilateral triangle shape demonstrating the high reversibility of this electrode material throughout the charge-discharge process (Viswanathan and Shetty 2017). It was observed that the electrode materials took additional charge-discharge time at lower current densities because of the slower diffusion of H⁺ ions. It takes more time to penetrate the micropores created in the electrode material surface at lower current densities and electrolyte access (Kannappan et al. 2013). The composite has shown a maximum specific capacitance of 584.32 F g⁻¹ with an energy density of 81.16 Wh Kg⁻¹ and a power density of 1598.9 W Kg⁻¹ at a 0.8 A g⁻¹ current density. The cell's specific capacitance drops proportionally with current density, which is the standard behavioral attribute of ESCs (Li et al. 2011b).

Likewise, the AC-PV₄W₈ composite's (**Fig. 7.10B**) GCD was also performed at various current densities of 0.6, 0.8, 1, 2, 3 A g⁻¹. The capacitance value is 62.40, 63.20, 61.00, 54.00, and 51.00 F g⁻¹. At a higher current density, the stability of the electrode deteriorated. It is observed that PANI-PV₄W₈ electrode material showed better specific capacitance of 584.32 F g⁻¹ (0.8 A g⁻¹) than AC-PV₄W₈ (62.40 F g⁻¹ at 0.6 A g⁻¹) current density, GCD was calculated using **equation (2.2)** for all cases (Sowmya and Selvakumar 2018). Pure PANI exhibits the specific capacitance of 57 F g⁻¹ at 0.6 current density. The enhanced specific capacitance value of PANI- PV₄W₈ compared to the AC-PV₄W₈ and pure PANI could be attributed to the strongly engulfed more pseudocapacitive materials (PV₄W₈) onto the PANI matrix (Dhbar et al. 2013). The paramount specific capacitance of PANI-PV₄W₈ composites may be because of the following possible reasons: i) The uniform integration of PV₄W₈ on PANI matrix, which enhanced capacitance, (ii) There must be a synergistic interaction between the π -bonded conjugated PANI backbone and

PV₄W₈ in the genesis of oxidative polymerization techniques. Hence, there is a probability of charge transfer from PANI polymer matrices to PV₄W₈ due to the strong synergistic interaction increasing the faradic reaction's active sites and eventually enhancing the specific capacitance (Dhibar et al. 2014; Zhang et al. 2009a). To check the IR drops for PANI-PV₄W₈, PV₄W₈, and PANI, a comparison GCD plot is presented in **Fig. 7.10C**, which demonstrates that the comparison of GCD plots of PANI, PV₄W₈, and PANI-PV₄W₈ at 1 A g⁻¹ current density and exhibits the higher IR drops for PV₄W₈ (0.625V) than PANI (0.208V), and hence the specific capacitance is less for the former.

The behavior of supercapacitive materials is very much dependent on energy and power density. The biggest disadvantage of the supercapacitor's material is its low specific energy. In this study, the PANI-PV₄W₈ composite electrode showed improved specific energy (81.16 Wh kg⁻¹) and specific power (1598.9 W kg⁻¹) at 0.8 A g⁻¹ current density. The electrode is maintained specific energy and power of 40.0 Wh kg⁻¹, and 20571.4 W kg⁻¹, respectively, until the 10 A g⁻¹ current density. The specific energy and specific power values were acquired from charge/discharge profiles of the PANI-PV₄W₈ composite electrode shown in **Fig. 7.10D**. PANI-PV₄W₈ composite showing 98% Coulomb efficiency. However, the AC-PV₄W₈ offers the specific energy and specific power of 8.66 Wh kg⁻¹ and 1280 W kg⁻¹, respectively, at 0.6 A g⁻¹ current density, indicating the PANI-PV₄W₈ is a better supercapacitor than the AC-PV₄W₈ composite and also indicating either the PANI support is better than the AC or PV₄W₈ is distributed uniformly onto the PANI matrix.

Interestingly, the PANI-PV₄W₈ composite could show higher specific capacitance and power at 10 A g⁻¹ current density. At the same time, the AC-PV₄W₈ composite becomes unstable after 3 A g⁻¹ current density at a 1V potential window. Compared with two supporting materials (PANI and AC), PANI provides better energy storage capacitance than AC despite higher surface areas.

All electrode material's specific energy and power were estimated using **equations (2.5) and (2.4)**. The plot of specific energy vs power (Ragone plot) is shown in **Fig. 7.11D**. The Ragone plot revealed that the PANI-PV₄W₈ composite exhibits the highest specific energy and power than AC-PV₄W₈, indicating PV₄W₈ is more integrated on the PANI matrix than the AC surface. Hence, this particular metal-oxide's surface area plays an essential role in enhancing electrochemical behavior.

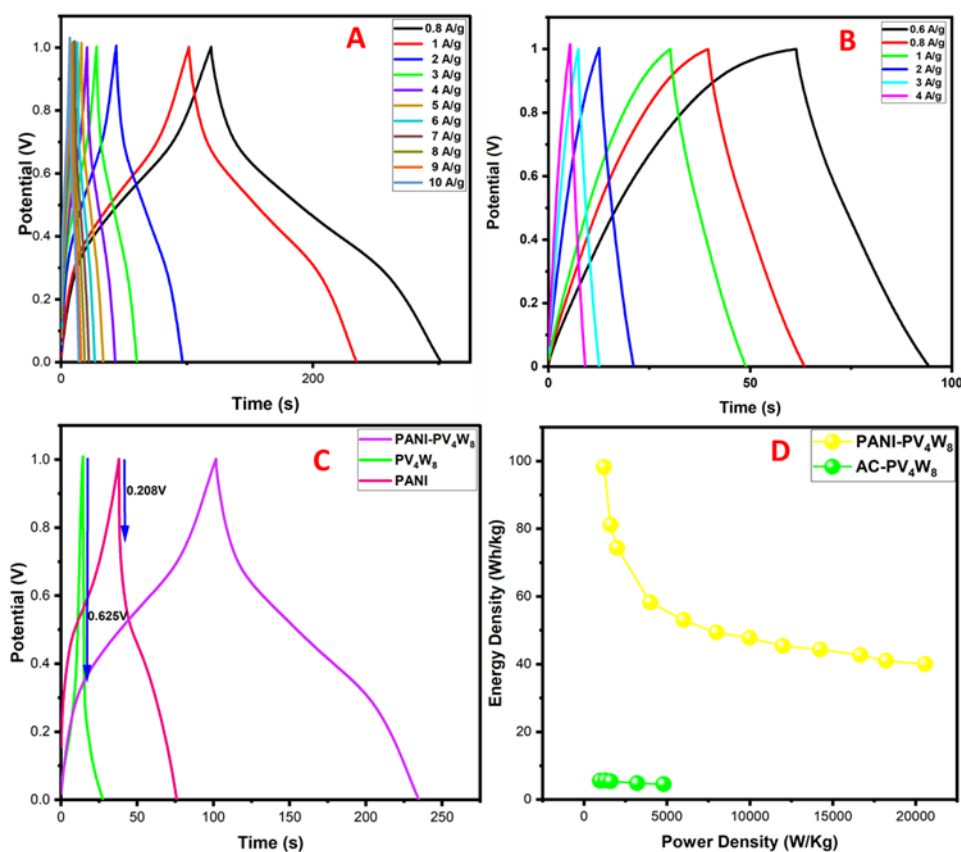


Fig. 7.10 A) GCD graph for PANI-PV₄W₈ at different current densities, B) GCD graph for AC-PV₄W₈ at different current densities, and C) GCD graph for PANI-PV₄W₈, PV₄W₈, and PANI at 1 A g⁻¹, D) Ragone plot for PANI-PV₄W₈ and AC-PV₄W₈.

7.2.3 EIS studies

Electrochemical impedance spectroscopy (EIS) of both the electrodes was performed for the symmetric system presented in Nyquist plots in **Fig. 7.12A**. The impedance was

determined within a frequency range of 0.01 to 10^5 Hz with an AC amplitude of 1 mV for both cases, exhibiting the redox reaction-mediated electron transfer kinetics because of the mass transfer limitation at the electrode-electrolyte interface at lower frequencies. The R_s values of PANI-PV₄W₈ and AC-PV₄W₈ are 0.81 and 1.58 Ω , respectively, indicating the lower resistance of PANI-PV₄W₈ than AC-PV₄W₈. After comparing PANI-PV₄W₈ with the AC-PV₄W₈, it can be concluded that the PANI-PV₄W₈ composite shows better capacitive behavior than the AC-PV₄W₈ composite. We only did the equivalent circuit fitting and cycle stability with the PANI-PV₄W₈ composite, as shown in **Fig. 7.12B**. The fitted data and equivalent circuit for the PANI-PV₄W₈ composite are shown in **Fig. 7.12B**. The circuit corresponds to the symmetric system of PANI-PV₄W₈, so C_1 and $C_2 = C$; similarly, R_1 and $R_2 = R_{ct}$, with W representing the Warburg Impedance.

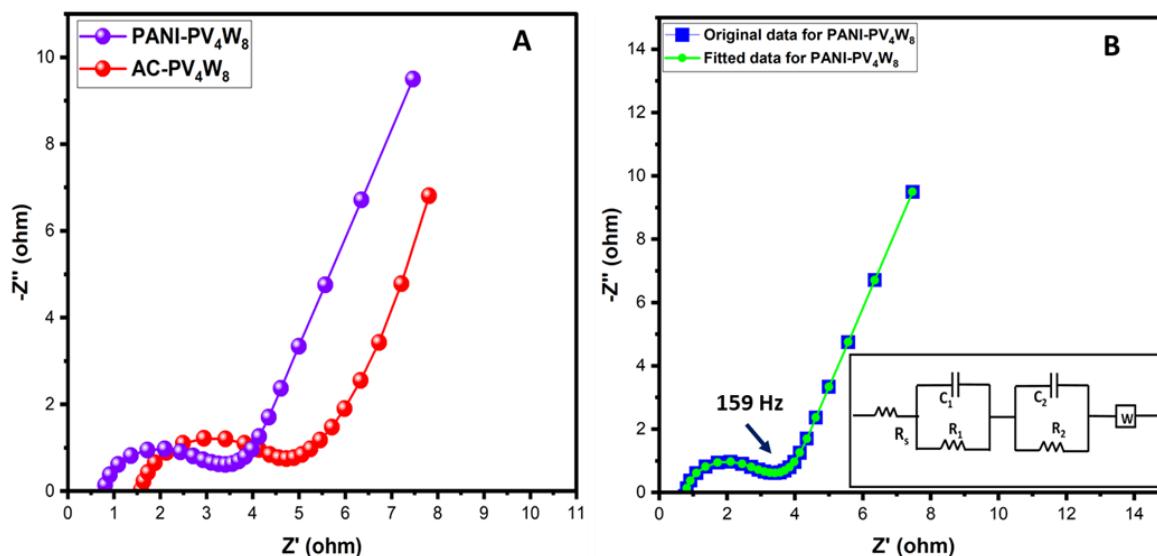


Fig. 7.11 A) EIS graphs for PANI-PV₄W₈ and AC-PV₄W₈ and B) Original and fitted EIS data of PANI-PV₄W₈ with knee frequency and equivalent Circuit.

To light up the bulb for a practical application, four carbon cloth pairs (dimension 2 cm \times 2 cm) were coated with PANI-PV₄W₈ electrode material (\sim 52 m). The circuit was made by connecting this electrode in series, as presented in **Fig. 7.13a and b**. This fabricated circuit was capable of light-up yellow (2.0-2.3 V) and red (1.8 V) light-emitting diodes

(LEDs) upon charging with an electrochemical workstation. The LED continued to glow for 85 s (red) upon discharging, taking energy from the device.

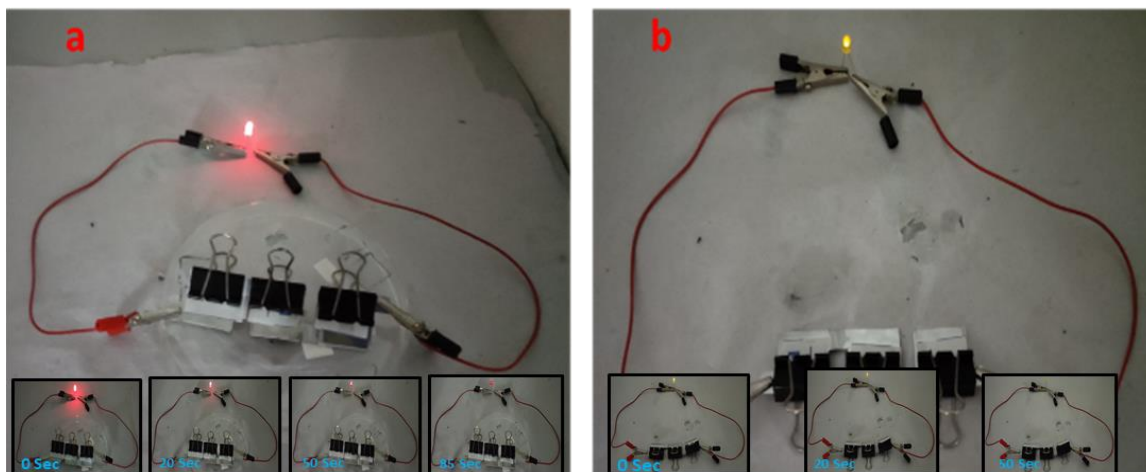


Fig. 7.12 (a) and (b) are the fabricated SC that energize red and yellow light-emitting diodes

7.2.4 Cycle stability studies

The PANI-PV₄W₈ electrode material's electrochemical stability was further inspected by cyclic voltammetric tests at 500 mA s⁻¹ scan rates in 0.5 M H₂SO₄, as given in **Fig. 7.14A**. The polyaniline conducting polymer-supported PV₄W₈ composite material showed excellent stability even after 4500 cycles and retained 93.13% of the initial capacity. The first and last stability cycles of PANI-PV₄W₈ are demonstrated in **Fig. 7.14B**. From the first and final cycle, it is clear that the composite's stability is excellent.

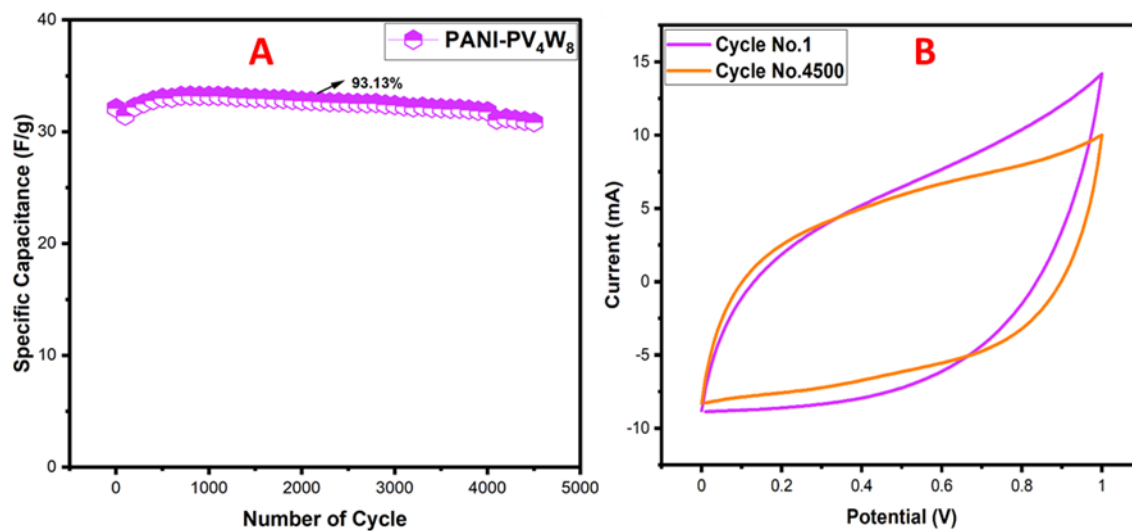


Fig. 7.13 A) Cycle stability of PANI-PV₄W₈ and B) First and final cycle of PANI-PV₄W₈.

CHAPTER 8



**Polyoxovanadate-Activated Carbon-Based
Hybrid Materials for
High-Performance Electrochemical Capacitors**

This chapter discusses the electrochemical performance of two distinct polyoxovanadates derivatives, $K_5Mn^{IV}V_{11}O_{32} \cdot 10 H_2O$ (MnV_{11}) and $K_7Mn^{IV}V_{13}O_{38} \cdot 18 H_2O$ (MnV_{13}), and two newly synthesized composites AC- MnV_{11} and AC- MnV_{13} (polyoxovanadates were deposited on activated carbon (AC) surface).

8 Result and Discussion

8.1 Structural, chemical, and morphological characterizations

8.1.1 Fourier transform infrared spectroscopy

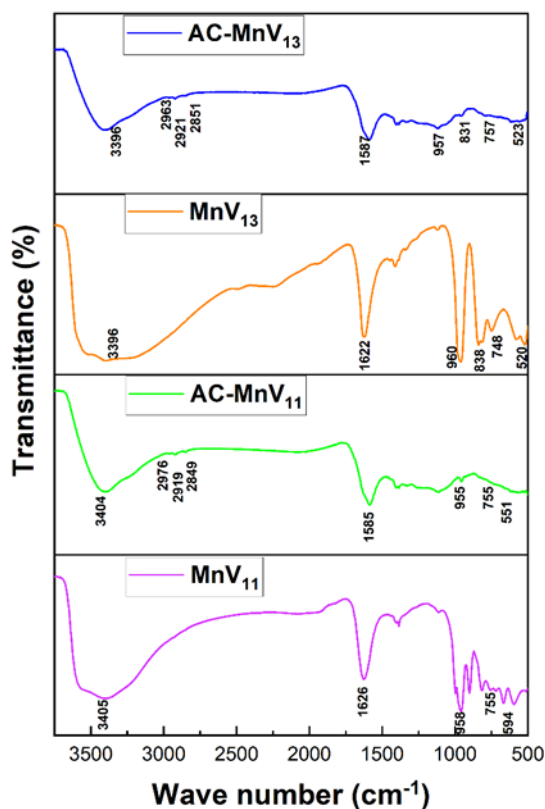


Fig. 8.1 FTIR of MnV_{11} , AC- MnV_{11} , MnV_{13} , and AC- MnV_{13} .

The FTIR spectra of pure MnV₁₁, MnV₁₃, and activated carbon-supported AC-MnV₁₁ and AC-MnV₁₃ composites are shown in **Fig. 8.1a**. The characteristic IR bands of Mn-O and V-O bond vibration have appeared within the 500–1000 cm⁻¹ range. The distinct IR bands for Mn-O have appeared at 512 (MnV₁₁) and 520 (MnV₁₃) cm⁻¹, respectively. The IR bands of V=O bond vibration were evaluated at 958 and 996 cm⁻¹ for MnV₁₁ and 960 cm⁻¹ for MnV₁₃, respectively. The IR bands that appeared at 815, 594, and 755 cm⁻¹ are assigned to several V-O-V bridging bond vibrations in MnV₁₁. Similarly, the IR bands at 838, 813, 579, and 520 cm⁻¹ are ascribed to V-O-V bonds for MnV₁₃, which are fully ratified with the reported result (Flynn and Pope 1970a). The medium-intensity bands at 1585 (AC-MnV₁₁) and 1587 (MnV₁₃) cm⁻¹ are due to the C=C stretch of the activated carbon. All the composite (AC-MnV₁₁ and AC-MnV₁₃) materials exhibit Mn-O, V=O, and V-O-V characteristic bands, ranging from 500-1000 cm⁻¹, indicating the integration of the vanadomanganate within the activated carbon surface.

8.1.2 Thermogravimetry analysis

Thermal stability is crucial for any electrode materials for their electronic gadget's applications. Therefore, thermogravimetry (TGA) analysis was studied for all electrode materials to determine their thermal stability. **Fig. 8.2a** depicts the combined TGA graphs of MnV₁₁, MnV₁₃, AC-MnV₁₁, and AC-MnV₁₃. The DTG graph of pure MnV₁₁ and MnV₁₃ revealed initial weight loss at 127.0 and 142.33 °C temperatures (**Fig. 8.2b, 8.2c**), which were attributed to removing crystal water molecules. On further heating, the complete decomposition of the materials was observed at a pretty high temperature of 461.33 and 599 °C for MnV₁₁ and MnV₁₃, respectively, as shown in the DTG graph (**Fig. 8.2b, 8.2c**). The AC-MnV₁₁ composite's first weight loss (3.65%) was observed at 78.0 °C, attributed to removing moisture from hybrid material (**Fig. 8.2d**). The steady weight loss (23.25%) noticed until 607.67 °C is assigned to the decomposition of the inorganic moieties of the vanadomanganate AC-MnV₁₁ electrode material (**Fig. 8.2d**). Likewise, The AC-MnV₁₃ composite's first weight loss (3.65%) was observed at 100.33 °C because of the removal of moisture from the hybrid material (**Fig. 8.2e**). Again, the steady weight loss is noticed

until 800°C is assigned to the decomposition of the inorganic moieties of the vanadomanganese AC-MnV₁₃ electrode material (**Fig. 8.2e**).

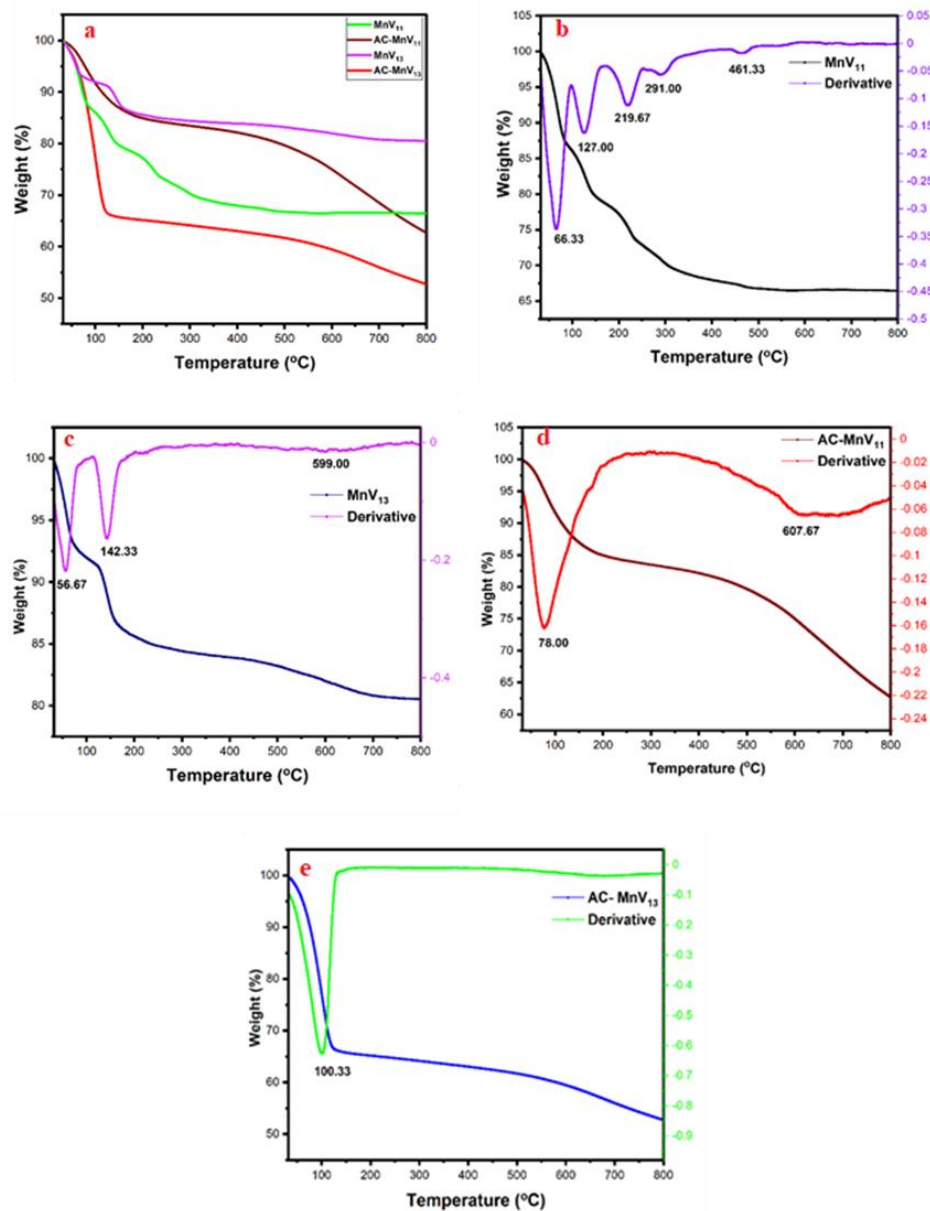


Fig. 8.2 a) All TGA curves, TGA curves, and DTA graphs of b) MnV₁₁, c) MnV₁₃, d) AC-MnV₁₁, and e) AC-MnV₁₃.

8.1.3 X-ray diffraction spectroscopy

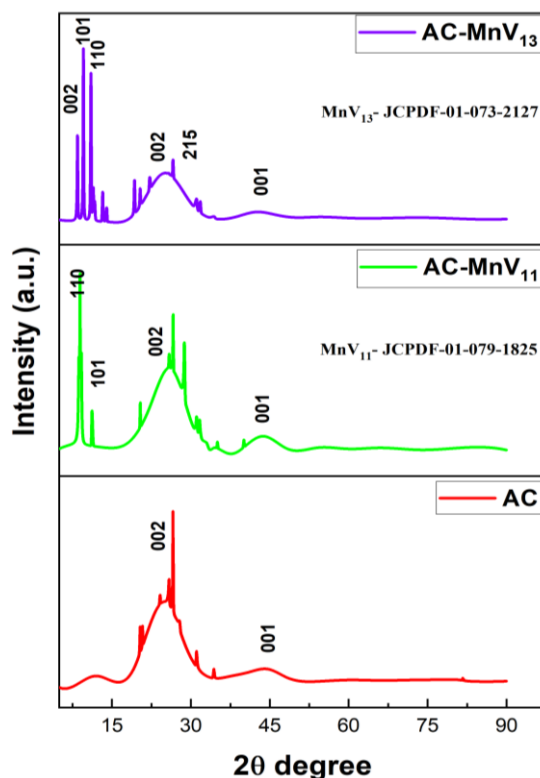


Fig. 8.3 Powder XRD patterns for AC, AC-MnV₁₁, AC-MnV₁₃

The powder XRD patterns of AC, AC-MnV₁₁, and AC-MnV₁₃ composites are depicted in **Fig. 8.3**. The broad peak appearing in the 2θ range of $20\text{--}30^\circ$ confirms the amorphous nature of AC, as shown in Figure 3. The AC-MnV₁₁ composite shows sharp peaks at 2θ of 28.74 , 31.05 , 31.65 , 32.9 , 34.7 , 35.03 , and 40.07° , which are ascribed to the characteristic peaks of MnV₁₁. Likewise, the same region's sharp peaks originating in AC-MnV₁₃ are attributed to MnV₁₃. Interestingly, both the composites revealed a combination of amorphous and crystalline features of the composites. Thus, the appearance of POM characteristics peaks in the composite's XRD pattern, suggesting that the crystalline structure of the POMs retains on the composite.

8.1.4 Field emission scanning electron microscopy and Energy-Dispersive X-ray spectroscopy

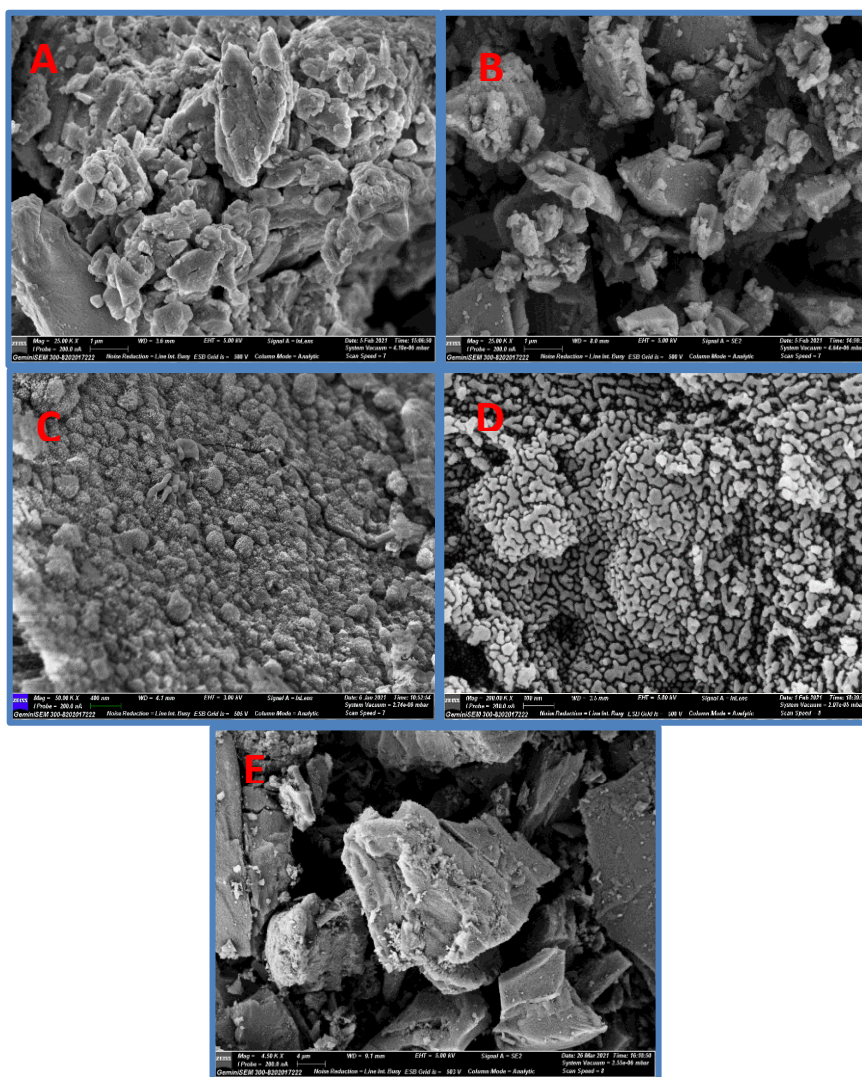


Fig. 8.4 FESEM image for A) MnV₁₁, B) MnV₁₃, C) AC-MnV₁₁, D) AC-MnV₁₃ and E) Pure AC.

The surface morphological features of the electrode material were collected using FESEM. **Fig. 8.4A and B** illustrate the micrograph of the pristine MnV_{11} , and MnV_{13} shows the polyanion's block structure. FESEM image indicated the modification of the surface of AC because of the deposition of redox polyanions. The porous structure of AC required active sites for anchoring the inorganic component on the surface. However, the open porous morphology of AC does not alter even after modifying the AC surface. **Fig. 8.4C-D** shows that AC's micropore is blocked because of MnV_{11} and MnV_{13} polyanions deposition. However, MnV_{11} and MnV_{13} polyanions are well dispersed over the AC surfaces without forming crystalline bulk species. **Fig. 8.4E** is the surface morphology of pure AC. It shows rock kind of porous structure.

The EDS spectra for MnV_{11} , MnV_{13} , AC- MnV_{11} , and AC- MnV_{13} are illustrated in **Fig. 8.5**. The EDS measurement confirms the occurrence of all the constituent elements on the AC surface.

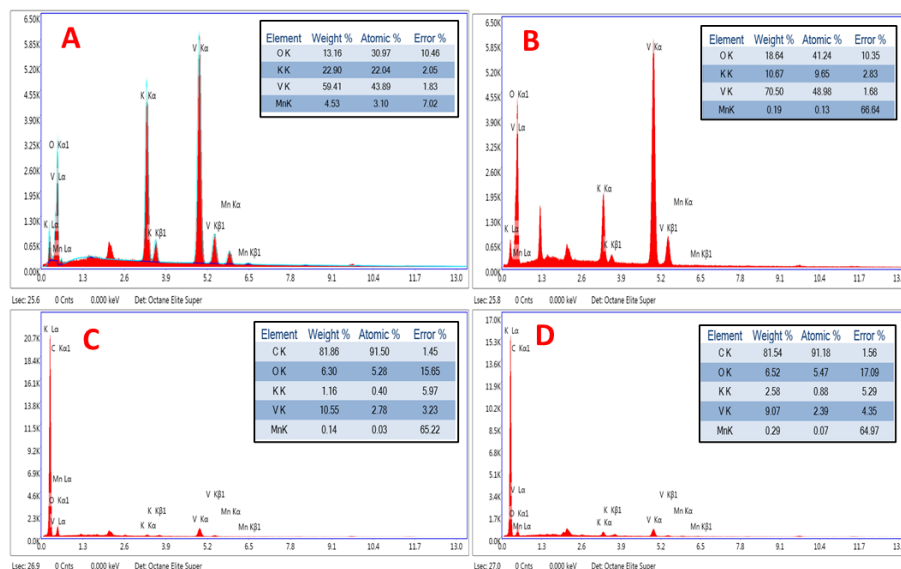


Fig. 8.5 EDS image for A) MnV_{11} , B) MnV_{13} , C) AC- MnV_{11} , and D) AC- MnV_{13}

8.1.5 Brunauer–Emmett–Teller

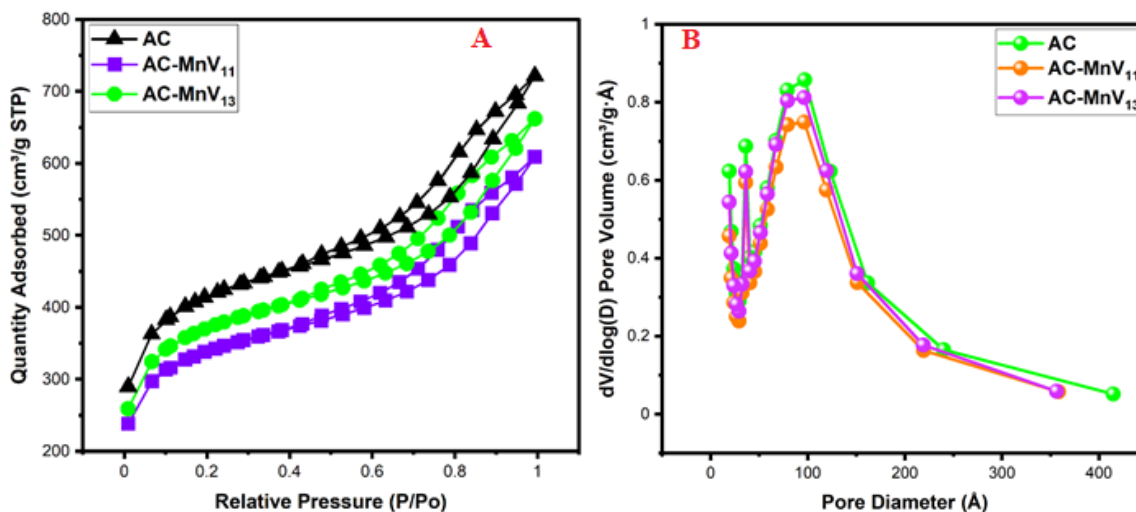


Fig. 8.6 A) N₂ adsorption/desorption isotherm. B) pore distribution of AC, AC-MnV₁₁, and AC-MnV₁₃.

A Brunauer–Emmett–Teller (BET) surface area is determined for AC, AC-MnV₁₁, and AC-MnV₁₃ using N₂ adsorption-desorption isotherms data are shown in **Fig. 8.6A**. The estimated surface areas of AC, AC-MnV₁₁, and AC-MnV₁₃ are 1340, 1097, and 1206 m²g⁻¹, respectively. The lower surface area of the two composites compared to the surface area of AC is mainly attributed to the dispersion of MnV₁₁ and MnV₁₃ on the AC surface and the blockage of the micropores of AC. All composite materials showed typical type IV nitrogen adsorption isotherm per IUPAC classification with a narrow hysteresis loop indicating a smaller mesopore fraction, as depicted in **Fig. 8.6A**. However, the sharp rise in N₂ uptake at low relative pressure ($P/P_0 < 0.05$) confirms the presence of micropores. The pore size distribution curves (PSD) determined by Barrett Joyner Halenda's (BJH) method for AC, AC-MnV₁₁, and AC-MnV₁₃ composites are shown in **Fig. 8.6B**. The peak intensity in PSD decreased with the deposition of MnV₁₁. However, the micropore volume was reduced from 0.36 cm³g⁻¹ (AC) to 0.30 cm³g⁻¹ for AC-MnV₁₁, whereas the micropore volume was increased to 0.32 cm³g⁻¹ for AC-MnV₁₃. These results suggest that the MnV₁₁

was deposited primarily in the micropores of the AC. However, MnV₁₃ was deposited on the available mesopores of AC. The deposition of MnV₁₃ on the mesopores transforms the mesopores into micropores resulting in a slight increase in the micropore volume of AC-MnV₁₃. Nonetheless, the above discussion confirms the anchoring of both the POMs on the AC.

8.1.5 X-ray photoelectron spectroscopy

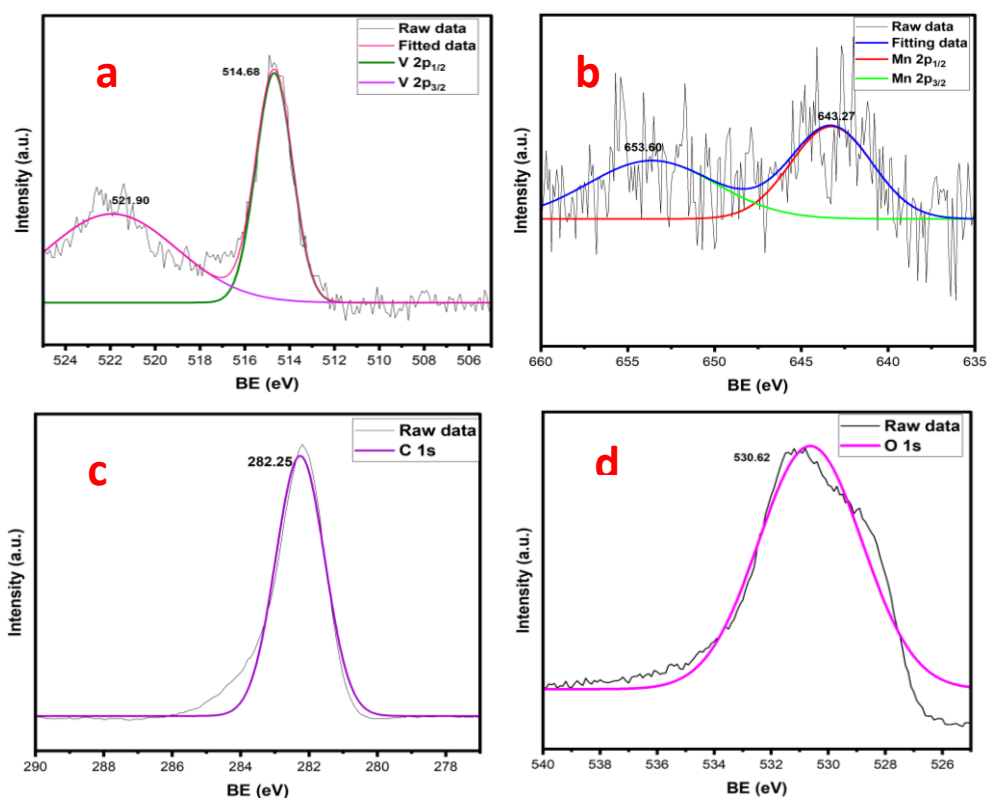


Fig. 8.7 XPS image of AC-MnV₁₁ a) V 2p b) Mn 2p c) C 1s and d) O

XPS spectra of AC-MnV₁₁ are given in **Fig. 8.7**. It shows the V 2p, Mn 2p, C 1s, and O 1s spectra (**Fig. 8.7a-d**). The strong peak at 521.90 and 514.68 eV represents the V 2p_{1/2} and V 2p_{3/2} peaks (Yagci et al. 2005); the Mn 2p_{1/2} and Mn 2p_{3/2} are given corresponding peaks at 653.60 and 643.27 eV (Simon et al. 2014). The C 1s and O 1s show corresponding peaks at 282.25 and 530.62 eV (Kumari et al. 2020).

8.2 Electrochemical measurements

8.2.1 CV studies

A simple two-electrode cell was used to evaluate the potential of the activated supported two faradic POMs (MnV_{11} and MnV_{13}) materials for SCs electrodes, depicted schematically in **Fig. 8.8a**. This device comprises two AC- MnV_{11} (or AC- MnV_{13}) electrodes on current collectors and a porous separator. The assay of the AC- MnV_{11} (or AC- MnV_{13}) coated on each carbon cloth was estimated to be 1.28 mg each. The AC- MnV_{11} (or AC- MnV_{13}) electrodes and separator were sandwiched together in a stainless-steel cell to fabricate the fully assembled two-electrode cell device. **Fig. 8.8a** exhibits cyclic voltammetry (CV) curves obtained for the supercapacitor assembled with AC- MnV_{11} electrodes for voltages up to 1.2 V with several scan rates of 10, 20, 30, 50, 70, and 100 m Vs^{-1} . The highest specific capacitance of 100.16 F g^{-1} was obtained at a scan rate of 10 m Vs^{-1} (calculated using **Equation (2.1)**). Likewise, **Fig. 8.8b** shows the CV curves obtained for AC- MnV_{13} electrode voltages up to 1.2 V with the same scan rates using 0.1M H_2SO_4 electrolyte solution. Moreover, the less specific capacitance of 85.22 F g^{-1} was observed at a 10 m Vs^{-1} scan rate than the AC- MnV_{11} electrode.

Interestingly, both the electrode's CV appeared relatively close to rectangular in shape even at a higher scan rate of 100 m Vs^{-1} , which is characteristic of capacitive behaviour for activated carbon-based SCs (Cao and Zheng 2012). Notably, the CV area increases with increasing the scan rate without detectable changes in shape. These results suggest that the electrolyte ions are swiftly relocated between the electrode-electrode interface and the electrolyte (Zhao et al. 2013).

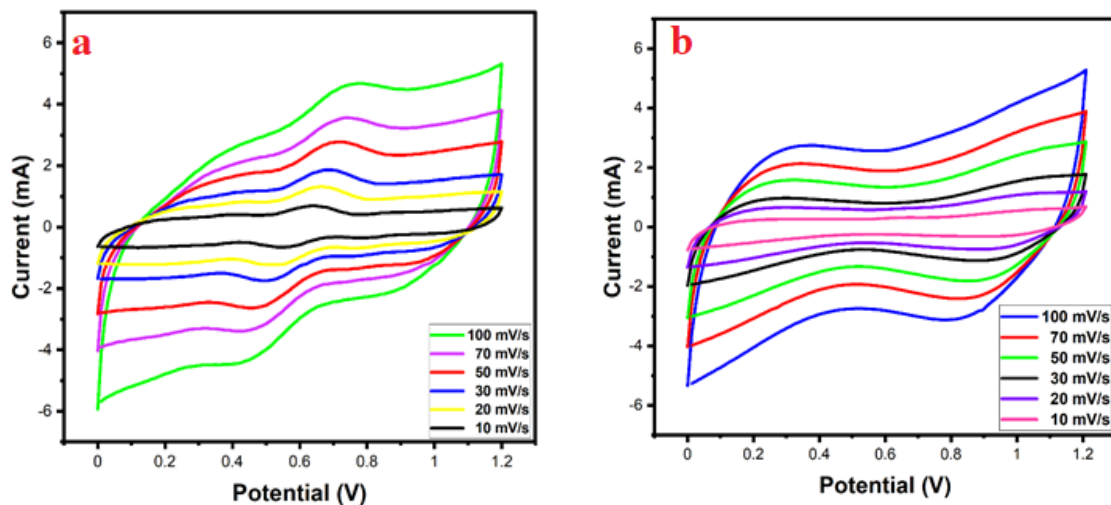


Fig. 8.8 CV graph of a) AC-MnV₁₁ and b) AC-MnV₁₃ at various scan rates at 0.1M H₂SO₄ electrolyte solution.

8.2.2 GCD studies

According to **equation (2.2)**, the specific capacitance is proportional to the integrated area of the CV curve. **Fig. 8.9** shows that AC-MnV₁₁'s CV area is well-distinguished than AC-MnV₁₃ at the same scan rates, implying a significant transport of electrolyte ions in AC-MnV₁₁. The galvanostatic charge-discharge (GCD) curves were accrued at numerous current densities of 10, 9, 8, 7, 6, 5, 4, 3, 2, 1, 0.8, 0.6 A g⁻¹ over a potential window of 0-1.2 V for both AC-MnV₁₁ and AC-MnV₁₃ electrodes are shown in **Fig. 8.9**. Consequently, The GCD curves illustrated the symmetrical triangle shape attributed to the electrical double-layer capacitor (EDLC). A few oxidation/reduction peaks have been observed due to the faradaic materials (POMs) that help to exhibit excellent electrochemical reversibility of these electrodes (Jiang et al. 2016). Notably, the AC-MnV₁₁ electrode showed the highest specific capacitance of 479.73 F g⁻¹ at 0.6 A g⁻¹ current density (**Fig. 8.9a**). Similarly, the AC-MnV₁₃ electrode exhibited a specific capacitance of 357.33 F g⁻¹ at the same current density (**Fig. 8.9b**). The higher capacitance value of the AC-MnV₁₁ electrode

might be due to the enhancement of electrical conductivity from the association with MnV_{11} , making ion transportation faster. Moreover, upon decreasing the current densities, the surface charge diffusion of the electrolyte ions through the porous AC surface increases and eventually yields higher capacitance and energy. Nonetheless, we have observed that the AC- MnV_{11} hybrid material steadily decreases its capacitance by 66.64% (from 479.73 to 160 F g^{-1}), increasing the current densities from 0.6 to 10 A g^{-1} . Likewise, the AC- MnV_{13} electrode showed a fast declination of the capacitance up to 63.56% (from 357.33 to 130.20 F g^{-1}) from 0.4 to 10 A g^{-1} . The relative capacitance retention with increasing the current density is displayed in **Fig. 8.9c**, which indicates a superior rate capability for both electrode materials.

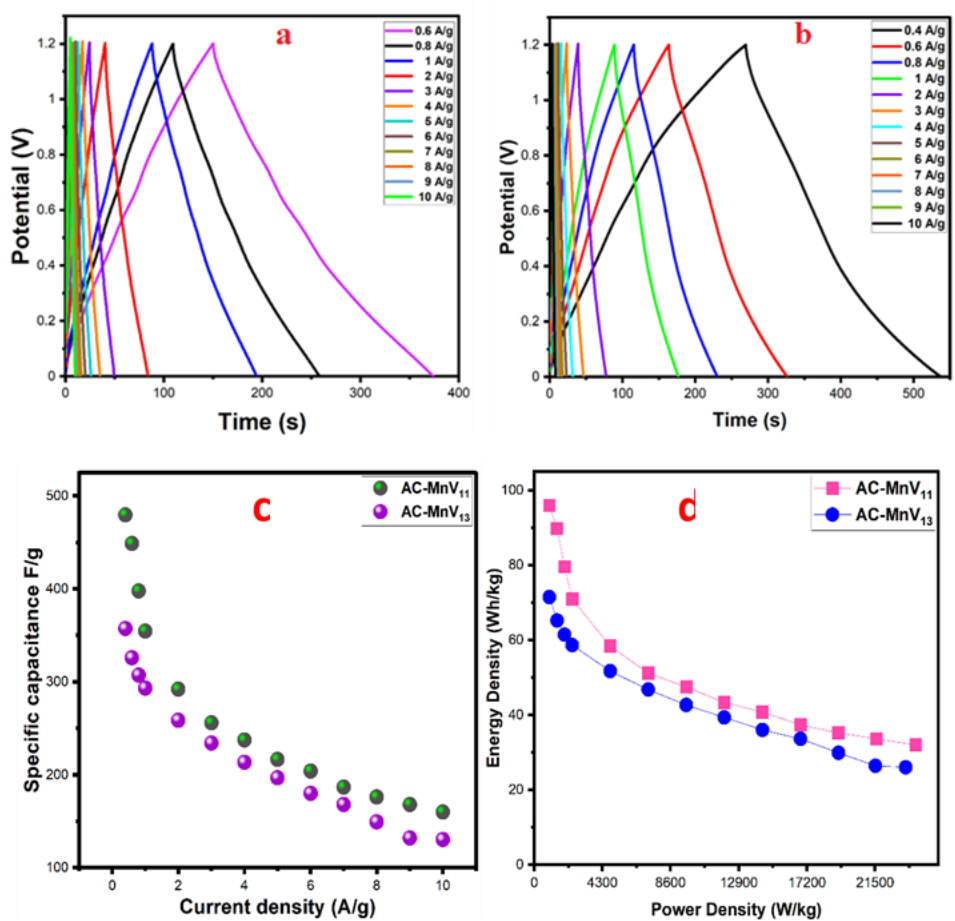


Fig. 8.9 Galvanic charge-discharge curves of (a) AC-MnV₁₁ and (b) AC-MnV₁₃-based SCs at different current densities, c) capacitance retention vs current density, and d) Ragone plot (Specific Energy vs Power) for AC-MnV₁₁ and AC-MnV₁₃ electrodes.

The specific energy and power were calculated using **Equations (2.5)** and **(2.4)**. High specific energy and power are desired for SCs electrode materials. In this study, the AC-MnV₁₁ and AC-MnV₁₃ showed specific energy and power of 95.95, 71.46 Wh kg⁻¹, and 960.00, 959.91 W kg⁻¹, respectively at 0.6 and 0.4 A g⁻¹ current density. Furthermore, even at a higher specific current (10 A g⁻¹), electrodes showed specific energy of 32.0, 26.04 Wh kg⁻¹ at a higher specific power of 24075.00, and 23436.00 W kg⁻¹, exhibiting excellent electrochemical features of the two electrodes. Lately, Mal et al. reported that the graphene oxide-supported MnV₁₃ composite displayed specific energy of 37.38 Wh kg⁻¹ (1M LiCl) and 53.75 Wh kg⁻¹ (1M Na₂SO₄), respectively, based on the CV plot (Zhu et al. 2018). The values are considerably lower than the current electrodes-based SCs. The excellent value of specific capacitance, energy, and power is mainly due to the redox ability of MnV₁₁ and MnV₁₃. A Ragone (specific Energy vs. Power) plot is illustrated in **Fig. 8.9d** and displays that the AC-MnV₁₁ exhibits higher specific energy than the other electrodes.

8.2.3 EIS studies

Nyquist plots of AC-MnV₁₁ and AC-MnV₁₃-based SCs are depicted in **Fig. 8.10**. To further evaluate the device performance, the electrochemical impedance spectroscopic (EIS) was studied for both the electrodes in the frequency ranging from 0.01 Hz to 10000 Hz with a dc potential of 0.01V at a low amplitude of dc potential to estimate the power-cell impedance at a varying frequency (Huang et al. 2019). The AC-MnV₁₁ electrode shows lower ESR values of 3.38 Ω than the AC-MnV₁₃ electrode of 5.45. This could be the ionic conductivity of AC-MnV₁₁ higher than that of the AC-MnV₁₃ composite. The charge transfer resistance (R_{ct}) illustrates the semicircle diameter resulting from the reversible redox reaction within the electrode materials. Higher the arch diameter signifies higher charge transfer resistance and storing or discharging the lower amount of charge (Miras et al. 2012). However, minimal resistance is expected for a high-performing electric device

for better performance. The charge transfer resistance (circuit resistance, R_{ct}) is higher for AC-MnV₁₃ (4.13 Ω) than the AC-MnV₁₁ (2.14 Ω) electrode, implying the higher specific conductance of AC-MnV₁₁. Moreover, the AC-MnV₁₁ electrode shows a steeper verticle (f_k) line at a low-frequency regime, indicating enhanced electrical conductivity and rapid charge kinetics than the AC-MnV₁₃.

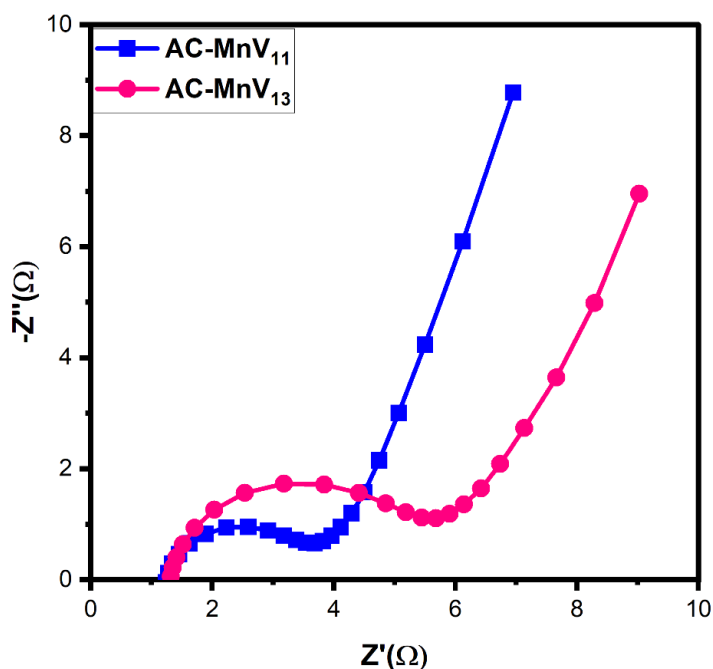


Fig. 8.10 Nyquist Plot for AC-MnV₁₁ and AC-MnV₁₃ composites.

About 42 mg of AC-MnV₁₁ was coated on three pairs of carbon clothes (4 cm \times 4 cm) following the above-mentioned fabrication method to examine the possible applications. After charging with an electrochemical workstation, this setup was appropriate for light-up red (1.8 V) and yellow (2.0-2.3 V) LEDs (**Fig. 8.11A, B**). The LED was kept glowing for 65 s (red) and 30s (yellow), removing the device's energy upon discharging. Likewise, the AC-MnV₁₃ electrode has been used in the same setup. It could light up red (1.8 V) and blue (3.5 V) LED and, upon discharging, the LED to glow for the period of 80 s (red) and 10 s (blue), respectively, using 143mg material.

The equivalent circuit for AC-MnV₁₁ electrode material is documented in **Fig. 8.11C**. C₁ and C₂= C; similarly, R₁ and R₂ = R_{ct} with W denoting the Warburg Impedance.

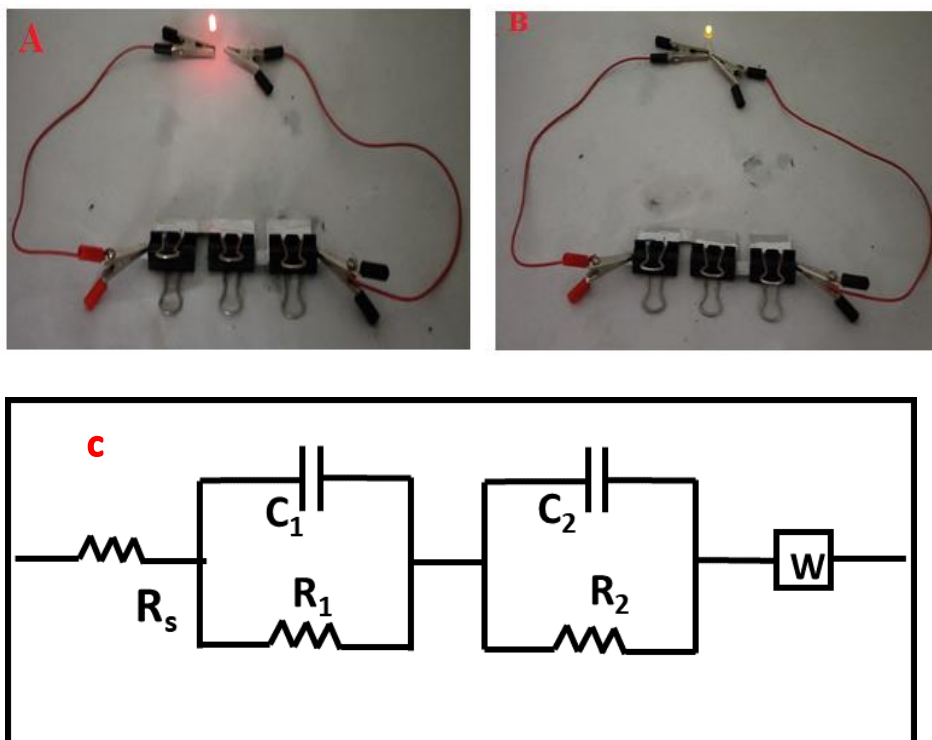


Fig. 8.11(A) and (B) are the fabricated SCs that are energizing red and yellow light-emitting diodes by AC-MnV₁₁ composite, (C) The equivalent circuit is used for fitting the Nyquist plots.

8.2.4 Cycle stability studies

Cycle stability is another important parameter for energy storage devices. High cycle stability is the desire for any electronic device to maintain its cost. All electrode material cycle stability was studied using 0.1 M H₂SO₄ aqueous electrolyte at a 10A g⁻¹ current density in **Fig. 8.12**. As shown in **Fig. 8.12**, the MnV₁₁ doped on AC, AC-MnV₁₁ electrode retains about 95.93% of its original capacitance after 10000 cycles as long-term electrochemical stability. However, the AC-MnV₁₃ electrode displayed 83.32 % retentions after 10000 cycles, respectively which signify the changing of the hierarchical structure of

the electrode material. The improved cycle stability of AC-MnV₁₁ nanohybrid is because of the strong electrostatic interaction of MnV₁₁ with AC, which might increase cycle stability. The pure POMs MnV₁₁ and MnV₁₃ are less stable than composites because the POMs are leaching from the electrode.

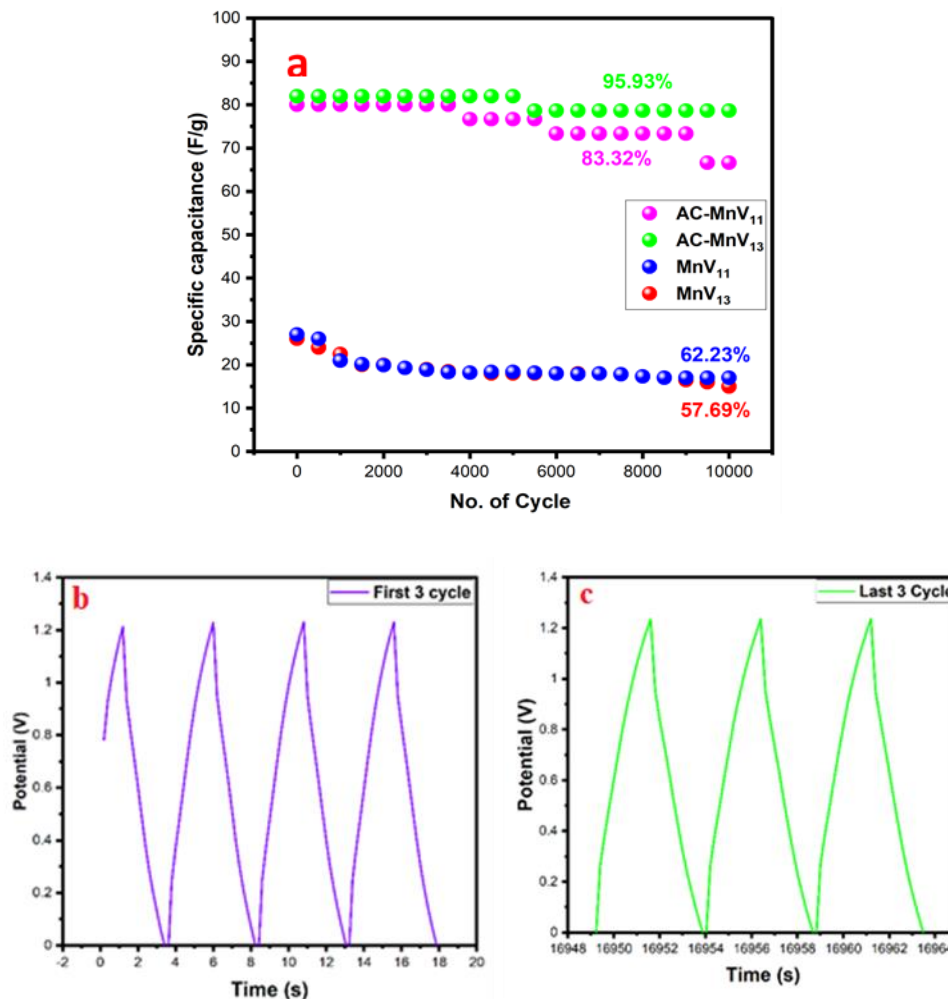
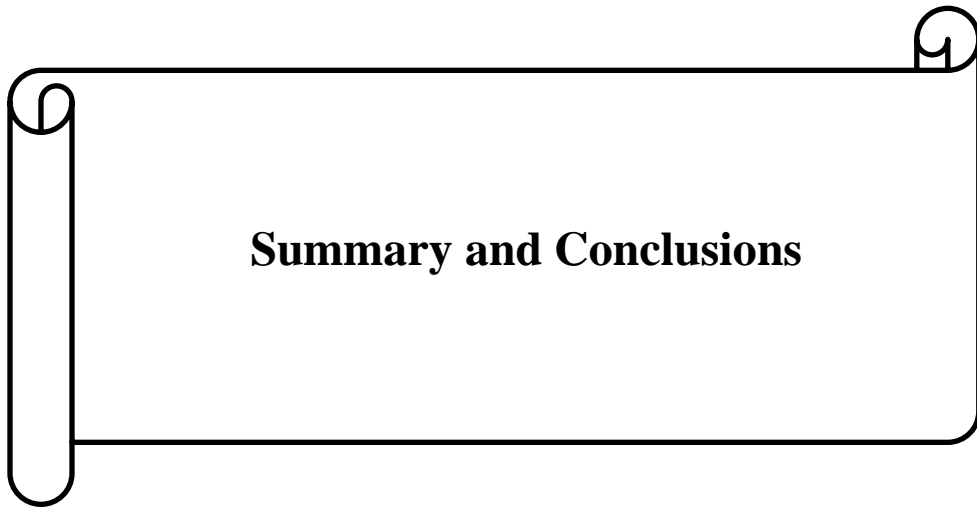


Fig. 8.12 a) cycle stability of AC-MnV₁₁, AC-MnV₁₃, MnV₁₁ and MnV₁₃ stability response of (b) first cycle of AC-MnV₁₁, and (b) last cycle of AC-Mn₁₁ over 10000 cycles at a fixed current density of 10 A g⁻¹.

CHAPTER 9



Summary and Conclusions

9.1 Summary

In brief, the present study reports the successful doping of two distinct polyoxometalates, namely $H_5[PVMo_{11}O_{40}]$ and $H_4[PV_2Mo_{10}O_{40}]$, into the conducting polypyrrole backbone unit using a facile synthesis approach, resulting in the formation of PPy- $H_5[PVMo_{11}O_{40}]$ and PPy- $H_4[PV_2Mo_{10}O_{40}]$ nanohybrid electrodes. The PPy- $H_4[PV_2Mo_{10}O_{40}]$ compound has been demonstrated as a promising candidate for utilisation as electrode materials in supercapacitors. The supercapacitor electrode composed of PPy- $H_4[PV_2Mo_{10}O_{40}]$ demonstrates a notable capacitance of 561.01 F g^{-1} when tested in a $0.1M \text{ H}_2\text{SO}_4$ solution at a current density of 0.2 A g^{-1} . Additionally, the electrode displays an improved energy density of 19.8 Wh Kg^{-1} and a power density of $780.10W \text{ Kg}^{-1}$. Moreover, the identical electrode exhibits remarkable cycle durability, maintaining approximately 95% of its capacitance after undergoing 4500 cycles.

Subsequently, a facile and effective one-pot synthetic approach was employed to fabricate two novel hybrid composite materials (PIn/PV Mo_{11} and PIn/PV Mo_{10}) using identical polyoxometalates (POMs) for the purpose of supercapacitor applications. Furthermore, the electrochemical investigations were conducted using a device configuration consisting of two electrodes. The PIn/PV Mo_{11} and PIn/PV Mo_{10} materials demonstrate an enhanced specific capacitance measurement of 177.36 and 198.54 F g^{-1} , respectively, when tested in a $0.25M \text{ H}_2\text{SO}_4$ solution. The electrochemical faradic charge storage performance of PIn/PV Mo_{10} is superior to that of PIn/PV Mo_{11} . This difference in performance may be due to the higher conductivity of PIn/PV Mo_{10} compared to PIn/PV Mo_{11} . Additionally, the electrode material of PIn/PV Mo_{10} exhibits good reversibility. The electrode exhibits a notable energy density of 10.19 Wh Kg^{-1} and satisfactory cycle stability even after undergoing 10000 cycles at a current density of 4 A g^{-1} .

Afterwards, a chemical bath deposition technique was employed to introduce doping into $H_5[PV_2Mo_{10}O_{40}]$ and $H_4[PVMo_{11}O_{40}]$ polyoxometalates (POMs) on the conductive polyaniline (PAni) electrode, resulting in the formation of $PVMo_{11}@PAni$ and $PV_2Mo_{10}@PAni$ composites. The electrode denoted as $PVMo_{11}@PAni$ exhibits a notable capacitance of 1371 F g^{-1} and an exceptional energy density of 137.5 Wh kg^{-1} when subjected to a current density of 3 A g^{-1} . According to the EIS plots, it was observed that the $PVMo_{11}@PAni$ electrode material exhibits a higher degree of capacitive behaviour in comparison to the other electrode materials. The electrode materials denoted as $PVMo_{11}@PAni$ exhibited a specific capacitance retention of 94.83% throughout 4500 charge and discharge cycles. Furthermore, in terms of device application, the $PVMo_{11}@PAni$ electrode demonstrates the highest total capacitance value of 72.3 mF, indicating its potential suitability for employment in a compact storage device. Subsequently, the pragmatic utilisation of the artificially produced $PVMo_{11}@PAni$ supercapacitor was assessed, and it demonstrated the ability to effectively illuminate LED lights.

The next chapter demonstrates an overview of the polyoxometalate ($K_5H_2[PV_4W_8O_{40}]\cdot 11H_2O$), PV_4W_8 , which is a metal-oxide cluster. This cluster was incorporated into the polypyrrole (PPy) matrix to address the stability concerns associated with the polymer. Consequently, a novel PV_4W_8/PPy (symmetric) composite electrode was developed and reported. However, the introduction of PV_4W_8 onto the surface of the conductive PPy matrix has been shown to enhance ion transfer efficiency. The PV_4W_8 -PPy/PPy composite exhibits exceptional electrochemical properties, attributed to its elevated conductivity and abundant porosity, resulting in a specific capacitance of 291 F g^{-1} . This value rises above those of PPy (90.01 F g^{-1}) and PV_4W_8 (39.03 F g^{-1}) at a current density of 0.4 A g^{-1} . Moreover, the electrodes exhibit an energy density of 16.4 Wh kg^{-1} in contrast to alternative electrode materials. The asymmetric electrodes exhibited exceptional stability and introduced a novel aspect in the realm of supercapacitor applications. The electrode

exhibited sustained illumination of a red and yellow LED bulb for a duration exceeding one minute.

The next part discusses the comparative analysis of two distinct supporting-POM composites by utilizing a two-electrode symmetric device system. The hierarchical structure is exclusively affected by CPs during the charging and discharging process, resulting in the initiation of swelling. The integration of polyoxometalates (POM) into the cathode protection (CP) system is expected to enhance the electrode material's stability. The present study is centered on a comparative analysis of two recently produced composites, both of which contain the identical polyoxometalate ($\text{K}_5\text{H}_2[\text{PV}_4\text{W}_8\text{O}_{40}]\cdot 11\text{H}_2\text{O}$, (PV_4W_8)) that has been integrated into a matrix of polyaniline (PANI) and activated carbon (AC). The PANI- PV_4W_8 and AC- PV_4W_8 were synthesized using a single-step reaction, and the function of PV_4W_8 was examined. Despite the larger surface area of AC, the PANI- PV_4W_8 composite demonstrated a superior specific capacitance of 584.32 F g^{-1} at 0.8 A g^{-1} , in contrast to the AC- PV_4W_8 composite, which exhibited a specific capacitance of 62.40 Fg^{-1} . The observed phenomenon may be attributed to the intrinsic pseudocapacitive nature of PANI, which is believed to augment its capacitance. The PANI- PV_4W_8 composite exhibits energy and power densities of 81.16 Wh Kg^{-1} and 1598.9 W Kg^{-1} , respectively. The cyclic voltammetry measurement indicated a retention rate of 93.13% after 4500 cycles, with a scan rate of 500 mV s^{-1} , as demonstrated by the composite. Hence, it can be inferred that the PANI- PV_4W_8 composite synthesized has the potential to serve as a favourable electrode material in the production of supercapacitors with greater power and energy density. Nevertheless, it is noteworthy that the conductivity of both AC- PV_4W_8 and PANI- PV_4W_8 electrodes surpasses that of PV_4W_8 in its pure form. The PANI- PV_4W_8 electrode materials exhibit a symmetric device that demonstrates a persistent luminescence with red and yellow colour LED bulbs for a duration exceeding one minute, thereby exhibiting potential as a viable material for supercapacitors.

Finally, two different polyoxovanadates derivatives, $\text{K}_5\text{Mn}^{\text{IV}}\text{V}_{11}\text{O}_{32}\cdot 10 \text{ H}_2\text{O}$ (MnV_{11}) and $\text{K}_7\text{Mn}^{\text{IV}}\text{V}_{13}\text{O}_{38}\cdot 18\text{H}_2\text{O}$ (MnV_{13}) have been studied to evaluate their electrochemical

performance. These polyoxovanadates were deposited on activated carbon (AC) to prepare AC-MnV₁₁ and AC-MnV₁₃ composites. The electrochemical performance of the AC-MnV₁₁ electrode exhibits the remarkable specific capacitance of 479.73 F g⁻¹ at a current density of 0.6 A g⁻¹, along with incredible specific power and energy of 960 W kg⁻¹. Likewise, the AC-MnV₁₃ exhibits a specific capacitance of 357.33 F g⁻¹ at the current density of 0.6 A g⁻¹ with a specific energy of 71.46 Wh kg⁻¹. Interestingly, the AC-MnV₁₁ could light up the red and yellow color LED bulbs for a duration of 80 and 60 s, respectively, indicating a considerable specific power of the material. The AC-MnV₁₃ electrode shows significantly less lighting up during the 65 and 30 s periods with red and yellow LED bulbs.

9.2 Conclusions

- The formation of PPy-H₄[PVMo₁₁O₄₀] and PPy-H₅[PV₂Mo₁₀O₄₀] provided two novel electrode materials for SC applications. It is observed that PPy-H₅[PV₂Mo₁₀O₄₀] vanadomolybdate demonstrates the highest specific capacitance, energy density, power density, and stability due to the fast multi-electron redox property between the POM and polypyrrole.
- One-pot synthesis of vanadomolybdate and indole polymer results in the two novel nanohybrids PIn/PVMo₁₁ and PIn/PV₂Mo₁₀, which proves the improvement in the stability of the polyindole.
- The facile and one-pot *in-situ* polymerization of polyaniline via vanadomolybdates enhances the pseudocapacitance and increases the multiple-proton exchange between composite and electrolyte. The presence of vanadomolybdates throughout the polyaniline backbone results in high energy density.
- PV₄W₈ was successfully impregnated on the PPy matrix (PV₄W₈/PPy) (symmetric) by a simple *in-situ* chemical reaction method. The electrode PV₄W₈-PPy/PPy (asymmetric) displays excellent electrochemical performance due to its high

conductivity and rich porosity. The asymmetric electrodes showed very high stability and provided a new dimension to the supercapacitor applications.

- The pseudocapacitive electrode material (PANI-PV₄W₈) and hybrid electrode material (AC-PV₄W₈) prove that PANI-PV₄W₈ owing maximum results due to its faradic reaction of PANI and PV₄W₈. But AC-PV₄W₈ provides fewer results because the abundance of activated carbon micro and mesopores facilitates the polyanion's adsorption, reducing the interface transportation path for the ions.
- A simple deposition method was used to deposit MnV₁₁ and MnV₁₃ on a high surface area of AC as AC-MnV₁₁ and AC-MnV₁₃, confirmed by various analytical techniques. Two different vanadium-substituted POMs on the surface of AC enhance the pseudocapacitance and create macropores for a better electrolyte ion diffusion mechanism, showing incredible capacitance value.

9.3 Scope for future work

- Ternary composites can be prepared with different vanadium-substituted polyoxometalates from kegging family, which are not reported in this thesis.
- Other polyoxometalate family molecules can be synthesized and dop with various conducting polymers, which can be a novel material for future studies.
- POMs and deposits on the surface of the conducting polymer nanotubes are not reported in this thesis.
- A combination of conducting polymer and other carbonaceous materials can be used.

List of Publications

1. **Vannathan, A. A.**, Maity, S., Kella, T., Shee, D., Das, P. P., & Mal, S. S. (2020). In situ vanadophosphomolybdate impregnated into conducting polypyrrole for supercapacitor. *Electrochimica Acta*, 364, 137286.
2. **Vannathan, A. A.**, Kella, T., Shee, D., & Mal, S. S. (2021). One-pot synthesis of polyoxometalate decorated polyindole for energy storage supercapacitors. *ACS omega*, 6(17), 11199-11208.
3. **Vannathan, A. A.**, Chandewar, P. R., Shee, D., & Mal, S. S. (2022). Asymmetric polyoxometalate-polypyrrole composite electrode material for electrochemical energy storage supercapacitors. *Journal of Electroanalytical Chemistry*, 904, 115856.
4. **Vannathan, A. A.**, Kella, T., Shee, D., & Mal, S. S. (2022). Investigations of redox-active polyoxomolybdate embedded polyaniline-based electrode material for energy application. *Ionics*, 1-16.
5. **Vannathan, A. A.**, Chandewar, P. R., Shee, D., & Mal, S. S. (2022). Polyoxovanadate-Activated Carbon-Based Hybrid Materials for High-Performance Electrochemical Capacitors. *Journal of The Electrochemical Society*, 169(5), 050538.
6. **Vannathan, A. A.**, Chandewar, P. R., Shee, D., & Mal, S. S. (2023). Polyoxometalate ($[PV_4W_8O_{40}]^{7-}$) integrated into polyaniline and activated carbon-based electrodes for high-performance electrochemical supercapacitors. (**under review**)

Journal publications from other projects

- **Vannathan, A. A.**, Thakre, D., Ali, S. R., De, M., Banerjee, A., & Mal, S. S. (2021). Investigations into the supercapacitor activity of bisphosphonate-polyoxovanadate compounds. *Journal of Solid State Chemistry*, 304, 122566.
- P K, M. A., **Vannathan, A. A.**, Kella, T., Shee, D., & Mal, S. S. (2021). Organic cation linkers polyoxomolybdate-polypyrrole nanocomposite-based supercapacitors. *Ionics*, 27(9), 4023-4035.

- Thakre, D., **Anandan Vannathan, A.**, Banerjee, A., & Mal, S. S. (2022). Supercapacitor activity studies of a unique triangular oxo-vanadate-bisphosphonate composite with activated carbon. *Ionics*, 1-10
- Kumari, S., Maity, S., **Vannathan, A. A.**, Shee, D., Das, P. P., & Mal, S. S. (2020). Improved electrochemical performance of graphene oxide supported vanadomanganate (IV) nanohybrid electrode material for supercapacitors. *Ceramics International*, 46(3), 3028-3035.
- Marques-da-Silva, D., Fraqueza, G., Lagoa, R., **Vannathan, A. A.**, Mal, S. S., & Aureliano, M. (2019). Polyoxovanadate inhibition of Escherichia coli growth shows a reverse correlation with Ca²⁺-ATPase inhibition. *New Journal of Chemistry*, 43(45), 17577-17587.
- Maity, S., **Vannathan, A. A.**, Kella, T., Shee, D., Das, P. P., & Mal, S. S. (2021). Electrochemical performance of activated carbon-supported vanadomolybdates electrodes for energy conversion. *Ceramics International*, 47(19), 27132-27141.
- Anees, P. M., **Vannathan, A. A.**, Abhijith, M. B., Kella, T., Shee, D., & Mal, S. S. (2022). Imidazolium cation linkers of polyoxomolybdate-polypyrrole nanocomposite electrode-based energy storage supercapacitors. *Materials Chemistry and Physics*, 277, 125441.
- Maity, S., **Vannathan, A. A.**, Kumar, K., Das, P. P., & Mal, S. S. (2021). Enhanced Power Density of Graphene Oxide–Phosphotetradecavanadate Nanohybrid for Supercapacitor Electrode. *Journal of Materials Engineering and Performance*, 30(2), 1371-1377.
- Maity, S., **Vannathan, A. A.**, Chandewar, P. R., Shee, D., Das, P. P., & Mal, S. S. (2022). Vanadomanganate as a synergistic component in high-performance symmetric supercapacitor. *Journal of Alloys and Compounds*, 899, 163239.
- Banik, S., Melanthota, S. K., **Vannathan, A. A.**, Mahato, K. K., Mal, S. S., & Mazumder, N. (2022). Spectroscopic methods for assessment of hand sanitizers. *Chemical Papers*, 1-12.

Patents

1. Method of preparation of high energy density conducting polyaniline-phosphovanadomolybdate nanohybrid electrode for supercapacitor device application (Sib Sankar Mal and **Anjana Anandan Vannathan**), India patent application no. 202041047969 dated 03/11/2020
2. A high-performance supercapacitor device of polyaniline-triethyl amine ionic liquid combined phosphomolybdate electrode and method thereof (Sib Sankar Mal, Saikat Dutta, **Anjana Anandan Vannathan**, Muhammed Anees P K), Filed India patent application no. 202141007885 dated 24/02/2021

Workshops and Conferences Attended

- Participation in one day National Workshop on “Recent Advances In Material Chemistry (RAMC)” on Sep 26, 2019, held at NITK, Surathkal.
- Poster Presentation in International Conference on Advances in Chemical and Material Science during Oct 17-19, 2019, held at Department of Chemistry, Mangalore University.
- Participated and presented a research paper in an International Conference on “Energy and Environmental Technologies for Sustainable Development (CHEM-fulx20)” During Feb 14-15, 2020, held at MNNIT Allahabad, Prayagraj.
- Best oral presentation during Sustainable and Green Technologies session in an International Conference on “Energy and Environmental Technologies for Sustainable Development (CHEM-fulx20)” During Feb 14-15, 2020 held at MNNIT Allahabad, Prayagraj.
- participated in the five-day e-workshop titled “Advancements in the Molecular World: Materials and Catalysis” (AMWMC-2021) conducted by the Department of Chemistry, NITK Surathkal during February 15-19, 2021.

- Participated and presented a research paper in a (Virtual Conference) SRM Institute of Science and Technology International Conference on Nanoscience and Nanotechnology (ICONN 2021) organized by Department of Physics and Nanotechnology, SRM IST, India during February 01 – 03, 2021
- First International Conference on Technologies for Smart Green Connected Society 2021 29th-30th November 2021 | Online | World Wide.

References

- Adhikari, A. D., Oraon, R., Tiwari, S. K., Saren, P., Lee, J. H., Kim, N. H., and Nayak, G. C. (2018). “CdS-CoFe₂O₄@Reduced Graphene Oxide Nanohybrid: An Excellent Electrode Material for Supercapacitor Applications.” *Ind. Eng. Chem. Res.*, 57(5), 1350–1360.
- Akba, O., Güzel, F., Yurdakoc, K., Gümgüm, B., and Tez, Z. (1997). “Preparation and Characterization of Polyoxometallates of Molybdenum, Tungsten and Their Salts.” *Synthesis and Reactivity in Inorganic and Metal-Organic Chemistry*, 27(9), 1399–1415.
- Anandan Vannathan, A., Chandewar, P. R., Shee, D., and Sankar Mal, S. (2022). “Asymmetric polyoxometalate-polypyrrole composite electrode material for electrochemical energy storage supercapacitors.” *Journal of Electroanalytical Chemistry*, 904, 115856.
- Anjitha, T., Anilkumar, T., Mathew, G., and Ramesan, M. T. (2019). “Zinc ferrite @ polyindole nanocomposites: Synthesis, characterization and gas sensing applications.” *Polym. Compos.*, 40(7), 2802–2811.
- Barth, M., Lapkowski, M., and Lefrant, S. (1999). “Electrochemical behaviour of polyaniline films doped with heteropolyanions of Keggin structure.” *Electrochimica Acta*, 44(12), 2117–2123.
- Basnayaka, P. A., and Ram, M. K. (2017). “A Review of Supercapacitor Energy Storage Using Nanohybrid Conducting Polymers and Carbon Electrode Materials.” *Conducting Polymer Hybrids*, Springer Series on Polymer and Composite Materials, V. Kumar, S. Kalia, and H. C. Swart, eds., Cham: Springer International Publishing, 165–192.
- Benadji, S., Eloy, P., Léonard, A., Su, B. L., Bachari, K., Rabia, C., and Gaigneaux, E. M. (2010). “Preparation and characterization of HMS supported 11-molybdo-vanadophosphoric acid for selective oxidation of propylene.” *Microporous and Mesoporous Materials*, 130(1–3), 103–114.

- Boudjema, S., Vispe, E., Choukchou-Braham, A., Mayoral, J. A., Bachir, R., and Fraile, J. M. (2015). "Preparation and characterization of activated montmorillonite clay supported 11-molybdo-vanado-phosphoric acid for cyclohexene oxidation." *RSC Adv.*, 5(9), 6853–6863.
- Cao, W. J., and Zheng, J. P. (2012). "Li-ion capacitors with carbon cathode and hard carbon/stabilized lithium metal powder anode electrodes." *Journal of Power Sources*, 213, 180–185.
- Chandran, M., Thomas, A., Raveendran, A., Vinoba, M., and Bhagiyalakshmi, M. (2020). "MoS₂ Confined MXene Heterostructures as Electrode Material for Energy Storage Application." *Journal of Energy Storage*, 30, 101446.
- Chandrasekhar, P., and Gumbs, R. W. (1991). "Electrosyntheses, Spectroelectrochemical, Electrochemical, and Chronovoltabsorptometric Properties of Family of Poly (Aromatic Amines), Novel Processible Conducting Polymers: I . Poly(Benzidines)." *J. Electrochem. Soc.*, 138(5), 1337–1346.
- Chen, H.-Y., Al-Oweini, R., Friedl, J., Lee, C. Y., Li, L., Kortz, U., Stimming, U., and Srinivasan, M. (2015). "A novel SWCNT-polyoxometalate nanohybrid material as an electrode for electrochemical supercapacitors." *Nanoscale*, 7(17), 7934–7941.
- Chen, K., and Xue, D. (2016). "Colloidal supercapacitor electrode materials." *Materials Research Bulletin*, 83, 201–206.
- Chen, T., and Dai, L. (2013). "Carbon nanomaterials for high-performance supercapacitors." *Materials Today*, 16(7–8), 272–280.
- Chen, W.-C., Wen, T.-C., and Teng, H. (2003). "Polyaniline-deposited porous carbon electrode for supercapacitor." *Electrochimica Acta*, 48(6), 641–649.
- Cheng, D., Li, B., Sun, S., Zhu, L.-J., Li, Y., Wu, X.-L., and Zang, H.-Y. (2021). "Proton-Conducting Polyoxometalates as Redox Electrolytes Synergistically Boosting the Performance of Self-Healing Solid-State Supercapacitors with Polyaniline." *CCS Chem.*, 3(3), 1649–1658.

- Cheng, Q., Tang, J., Shinya, N., and Qin, L.-C. (2013). "Polyaniline modified graphene and carbon nanotube composite electrode for asymmetric supercapacitors of high energy density." *Journal of Power Sources*, 241, 423–428.
- Chiang, C. K., Fincher, C. R., Park, Y. W., Heeger, A. J., Shirakawa, H., Louis, E. J., Gau, S. C., and MacDiarmid, A. G. (1978). "Electrical Conductivity in Doped Polyacetylene." *Phys. Rev. Lett.*, 40(22), 1472–1472.
- Chitte, H. K., Shinde, G. N., Bhat, N. V., and Walunj, V. E. (2011). "Synthesis of Polypyrrole Using Ferric Chloride (FeCl_3) as Oxidant Together with Some Dopants for Use in Gas Sensors." *JST*, 01(02), 47–56.
- Choi, K. M., Kim, C. Y., and Kim, K. H. (1992). "Polymerization mechanism and physicochemical properties of electrochemically prepared polyindole tetrafluoroborate." *J. Phys. Chem.*, 96(9), 3782–3788.
- Choudhary, R. B., Ansari, S., and Purty, B. (2020). "Robust electrochemical performance of polypyrrole (PPy) and polyindole (PIn) based hybrid electrode materials for supercapacitor application: A review." *Journal of Energy Storage*, 29, 101302.
- Conte, M. (2010). "Supercapacitors Technical Requirements for New Applications." *Fuel Cells*, 10(5), 806–818.
- Conway, B. E. (2013). *Electrochemical supercapacitors: scientific fundamentals and technological applications*. Springer Science & Business Media.
- Cuentas-Gallegos, A. K., Lira-Cantú, M., Casañ-Pastor, N., and Gómez-Romero, P. (2005). "Nanocomposite Hybrid Molecular Materials for Application in Solid-State Electrochemical Supercapacitors." *Adv. Funct. Mater.*, 15(7), 1125–1133.
- Dhawale, D. S., Salunkhe, R. R., Jamadade, V. S., Dubal, D. P., Pawar, S. M., and Lokhande, C. D. (2010). "Hydrophilic polyaniline nanofibrous architecture using electrosynthesis method for supercapacitor application." *Current Applied Physics*, 10(3), 904–909.
- Dhibar, S., Bhattacharya, P., Hatui, G., Sahoo, S., and Das, C. K. (2014). "Transition metal-doped polyaniline/single-walled carbon nanotubes nanocomposites: efficient electrode

- material for high performance supercapacitors.” *ACS Sustainable Chemistry & Engineering*, 2(5), 1114–1127.
- Dhibar, S., Sahoo, S., and Das, C. K. (2013). “Copper chloride-doped polyaniline/multiwalled carbon nanotubes nanocomposites: Superior electrode material for supercapacitor applications.” *Polym Compos*, 34(4), 517–525.
- Diaz, A. F., and Logan, J. A. (1980). “Electroactive polyaniline films.” *Journal of Electroanalytical Chemistry and Interfacial Electrochemistry*, 111(1), 111–114.
- Dubal, D. P., Ballesteros, B., Mohite, A. A., and Gómez-Romero, P. (2017a). “Functionalization of Polypyrrole Nanopipes with Redox-Active Polyoxometalates for High Energy Density Supercapacitors.” *ChemSusChem*, 10(4), 731–737.
- Dubal, D. P., Chodankar, N. R., Vinu, A., Kim, D.-H., and Gomez-Romero, P. (2017b). “Asymmetric Supercapacitors Based on Reduced Graphene Oxide with Different Polyoxometalates as Positive and Negative Electrodes.” *ChemSusChem*, 10(13), 2742–2750.
- Flynn, C. M., and Pope, M. T. (1970a). “1:13 Heteropolyvanadates of manganese(IV) and nickel(IV).” *J. Am. Chem. Soc.*, 92(1), 85–90.
- Flynn, C. M., and Pope, M. T. (1970b). “Heteropolyvanadomanganates(IV) with Mn:V=1:11 and 1:4.” *Inorg. Chem.*, 9(9), 2009–2014.
- Forouzandeh, P., Ganguly, P., Dahiya, R., and Pillai, S. C. (2022). “Supercapacitor electrode fabrication through chemical and physical routes.” *Journal of Power Sources*, 519, 230744.
- Gao, Y., Gao, R., Zhang, G., Zheng, Y., and Zhao, J. (2018). “Oxidative desulfurization of model fuel in the presence of molecular oxygen over polyoxometalate based catalysts supported on carbon nanotubes.” *Fuel*, 224, 261–270.
- Genovese, M., and Lian, K. (2017). “Polyoxometalates.” *Metal Oxides in Supercapacitors*, Elsevier, 133–164.
- Gómez Costa, M. B., Juárez, J. M., Martínez, M. L., Cussa, J., and Anunziata, O. A. (2012). “Synthesis and characterization of a novel composite: Polyindole included in

- nanostructured Al-MCM-41 material.” *Microporous and Mesoporous Materials*, 153, 191–197.
- Gómez-Romero, P., Chojak, M., Cuentas-Gallegos, K., Asensio, J. A., Kulesza, P. J., Casañ-Pastor, N., and Lira-Cantú, M. (2003). “Hybrid organic–inorganic nanocomposite materials for application in solid state electrochemical supercapacitors.” *Electrochemistry Communications*, 5(2), 149–153.
- González, A., Goikolea, E., Barrena, J. A., and Mysyk, R. (2016). “Review on supercapacitors: Technologies and materials.” *Renewable and Sustainable Energy Reviews*, 58, 1189–1206.
- Halper, M. S., and Ellenbogen, J. C. (2006). “Supercapacitors: A brief overview.” *The MITRE Corporation, McLean, Virginia, USA*, 1.
- Herrmann, S., Aydemir, N., Nägele, F., Fantauzzi, D., Jacob, T., Travas-Sejdic, J., and Streb, C. (2017). “Enhanced Capacitive Energy Storage in Polyoxometalate-Doped Polypyrrole.” *Adv. Funct. Mater.*, 27(25), 1700881.
- Hou, R., Miao, M., Wang, Q., Yue, T., Liu, H., Park, H. S., Qi, K., and Xia, B. Y. (2020). “Integrated Conductive Hybrid Architecture of Metal–Organic Framework Nanowire Array on Polypyrrole Membrane for All-Solid-State Flexible Supercapacitors.” *Adv. Energy Mater.*, 10(1), 1901892.
- Hu, C., Zhao, E., Nitta, N., Magasinski, A., Berdichevsky, G., and Yushin, G. (2016). “Aqueous solutions of acidic ionic liquids for enhanced stability of polyoxometalate-carbon supercapacitor electrodes.” *Journal of Power Sources*, 326, 569–574.
- Huang, B., Wang, W., Pu, T., Li, J., Zhao, C., Xie, L., and Chen, L. (2019). “Rational design and facile synthesis of two-dimensional hierarchical porous M₃V₂O₈ (M = Co, Ni and Co–Ni) thin sheets assembled by ultrathin nanosheets as positive electrode materials for high-performance hybrid supercapacitors.” *Chemical Engineering Journal*, 375, 121969.
- Iordache, I., Gheorghe, A. V., and Iordache, M. (2013). “Towards a hydrogen economy in Romania: Statistics, technical and scientific general aspects.” *International Journal of Hydrogen Energy*, 38(28), 12231–12240.
-

- Iro, Z. S., Subramani, C., and Dash, S. S. (2016). "A brief review on electrode materials for supercapacitor." *Int. J. Electrochem. Sci*, 11(12), 10628–10643.
- Jain, A., and Tripathi, S. K. (2015). "Nano-porous activated carbon from sugarcane waste for supercapacitor application." *Journal of Energy Storage*, 4, 121–127.
- Jamadade, V. S., Dhawale, D. S., and Lokhande, C. D. (2010). "Studies on electrosynthesized leucoemeraldine, emeraldine and pernigraniline forms of polyaniline films and their supercapacitive behavior." *Synthetic Metals*, 160(9–10), 955–960.
- Jiang, Y., Chen, L., Zhang, H., Zhang, Q., Chen, W., Zhu, J., and Song, D. (2016). "Two-dimensional Co₃O₄ thin sheets assembled by 3D interconnected nanoflake array framework structures with enhanced supercapacitor performance derived from coordination complexes." *Chemical Engineering Journal*, 292, 1–12.
- Kannappan, S., Kaliyappan, K., Manian, R. K., Pandian, A. S., Yang, H., Lee, Y. S., Jang, J.-H., and Lu, W. (2013). "Graphene based Supercapacitors with Improved Specific Capacitance and Fast Charging Time at High Current Density."
- Kato, H., Nishikawa, O., Matsui, T., Honma, S., and Kokado, H. (1991). "Fourier transform infrared spectroscopy study of conducting polymer polypyrrole: higher order structure of electrochemically-synthesized film." *J. Phys. Chem.*, 95(15), 6014–6016.
- Konwer, S., Maiti, J., and Dolui, S. K. (2011). "Preparation and optical/electrical/electrochemical properties of expanded graphite-filled polypyrrole nanocomposite." *Materials Chemistry and Physics*, 128(1–2), 283–290.
- Krishnan, S. G., Reddy, M. V., Harilal, M., Vidyadharan, B., Misnon, I. I., Rahim, M. H. A., Ismail, J., and Jose, R. (2015). "Characterization of MgCo₂O₄ as an electrode for high performance supercapacitors." *Electrochimica Acta*, 161, 312–321.
- Kumar, S. K. N., and Renuga, P. (2012). "OPTIMAL VAR PLANNING USING FACTS." *International Journal of Power and Energy Systems*, 32(2).
- Kumari, S., Maity, S., Vannathan, A. A., Shee, D., Das, P. P., and Mal, S. S. (2020). "Improved electrochemical performance of graphene oxide supported vanadomanganate (IV) nanohybrid electrode material for supercapacitors." *Ceramics International*, 46(3), 3028–3035.

- Lange, V., Picotti, P., Domon, B., and Aebersold, R. (2008). "Selected reaction monitoring for quantitative proteomics: a tutorial." *Mol Syst Biol*, 4(1), 222.
- Largeot, C., Portet, C., Chmiola, J., Taberna, P.-L., Gogotsi, Y., and Simon, P. (2008). "Relation between the Ion Size and Pore Size for an Electric Double-Layer Capacitor." *J. Am. Chem. Soc.*, 130(9), 2730–2731.
- Lei, Z., Christov, N., and Zhao, X. S. (2011). "Intercalation of mesoporous carbon spheres between reduced graphene oxide sheets for preparing high-rate supercapacitor electrodes." *Energy Environ. Sci.*, 4(5), 1866.
- Li, G.-R., Feng, Z.-P., Zhong, J.-H., Wang, Z.-L., and Tong, Y.-X. (2010). "Electrochemical Synthesis of Polyaniline Nanobelts with Predominant Electrochemical Performances." *Macromolecules*, 43(5), 2178–2183.
- Li, J., Xie, H., Li, Y., Liu, J., and Li, Z. (2011a). "Electrochemical properties of graphene nanosheets/polyaniline nanofibers composites as electrode for supercapacitors." *Journal of Power Sources*, 196(24), 10775–10781.
- Li, Z., Wang, J., Liu, X., Liu, S., Ou, J., and Yang, S. (2011b). "Electrostatic layer-by-layer self-assembly multilayer films based on graphene and manganese dioxide sheets as novel electrode materials for supercapacitors." *J. Mater. Chem.*, 21(10), 3397.
- Lin, J., Yan, S., Zhang, X., Liu, Y., Lian, J., Lin, H., Wei, W., Lu, D., and Han, S. (2019). "Facile Preparation of Holey Anderson-type Polyoxometalate/Polyaniline/Graphene Nanocomposites for Supercapacitors." *NANO*, 14(04), 1950049.
- Liu, H., Xu, B., Jia, M., Zhang, M., Cao, B., Zhao, X., and Wang, Y. (2015). "Polyaniline nanofiber/large mesoporous carbon composites as electrode materials for supercapacitors." *Applied Surface Science*, 332, 40–46.
- Liu, Z., Liang, G., Zhan, Y., Li, H., Wang, Z., Ma, L., Wang, Y., Niu, X., and Zhi, C. (2019). "A soft yet device-level dynamically super-tough supercapacitor enabled by an energy-dissipative dual-crosslinked hydrogel electrolyte." *Nano Energy*, 58, 732–742.
- Long, D.-L., Tsunashima, R., and Cronin, L. (2010). "Polyoxometalates: Building Blocks for Functional Nanoscale Systems." *Angew. Chem. Int. Ed.*, 49(10), 1736–1758.

- Luo, X., Wang, J., Dooner, M., and Clarke, J. (2015). “Overview of current development in electrical energy storage technologies and the application potential in power system operation.” *Applied Energy*, 137, 511–536.
- Mai, L.-Q., Minhas-Khan, A., Tian, X., Hercule, K. M., Zhao, Y.-L., Lin, X., and Xu, X. (2013). “Synergistic interaction between redox-active electrolyte and binder-free functionalized carbon for ultrahigh supercapacitor performance.” *Nat Commun*, 4(1), 2923.
- Maity, S., Bm, N., Kella, T., Shee, D., Das, P. P., and Mal, S. S. (2021a). “Activated carbon- supported Vanado-nickelate (IV) based hybrid materials for energy application.” *Journal of Energy Storage*, 40, 102727.
- Maity, S., Vannathan, A. A., Kella, T., Shee, D., Das, P. P., and Mal, S. S. (2021b). “Electrochemical performance of activated carbon-supported vanadomolybdates electrodes for energy conversion.” *Ceramics International*, 47(19), 27132–27141.
- Majumder, M., Choudhary, R. B., Koiry, S. P., Thakur, A. K., and Kumar, U. (2017). “Gravimetric and volumetric capacitive performance of polyindole/carbon black/MoS₂ hybrid electrode material for supercapacitor applications.” *Electrochimica Acta*, 248, 98–111.
- Manivel, A., Asiri, A. M., Alamry, K. A., Lana-Villarreal, T., and Anandan, S. (2014). “Interfacially synthesized PANi-PMo₁₂ hybrid material for supercapacitor applications.” *Bull Mater Sci*, 37(4), 861–869.
- Miao, J., Chen, Y., Li, Y., Cheng, J., Wu, Q., Ng, K. W., Cheng, X., Chen, R., Cheng, C., and Tang, Z. (2018). “Proton Conducting Polyoxometalate/Polypyrrole Films and Their Humidity Sensing Performance.” *ACS Appl. Nano Mater.*, 1(2), 564–571.
- Midilli, A., Ay, M., Dincer, I., and Rosen, M. A. (2005). “On hydrogen and hydrogen energy strategies.” *Renewable and Sustainable Energy Reviews*, 9(3), 255–271.
- Miras, H. N., Yan, J., Long, D.-L., and Cronin, L. (2012). “Engineering polyoxometalates with emergent properties.” *Chem. Soc. Rev.*, 41(22), 7403.
- Morishita, T., Soneda, Y., Hatori, H., and Inagaki, M. (2007). “Carbon-coated tungsten and molybdenum carbides for electrode of electrochemical capacitor.” *Electrochimica Acta*, 52(7), 2478–2484.
-

- Mostafaei, A., and Zolriasatein, A. (2012). "Synthesis and characterization of conducting polyaniline nanocomposites containing ZnO nanorods." *Progress in Natural Science: Materials International*, 22(4), 273–280.
- Mu, A., Li, J., Chen, W., Sang, X., Su, Z., and Wang, E. (2015). "The composite material based on Dawson-type polyoxometalate and activated carbon as the supercapacitor electrode." *Inorganic Chemistry Communications*, 55, 149–152.
- Mudila, H., Rana, S., Zaidi, M. G. H., and Alam, S. (2015). "Polyindole/Graphene Oxide Nanocomposites: The Novel Material for Electrochemical Energy Storage." *Fullerenes, Nanotubes and Carbon Nanostructures*, 23(1), 20–26.
- Murali, G., Rawal, J., Reddy Modigunta, J. K., Ho Park, Y., Lee, J.-H., Lee, S.-Y., Park, S.-J., and In, I. (2021). "A review on MXenes: new-generation 2D materials for supercapacitors." *Sustainable Energy & Fuels*, 5(22), 5672–5693.
- Muzaffar, A., Ahamed, M. B., Deshmukh, K., and Thirumalai, J. (2019). "A review on recent advances in hybrid supercapacitors: Design, fabrication and applications." *Renewable and Sustainable Energy Reviews*, 101, 123–145.
- Naarmann, H. (2000). "Polymers, Electrically Conducting." *Ullmann's Encyclopedia of Industrial Chemistry*, Wiley-VCH Verlag GmbH & Co. KGaA, ed., Weinheim, Germany: Wiley-VCH Verlag GmbH & Co. KGaA, a21_429.
- Padmanathan, N., and Selladurai, S. (2014). "Shape controlled synthesis of CeO₂ nanostructures for high performance supercapacitor electrodes." *RSC Adv.*, 4(13), 6527.
- Palomino, P., Suarez-Guevara, J., Olivares-Marín, M., Ruiz, V., Dubal, D. P., Gómez-Romero, P., Tonti, D., and Enciso, E. (2017). "Influence of texture in hybrid carbon-phosphomolybdcic acid materials on their performance as electrodes in supercapacitors." *Carbon*, 111, 74–82.
- Pan, C., Gu, H., and Dong, L. (2016). "Synthesis and electrochemical performance of polyaniline @MnO₂/graphene ternary composites for electrochemical supercapacitors." *Journal of Power Sources*, 303, 175–181.

- Panwar, N. L., Kaushik, S. C., and Kothari, S. (2011). "Role of renewable energy sources in environmental protection: A review." *Renewable and Sustainable Energy Reviews*, 15(3), 1513–1524.
- Pawar, S. G., Patil, S. L., Chougule, M. A., Mane, A. T., Jundale, D. M., and Patil, V. B. (2010). "Synthesis and Characterization of Polyaniline:TiO₂ Nanocomposites." *International Journal of Polymeric Materials*, 59(10), 777–785.
- Ponja, S. D., Sathasivam, S., Davies, H. O., Parkin, I. P., and Carmalt, C. J. (2016). "Polyoxometalate Complexes as Precursors to Vanadium-Doped Molybdenum or Tungsten Oxide Thin Films by Means of Aerosol-Assisted Chemical Vapour Deposition." *ChemPlusChem*, 81(3), 307–314.
- Purty, B., Choudhary, R. B., Biswas, A., and Udayabhanu, G. (2019). "Chemically grown mesoporous f-CNT/ α -MnO₂/PIn nanocomposites as electrode materials for supercapacitor application." *Polym. Bull.*, 76(4), 1619–1640.
- Rajagopalan, B., and Chung, J. S. (2014). "Reduced chemically modified graphene oxide for supercapacitor electrode." *Nanoscale Res Lett*, 9(1), 535.
- Rajaitha, P. M., Hajra, S., Mistewicz, K., Panda, S., Sahu, M., Dubal, D., Yamauchi, Y., and Kim, H. J. (2022). "Multifunctional materials for photo-electrochemical water splitting." *J. Mater. Chem. A*, 10(30), 15906–15931.
- Ran, F., Tan, Y., Dong, W., Liu, Z., Kong, L., and Kang, L. (2018). "In situ polymerization and reduction to fabricate gold nanoparticle-incorporated polyaniline as supercapacitor electrode materials." *Polymers for Advanced Technologies*, 29(6), 1697–1705.
- Ruckenstein, E., and Chen, J.-H. (1991). "Polypyrrole conductive composites prepared by coprecipitation." *Polymer*, 32(7), 1230–1235.
- Ruiz, V., Suárez-Guevara, J., and Gomez-Romero, P. (2012). "Hybrid electrodes based on polyoxometalate–carbon materials for electrochemical supercapacitors." *Electrochemistry Communications*, 24, 35–38.
- Saikia, B. K., Benoy, S. M., Bora, M., Tamuly, J., Pandey, M., and Bhattacharya, D. (2020). "A brief review on supercapacitor energy storage devices and utilization of natural carbon resources as their electrode materials." *Fuel*, 282, 118796.
-

- Salanne, M., Rotenberg, B., Naoi, K., Kaneko, K., Taberna, P.-L., Grey, C. P., Dunn, B., and Simon, P. (2016). “Efficient storage mechanisms for building better supercapacitors.” *Nat Energy*, 1(6), 16070.
- Sapurina, I., Osadchev, A. Yu., Volchek, B. Z., Trchová, M., Riede, A., and Stejskal, J. (2002). “In-situ polymerized polyaniline films.” *Synthetic Metals*, 129(1), 29–37.
- Sarno, M. (2020). “Nanotechnology in energy storage: the supercapacitors.” *Studies in Surface Science and Catalysis*, Elsevier, 431–458.
- Shao, Y., El-Kady, M. F., Sun, J., Li, Y., Zhang, Q., Zhu, M., Wang, H., Dunn, B., and Kaner, R. B. (2018). “Design and Mechanisms of Asymmetric Supercapacitors.” *Chem. Rev.*, 118(18), 9233–9280.
- Shown, I., Ganguly, A., Chen, L., and Chen, K. (2015). “Conducting polymer-based flexible supercapacitor.” *Energy Sci Eng*, 3(1), 2–26.
- Simon, P., and Burke, A. (2008). “Nanostructured carbons: double-layer capacitance and more.” *The electrochemical society interface*, 17(1), 38.
- Simon, P., Gogotsi, Y., and Dunn, B. (2014). “Where Do Batteries End and Supercapacitors Begin?” *Science*, 343(6176), 1210–1211.
- Singh, A. P., Tiwari, N. K., Karandikar, P. B., and Dubey, A. (2015). “Effect of electrode shape on the parameters of supercapacitor.” *2015 International Conference on Industrial Instrumentation and Control (ICIC)*, Pune, India: IEEE, 669–673.
- Smith, D. P., and Pope, M. T. (1973). “Heteropoly 12-metallophosphates containing tungsten and vanadium. Preparation, voltammetry, and properties of mono-, di-, tetra-, and hexavanado complexes.” *Inorg. Chem.*, 12(2), 331–336.
- Snook, G. A., Kao, P., and Best, A. S. (2011). “Conducting-polymer-based supercapacitor devices and electrodes.” *Journal of Power Sources*, 196(1), 1–12.
- Sowmya, and Selvakumar, M. (2018). “Multilayered electrode materials based on polyaniline/activated carbon composites for supercapacitor applications.” *International Journal of Hydrogen Energy*, 43(8), 4067–4080.

- Suárez-Guevara, J., Ruiz, V., and Gomez-Romero, P. (2014). “Hybrid energy storage: high voltage aqueous supercapacitors based on activated carbon–phosphotungstate hybrid materials.” *J. Mater. Chem. A*, 2(4), 1014–1021.
- Swain, N., Saravanakumar, B., Kundu, M., Schmidt-Mende, L., and Ramadoss, A. (2021). “Recent trends in template assisted 3D porous materials for electrochemical supercapacitors.” *J. Mater. Chem. A*, 9(45), 25286–25324.
- Taberna, P. L., Simon, P., and Fauvarque, J. F. (2003). “Electrochemical Characteristics and Impedance Spectroscopy Studies of Carbon-Carbon Supercapacitors.” *J. Electrochem. Soc.*, 150(3), A292.
- Tan, Y.-T., Ran, F., Kong, L.-B., Liu, J., and Kang, L. (2012). “Polyaniline nanoparticles grown on the surface of carbon microspheres aggregations for electrochemical supercapacitors.” *Synthetic Metals*, 162(1), 114–118.
- Uma, T., and Nogami, M. (2007). “Structural and Transport Properties of Mixed Phosphotungstic Acid/Phosphomolybdic Acid/SiO₂ Glass Membranes for H₂/O₂ Fuel Cells.” *Chem. Mater.*, 19(15), 3604–3610.
- Vaillant, J., Lira-Cantu, M., Cuentas-Gallegos, K., Casañ-Pastor, N., and Gómez-Romero, P. (2006). “Chemical synthesis of hybrid materials based on PANi and PEDOT with polyoxometalates for electrochemical supercapacitors.” *Progress in Solid State Chemistry*, 34(2–4), 147–159.
- Vangari, M., Pryor, T., and Jiang, L. (2013). “Supercapacitors: Review of Materials and Fabrication Methods.” *J. Energy Eng.*, 139(2), 72–79.
- Vannathan, A. A., Kella, T., Shee, D., and Mal, S. S. (2021). “One-Pot Synthesis of Polyoxometalate Decorated Polyindole for Energy Storage Supercapacitors.” *ACS Omega*, 6(17), 11199–11208.
- Vannathan, A. A., Kella, T., Shee, D., and Mal, S. S. (2022). “Investigations of redox-active polyoxomolybdate embedded polyaniline-based electrode material for energy application.” *Ionics*, 28(3), 1295–1310.

- Vannathan, A. A., Maity, S., Kella, T., Shee, D., Das, P. P., and Mal, S. S. (2020). “In situ vanadophosphomolybdate impregnated into conducting polypyrrole for supercapacitor.” *Electrochimica Acta*, 364, 137286.
- Viswanathan, A., and Shetty, A. N. (2017). “Facile in-situ single step chemical synthesis of reduced graphene oxide-copper oxide-polyaniline nanocomposite and its electrochemical performance for supercapacitor application.” *Electrochimica Acta*, 257, 483–493.
- Walkowiak, M., Wasinski, K., Polrolniczak, P., Martyla, A., Waszak, D., Surendran, A. A., and Lota, G. (2015). “Graphene and Graphene Composites in Electrochemical Capacitors and Li-Ion Batteries.” *ECS Trans.*, 70(1), 27–36.
- Wang, G., Zhang, L., and Zhang, J. (2012). “A review of electrode materials for electrochemical supercapacitors.” *Chem. Soc. Rev.*, 41(2), 797–828.
- Wang, H.-N., Zhang, M., Zhang, A.-M., Shen, F.-C., Wang, X.-K., Sun, S.-N., Chen, Y.-J., and Lan, Y.-Q. (2018a). “Polyoxometalate-Based Metal–Organic Frameworks with Conductive Polypyrrole for Supercapacitors.” *ACS Appl. Mater. Interfaces*, 10(38), 32265–32270.
- Wang, H.-N., Zhang, M., Zhang, A.-M., Shen, F.-C., Wang, X.-K., Sun, S.-N., Chen, Y.-J., and Lan, Y.-Q. (2018b). “Polyoxometalate-Based Metal–Organic Frameworks with Conductive Polypyrrole for Supercapacitors.” *ACS Appl. Mater. Interfaces*, 10(38), 32265–32270.
- Wang, L., Yang, H., Pan, G., Miao, L., Chen, S., and Song, Y. (2017). “Polyaniline-Carbon Nanotubes@Zeolite Imidazolate Framework-67-Carbon Cloth Hierarchical Nanostructures for Supercapacitor Electrode.” *Electrochimica Acta*, 240, 16–23.
- Wang, M., Yu, Y., Cui, M., Cao, X., Liu, W., Wu, C., Liu, X., Zhang, T., and Huang, Y. (2020a). “Development of polyoxometalate-anchored 3D hybrid hydrogel for high-performance flexible pseudo-solid-state supercapacitor.” *Electrochimica Acta*, 329, 135181.
- Wang, S., Tan, Z., Li, Y., Sun, L., and Zhang, T. (2006). “Synthesis, characterization and thermal analysis of polyaniline/ZrO₂ composites.” *Thermochimica Acta*, 441(2), 191–194.

- Wang, W., and Wu, S. (2017). “A new ternary composite based on carbon nanotubes/polyindole/graphene with preeminent electrocapacitive performance for supercapacitors.” *Applied Surface Science*, 396, 1360–1367.
- Wang, Y., Song, Y., and Xia, Y. (2016). “Electrochemical capacitors: mechanism, materials, systems, characterization and applications.” *Chem. Soc. Rev.*, 45(21), 5925–5950.
- Wang, Z., Zhu, M., Pei, Z., Xue, Q., Li, H., Huang, Y., and Zhi, C. (2020b). “Polymers for supercapacitors: Boosting the development of the flexible and wearable energy storage.” *Materials Science and Engineering: R: Reports*, 139, 100520.
- White, A. M., and Slade, R. C. T. (2003a). “Polymer electrodes doped with heteropolymetallates and their use within solid-state supercapacitors.” *Synthetic Metals*, 139(1), 123–131.
- White, A. M., and Slade, R. C. T. (2003b). “Investigation of vapour-grown conductive polymer/heteropolyacid electrodes.” *Electrochimica Acta*, 48(18), 2583–2588.
- Wu, H. P., He, D. W., Wang, Y. S., Fu, M., Liu, Z. L., Wang, J. G., and Wang, H. T. (2010a). “Graphene as the electrode material in supercapacitors.” *2010 8th International Vacuum Electron Sources Conference and Nanocarbon*, Nanjing: IEEE, 465–466.
- Wu, H.-C., Lin, Y.-P., Lee, E., Lin, W.-T., Hu, J.-K., Chen, H.-C., and Wu, N.-L. (2009). “High-performance carbon-based supercapacitors using Al current-collector with conformal carbon coating.” *Materials Chemistry and Physics*, 117(1), 294–300.
- Wu, Q., Xu, Y., Yao, Z., Liu, A., and Shi, G. (2010b). “Supercapacitors Based on Flexible Graphene/Polyaniline Nanofiber Composite Films.” *ACS Nano*, 4(4), 1963–1970.
- Xia, X., Hao, Q., Lei, W., Wang, W., Wang, H., and Wang, X. (2012). “Reduced-graphene oxide/molybdenum oxide/polyaniline ternary composite for high energy density supercapacitors: Synthesis and properties.” *J. Mater. Chem.*, 22(17), 8314.
- Xu, Y., Schwab, M. G., Strudwick, A. J., Hennig, I., Feng, X., Wu, Z., and Müllen, K. (2013). “Screen-Printable Thin Film Supercapacitor Device Utilizing Graphene/Polyaniline Inks.” *Adv. Energy Mater.*, 3(8), 1035–1040.

- Yagci, Y., Yilmaz, F., Kiralp, S., and Toppare, L. (2005). "Photoinduced Polymerization of Thiophene Using Iodonium Salt." *Macromol. Chem. Phys.*, 206(12), 1178–1182.
- Yan, D., Liu, Y., Li, Y., Zhuo, R., Wu, Z., Ren, P., Li, S., Wang, J., Yan, P., and Geng, Z. (2014). "Synthesis and electrochemical properties of MnO₂/rGO/PEDOT:PSS ternary composite electrode material for supercapacitors." *Materials Letters*, 127, 53–55.
- Zhang, J., Kong, L.-B., Wang, B., Luo, Y.-C., and Kang, L. (2009a). "In-situ electrochemical polymerization of multi-walled carbon nanotube/polyaniline composite films for electrochemical supercapacitors." *Synthetic Metals*, 159(3–4), 260–266.
- Zhang, M., Liu, J., Li, H., Wei, Y., Fu, Y., Liao, W., Zhu, L., Chen, G., Zhu, W., and Li, H. (2020). "Tuning the electrophilicity of vanadium-substituted polyoxometalate based ionic liquids for high-efficiency aerobic oxidative desulfurization." *Applied Catalysis B: Environmental*, 271, 118936.
- Zhang, Q., Uchaker, E., Candelaria, S. L., and Cao, G. (2013). "Nanomaterials for energy conversion and storage." *Chem. Soc. Rev.*, 42(7), 3127.
- Zhang, Y., Feng, H., Wu, X., Wang, L., Zhang, A., Xia, T., Dong, H., Li, X., and Zhang, L. (2009b). "Progress of electrochemical capacitor electrode materials: A review." *International Journal of Hydrogen Energy*, 34(11), 4889–4899.
- Zhao, C., Zheng, W., Wang, X., Zhang, H., Cui, X., and Wang, H. (2013). "Ultrahigh capacitive performance from both Co(OH)₂/graphene electrode and K₃Fe(CN)₆ electrolyte." *Sci Rep*, 3(1), 2986.
- Zheng, M., Ding, Y., Cao, X., Tian, T., and Lin, J. (2018). "Homogeneous and heterogeneous photocatalytic water oxidation by polyoxometalates containing the most earth-abundant transition metal, iron." *Applied Catalysis B: Environmental*, 237, 1091–1100.
- Zhi, M., Xiang, C., Li, J., Li, M., and Wu, N. (2013). "Nanostructured carbon–metal oxide composite electrodes for supercapacitors: a review." *Nanoscale*, 5(1), 72–88.
- Zhong, C., Deng, Y., Hu, W., Qiao, J., Zhang, L., and Zhang, J. (2015). "A review of electrolyte materials and compositions for electrochemical supercapacitors." *Chem. Soc. Rev.*, 44(21), 7484–7539.
-

- Zhou, Q., Zhu, D., Ma, X., Xu, J., Zhou, W., and Zhao, F. (2016). “High-performance capacitive behavior of layered reduced graphene oxide and polyindole nanocomposite materials.” *RSC Adv.*, 6(35), 29840–29847.
- Zhou, W., and Xu, J. (2017). “Progress in Conjugated Polyindoles: Synthesis, Polymerization Mechanisms, Properties, and Applications.” *Polymer Reviews*, 57(2), 248–275.
- Zhu, J., Song, D., Pu, T., Li, J., Huang, B., Wang, W., Zhao, C., Xie, L., and Chen, L. (2018). “Two-dimensional porous ZnCo₂O₄ thin sheets assembled by 3D nanoflake array with enhanced performance for aqueous asymmetric supercapacitor.” *Chemical Engineering Journal*, 336, 679–689.

CURRICULAM VITAE

ANJANA A V

**Research Scholar, Department of Chemistry, National
Institute of Technology Karnataka, Surathkal-575025**



PROFESSIONAL SUMMARY

A highly dedicated Doctoral Research Fellow with hands-on experience and record accomplishment in the field of Supercapacitor Self-motivated and hardworking professional with methodical and detail-oriented approach. Diligent and reliable with a strong ability to solve scientific problems, highly organized, proactive, and punctual with a team-oriented mentality.

EDUCATIONAL EXPERIENCE

Ph.D. in Chemistry, National Institute of Technology Karnataka, India. 2018- 2023

National Eligibility Test [NET] for Lectureship in Chemistry, CSIR, New Delhi. 2016

M. Sc. in Chemistry, St. Agnes College, Mangalore, Karnataka, India. 2013 – 2015

B. Sc. in Chemistry, Government College Kasaragod, Kerala, India. 2010 – 2013

RESEARCH EXPERIENCE

- ❖ PhD Scholar (July 2018 – Thesis Submitted) Department of Chemistry, National Institute of Technology Karnataka, Surathkal, India.
- ❖ Masters Research Internship (December 2014 – May 2015) Topic: Acid-modified clay and an efficient catalyst for benzylation at Government College, Kasaragod

MAJOR PUBLICATIONS

1. **Vannathan, A. A.**, Maity, S., Kella, T., Shee, D., Das, P. P., & Mal, S. S. (2020). In situ vanadophosphomolybdate impregnated into conducting polypyrrole for supercapacitor. *Electrochimica Acta*, 364, 137286.
2. **Vannathan, A. A.**, Chandewar, P. R., Shee, D., & Mal, S. S. (2022). Asymmetric polyoxometalate-polypyrrole composite electrode material for electrochemical energy storage supercapacitors. *Journal of Electroanalytical Chemistry*, 904, 115856.
3. **Vannathan, A. A.**, Kella, T., Shee, D., & Mal, S. S. (2021). One-pot synthesis of polyoxometalate decorated polyindole for energy storage supercapacitors. *ACS omega*, 6(17), 11199-11208.
4. **Vannathan, A. A.**, Thakre, D., Ali, S. R., De, M., Banerjee, A., & Mal, S. S. (2021). Investigations into the supercapacitor activity of bisphosphonate-polyoxovanadate compounds. *Journal of Solid State Chemistry*, 304, 122566.
5. **Vannathan, A. A.**, Chandewar, P. R., Shee, D., & Mal, S. S. (2022). Polyoxovanadate-Activated Carbon-Based Hybrid Materials for High-Performance Electrochemical Capacitors. *Journal of The Electrochemical Society*, 169(5), 050538.
6. **Vannathan, A. A.**, Kella, T., Shee, D., & Mal, S. S. (2022). Investigations of redox-active polyoxomolybdate embedded polyaniline-based electrode material for energy application. *Ionics*, 28(3), 1295-1310.
7. P K, M. A., **Vannathan, A. A.**, Kella, T., Shee, D., & Mal, S. S. (2021). Organic cation linkers polyoxomolybdate-polypyrrole nanocomposite-based supercapacitors. *Ionics*, 27(9), 4023-4035.
8. Thakre, D., **Anandan Vannathan, A.**, Banerjee, A., & Mal, S. S. (2022). Supercapacitor activity studies of a unique triangular oxo-vanadate-bisphosphonate composite with activated carbon. *Ionics*, 1-10.
9. Kumari, S., Maity, S., **Vannathan, A. A.**, Shee, D., Das, P. P., & Mal, S. S. (2020). Improved electrochemical performance of graphene oxide supported vanadomanganate (IV) nanohybrid electrode material for supercapacitors. *Ceramics International*, 46(3), 3028-3035.
10. Marques-da-Silva, D., Fraqueza, G., Lagoa, R., **Vannathan, A. A.**, Mal, S. S., & Aureliano, M. (2019). Polyoxovanadate inhibition of *Escherichia coli* growth shows a reverse correlation with Ca^{2+} -ATPase inhibition. *New Journal of Chemistry*, 43(45), 17577-17587.
11. Maity, S., **Vannathan, A. A.**, Kella, T., Shee, D., Das, P. P., & Mal, S. S. (2021). Electrochemical performance of activated carbon-supported vanadomolybdates electrodes for energy conversion. *Ceramics International*, 47(19), 27132-27141.
12. Anees, P. M., **Vannathan, A. A.**, Abhijith, M. B., Kella, T., Shee, D., & Mal, S. S. (2022). Imidazolium cation linkers of polyoxomolybdate-polypyrrole nanocomposite electrode-based energy storage supercapacitors. *Materials Chemistry and Physics*, 277, 125441.

13. Maity, S., **Vannathan, A. A.**, Kumar, K., Das, P. P., & Mal, S. S. (2021). Enhanced Power Density of Graphene Oxide–Phosphotetradecavanadate Nanohybrid for Supercapacitor Electrode. *Journal of Materials Engineering and Performance*, 30(2), 1371-1377.
14. Maity, S., **Vannathan, A. A.**, Chandewar, P. R., Shee, D., Das, P. P., & Mal, S. S. (2022). Vanadomanganate as a synergistic component in high-performance symmetric supercapacitor. *Journal of Alloys and Compounds*, 899, 163239.
15. Banik, S., Melanthota, S. K., **Vannathan, A. A.**, Mahato, K. K., Mal, S. S., & Mazumder, N. (2022). Spectroscopic methods for assessment of hand sanitizers. *Chemical Papers*, 1-12.

PATENTS

1. Method of preparation of high energy density conducting polyaniline-phosphovanadomolybdate nanohybrid electrode for supercapacitor device application (Sib Sankar Mal and Anjana Anandan Vannathan), India patent application no. 202041047969 dated 03/11/2020
2. A high-performance supercapacitor device of polyaniline-triethyl amine ionic liquid combined phosphomolybdate electrode and method thereof (Sib Sankar Mal, Saikat Dutta, Anjana Anandan Vannathan, Muhammed Anees P K), Filed India patent application no. 202141007885 dated 24/02/2021

WORKSHOP AND CONFERENCE ATTENDED

- Participation in one day National Workshop on “Recent Advances in Material Chemistry (RAMC)” on Sep 26, 2019, held at NITK, Surathkal.
- Poster Presentation in International Conference on Advances in Chemical and Material Science during Oct 17-19, 2019, held at Department of Chemistry, Mangalore University.
- Participated and presented a research paper in an International Conference on “Energy and Environmental Technologies for Sustainable Development (CHEM-fulx20)” During Feb 14-15, 2020, held at MNNIT Allahabad, Prayagraj.
- Best oral presentation during Sustainable and Green Technologies session in an International Conference on “Energy and Environmental Technologies for Sustainable Development (CHEM-fulx20)” During Feb 14-15, 2020 held at MNNIT Allahabad, Prayagraj.
- participated in the five-day e-workshop titled “Advancements in the Molecular World: Materials and Catalysis” (AMWMC-2021) conducted by the Department of Chemistry, NITK Surathkal during February 15-19, 2021.

- Participated and presented a research paper in a (Virtual Conference) SRM Institute of Science and Technology International Conference on Nanoscience and Nanotechnology (ICONN 2021) organized by Department of Physics and Nanotechnology, SRM IST, India during February 01 – 03, 2021
 - First International Conference on Technologies for Smart Green Connected Society 2021 29th-30th November 2021 | Online | World Wide.
-

RELEVANT LABORATORY AND INSTRUMENTATION SKILLS

- Setting the reaction setup for catalysis reactions and electrochemical setups.
 - Synthesis of various polyoxometalates, conducting polymer and its composites
 - Synthesis of conducting polymer nanotubes.
 - Electrode coating for electrochemical reactions.
 - Operating and analysis of FT-IR spectroscopy, UV-VIS, TGA, Single crystal XRD, BET, XPS, XRD, FESEM, TEM and Electrochemical studies (CV, GCD, Impedence etc)
-

GENERAL SKILLS

- Microsoft Office, Microsoft Excel
 - Handling Xpert Highscore, Origin Pro 2022, ZSimpWin, chem draw, ImageJ software's
 - Guided 3 PG students with project works during my PhD
 - Problem-Solving & Critical Thinking
 - Lab Report Completion Procedures, Discussion Facilitation.
 - Tutoring and Mentoring, Class Work Submission Procedures.
 - Quantitative Research & Qualitative Research
 - Academic Writing, Academic Presentations & Project Support
 - Laboratory Oversight, Academic Monitoring
 - Group Assistance & Administrative Support
-

PERSONAL INFORMATION

Nationality : Indian
Gender : Female
Date of Birth : 13 - 01 - 1993
Email id : anjana201553@gmail.com

